SHAPE MEMORY POLYMERIC NANOCOMPOSITES FOR BIOLOGICAL APPLICATIONS

BIN XU

A dissertation submitted for the degree of Doctor of Philosophy

Heriot-Watt University
School of Engineering and Physical Sciences

MAY 2011

Abstract

The aim of this work is to develop novel shape memory polymers (SMPs) and nanocomposites for potential biological applications. A kind of commercial SMP, shape memory polyurethane (SMPU), was used to prepare nanocomposites by incorporating nano-clay into the SMPU substrate. The mechanical behaviour, thermal property and shape memory efficiency were studied with various nanofiller loadings. Chemical synthesis methods were also employed to prepare the other designable SMP and its nanocomposites, i.e. the shape memory polystyrene co-polymer (SMPS). Multiple technologies were adopted to enhance the SMPS matrix such as modifying the chemical components, introducing various functional nanoparticles into the polymeric network and improving the dispersion of the nanoparticles. Different methods were used to characterize the overall performance of the obtained materials. Mechanical tests were performed at different dimensional scales with a varied degree of localisation. Nanoindentation was firstly applied to assess the micro-mechanical properties of shape memory polymer nanocomposites at scales down to particle size. The micro-mechanical analysis provided the fundamental information on the SMPs and their nanocomposites for bio-MEMS applications. Potential applications were also explored through manufacturing different type of device models and testing their shape recovery efficiencies. Finally, theoretical contributions were made in two areas. The first one was the theoretical analysis on the nanoparticles enhancement to the soft polymeric matrix. The other was in developing a constitutive model to describe the thermo-viscoelastic property and shape memory behaviour for SMP nanocomposites.

ACADEMIC REGISTRY
Research Thesis Submission

Name*:*	BIN XU		
School/PGI:	School of Engineering and Physical Sciences		
Version: *(i.e. First, Resubmission, Final)*	Final	Degree Sought (Award **and** Subject area)	PhD Mechanical Engineering

Declaration

In accordance with the appropriate regulations I hereby submit my thesis and I declare that:

1) the thesis embodies the results of my own work and has been composed by myself
2) where appropriate, I have made acknowledgement of the work of others and have made reference to work carried out in collaboration with other persons
3) the thesis is the correct version of the thesis for submission and is the same version as any electronic versions submitted*.
4) my thesis for the award referred to, deposited in the Heriot-Watt University Library, should be made available for loan or photocopying and be available via the Institutional Repository, subject to such conditions as the Librarian may require
5) I understand that as a student of the University I am required to abide by the Regulations of the University and to conform to its discipline.

* *Please note that it is the responsibility of the candidate to ensure that the correct version of the thesis is submitted.*

Signature of Candidate*:*		Date:	

Submission

Submitted By *(name in capitals):*	BIN XU
Signature of Individual Submitting:	
Date Submitted:	

For Completion in Academic Registry

Received in the Academic Registry by *(name in capitals):*			
Method of Submission *(Handed in to Academic Registry; posted through internal/external mail):*			
E-thesis Submitted (mandatory for final theses from January 2009)			
Signature:		Date:	

Dedication

To my wonderful parents

A.G Xu, W.Y Ye

and lovely wife

伊兰 (Yilan)

Acknowledgements

I would like to take this opportunity to thank my supervisor, Dr Richard Y. Q. FU, for his kindness advices, supports, encouragements and friendship in the past exciting and fruitful three years.

I also wish to express my gratitude to my co-supervisors, Prof. Bob Reuben and Dr. Arno Kraft, who provided me great help from their own academic fields. I would like to thank to School of EPS, Heriot-Watt University for providing financial support for my studies.

I appreciate the contributions from the collaborated institutes and project partners, which are:

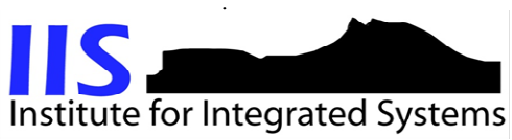




Sincerely thanks for the staffs who have assisted me on my research, especially Marian Millar, George Smith, Cameron Smith and the technician team led by Richard Kinsella. I am also very thankful to all secretaries in HWU who always provided great help through the administrative processes.

And there are some many friends I should never forget, W.L. Chang, J.N. Sun, W. Wei, H. Valera, Daniele N. M. Santonocito, W.X Wang, Y.F. Li, etc.

Finally, I would like to thank my parents and my wife for supporting me on studying aboard.

IMPORTANT NOMENCLATURE AND ABBREVIATIONS

SMP	shape memory polymer
SMPU	shape memory polyurethane
SMPS	shape memory polystyrene
RR	shape recovery ratio
R_r	cyclic strain recovery ratio
T	temperature
T_{trans}	transition temperature
T_g	glass transition temperature
T_m	melting temperature
DMTA	dynamic mechanical thermal analysis
DSC	differential scanning calorimetry
TGA	thermalgravimetry analysis
AFM	atom force microscopy
OM	optical microsocy
DE	dissipation energy
E	elastic modulus
H	hardness
$tan\ \delta$	phase angle, Tan (delta)
φ	volume fraction
Ξ	conductivity
Ø	complex permittivity
tan Э	dielectric loss
l/d	aspect ratio
ε	stress
δ	strain

Table of Contents

List of publications

- ***Journal paper:***

1. ***Bin Xu***, W.M. Huang, Y.T. Pei, Z.G. Chen, A. Kraft, R. Reuben, J.Th.M. De Hosson and Y.Q. Fu. Mechanical properties of attapulgite clay reinforced polyurethane shape memory nanocomposites, *European Polymer Journal,45 (2009), pp. 1904–11*.

2. ***Bin Xu***, Y. Q. Fu, M. Ahmad, J. K. Luo, W. M. Huang, A. Kraft, R. Reuben, Y. T. Pei, Z. G. Chen and J. Th. M. De Hosson. Thermo-mechanical properties of polystyrene-based shape memory nanocomposites, *Journal of Materials Chemistry,20(2010), pp. 3442-8.*

3. ***Bin Xu***, Yong Qing Fu, Wei Min Huang, Yu Tao Pei, Zhen Guo Chen, Jeff T.M. De Hosson, Arno Kraft and R. L. Reuben. Thermal-Mechanical Properties of Polyurethane-Clay Shape Memory Polymer Nanocomposites. *Polymers, 2(2010), pp.31-9.*

4. ***Bin Xu***, Y. Q. Fu, *et al.*, Electro-actuating smart polymer nanocomposites: electrical, dielectric and shape recovery characterization, *Physical Chemistry Chemical Physics, correction with editor suggestion.*

5. Y.Q. Fu, C Shearwood, ***B. Xu***, L G Yu and K A Khor. Characterization of spark plasma sintered Ag nano-powders, *Nanotechnology 21 (2010) 115707 (7pp).*

6. Yinzhu Jiang, Wenping Sun, ***Bin Xu***, Mi Yan, Naoufal Bahlawane. Unusual enhancement in electrical conductivity of tin oxide thin films with zinc doping. *Physical Chemistry Chemical Physics, DOI: 10.1039/c0cp00816h.*

7. M. Ahmad, J.K. Luo, ***B. Xu***, H. Purnawali, P.J. King, P. Chalker, Y.Q. Fu, W.M. Huang and M. Miraftab. Synthesis and Characterization of Polyurethane-based Shape Memory Polymer for tailored Tg around Body Temperature for Medical Applications, *Macromolecular Chemistry and Physics, 121(2011), pp. 592-602.*

8. Nano-mechanics of carbon nanofillers /PS shape memory composites, *to be submited*.

9. Visco-elastic behaviour and surface mechanics of carbon nano-filler or carbon nanotube filled composites on nanoindentation process, *to be submited*.

10. FIB micro-manufacture and recovery investigation for the CNT/PS shape memory composites based device, *to be submited*.

- ***Conference & seminar:***

1. Nano carbon filled smart materials: electrical, micro/nano mechanical properties and Nano-fabrication technique with Focus Ion Beam, *THINFILMS 2010, HAERBIN, CHINA,2010, Page 380*. (**ORAL PRESENTATION**)

2. Polystyrene based shape memory nanocomposites, *ICCM 17, Edinburgh, 2009,28:IE6:2*. (**POSTER**)

3. Polyurethane/nano-clay shape memory polymer nanocomposites, *Hybrid Material 2009, France, B19*. (**ORAL PRESENTATION**)

4. 5/12/2008, Invited seminar, Speaker: Mr Bin Xu, Mechanical Dept., HWU
Title: Investigation on the response behaviour, mechanism and MEMS application of shape memory polymer

Chapter 1

INTRODUCTION

The aim of the work presented in this thesis is to investigate aspects of the fabrication and properties of new functional materials, namely shape memory polymers (SMPs) and their associated nanocomposites, made by reinforcing the polymer with nanoparticles. The main objectives of this research are to reveal the effects of nanoparticle reinforcement on mechanical, thermal and thermo-mechanical properties and also on the shape memory effect, and to design and test devices based on these shape memory materials as an exploration of potential application areas.

1.1 Background of shape memory polymer and nanocomposites

Polymeric materials are capable of a shape memory effect, although the mechanisms responsible differ dramatically from those of shape memory alloys (SMAs). Current opinion is that SMPs achieve temporary strain fixing and recovery through a variety of physical means, with the underlying very large extensibility being derived from the intrinsic elasticity of polymeric networks. Earlier studies of SMPs were mainly into the shape memory phenomenon itself and the main focus was preparation of these new materials for various applications. More recent work has focused on particular aspects, for example by Lendlein *et al.*[1-5] (synthesis, functionalizing and biological application), Gall *et al.* [6-9] (functionalizing and shape memory mechanism), Tobushi *et al.* [10-15] (SMP structure-property relationships), Hu *et al.* [16-23] (SMP synthesis and smart textile fibers), Huang *et al.* [24-29] (SMP and nanocomposite physical properties), Leng *et al.* [30-38] (functionalizing and SMP physical properties), Wilson *et al.* [39-47] (structure-property relationships and bio-medical applications), and Nguyen *et al.* [48-50] (modelling and mechanisms). It is widely acknowledged that the particular properties of SMPs can fulfil important roles in many applications, and new techniques are continually sought to modify their properties according to new conditions. Developments on theories and mechanisms have revealed the internal changes during the shape recovery, which offer a better understanding and open up the possibility of modelling shape memory behaviour for different polymeric materials.

Although much work has already been done on SMPs as outlined above, several critical issues remain unsolved as far as we know. For example, there are no detailed studies on the enhancing mechanisms of nano-particles for either mechanical or electrical properties which should be supported by clear structure-property explanations. There is also, as yet, no constitutive model to predict the shape memory behaviour of the nanocomposite system.

1.2 Objectives

The overall aim of the work is to find a class of SMPs or nanocomposites with stable chemical and physical properties, which meet the requirements for potential biological applications. The work involves the application of a range of advanced chemical, physical and mechanical testing techniques, since the related materials synthesis through the chemical reactions and the characterizations demand extensive physical structure-properties knowledge.

The approach was to use commercial SMPs as a reference for the mechanical, thermal and shape memory properties, and then systematically to design SMPs and nanocomposites using appropriate fabrication technology. Specific consideration was given to the control of the chemical synthesis, especially on the dispersion treatment for the nanocomposites. The chosen SMPs and nanocomposites were characterised at the macroscopic and microscopic scales and their overall performance were assessed.

Mechanical properties were evaluated using a combination of uniaxial tensile testing, Vickers micro-indentation and nanoindentation. Tensile testing gives the bulk mechanical property, whereas microhardness offered a degree of localisation and was also used to obtain microhardness-transition temperature relations. Nanoindentation was used to provide further information for structure-property relations allowing measurement down to particle level. Other tests, such as thermal analysis and electron microscopy were used to provide microstructural information directly or indirectly to support the development of structure-property relationships.

Shape memory behaviour was assessed using a range of triggering conditions. Some ancillary measurements, such as conductivity and dielectric tests were also carried out to assess the material modification efficiency as well as to obtain the setting factors for

shape memory tests. Various demonstrations were carried out and a thermal-mechanical tensile test was used to quantify the shape memory effect. Finally, dynamical thermal mechanical analysis (DMTA) was also used to provide thermo-mechanical information for the specimen materials.

It was anticipated that novel SMPs or SMP-based nanocomposites would be identified in this research, alongside the establishment of a method for the evaluation of shape memory efficiency for this type of SMP. Analysis of the data was expected to result in the recognition of structure-property relationships in these polymeric systems, as well as a general understanding of shape memory behaviour in SMPs. Advances in the biological applications were also expected with proper design and demonstration with the specific materials.

The objectives of this thesis are listed as follows:

a. To understand mechanical/thermal behaviours of soft polymeric systems and the relationship between inorganic and organic phases after introducing the nano inorganic particles into a soft polymeric matrix;
b. To synthesise and characterize SMPs and nanocomposites with designed properties by incorporating nanoparticles, mainly focusing on mechanical properties and shape memory performance;
c. To explore the different triggering methodologies by functionalising the matrix with selected nano-particles and validate the shape memory effects;
d. To analyse theoretically the structure-property relationships and the shape memory mechanism.

1.3 Outline of thesis

Chapter 1: Introduction. A description of how the present work was inspired and its contributions to the development of SMPs and its nanocomposites will be given.

Chapter 2: Literature review. The origins of the shape memory phenomenon and the history of SMPs are introduced. Classifications and recent developments of SMPs are explained in detail. The shape memory nanocomposite concept is provided, with a brief

introduction on the different fabrication technologies for nanocomposites. The potential applications and related published work is highlighted.

Chapter 3: Materials and experimental methodology. This chapter describes the experimental apparatus, materials and fabrication / characterization techniques used for this research.

Chapter 4: Nanoclay reinforced polyurethane shape memory nanocomposites. This chapter compares the experimental results for shape memory polyurethane (SMPU) and nanoclay/SMPU nanocmposites.

Chapter 5: Thermal triggering in polystyrene based shape memory nanocomposites reinforced by different nanofillers. This chapter provided an overall description on the experimental results covering the important aspects related to the shape memory polystyrene copolymer (SMPS) and its nanocomposites.

Chapter 6: Spherical carbon nanoparticle/polystyrene electro-active nanocomposites. This chapter systematically studies the properties of SMPS nanocomposites with conductive spherical carbon nano-particles, focusing more on the electrical properties. Other characterization results on mechanical, thermal and shape memory properties are also presented.

Chapter 7: Carbon nano fibre / carbon nanotube based polystyrene shape memory nanocomposites. Further investigations on SMPS nanocomposites containing carbon nano fibres and nanotubes are discussed here. Measurements at the micro/sub-micron scales are used to reveal the structure-property relationship. The shape recovery efficiency evaluation which design different stents on various materials are provided to forecast the potential applications in biological area.

Chapter 8: Discussion. The structure-property relationship for SMP nanocomposites is discussed including the particle size effect and geometrical aspect ratio effect. Constitutive models describing the thermo-viscoelastic behaviour and shape memory effect are proposed and the modelling results are compared with the experimental ones.

Chapter 9: Conclusions. Major conclusions from this research work are summarized in this section.

Chapter 10: Future work. Potential future work is outlined here.

Contribution to knowledge:

The author claims two contributions in this thesis. The first contribution is the clarification of the particle enhancing effects for SMPs by fully analysing the tested data of shape memory nanocomposites with different types of nanoparticle. The second contribution is to create a constitutive model for shape memory nanocomposites, which predicts the thermal-mechanical behaviour and shape memory behaviour.

Chapter 2

LITERATURE REVIEW

A comprehensive literature survey is presented in this chapter, covering the shape memory phenomenon, SMP nanocomposites, simulation/modelling of shape memory nanocomposites and, finally, applications of SMPs and their nanocomposites.

2.1 Shape memory polymer: phenomenon and effects

Shape memory materials (SMMs) are particular types of materials that can "remember" their geometry, *i.e.* after a sample of SMM has been deformed from its original shape, it recovers toward its original geometry by itself under an external stimulus, such as light, temperature, or moisture, (often called shape memory effect, SME), or simply during unloading (superelasticity).

The SME was first reported in 1932 for a gold-cadmium alloy [51]. However, it was not until 1951 that the phenomenon was explained crystallographically [52]. In the late of 1950s, two viable engineering materials, CuZnAl [53] and CuAlNi [54] alloys, were found to exhibit SME. In 1962, Buehler *et al.* at the Naval Ordnance Laboratory discovered that the nickel-titanium system (NiTi, also called Nitinol) shows the shape memory effect [55]. The martensitic transformation of NiTi was described fully in 1965, when the term ‘memory’ was firstly used to describe the shape recovery behaviour [56], so that NiTi became the archetypal shape memory alloy (SMA). Shape memory effects have been already found in many materials, such as metals, ceramics, and polymers. Among all these materials, NiTi based alloys have been extensively studied and have found many commercial applications, due to their distinct properties of shape memory effect, super-elasticity, biocompatibility, corrosion resistance and high damping capacity [57-61].

The SMPs have drawn increasing attention since the middle of the 1980s because of their scientific and technological significance [2, 4, 62]. They have extraordinary properties such as high degree of deformation, good biocompatibility, non-toxicity, biodegradability, wide ranges of mechanical properties, low-cost, light weight and easy processability [63-65]. Compared with SMAs, the advantages of SMPs are high elastic deformation and high recoverable strain (up to 400%), low cost for fabrication and

processing, low density, excellent chemical properties, biocompatibility and potential biodegradability [57, 66-68]. A variety of different stimulating methods can be applied, including heat (direct heating, Joule heating, infrared/radiation heating, laser heating, etc), moisture or water, and light. Such flexibility on triggering methods ensures great potential applications in making actuation, sensing and control devices with SMPs. They also have a broad range of application temperatures and stiffness, which can be tailored through the molecular structure. The shape recovery theory for SMPs originates from the principle of phase/structure movements controlled by an energy threshold and frozen energy barrier. For instance, the shape of thermally responsive shape memory polymers can be readily changed above the shape memory transition temperature (T_{trans} or T_s) and the deformation can be fixed below this temperature. As a result, when they are heated above T_{trans}, their original shape can be recovered automatically. The T_{trans} can be either a glass transition temperature (T_g) or the melting temperature of the polymer (T_m), which is required to remian the activation energy for recovery. The process is shown schematically in **Figure 2.1**, and detailed mechanisms will be presented specifically for different types of SMP in **Section 2.1.1**.

There are a lot of polymer materials which show the shape memory effect, for example, epoxy [9,69,70], EVA (Ethylene-Vinyl Acetate copolymer) [16,71], polyurethane (PU)/PU copolymer [72-74] and polytetra methylene oxide/poly (acrylic acid-co-acrylonitrile) [75].

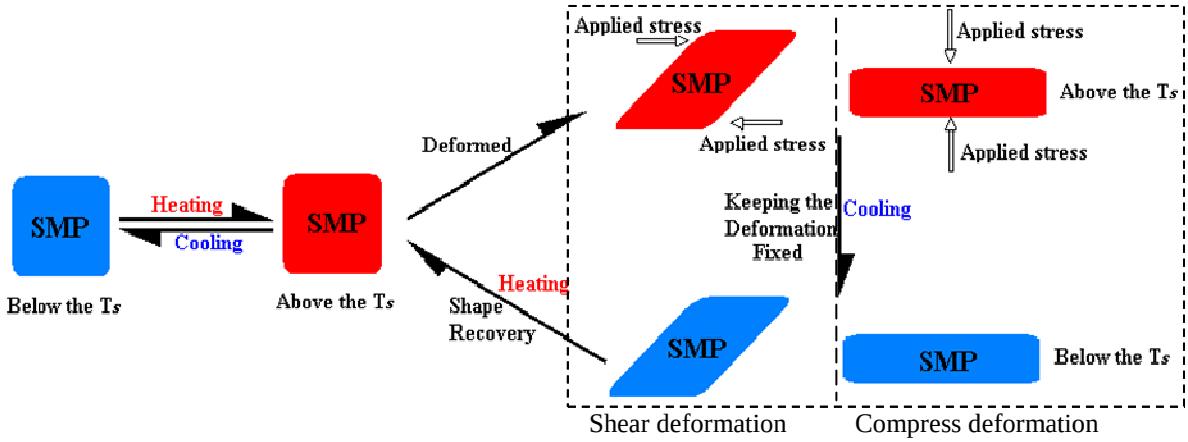

Figure 2.1 Schematic of Shape memory effect triggered by temperature

Mitsubishi Heavy Industries (MHI) have been engaged in research on SMPU since the 1980s, and have successfully developed polyurethane-based thermoplastic polymers [76]. The T_g values of the MHI shape memory polyurethane (SMPUs) possess a broad temperature range from –30 to 65 ºC. The shape memory of PU has had an enormous

commercial effect, with successfully uses in such applications as kitchen tools, textiles and automotive engineering. A lot of research work has been established on SMPUs [71, 77-79]. Baer *et al* investigated the thermomechanical properties of the Mitsubishi SMPs for potential application as medical devices, using thermal analysis methods [45]. Hu and co-workers in Hong Kong Polytechnic University have worked on the SMPUs and have fabricated shape memory composites based on the Mitsubishi SMPs. They also synthesized a SMPU resin, which mainly aims for textile applications [74, 80-82]. Huang *et al.* have studied intensively on the enhancement and triggering mechanisms of the SMP, etc. [24 26, 28, 83-85]. They also discovered some special triggering mechanisms, such as a water-induced shape recovery effect [24, 25, 85, 86]. The promising application fields of SMPs are biological applications, MEMS, and medical applications [16, 87-91], for example in minimally invasive surgery [6, 73, 92-95]. In some cases, another benefit of using SMPs is that there is a possibility to use degradable SMP if the biological device is not intended to be permanent [66, 67, 96, 97].

2.1.1 *Mechanisms and classification in SMPs*

SMPs achieve temporary strain fixing and recovery through a variety of physical processes, the underlying extraordinary extensibility being derived from the intrinsic elasticity of polymeric structures. SMPs can be classified in a number of different categories. With their different thermal processing properties, they can be divided into thermoplastic and thermoset polymers. The SMPs can also be divided according to the different chemical compositions of the macromolecular matrix, such as shape memory alkenes, shape memory polyurethane and shape memory polyester. In the following sections, the SMPs will be discussed based on categorization according to the molecular chain structure, amorphous or covalently cross-linked.

2.1.2 *Amorphous shape memory polymers*

In the amorphous phase switching mechanism, crystalline or rigid amorphous domains in thermoplastics may serve as physical cross-linking points affording the elasticity required for shape memory to be developed, mainly in the form of phase-separated block copolymers. When the temperature exceeds the T_m or T_g (T_{high}) of these discrete physical domains, the material can be reshaped. The continuous phase, having a lower

T_m or T_g (T_{low}), often exists in a rubbery state at $T_{low}<T<T_{high}$ and fixes a secondary shape on cooling to $T<T_{low}$. As shown in some research work on block copolymers and polyurethanes, the soft domains show a sharp glass-transition which could be considered as a symbol for shape memory properties as the frozen internal energy releases [4, 62-64, 98]. In this system, the crystalline phase functions as physical cross-linking joints (or hard segments), and the T_g of the amorphous region functions as T_{trans} (the transition temperature). This kind of SMP includes some polymers with low crystallinity or semicrystalline homopolymers, melt-miscible polymer blends which are compatible in the molten and amorphous states, but have at least one semi-crystalline component [99]. For these miscible blends, the T_g of the amorphous phase during shape recovery can be easily changed by modifying the composition.

In some block copolymers, the soft segments crystallize and the shape memory property are determined by the crystallization, T_m of the crystalline phase, which functions as T_{trans} [100, 101]. Polycaprolactone (PCL) has been extensively used for synthesis of PU with a crystalline soft phase, which performs the typical crystallization switching recovery. The recovery temperature, at which fast recovery takes place, can vary from 40°C to 60°C depending on the soft phase/hard phase composition and molecular weight of PCL [21, 102, 103]. The relation between the shape memory effect and molecular structure has been investigated and it was concluded that high crystallinity of the soft-segment-region at room temperature was a necessary prerequisite for segmented PUs to demonstrate shape-memory behaviour [104]. The recent research focuses on such PU based SMPs are to achieve maximum crystallization and stable-hard segment domains. Many modifications have been made to achieve micro-phase separation, such as incorporation of new segments and new groups [66, 72, 92, 105, 106]. Zhu *et al.* [82] synthesised the SMPU cationomers composed of PCL, methylene diphenyl diisocyanate (MDI), 1,4-Butanediol (1,4-BDO), and N-methyl-D-aspartic acid (NMDA) or N,N-bis(2-hydroxyethyl) isonicotinamide (BIN). The results showed that the stress at 100% elongation was reduced with increasing ionic group content. Shape recovery testing indicated that the NMDA series can be improved by the simultaneous insertion of cationic groups within hard segments, although not for the BIN series. Thermal analysis with DSC and DMA suggests that the crystallisability of soft segments in SMPU cationomers is enhanced by incorporation of ionic groups into hard segments, leading to a relatively high degree of soft segment crystallization. Compared with the corresponding nonionomers, incorporation of charged ionic groups within hard

segments can enhance the cohesion force among hard segments particularly at high ionic group content. This indicates that the content and category of cationic groups have a significant influence on the shape memory properties of PU. Gouher *et al.* [107-109], fabricated a number of segmented copolymers with PCL of various *Mn* (2000, 3000 and 4000 g/mol). Promising shape-memory properties were observed for two polymers that contained comparatively short, semicrystalline PCL soft segments of molecular weight 3000 g/mol and either terephthalamide or 2,6-naphthalenedicarboxyamide hard segments. Loading could be conveniently achieved by cold-drawing at room temperature and strain recovery took place upon heating above the melting temperature of the soft segment (35°C). Film elasticity testing showed uniform deformation properties with strain recovery rates as high as 99% and strain fixity values of 78% after passing through only one or two training cycles.

2.1.3 *Cross-linked shape memory polymers*

Creep and the scale of irreversible deformation limit the application of physically cross-linked shape memory polymers. Generation of some covalent forces between the long molecular chains can not only enhance the polymer, but also improve the shape memory property. Some research work based on polymers or blends such as polyethylene (PE) and PU/PVC has been reported [99, 110-112], and the results showed that the polymers have a shape memory property when they are cross-linked. Zhu *et al.* investigated the properties of cross-linked PCL with different molecular weight using γ-radiation [113]. The shape-memory testing results indicated that it can be stretched and deformed at about 60°C and, after cooling to room temperature, the deformation can be maintained effectively. The PCL based SMP was characterized by its low recovery temperature and large recovery deformation that results from the aliphatic polyester chain of PCL.

There are also two kinds of covalently cross-linked shape memory polymer. One is the covalently cross-linked glassy thermoset polymer, the other is the covalently cross-linked semi-crystalline SMP. The covalently cross-linked glassy polymer has a sharp T_g at the temperature of interest and rubbery elasticity above T_g derived from covalent cross-links. An example of this class is a chemically cross-linked vinylidene random copolymer consisting of two vinylidene monomers (methyl methacrylate and butyl methacrylate) whose homopolymers show two very different T_g values of 110 °C and

20 °C, respectively [114]. The work capacity, dictated by the rubbery modulus, is precisely adjustable to accommodate each particular application by varying the extent of crosslinking. This is achieved by copolymerization with a tetraethylene glycol dimethacrylate. This thermoset polymer shows complete shape fixing and fast, complete shape recovery in hot water at the stress-free stage. Larock *et al* worked on copolymerization and chemical cross-linking of renewable natural oils, which have a high degree of unsaturation, with styrene and divinylbenzene (DVB) to obtain random copolymer networks [115]. These networks showed flexible glass transitions and rubbery properties upon varying the monomer ratio.

The covalently cross-linked semi-crystalline SMPs can be employed to trigger shape recovery, typically giving a large recovery. Compared with glassy materials, this class of materials is generally more compliant below the critical temperature, with a stiffness that is sensitive to the degree of crystallinity, and thus indirectly to the extent of cross-linking. Shape recovery speeds are faster for this first-order transition than the amorphous ones. The chemically cross-linked trans-polyisoprene (TIP), one typical material in this kind, has a melting point (T_m) of 67 °C and crystallinity degree around 40%, giving a stiffness of about 100 MPa at room temperature [116]. Lendlein and co-workers have developed biodegradable SMPs by synthesizing and copolymerizing a narrowly dispersed, oligomeric poly(ε-caprolactone) dimethacrylate with n-butyl acrylate under UV radiation to yield a multiblock structure [5]. The materials showed excellent shape-memory properties, with a total strain recovery rate between 92% and 97% and average recovery ratio between 86% and 97% after five cycles. The materials were adjustable with respect to T_{trans} from 30 to 50 °C via the molecular weight of the macro-dimethacrylates used in the synthesis, and the crystallization process could be controlled for new applications.

2.1.4 *Current research problems in SMPs*

As previously mentioned, the basic advantages of the SMPs over other shape memory materials, such as SMAs, are their inherently high recoverable strain of several hundred percents and much lower density. In addition, SMPs possess conveniently adjustable material properties and can be easily produced and shaped by conventional polymer processing techniques. However, in many cases, the mechanical strength of SMPs under

ambient conditions or thermo-mechanical service cannot fully meet application demands, which increases the uncertainty as to the response of devices because of the soft nature of these materials. For instance, SMPs have relatively low recovery stress, which is usually 1–3 MPa compared to 0.5–1 GPa for shape memory metal alloys [65]. The relatively low recovery stress becomes a limiting factor in many applications especially in cases where SMP devices need to overcome a large resisting load during shape recovery.

Many attempts at enhancing the soft SMPs have been reported by either trimming the molecular structure internally or incorporating enhancers to the system externally, both of which have proven to be effective solutions, although the latter one has gained more academic concentration with lower operation risk and higher enhancement. Various fillers with dimensions in the nano/micrometer scale have been considered [99, 114, 117] in shape memory polymer composites in efforts to augment mechanical properties and to obtain multiple functionalities. It has been observed that there is a trade-off between enhancement of elastic modulus and reduction of recoverable strain ratio. Generally, fillers have a negative impact on recoverable strain due to their size, and substantially higher stiffness compared to the matrix polymer. In some cases, they even disturb the polymer networks responsible for shape memory functions, especially at high loading levels. As will be apparent below, research efforts to strike a balance between the recovery stress and the recovery strain with the use of fillers are still evolving. Gunes *et al* [118] have presented a systematic review of recent progress made on SMPs and their nanocomposites. Developments in allied fields were also presented in an effort to identify the current and future trends in this area. The physical mechanisms of shape memory actions, polymer-nanofiller interactions, and the resultant properties of SMP nanocomposites were discussed. Examples were presented to highlight the influence of processing conditions, filler geometry and filler surface characteristics, and the nature of matrix polymers on shape memory properties.

Leaving aside the above-mentioned mechanical limitations arising from the recent appearance of SMPs to which solutions are gradually being found, there is one crucial issue that makes it impossible on many occasions to use these polymers to replace other active materials. As shape memory recovery is usually a thermally induced process, their triggering conditions or controlling method are not so practical since thermal triggering shape memory is not the best control method in most applications. Also, there

exist many uncertainties in the thermal triggering procedure such as stress relaxation, stress reduction with increasing temperature and critical application conditions [39, 42, 44]. These shortcomings on triggering conditions could possibly be changed by adding nanoparticles with different functionalizing mechanisms.

2.2 Shape memory polymer nanocomposites

2.2.1 *Why shape memory polymer nanocomposites?*

The term “Composites” originally arose in engineering to describe the situation when two or more materials are combined in order to modify the shortcomings of a single specific component. Polymer nanocomposites are commonly defined as the combination of a polymer matrix and additives that have at least one dimension in the nanometre range. The additives can be one-dimensional (for example, nanotubes and fibres), two-dimensional (such as layered minerals of clay), or three-dimensional (for example, spherical particles). Over the past decade, polymer nanocomposites have attracted considerable interests in both academia and industry, owing to their outstanding importance in mechanical properties such as elastic modulus and strength with only a small amount of the nanoscale additives. This is caused by the large surface area to volume ratio of nanoadditives when compared to the micro- and macro-additives. Other superior properties of polymer nanocomposite include barrier resistance, flame retardancy, scratch/wear resistance, as well as optical, magnetic and electrical properties. The incorporation of reinforcing fillers has been investigated in order to improve the mechanical properties, fulfill the practical triggering conditions and to diversify the applications of SMPs [30, 31, 39, 119-121].

2.2.2 *Nano particles and their enhancement in SMP*

These materials are characterized by at least one dimension in the nanometre range. Nanostructures constitute a bridge between molecules and bulk systems. Individual nanostructures include clusters, quantum dots, nano crystals, nanowires, and nanotubes, while multi-nanostructures involve arrays, assemblies, and super lattices of the individual nanostructures [122, 123]. The physical and chemical properties of nanomaterials can differ significantly from those of the atomic-molecular or the bulk

materials of the same composition. Size effects are important in nanomaterials, and this has two aspects: one is concerned with specific size effects (numbers of atoms in metal clusters, quantum mechanical effects at small sizes) and the other with size-scaling applicable to relatively larger nanostructures (surface and interface effects, volume effects) (**Table 2.1** & **2.2**).

Shapes of nanoparticles also play an important role in determining properties, such as reactivity and electronic spectra. Since the discovery of carbon nanotubes (CNTs) by Iijima in 1991 [124], tremendous efforts have been expended to control their production and properties. Recent theoretical and experimental studies suggest that CNTs have remarkable mechanical and electrical properties [125-127]. The construction of ordered arrays of nanostructures by employing techniques of organic self-assembly provides alternative strategies for nanodevices. 2D and 3D arrays of nanocrystals of semiconductors, metals, and magnetic materials have been assembled by using suitable organic reagents. The rest of this section will review the recent developments in shape memory nanocomposites according to the effects of the nanofiller shape on enhancement of the matrix.

Table 2.1 Relationship between nano-particles size and the amount of surface atoms

Nano particles dimension (nm)	Atom No.	Surface atom percentage(%)
10	3×10^4	20
4	4×10^3	40
2	2.5×10^2	80
1	30	96

Table 2.2 Nanostructures and classifications

Nanostructure	Dimension	Material
Clusters, quantum dots	Radius,1-10nm	Insulators, semiconductors, metals, magnetical materials
Nano particles	Radius,1-100nm	Ceramic oxide
Nano tubes	Diameter, 1-100nm	Carbon, BN, GaN
Nano wires	Diameter, 1-100nm	semiconductors, metals, oxides, sulfides, nitrides
Nano rods	Diameter, 5 nm	DNA
Two dimensional nano particles	Nano scale to micron scale	semiconductors, metals, magneti materials
Thin films	Thickness,1-100nm	Insulators, semiconductors, metals, DNA
Three dimensional nano particles	Nano scale in three dimensions	semiconductors, metals, magnetical materials

2.2.2.1 Spherical inorganic nanofillers

Silica as a widely used spherical inorganic nano-particle, as has been claimed as a reinforcing agent in SMPs. Studies have shown that the constrained bending recovery force of SMPs can be dramatical with the addition of silica as low as 2 wt.% [117, 128]. In another study, PU block copolymer was synthesized, followed by a sol–gel reaction with tetraethoxysilane (TEOS) to prepare high performance PU–silica hybrids with shape memory function. An improvement in the mechanical properties and shape recovery force of PU was achieved without any deterioration in shape recovery effect by silica hybridization [129]. Similar enhancements have also been reported for other spherical nanofillers [130-132].

2.2.2.2 Rod like inorganic nanofillers

Rod like nanofillers, normally include two different classifications, carbon fibre/tubes and the other inorganic nano-rods or fibres. The carbon series will be dealt with in **Section 2.2.3**. As reported by ref.[84], attapulgite (playgorskite), a kind of nanosized fibrous clay mineral, may provide a simple and cheap alternative of some existing expensive rod nanofillers such like carbon fibre/tubes, to improve the stiffness and actuation stress of SMPs. The T_g of a SMPU reinforced with treated/non-treated attapulgite was monitored in both of wet and dry conditions, and the results revealed that non-treated clay significantly reduces T_g of the composites, while the influence of treated clay on T_g is limited [84]. Organic fibre has also been used to enhance the mechanical and shape memory properties of a SMP matrix. Auad *et al.* [133] prepared composites by casting stable nanocellulose/segmented polyurethane suspensions. These composites showed higher tensile modulus and strength than unfilled films (53 % modulus increase at 1 wt.% nanocellulose), with higher elongation at break. And creep deformation decreased as the cellulose concentration increased (36 % decreasing in 60-minute creep by addition of 1 wt.% nanocellulose). The nanocomposites displayed shape memory properties equivalent to those of the neat polyurethane, with recoveries of the order of 95 % (referred to second and further cycles).

2.2.2.3 Platelets or layer type nanofillers

Layered clay, *i.e.* sodium montmorillonite (MMT), is the most common particle used in reinforcing polymers. Cao and Jana [134] reported that clay particles exfoliated well in the polymer, decreased the crystallinity of the soft segment phase, and promoted phase mixing between the hard and soft segment phases. Nevertheless, the soft segment crystallinity was enough and, in some cases, increased due to stretching to exhibit excellent shape fixity and shape recovery ratio. A 20 % increment in the magnitude of shape recovery stress was obtained with the addition of 1 wt% nanoclay. Tensile tests indicated that the strength was highly dependent on the competing influences of reduced soft segment crystallinity and the clay content. However, the tensile modulus measured at temperatures above the melting point of the soft segment crystals showed continued increases with clay content. A different macromolecular system containing a poly(ethylene glycol) (PEG) segment was studied by Kim *et al.* [135] through introducing Na-MMT into matrix. The X-ray diffraction pattern and the morphology observed with a transmission electron microscope showed that Na-MMT intercalated with a PEG segment was heterogeneously dispersed in the polymer matrix [135]. Thus Na-MMT intercalated with a PEG segment effectively enhanced the mechanical properties of PEMA. Shape memory behaviour and rheological properties showed that Na-MMT intercalated with a PEG segment performed its role as a physical crosslinker effectively even with 1.2 wt% of Na-MMT [135].

Despite the fact that clay is physically incorporated into polymer systems, Rezanejad and Kokabi [136] illustrated the effect of adding clay in chemically cross-linking composite system. The resulting nanocomposite showed higher modulus/strength at small clay loading levels (0–10 wt.%), and also demonstrated higher recovery force, which is required to if it is act as an actuator. The effect of modified MMT on mechanical and shape memory properties as well as the force generation of a shape memory cross-linked low density polyethylene were also investigated. The results showed that the modulus of elasticity, the recovery temperature, the recovery force and force recovery rate increase with increasing organic treated clay content in nanocomposites, but the final recovery strain decreases slightly.

2.2.3 *Electro-active SMP nanocomposites*

Carbon fillers have been extensively applied to transform the organic matrix from electrical insulation into conductor. In this section, recent developments in applying different types carbon filler in SMPs will be listed with respect to the different geometry effects.

2.2.3.1 Spherical carbon nanoparticles filled SMP nanocomposites

Li *et al.* [137] reported the strain recovery of spherical nanoparticles filled SMPs. These PU composites with conducting carbon nanoparticles (CNP) were prepared by a solution-precipitation process, which was followed by melt compression molding. It was found that the CNP filler exists in the form of aggregates. The percolation threshold was reached at a CNP concentration of 20 wt %. The presence of CNP fillers decreased the degree of crystallinity of soft PCL segments of the polyurethane. However, the composites still have enough soft-segmented PU crystals to fulfil the necessary condition for shape memory properties. Dynamic mechanical data showed that CNP is a kind of effective filler for the reinforcement of the PU matrix without deteriorating the stable physical cross-linking structure of the polyurethane, which is necessary to store the elastic energy. The addition of CNP reinforcement to PU influenced the strain recovery properties, especially for those samples with CNP concentrations above the percolation threshold. The response temperature of the shape memory effect was not affected too much. The final recovery rates and strain recovery speeds of the shape memory measurements, however, decreased obviously. This was expected and was ascribed to the increased bulk viscosity as well as the impeding effect of the inter-connective structure of CNP fillers in the polymer.

Leng *et al.* [38, 138, 139] demonstrated multiple progress in conductive SMPs with added CNPs. They provided approaches to reduce significantly the electrical resistivity in a SMPU filled with randomly distributed CNP and an additional small amount of randomly distributed Ni microparticles (0.5 vol.%) in the SMP/CNP composite. The electrical resistivity was only reduced slightly. However, if these Ni particles were aligned into chains (by applying a low straight magnetic field to the SMP/CNP/Ni solution before curing), the significant drop in the electrical resistivity was detected. The related electro-triggering efficiency was also reported [138, 139].

2.2.3.2 Carbon nano-fiber (CNF) filled SMP nanocomposites

Gunes *et al.* [71] fabricated CNF/SMPU composites by melt mixing after the chain extension of a T_m (melting transition temperature as the switch temperature) type SMPU. CNFs with a diameter of 60–200 nm and length of 30–100 mm were introduced into the SMPU synthesized from MDI, 1,4-BDO, and PCL diols. The composites were prepared by melt mixing of extended chain PU with the nano-fillers. Results showed that the CNFs diminished the shape memory function of SMPUs which was ascribed to the interference of CNFs on the crystallization of the soft segment. Koerner *et al.* [140] fabricated CNF/SMPU composites by solution mixing in a polar solvent, and slow evaporation of the solvent. The CNFs had an average diameter of 100 nm and length above 10 micron. Shape recovery ratio was improved due to the enhanced strain-induced crystallization. In comparison with pure SMPs, shape memory composites with a uniform dispersion of 1– 5 vol.% CNFs produced up to 50% more recovery stress.
Lan *et al.* [141] investigated the shape recovery behaviour of thermoset styrene-based shape-memory polymer composites (SMPCs) reinforced by carbon fiber, and demonstrated the feasibility of using an SMPC hinge as a deployable structure. Results revealed that the SMPC exhibits a higher storage modulus than that of a pure SMP. At/above *T*g, the shape recovery ratio of the SMPC upon bending was above 90%. The shape recovery properties of the SMPC become relatively stable after some packaging/deployment cycles. Additionally, fibre microbuckling was the primary mechanism for obtaining a large strain in the bending of the SMPC. Moreover, an SMPC hinge was fabricated, and a prototype of a solar array actuated by the SMPC hinge was successfully deployed [141].

2.2.3.3 CNTs filled SMP nanocomposites

Miaudet *et al.* [142] reported on the properties of composite nanotube fibres that exhibit the particular feature of aspect ratio. It was observed that these composites can generate a stress upon shape recovery up to two orders of magnitude greater than that generated by conventional polymers. In addition, the nanoparticles induced a broadening of the glass transition and a temperature memory with a peak of recovery stress at the temperature of their initial deformation. Meng *et al.* [19] studied a multi-walled carbon nanotube (MWNT) filled SMPU system prepared with *in situ* polymerization and melt

spinning. It was found that in the SMPU matrix, the MWNTs were preferentially aligned in the fiber axial direction. The shape recovery ratio and recovery force were distinctly improved by the aligned MWNTs. The results suggest that aligned MWNTs could help storing and releasing the internal elastic energy during stretching and relaxation. Besides, it was found that the self-aligned MWNT fibers caused the shape recovering of composite to original length quicker [19].

Park *et al.* [90] developed conducting shape memory polyurethane (CSMPU) actuators with better electrical characteristics, fabricated using *in situ* polymerization. The electrical resistance and specific resistance were almost constant up to the transition temperature. The electrical resistance increased by about 100% as the elongation increased up to 100%. This initial elongation force could be stabilized after a time, which was a kind of 'break-in procedure'. The actuation displacement decreased linearly as the actuation force increased. Cho *et al.* [143] synthesized electro-active shape-memory composites using conducting PU and MWNTs. Surface modification of the MWNTs (by acid treatment) improved the mechanical properties of the composites. The modulus and stress at 100% elongation increased with increasing surface-modified MWNT content, while elongation at break decreased. MWNT surface modification also resulted in a decrease in the electrical conductivity of the composites. However, as the surface modified MWNT content increased, the conductivity increased. Electro-active shape recovery was observed for the surface-modified MWNT composites with an energy conversion efficiency of 10.4%.

2.2.3.4 Graphene filled SMP nanocomposites

Graphene was discovered in 2004 by Geim *et al*., which has been suggested as a "next generation material". Its remarkable optical, electronic, and thermal properties, chemical and mechanical stability, and extraordinary physical surface feature have been widely studied, potential applications fields such as transistors, sensors, polymer nanocomposites and energy devices have also been proposed [144-146]. So far, few publications have found on SMP/graphene nanocomposites, but it can be expected that their extraordinary physical properties will benefit SMPs and offer more advantages according to the applications than the existing nanoparticles.

2.2.4 *SMP nanocomposite fabrication methods*

From the fabrication side, shape memory polymer nanocomposites is similar to the other nanocomposites. According to the different ways of incorporating nanoparticles, different kinds of methods can be classified: mechanical melting processing using specifically designed equipment, the wet chemical solution method, molecular level mixing technique with chemical reaction, and *in situ* polymerization.

2.2.4.1 Mechanical melting processing method

Most nanocomposites based on SMPU from MHI are fabricated using this technique. Investigations by Tobushi *et al* [13-15, 147] on SMPs composites were based on fabricating composites with melt SMPU and nano-filler. Many important phenomena were found and several models on the shape recovery mechanism were proposed and validated in practical experiments.

Yang *et al.* [28, 148] produced electrically conductive polymers by filling the polymeric matrix with conductive powders and investigated the effects of moisture on the glass transition temperature of a SMPU filled with nano-carbon powders. It was found that the SMP composites before immersion in water have a slightly lower T_g, and the moisture fraction at the saturation point upon immersion is also lower. Another interesting point was that the moisture can significantly reduce the T_g of the composites, which also led to the idea that the water actuating recovery of SMP composites [28, 148].

2.2.4.2 Wet chemical processing solution

Wet chemical processing usually performed by pre-scattering nanoparticles in a solvent, and adding surfactant to reduce the high surface energy of nanofillers, to modify the surface to improve the compatibility and protect the nanostructure from the outer environment. Ultrasonic processing techniques had also been used to achieve the lowest level aggregation of particles. Lu *et al.* [88] fabricated SMP composites by incorporating various nanofillers into a styrene-based SMP with sensing and actuating capabilities. Static mechanical results of the SMP composites containing various filler concentrations of hybrid filler reinforcement were studied and confirmed that the mechanical properties were significantly improved by adding chopped short carbon fibers (SCF). The

excellent electrical outcomes and sensing data of SMP composites filled with 5 wt.% CNP and 2 wt.% SCF proved that temperature or mechanical loads could be significantly affected. The actuating capability of SMP composites was also validated and demonstrated. Dynamic mechanical analysis revealed that the output strength of SMP composites is improved by an increase in SCF content.

Gunes *et al.* [149] used this method as the second step to achieve nanocomposites by mixing nanofillers and synthesized SMPU. A reduction in soft segment crystallinity was observed in the presence of CNP, CNF and treated CNF; the reduction was smaller in the case of treated CNF. Only the composites with CNP showed pronounced positive temperature coefficient (PTC) effects. The observed PTC effects exhibited a close relationship with non-linear thermal expansion during heating. Composites of CNF and treated CNF did not show PTC effects due to low levels of soft segment crystallinity. The resistivity of composites with CNP significantly increased by several orders of magnitude after imposing a tensile strain while composites of CNF and treated CNF showed weak dependence on strain.

2.2.4.3 Molecular level mixing

Molecular level mixing can be achieved via either a melting process or wet chemical mixing. The critical issue is the technique controls and composition design, as it needs the assistance from other chemicals. Physical adsorption helps the polymer molecular chain or monomer attached the particles and the polymerization causes the particles to be embedded. Armes *et al.* [150, 151] reported surfactant-free synthesis of colloidal dispersions of vinyl polymer−silica nanocomposite particles in aqueous media using a batch emulsion polymerization protocol using 4-vinylpyridine as an auxiliary in the synthesis. The strong interaction of this basic monomer with the acidic surface of the silica particles is essential for successful nanocomposite particle formation. Depending on the synthesis conditions, the mean particle diameter of the hybrid particles varied from 100 to 300 nm. Cho *et al.* [129, 143] synthesized SMPU based composites using silica and MWNTs through this method. As well as the improved mechanical properties, the conductivity was also dramatically elevated by adding MWNTs.

2.2.4.4 In situ polymerization

This is the most common method to obtain SMPs and their nanocomposites. The major advantage is that the modifications can be made both from organic molecular trimming or composition design and adding the nanoparticles with proper pre-treatment. The disadvantage is that in-situ polymerization needs a stable system with precise composition control. Nanoparticles are generally functionalized first and then added as a monomer in synthesis to obtain the hybrid composites. Sahoo *et al.* [152] obtained electroactive SMPU based nanocomposites through *in situ* polymerization with different components, MWNTs, polypyrrole (PPy) and PPy-coated MWNTs. A clear enhancement of mechanical properties was observed. When this composite was slightly coated with PPy (2.5 wt.%), its conductivity was higher than the other composites. This composite also showed good electroactive shape recovery properties when an electrical voltage was applied. Metal oxide nanoparticles clusters have attracted more and more attention recently. Behl *et al.* [2] reviewed different concepts for the creation of multifunctionality derived from the various polymer network architectures of thermally-induced SMP and summarized the *in situ* polymerization classifications as well as the multifunction for each nanocomposites.

Rana *et al.* [153] synthesised hyperbranched polyurethane (HBPU) nanocomposites with MWNTs by *in situ* polymerization on the basis of poly(ε-caprolactone)diol as the soft segment, 4,4'-methylene bis(phenylisocyanate) as the hard segment, and castor oil as the multifunctional group for the hyperbranched structure. A marked improvement in the dispersion of MWNTs in the HBPU matrix was found, and good solubility of HBPU–MWNT nanocomposites in organic solvents was shown. Due to the well-dispersed MWNTs, the nanocomposites resulted in excellent shape memory properties as well as enhanced mechanical properties compared to pure HBPU.

2.2.5 *Other functional SMP nanocompsoites*

There have been many different types of SMP nanocomposites. Some recent developments of these nanocomposites will be introduced here according to the different triggering methods. Lendlein *et al.*[5] reported that polymers containing cinnamic groups can be deformed and fixed into pre-determined shapes, such as (but not

exclusively) elongated films and tubes, arches or spirals, by ultraviolet light illumination. These new shapes were stable for long time periods, even when heated to 50 °C, and they can recover their original shape at ambient temperatures when exposed to ultraviolet light of a different wavelength. Leng *et al.* [30, 31] announced the successful actuation of shape memory behaviour by infrared light, though the direct triggering factor was a thermal stimulus, their attempts demonstrating the possibility of remote control. Vialle *et al.* [121] studied the remote activation of nanocomposites using remote induction of magnetic particles dispersed in the thermoset foam matrix. Material properties and foam performance were characterized and compared over a range of fillers, induction parameters, and packaging configurations. This investigation indicated an improvement in heating performance for increased weight percentage of filler without sacrifice in foam thermo-mechanical properties up to 10 wt% filler. Detailed analysis of the results implied that the primary factor in improving heating performance was heat transfer between the filler nanoparticles and the bulk foam.Another type of functional SMP composites, magnetically sensitive SMP composites, can be obtained by embedding ferromagnetic fillers. Schmidt *et al.* [154], Buckley *et al.* [93], Hosoda *et al.* [155] and Small *et al.* [39] explored this area with success although the theoretical model was not attempted. A typical magnetically induced SME of the composite is demonstrated in **Figure 2.2**, in which a shape change from a corkscrew-like spiral temporary shape to a plane permanent shape is shown. Indirect magnetic actuation has also been realized by the incorporation of Ni–Zn ferrite particles into thermoset polyurethane by Buckley *et al.* [93].

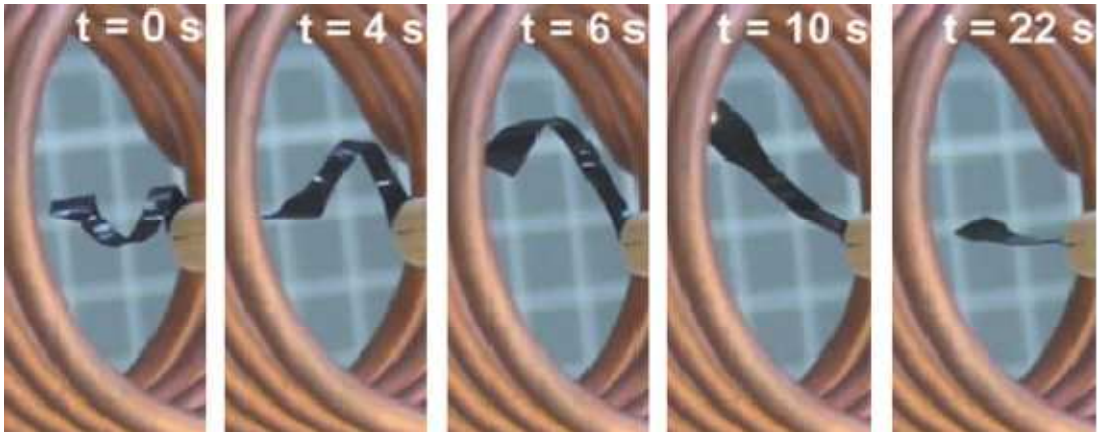

Figure 2.2 The magnetically responsive shape-memory effect of SMPU composite with 10 wt.% particle content [39].

2.3 Simulation and modelling of shape memory nanocomposites

This section introduces two aspects of the recent development of shape memory nanocomposites theories, particle enhancing theory in polymer nanocomposite system, and constitutive modelling of the shape memory system. The particle enhancing theory includes a particle size effect and a geometry effect.

2.3.1 *Theoretical model in nanoparticles enhancement*

Generally, when nanofillers with high modulus are added into a much lower-modulus polymer matrix, the modulus and strength of the nanocomposites will be enhanced through an improved load transfer from the matrix to the filler. **Figure 2.3** illustrates the microstructure of nanofillers with different geometries in a polymer matrix. When the aspect ratio of the particles equals unity (spherical nanoparticles), the composite modulus is dependent on a number of particle characteristics such as modulus, density, the particle geometry factors such as size and aspect ratio, the volume fraction and the nature of the interface between organic and inorganic phase.

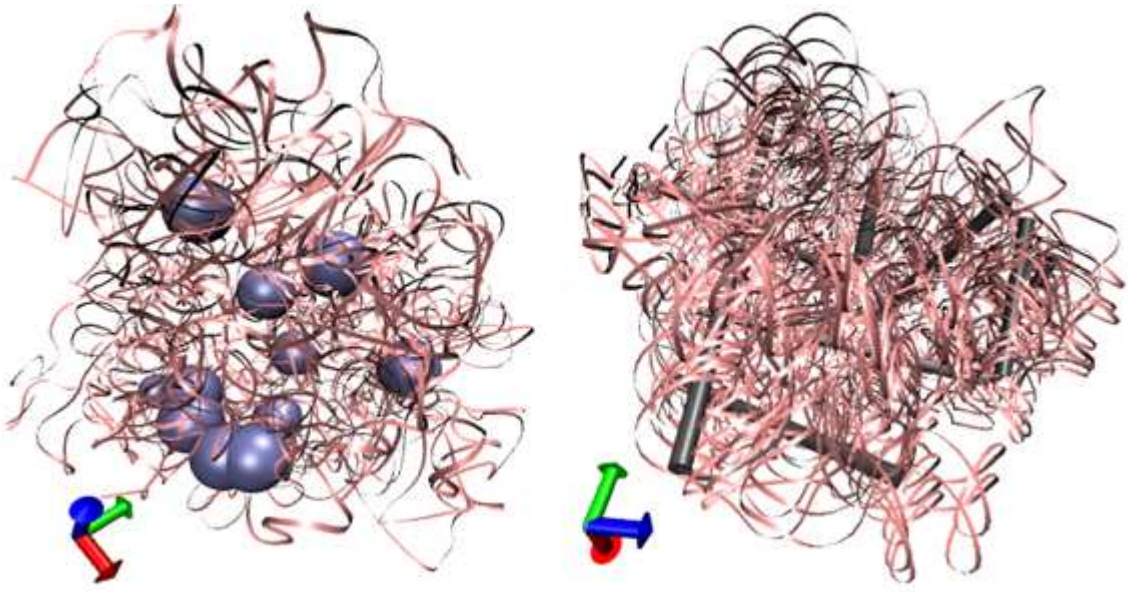

(a) **(b)**

Figure 2.3 3-D schematic of nanocomposite systems: (a) with spherical fillers (such as Al_2O_3, SiO_2, CNP), (b) with rod-like fillers (such as clay, CNF, CNTs)

Successive attempts have been made in the past decades to develop theoretical frameworks to predict mechanical properties of composite materials based on the

physical/chemical properties of the polymer matrix, additives and the composites microstructure [156]. Suprapakorn *et al.* [157] investigated nanoparticle size effect on the enhancement, and described that there exists a critical value for a given particle, below which the particulate composite modulus increases with decreasing of nanoparticle size and above which it was relatively increases. Cho *et al.* [158] investigated the effect of the particle size on the mechanical properties of polymeric composites reinforced with spherical particles. The size of particles varied from macro (500 μm) to nano (15 nm) scale. It was found that particle sizes at the micron scale have little influence on the Young's modulus of the composite and that Young's modulus increases as the size of particles decreases at the nano-scale. It was also observed that the tensile strength of the composite is strongly dependent on particle size. At a nanoparticle loading of 1 vol.%, the tensile strength increased as the particle size decreased. However, the trend for a composite with alumina nanoparticles of 3 % volume fraction was found to be the opposite [158]. Finite element analyses has been employed to understand the effect of the particle size at the micron scale on the failure process, and the results have shown that total strain energy release rate for particle/matrix debonding growth decreases as particle size decreases and that the sliding fracture mode becomes dominant during the growth of debonding [158].

Unlike the limited attempts on particle size effects, many empirical or semi-empirical equations have been proposed to predict the modulus of composites considering that most of the fillers are irregular in geometry and varied in specific aspect ratio. A simple equation was generated based on Einstein's equation [159] to predict the Young's modulus of composites reinforced with rigid particles [160].

$$\frac{E_{\mathrm{c}}}{E_m} = 1 + 2.5\phi_f \tag{2.1}$$

where E_{c} and E_{m} are the modulus of composite and matrix, respectively, and ϕ_f is the volume fraction of filler. **Equation (2.1)** is applicable only at low concentrations of filler and assumes perfect interface contact between filler and matrix, as well as a uniform dispersion of individual filler particles [161]. A number of attempts have been made to incorporate interactions between neighboring particles to allow for predictions also at higher volume fractions. Most of these models add one or more terms to a polynomial series expansion of the amplification factor. One of the most cited models of this class is the Guth model [162, 163].

$$E_c = E_m(1 + 2.5\phi_f + 14.1\phi_f^2) \tag{2.2}$$

In addition to these simple models specifically developed for filled polymers, a number of general composite theory models can be used. For example, the traditional Voigt upper bound [164] for a linear elastic isotropic material is given by

$$E_c = E_f\phi_f + E_m(1-\phi_f) \tag{2.3}$$

where E_f is the filler modulus.

The elastic theories, which are most widely used to discuss nanoparticle enhancement, are based on two major models. The first was proposed by Halpin and Tsai [165, 166] with a similar analytical equation, which has been adapted for a variety of reinforcement geometries, including discontinuous filler reinforcement. Halpin and Kardos [166] modified the Halpin and Tsai model by introducing the shape parameter based on aspect ratio, which was considered to be dependent on the filler geometry. This change made this model more effective in some conditions.

The other model is the Mori and Tanaka model [167, 168] which considered the effect of an volume fraction of inclusions in an aligned short-fibre composite. Tandon and Weng [168] have derived comprehensive analytical expressions for the elastic modulus of an isotropic matrix filled with spheroidal and unidirectionally aligned non-spherical inclusions. The longitudinal (along the inclusion alignment direction) and transverse elastic modulus can be generated through examining the influence of aspect ratio, from zero to infinity, on the load transfer in a transversely isotropic composite [168]. The evolved Mori and Tanaka model accounts of the effect of filler shape, for example, rod-like, plate-like, or disc-like. Given that nanofillers are rarely aligned, Fornes and Paul [169] suggested equations for random orientation in all three orthogonal directions, with focus on rod filler and disc filled composites. Generally, the elastic theory concentrates on filler geometry effects, especially on the high aspect ratio, and the evolved equations treat disc fillers as rods with consideration of all three orthogonal directions. The Halpin & Tsai model and the Mori & Tanaka model will be applied here to analyze the composite properties with different fillers, and the detailed equations will be presented in the discussion part.

2.3.2 *Constitutive models for thermo-mechanical behaviour and shape memory recovery*

As constitutive models for shape memory recovery vary with triggering conditions, the models will mainly involve thermal triggering recovery in amorphous systems, which is the most common type. It is considered that in addition to heat transfer, the important molecular mechanisms determining the time-dependence of the shape memory response of amorphous SMPs are structural relaxation in the glass transition region, and stress relaxation in the form of viscoelasticity in the high temperature (rubbery) and glass transition regions and viscoplasticity in the low temperature (glassy) region. Structural relaxation describes the time-dependent response to temperature and pressure changes, while stress relaxation describes the time-dependent response to a change in the mechanical, particularly deviatoric, loading. Combining the structural and stress relaxation mechanisms, constitutive models are normally developed for the finite-deformation, time-dependent thermo-mechanical behaviour of thermally active amorphous SMPs that include structural relaxation in the glass transition region, viscoelasticity in the rubbery and transition regions and viscoplasticity in the glassy region.

Tobushi *et al.* [12, 170-175] made significant contributions to constitutive modelling of the amorphous SMPU system. Detailed experimental results on various thermo-mechanical conditions provided an essential guideline on how to collect the fundamental data and how to divide the modelling regimes for amorphous systems, Tobushi also proposed a one-dimensional constitutive model for amorphous SMPU and simulated the thermo-mechanical behaviour at small strains, which was expanded and applied to larger strains by Liu *et al.* [176] and Diani *et al.* [177]. The work of Diani assumed a thermoviscoelastic approach that applied a phenomenological temperature dependence of the viscosity, which extended the work of Liu *et al.* [176]

A three dimensional finite-deformation model was developed by Qi *et al.* [48]. This model applied a phenomenological, first-order, phase transition approach that models the SMP as a continuum mixture of a glassy and rubbery phase. Constitutive relations were proposed for the temperature evolution of the volume fractions. The main disadvantage of this approach was that it was not representative of the physical processes of the glass transition and thus results in nonphysical parameters, such as the

volume fractions of the glassy and rubbery phases. Nguyen *et al.* [49, 50] summarized earlier constitutive model and viscoelastic properties by a thermo-mechanical investigation, linked with more kinematic relations and proposed a complicated model with three stages, and successfully simulated the shape recovery of amorphous SMPs.

So far, the constitutive models that have been developed are all on pure amorphous SMPs, and a constitutive model on SMP nanocomposites was not explored.

2.4 Applications of SMPs and their nanocomposites

Conventional applications of SMPs include the widespread areas of the packaging industry and construction industry, which can be simply accessed by a hot hair dryer [112]. Also many applications in memory storage, sensors and actuators have been explored for SMPs [178-181]. Hu *et al.* introduced SMPs into the textile industry using three main kinds of materials: linear polymer-polynorbornene, segmented polyurethane and graft copolymer–polyethylene/nylon-6 [23]. The applications of SMPs in textiles include breathable textiles and surgical protection, etc.

Currently, SMP applications in biotechnology and medicine have received much attention. For example, recent approaches for implanting medical devices often require complex surgery followed by device implantation, and, with the development of minimally invasive surgery, it is possible to place small devices inside the body. These types of surgical advances may create new opportunities to enable a micro-device to be implanted into the human body. Relevant research studies mainly focus on two areas: the first is the application of industrial polymers, such as the biodegradable properties of materials, polymer drug delivery systems and polymer biological construction. Lendlein and Langer [65] manufactured a group of degradable thermoplastic polymers for biomedicine, which are able to change their shape after an increase in temperature (see **Figure 2.4**). Their shape-memory capability enables bulky implants to be placed in the body through small incisions or to perform complex mechanical deformations automatically. An impressive force of 1.6 N could be generated upon shape recovery as the sample stretched to 200%. The second area is functional materials based on biomaterials, such as proteins.

Figure 2.4 A fiber of a thermoplastic SMP was stretched and formed a loose knot, both ends of the suture were fixed. The photos shows how the knot tightened in 20 s when heated to 40°C [65].

Rodríguez-Cabello *et al.* explored the protein-based polymers [182], which display many different properties including smart behaviour (sensitivity to certain stimuli), self-assembly and biocompatibility, as well as two main applications such as drug delivery systems and tissue engineering.

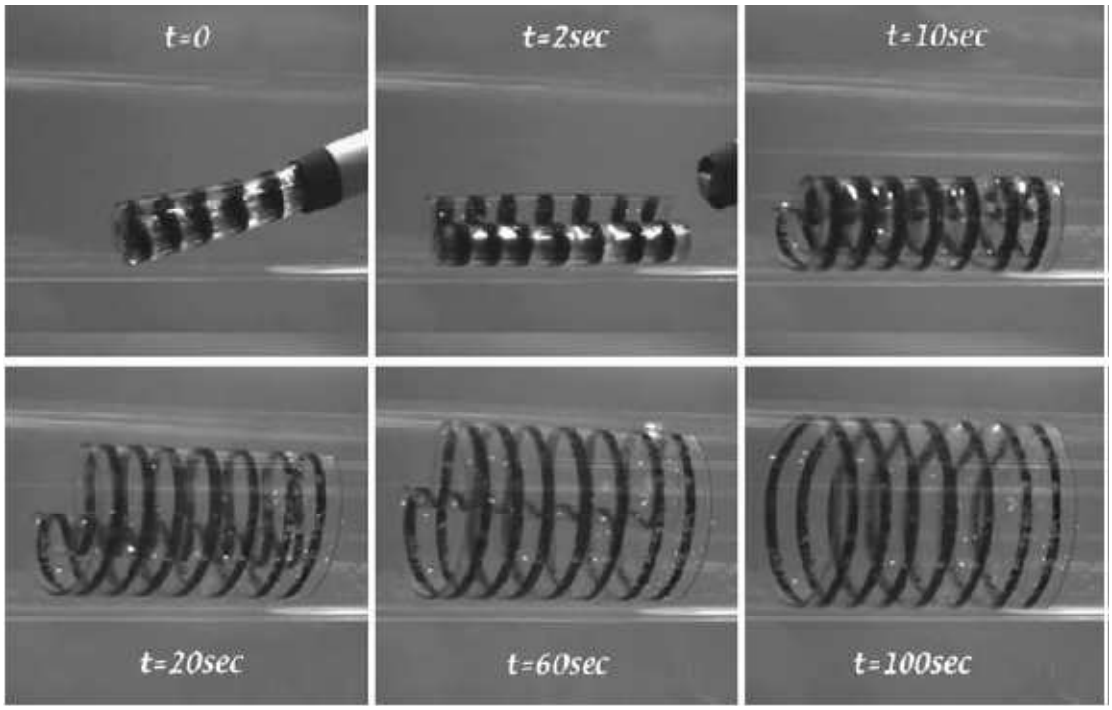

Figure 2.5 Recovery of a 20 wt.% crosslinked SMP stent with T_g=52 °C delivered via an 18 Fr. catheter into a 22 mm ID glass tube containing body temperature water at 37 °C. Black rings were drawn to facilitate deployment visualization [186].

SMPs also offer advantages in MEMS applications in rising to the challenge of creating transduction at small scales. The advantage of shape-memory polymer-based microactuators (pumps and valves) is that they can be integrated into the soft-lithography fabrication methodology with minimal process modification [183]. This alternative to traditional microactuators may be particularly useful for disposable on-

chip microfluidic laboratories. Polymer based microfluidic applications represent a rapidly evolving technology for chemical and biological processing and sensing [184, 185]. Yakacki *et al.* synthesized SMP networks via photopolymerization of *tert*-butyl acrylate and poly(ethylene glycol) dimethacrylate to provide precise control over the thermomechanical response of the system [186]. As shown in **Figure 2.5**, this polymer system exhibits a wide range of shape-memory and thermomechanical responses to meet the specific needs of minimally invasive cardiovascular devices.

2.5 Summary

SMPs and their nanocomposites have received extensive attention in recent years. The shape recovery behaviour of the SMPs have been shown to be an important phenomenon with wide potential application, particularly when the SMPs can act as instrumental parts in bio-MEMS devices. Meanwhile, the limitations such as low strength and lack of effective controlling methods for the pure SMPs have been identified. Nanoparticles are known to be effective enhancers and functionalizing agents in soft polymeric matrices. Various attempts at introducing nanoparticles into the polymeric matrix have been made but the theory of property enhancement has not yet been systematically explored.

Chapter 3

MATERIALS AND EXPERIMENTAL METHODOLOGY

This chapter describes the selection of the raw materials, the material synthesis and the characterization methods which were used in this research work.

3.1 Materials selection

In this project, two different shape memory polymers were chosen for investigation. One was SMPU, and the other was a shape memory polystyrene (SMPS) based copolymer. The specific features of the SMPU, all components for the SMPS and some relative auxiliary chemical reagents are listed in **Table 3.1.**

Table 3.1 Chemicals as received

Name	Formula	Type	Supplier	Technical specifics	usage	Ref.
Polyurethane	N/A	MM5520	MHI, Japan	See ref	Matrix	187-189
Styrene based precursor	N/A	Veriflex® part A	CRG ,US	See ref	Matrix	190-193
Curing agent	N/A	Veriflex® part B	CRG,US	See ref	Catalyst	190-193
Toluene	C_7H_8	N/A	SIGMA, UK	anhydrous, 99.8%	Solvent	194
Sodium dodecylbenzenesulfonate	$C_{18}H_{29}NaO_3S$	N/A	SIGMA, UK	Technical grade	Surface treatment	194
Benzoyl peroxide	$C_{14}H_{10}O_4$	Luperox ATC50	SIGMA, UK	50 wt. % in tricresylphosphate	Catalyst	190-193
divinyl benzene	$C_6H_4(CH=CH_2)_2$	80% (Aldrich)	SIGMA, UK	Technical grade	Cross-linker	190-193
Acetone	C3H6O		Fisher, UK	ACS reagent, ≥99.5%	Solvent	194

The SMPU used in this study is a thermoplastic resin in pellet form (MM5520, DiAPLEX Ltd, MHI), reported to be a segmented PU with a nominal glass transition temperature of 55 °C [1-3]. The MM5520 has an ether-based soft segment, whose

composition can be approximately inferred from the literature [187-189, 195]. Specifically, this SMPU should consist of the soft segments including adipic acid/polytetramethylene glycol (main part), bisphenol, ethylene or propylene oxide, and bis (2-hydroxyethyl) hydroquinone, as well as MDI dominated hard segments. The detailed segment distribution and molecule chain structure of the thermalplastic SMPU have been studied in the literature [196, 197] as illustrated in **Figure 3.1**.

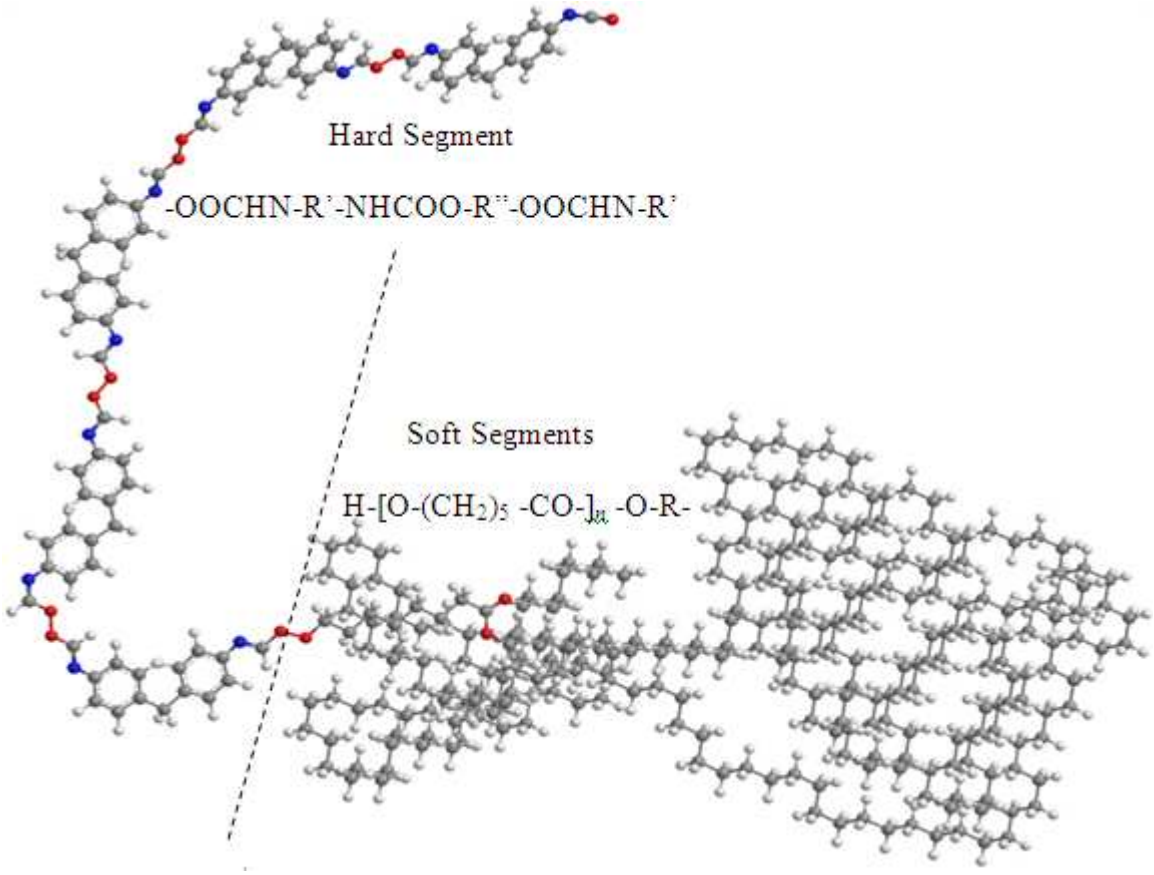

Figure 3.1 Molecular structure schematic for thermalplastic linear SMPU with functional segments classification

Unlike the commercial SMPU, the SMPS in this study was obtained through polymerization via thermal curing the prepolymer/precursor and catalyst (curing agent). For the Veriflex® precursor (96 wt.%) , although the precise composition was not provided by the manufacturer, the patent literature [190, 193] suggested that the 2-component precursor consists of a mixture of polystyrene (PS, 30 wt.%), styrene (St, 55.2 wt.%), divinyl benzene (DVB, 0.8 wt.%) and vinyl neodecanoate (10 wt.%). The curing agent (4 wt.%) include benzoyl peroxide (BPO, 2 wt.%) and ester plasticizers (2

wt.%). Hereafter, all the composition ratios are expressed as weight percentage by the final polymer mass otherwise indicated [190, 193].

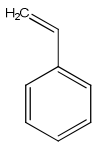

Styrene (molecular structure)

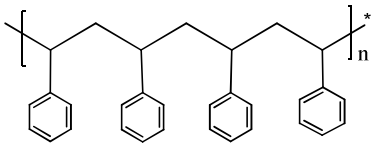

polystyrene

Styrene (Ball-stick model)

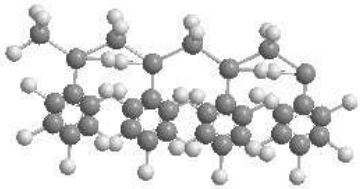

polystyrene

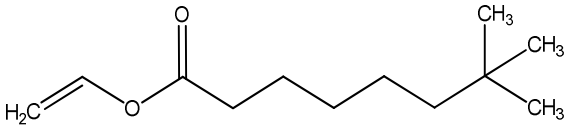

Vinyl neodecanoate (molecular structure)

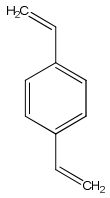

Divinyl benzene

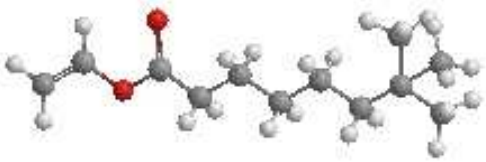

Vinyl neodecanoate (Ball-stick model)

Divinyl benzene

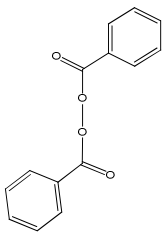

Benzoyl peroxide (molecular structure)

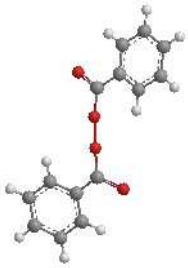

Benzoyl peroxide (Ball-stick model)

Figure 3.2 Formulation and ball-stick structure illustrations for the chemicals used

Various types of nanoparticles were used to prepare the polymer nanocomposites. The specific features for the selected nanoparticles and the related references describing the application of these nano fillers are listed in **Table 3.2.**

Table 3.2 Nanoparticles features as received

Name	Type	Supplier	Technical specifics	Ref.
Attapulgite clay	N/A	Denoted	*Non-treated Fibre, D=20 nm , l=3 μm; treated bundled platelets Thickness =20 nm , l=3 μm;*	84
Al_2O_3	N/A	Denoted	*D=30~100 nm*	198, 199
SiO_2	AEROSIL 200	Evonik-Degussa	*D=7~50 nm*	200
Carbon nanoparticles (CNP)	VXC72R	Cabot	*D=15~60 nm*	201, 202
Carbon nanofibre (CNF)	PR-19-XT-LHT-OX	Pyrograf	*D × L 70-200 × 10-200 μm*	203-205
Multi-wall carbon nanotube (MWCNT)	Product No. 659258	SIGMA,UK	*90% carbon, D × L 70-170 × 5-9 μm*	119, 149, 206
Single-wall carbon nanotube (SWNT)	Product No. 6 98695	SIGMA,UK	*40-60 wt. % carbon basis, D × L 2-20 nm × 1-5 μm*	99, 152, 207

3.2 Shape memory nanocomposite fabrication and synthesis

3.2.1 *Melting processing for PU/clay composites*

Attapulgite clay, with chemical composition $(Mg,Al)_2Si_4O_{10}(OH).4(H_2O)$, was heat-treated in an oven (in air) at 850 ºC for 2 hours, then both the treated clay and non-heat treated clay powders were put in an oven at 120 ºC. PU/clay nanocomposites were fabricated by melting and mixing the commercial SMPU pallets with treated or non-treated clay powders. A Haake Rheocord 90 Torque Mixer was used for the melting fabrication procedure at 200 ºC, and, subsequently, the SMP nanocomposite sample sheets (thickness of ~1 mm) were prepared via a hot press method. The composite samples were stored in a standard air-conditioned room with controlled atmosphere, where the ambient temperature was 20 ºC and the relative humidity was 50% [208]. All samples in this study were kept in this same storage condition.

3.2.2 *Thermo curing SMPS and its composites*

3.2.2.1 Thermal curing fabrication of pure SMPS

Styrene based prepolymer (28.8 g) was mixed with curing agent (1.2 g), i.e. with a fixed weight ratio (prepolymers/cure agent= 24/1). The mechanical stirring was operated for 45 min at a constant rotation speed of 1000 rpm. The experimental set-up is illustrated

in **Figure 3.3** with a sum of experimental parts. Samples were prepared by casting the mixture into PTFE moulds and baked in an oven at 75 °C for 36 hours.

Parts specifications:

1. ***Equipment and parts specifications***:

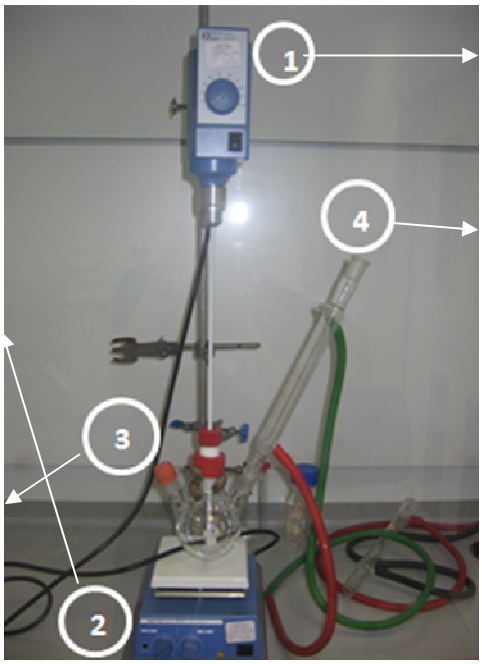

1. Overhead high speed stirrer

2. Hotplate with thermal thermocouple control

4. Glass condenser with cold water inlet (red pipe) and water out (green pipe)

3. Three neck round bottom glass flask acted as mixing container

Figure 3.3 Mixing equipment set-up illustration

3.2.2.2 Non-aqueous solution dispersing techniques of nanoparticles

Considering that the main composition of the precursors is styrene and polystyrene, toluene was selected as solvent for the solution dispersing techniques, because of its wide applications in polystyrene or styrene based co-polymer synthesis [209,210,211]. A surfactant, sodium dodecyl benzosulfonate (SDBS) [212], was employed in the dispersing system. The structure of SDBS is shown in **Figure 3.4**. The nonpolar tails (lipophilic group) became attached to the non polar phases, such as the solvent, while the polar or ionic ends (hydrophilic group) attach to the nanoparticle surfaces with ionic gathering or hydro bonds. Surfactants with concentration above the critical micelle concentration formed micelles around the individual nanoparticles or small bundles when the aggregated nanoparticle bundles were disunited by the combined effects of the high speed mechanical stirring and ultrasonic energy.

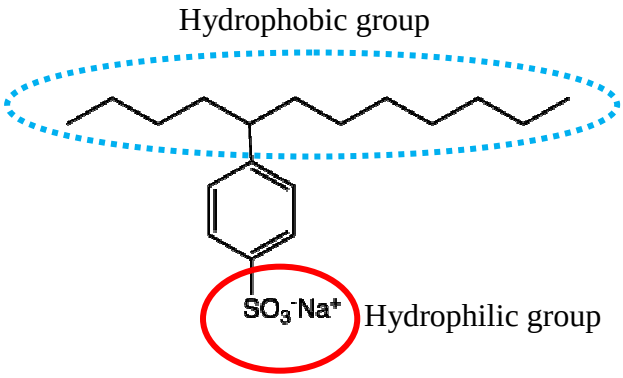

Figure 3.4 Molecular structure of SDBS

All the nanofillers were dried in an oven at 120 °C for at least 48 hours to remove the moisture. Toluene (90 ml), nano particles (0.1~1 g) and SDBS (0.01~0.5 g) were precisely weighed and put in a four neck round bottom flask. The amount of each chemical was suggested in reference [212]. The mixture was stirred ultrasonically at a speed of 1000-1200 rpm for 6 hours.

3.2.2.3 Synthesis of nanocomposites

Styrene-based precursor (Veriflex® part A) was added to the particle dispersing solution and the mixture was agitated ultrasonically for 3 hours at a rotational speed of 1000 rpm [213]. Benzoyl peroxide based curing agent was added and the mixture was stirred ultrasonically at 1000 rpm for another one hour. Film samples of SMP and nanocomposites with a thickness of 0.1-0.3 mm were cast into PTFE moulds and baked at 75-78 °C for 36 hours. Sample concentrations and conversion from weight percentage to volume fraction are presented in **Table 3.2**.

Table 3.2 Nanocomposites fabrication recipe and filler concentrations

Nano fillers	wt.% / vol.%	0.5 wt.%	1 wt.%	2 wt.%	3 wt.%	4 wt.%
Attapulgite clay		0.74	1.26	2.54	3.97	5.34
Al_2O_3		0.58	1.16	2.33	3.48	4.64
SiO_2		0.39	0.78	1.56	2.35	3.14
CNP		5.01	9.59	17.65	24.51	30.44
CNF		1.73	3.42	6.67	9.77	13.34
MWCNT		2.34	4.6	8.87	12.86	17.02
SWNT		3.34	6.6	12.5	17.78	--------

3.3 Characterizations

Different techniques have been used to characterize the SMP and nanocomposites which will be introduced in this section.

3.3.1 *Microstructure and morphology studies*

3.3.1.1 Fourier transform infrared spectrum (FTIR)

FTIR was used to identify the chemical group information as a check for the chemical structure [214,215]. A Fourier transform infrared spectrometer (Satellite FTIR Spectrometer, Mattson) was used to detect the absorption peaks of untreated and thermally treated attapulgite powders. The clay samples were prepared using a KBr pellet technique and scanned in the range of 400-4000 cm^{-1}.

An optical microscope (OM, Nikon, with N50 monochrome camera) with various magnifications was employed to examine the surface structure, indentation marks, and shape recovery of samples. Its resolution reaches as low as 5 μm. The computer assisted OM system is shown in **Figure 3.5**.

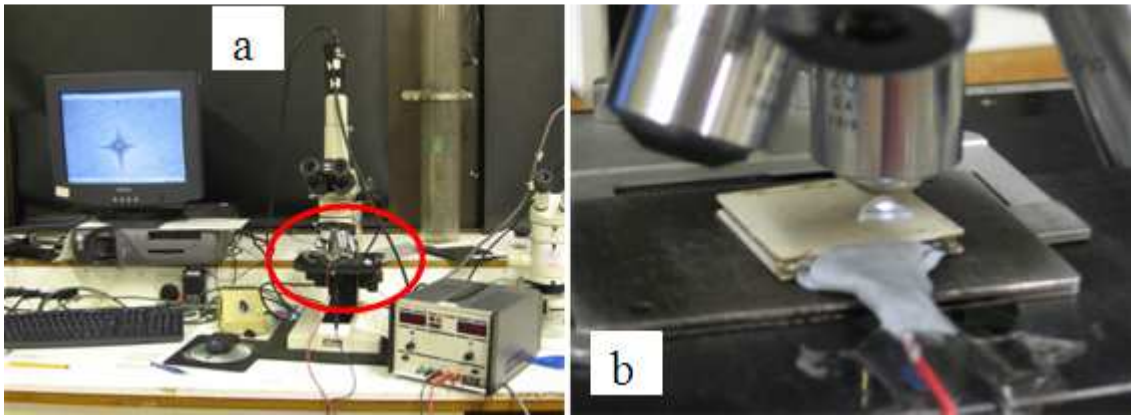

Figure 3.5 Computer assisted OM system (a), magnification of the observation stage (b), where polymer sample was placed on the Pieter device under the lens.

Electron microscopy is able to characterize the distribution of nanofillers inside the composite samples, as well as showing the microstructure of the materials. Scanning electron microscopy (SEM, Tescan Lyra FIB/SEM-FEG) and high resolution

transmission electron microscopy (HR-TEM, JEOL 2010F operating at 200 kV) were used to study the microstructure of the samples. The powder samples were dispersed in isopropanol in an ultrasonic bath for 10 min before SEM and TEM observations. Selected area electron diffraction patterns were also obtained to reveal the nanocrystalline nature of the nanofillers. The fracture surface morphology of the nanocomposites was studied using SEM by breaking the nanocomposites after immersing them in liquid N_2 for 2 minutes.

3.3.1.2 Metrological measurement of surface structure: Profilometer and Atomic Force Microscopy (AFM)

The profilometer operates by lightly dragging a sharp stylus over the surface of the substrate and recording the vertical profile of the surface. This can be used to measure the height or width of a feature of the sample surface. For this work, a profilometer (DEKTAK 3) was used to record the shape recovery of Vickers indentation marks on the sample surface. Samples were put on a Peltier heating device which was connected to a DC power supply. Multiple profiles scanned on the indents were carried out during shape recovery, so that the morphology changes could be recorded *in situ*.

Atomic force microscopy (AFM) with its unique 'contact' probe can provide the surface morphology of samples using point to point data acquisitions. 3D images and statistical profiling are also achievable through data processing. In this research, an AFM was employed to measure the surface morphology of the nanoindentation area, providing the surface topology and the deformation of the indentation marks. The AFM system was integrated with the TriboIndenter® (Triboscope, Hysitron Inc., Minneapolis, USA) hardware system. Two basic operating modes are available, Contact Mode and Wave Mode. The Contact Mode was selected in this study to reveal the real surface morphology. Series scans were performed with a scanning rate of 1 Hz as soon as the nanoindentation finished.

3.3.2 *Thermal analysis techniques*

Thermal analysis comprises a group of techniques used to investigate the physical behaviour of a substance as a function of temperature, while the substance is subjected

to a controlled temperature cycle. Three thermal analysis techniques were applied in this project, thermogravimetry (TGA), differential scanning calorimetry (DSC) and dynamic mechanical thermal analysis (DMTA).

TGA is commonly used to characterize the decomposition and thermal stability of materials during a variety of applied conditions and to detect the physicochemical processes occurring in specimens by measuring the weight changes as a function of temperature. In this project, TGA was used to investigate the mass change of attapulgite powder during controlled temperature ramping, in order to evaluate the clay structure condition by comparing the TGA results of non-treated and treated samples. TGA characterization was carried out using a TA Instrument TGA 2950, and a 5 mg sample was heated in an alumina crucible with a heating rate of 10 °C /min from room temperature to 900 °C under N_2 atmosphere.

DSC, as a comman thermal testing method for macromolecular systems, was used to characterize the glass transition temperature (T_g), melting temperature and crystallinity, and it can reveal the mobility of molecular chains by specific thermal energy variation. DSC was used in this project to identify the T_g of each sample, which indicates material structural modification at a molecular level. The DSC test was performed with a Thermal Advantage DSC 2010 (heat flux DSC) at a heating rate of 10 °C / min under a constant nitrogen flow.

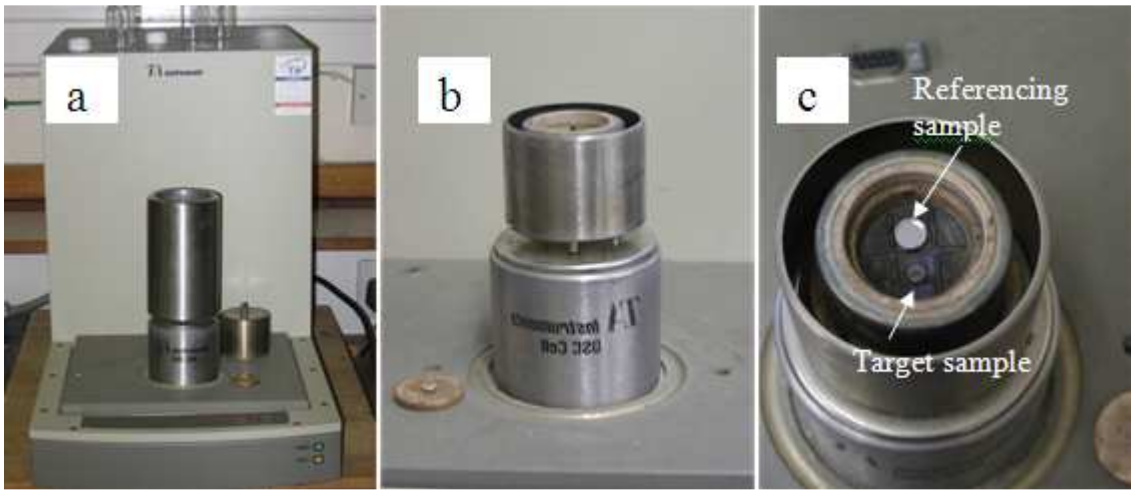

Figure 3.6 Images of DSC 1010 with highlighting functional parts, (a) overview, (b) side view, (c) core part with referencing/target sample positions

The thermal-mechanical behaviour was investigated by differential mechanical thermal analysis (DMTA), and specimens were subject to a sinusoidal tensile stress of frequency (ω) while the programmed temperature ramp, load and displacement were measured. Three parameters from DMTA which were used in this study:

$$\text{Storage modulus: } E' = \frac{\sigma_0}{\varepsilon_0}\cos\delta \tag{3.1}$$

$$\text{Loss modulus: } E'' = \frac{\sigma_0}{\varepsilon_0}\sin\delta \tag{3.2}$$

$$\text{The phase angle: } \tan\delta = \frac{E''}{E'} \tag{3.3}$$

where σ_0 is the maximum stress amplitude and the stress precedes the strain by a phase angle δ, ε_0 is the maximum strain amplitude. For a viscoelastic polymer, E' characterizes the ability of the polymer to store energy (elastic behaviour), while E'' reveals the tendency of the material to dissipate energy (viscous behaviour). DMTA is also a sensitive method to measure T_g of polymers. In this project, DMTA tests were carried out in tensile mode with a TA Instruments DMA 2980 (**Figure 3.7**) at a frequency of 1 Hz, a heating rate of 2 °C/min and a temperature range from 25 to 120°C. Constant nitrogen flow was provided to ensure atmospheric protection. Thermal expansion coefficients were also obtained using DMTA [48, 49]. The length, width, and thickness of the test samples was 10 mm, 6 mm and 0.2 mm respectively. The length/thickness ratio was bigger than 10 in order to eliminate the size dependence on the Poisson's ratio of the materials.

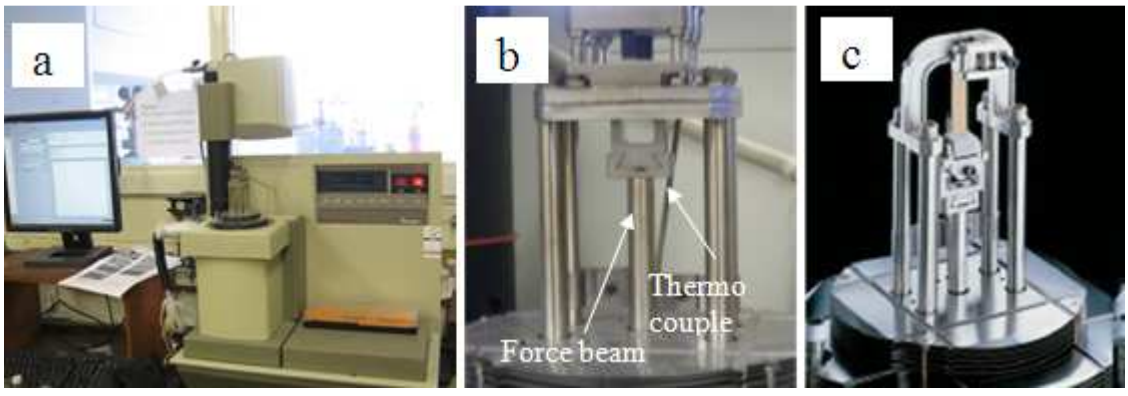

Figure 3.7 Images of DMTA 2980 with highlighting functional parts, (a) overview, (b) core parts, (c) tension mode images from TA Co'Ltd.

3.3.3 *Mechanical properties*

Various techniques were used to characterize the mechanical properties on the SMP and nanocomposites, including tensile tests, Vickers indentation and nano-indentation tests.

3.3.3.1 Uniaxial tensile test

A conventional macroscopic tensile test was used to obtain the mechanical strength of the materials. Tensile samples were cut into strips with length 50 mm × 6 mm, and thickness 0.1 to 0.2 mm. Tensile tests were carried out using an Instron universal test machine (Instron 5567), at a constant crosshead speed of 5 mm/min at room temperature (~20 °C). The experimental set-up and dimensions of the specimens followed the British Standards [216-219]. At least 5 specimens were tested for each sample, and a statistical average was made based on the batch results.

3.3.3.2 Vickers micro-indentation

The Vickers indentation test measures micro-hardness by pushing a square (equilateral) pyramid indenter into the sample with a fixed load and then measuring the size of the indent using a microscope, as shown in **Figure 3.8**.

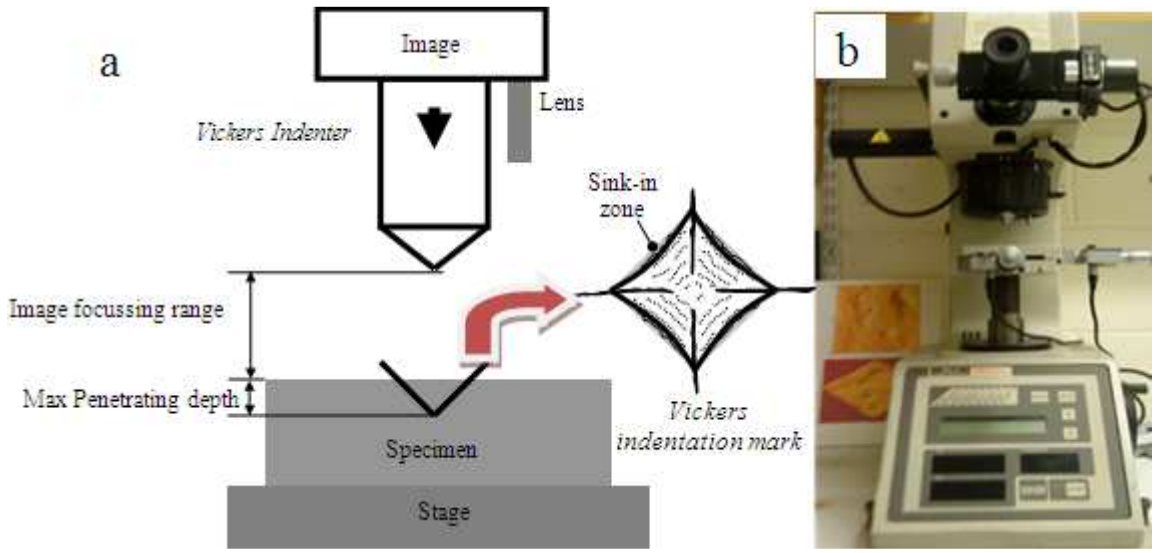

Figure 3.8 Schematic of measurement theory (a), indentation mark and experimental set-up image (b).

Various loads are achievable from 10 g to 1000 g. Since the fabricated sample normally has a fine surface, for a better comparison with the macroscale hardness values, only those samples with rough surface were polished. The experimental settings followed the standards [220, 221]. The Vickers microhardness tests were performed using a calibrated Mitutoyo, MVK-H1 machine. The averaged hardness was generated from at least five indentations. The indentation load was fixed at 245 mN (or 250 g), and a holding time of 20 s was set for each test. Hardness (*HV*) was calculated from:

$$HV = 1.854\frac{F}{A} \tag{3.4}$$

where F is the applied load in N, A is the indenter area in mm^2.

3.3.3.3 Nanoindentation test

Instrumented nanoindentation is employed to analyze the micro-mechanics of soft materials, such as static strength and visco-elastic behaviour. Nanoindentation was carried out using a TI 900 Triboindenter system (Triboscope, Hysitron Inc., Minneapolis, USA) with a Berkovich tip, *i.e.* a three-sided flat pyramidal diamond flat tip with an angle of 104.3^o. Integrated system is illustrated in **Figure 3.9**.

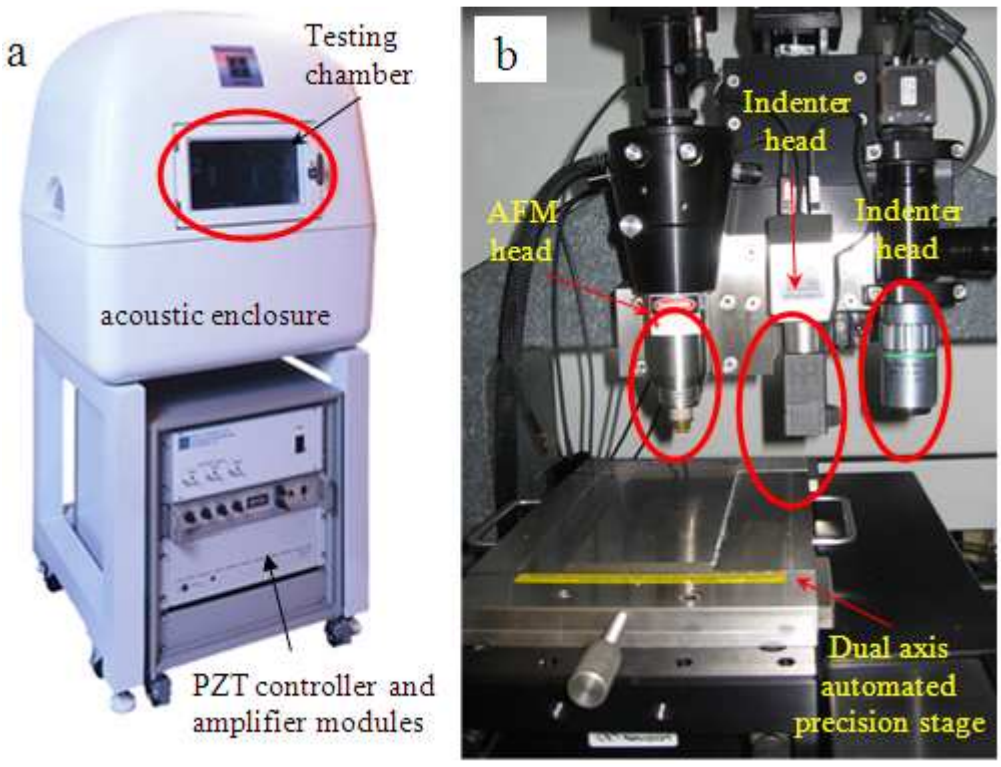

Figure 3.9 Illustration of Hysitron TI 900 TriboIndenter system, (a) overview, (b) function distribution and parts descriptions.

The measurement was taken at room temperature (~20 ^{o}C). An acoustic enclosure was adopted to prevent acoustic interference from the environment. The indentation procedure followed with three stages (see **Figure 3.10**). Here, h_{max} is the maximum penetration depth, P_{max} is the maximum indentation force; the stiffness of unloading curve S is the slope of a linear fit to the initial points of the unloading stage; h_p represents the permanent depth; h_c is the contact depth, and the inlet shows the surface mechanical deformation with possible pile-up effect at each stage.

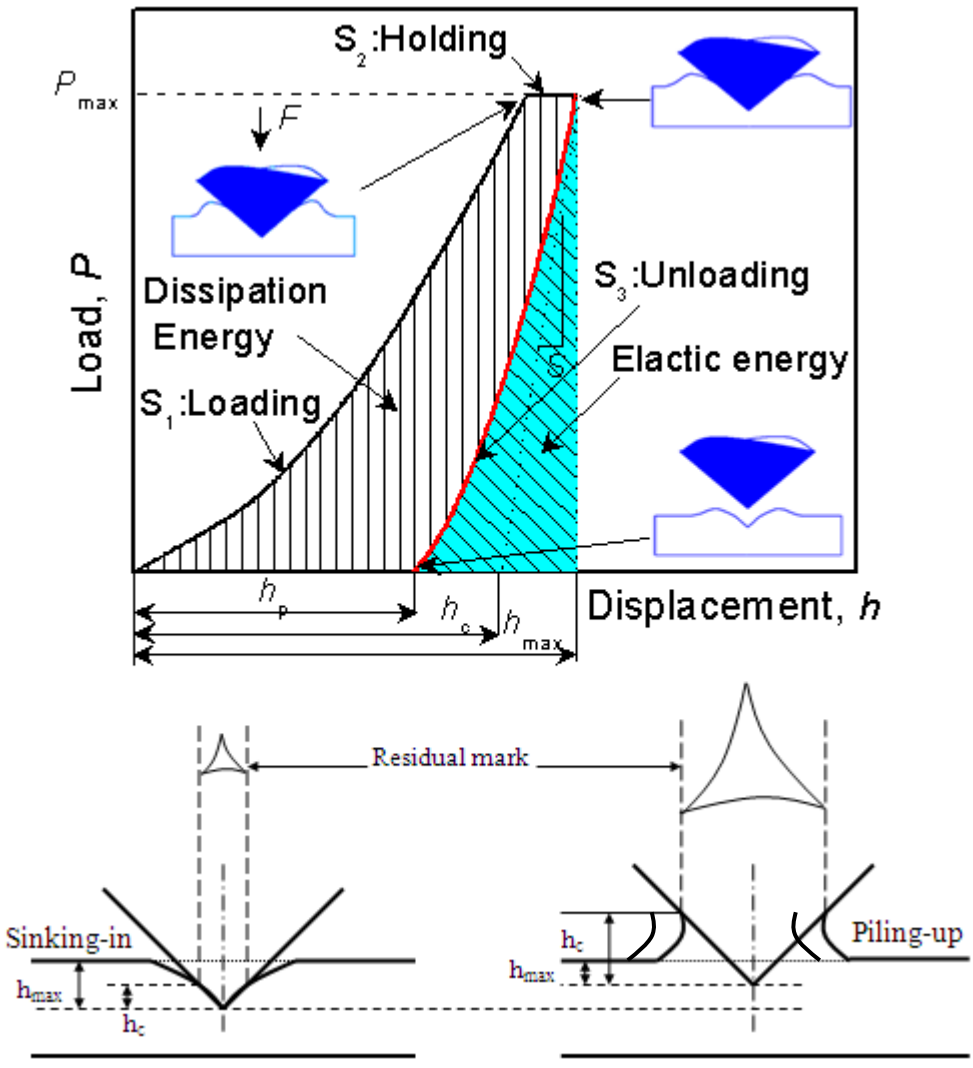

Figure 3.10 Schematic of typical load-displacement curve for nanoindentation on shape memory polymer. The elastic-plastic energy distributions are also labelled.

The first stage is to increase the load to a maximum value with a fixed loading rate, followed by a holding stage at the maximum load. The third stage is to retract the indenter tip from the sample with a fixed unloading rate. Two 2×2 arrays of indents were performed on each sample. Various peak loads were applied. The fixed load

holding segment was applied to minimize the effects of material creep on the estimated values of modulus and hardness [222]. A typical load (P) vs penetration depth (h) curve is shown in **Figure 3.10**, as well as typical material deformation after indentation [223,224].According to Oliver and Pharr [223,224,225], the various parameters from nanoindentation with a Berkovich tip are obtained from:

$$\text{Contact depth, } h_c = h_{\max} - 0.75\frac{P_{\max}}{S} \tag{3.5}$$

$$\text{Hardness, } H = \frac{P_{\max}}{A} \tag{3.6}$$

$$\text{Stiffness of unloading curve, } S = \frac{dP}{dh} \tag{3.7}$$

$$\text{Contact Area, } A = 24.5h_c^2 \tag{3.8}$$

$$\text{Reduced modulus, } E_r = \frac{S\sqrt{\pi}}{2\sqrt{A}} \tag{3.9}$$

$$\frac{1}{E_r} = \frac{1-\upsilon_{sample}^2}{E_{sample}} + \frac{1-\upsilon_{indentor}^2}{E_{indentor}} \tag{3.10}$$

where $h_{\max}$ is the maximum penetrating depth, $P_{\max}$ the max indentation force, h_c the contact depth, A the contact area, E_r the residual modulus. Stiffness S is the slope of a linear fit to the initial points at the unloading stage. As indicated by the *Triboindenter*® *User Manual* (Hysitron Inc., Minneapolis, USA), the elastic modulus E_{indenter} is 1140 GPa and Poisson's ratio $\upsilon_{\text{indenter}}$ is 0.07. For the nanocomposites used in this study, υ_{sample} was fallen to be 0.31. According to **equation 3.10**, the elastic modulus of sample can be derived from:

$$\text{Elastic modulus, } E_{sample} = \frac{E_r}{0.91} \tag{3.11}$$

The dissipation energy (DE) is defined as the enclosed area of load-displacement curve [226] which represents the energy absorbed by the material, and the elastic energy is the area beneath the unloading curve which represents the recoverable energy. The dissipation energy and elastic-plastic energy distributions were calculated from the load-depth curves of samples using MATLAB® software.

For hardness measurements, various loads were applied from 100 μN to 5000 μN, with a contact loading/unloading rate of 200 μN/s, and a holding time of 5 s. Dynamic elastic

behaviour or the viscoelastic properties of the sample were characterized by changing the loading/unloading rate and holding time, statistical analysis was carried out on the batch data to evaluate the sample response to different loading conditions.

3.3.4 *Electrical properties*

Hybrid composites obtained by embedding conductive inorganic nanoparticles into polymers have huge potential applications in microactuation and microsurgery applications. The electrical characterizations used in this project included conductivity, dielectric and electro-thermal tests. Electrical conductivity and electric thermal effects were tested with a specifically designed experimental set-up, and the dielectric property was obtained using a dielectric testing machine.

3.3.4.1 Resistivity/conductivity test

The resistivity was measured by a simple I-V test set-up consisting of a power supply, a multi-meter, and a digital thermometer. Square sample films were trimmed to 2 cm × 2 cm, and the thickness was 0.1 to 0.2 mm. The set-up was shown in **Figure 3.11**.

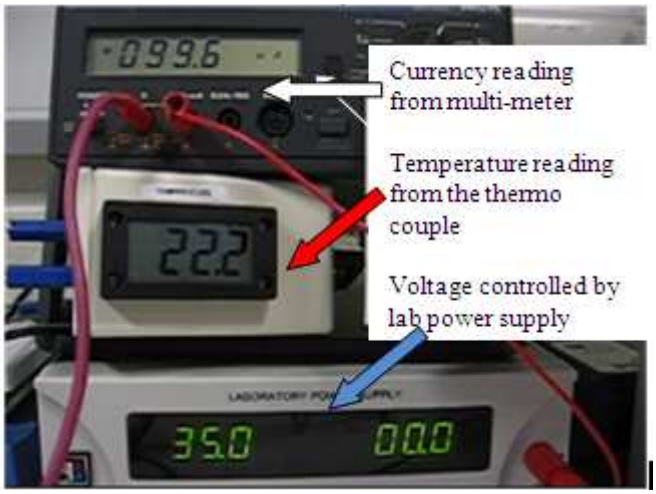

Figure 3.11 Illustration of resistivity/conductivity testing equipments

The tests were performed in a controlled atmosphere with a constant ambient temperature of 20 ^{o}C and humidity of 50 %. The conductivity was calculated from the measured resistance using the following equation:

$$\Xi = L/(TWR) \tag{3.12}$$

where Ξ is the conductivity, sample dimension length (L), thickness (T) and width (W) are pre-measured in cm, and R is the measured resistance of the specimen in ohms.

3.3.4.2 Dielectric test

The dielectric properties of SMPs and nanocomposites are important parameters for MEMS/ bio-device application. In this project, dielectric properties of square samples of 2 cm × 2 cm × 0.1 to 0.2 mm were measured. The dielectric measurements of the composites were performed in a frequency range from 10^{-2} to 10^{6} Hz using a Schlumberger Solartron 1250 Frequency Response Analyser. Testing was programmed from room temperature to 100 °C in ambient air.

3.3.5 *Shape memory recovery characterization*

3.3.5.1 Thermo-active shape recovery observation

Various patterns were designed to show shape recovery performance of the materials. Micro-patterns were ablated with a high power laser system (512 nm, 90 mW) [227]. An optical microscope and a digital camera (Canon A510) were used to record the real-time response to the thermal or electrical stimulus of obtained device.

3.3.5.2 Cycling thermal tensile test

Figure 3.12a show the thermo-mechanical cycling test set-up. Cycling tests (shown schematically in **Figure 3.12**b and c) were used to investigate the shape recovery ratio of the SMP and nanocomposites under certain conditions. There are four steps in each cycle: (1) stretching to ε_m at T_{high}; (2) cooling to T_{low} with holding strain; (3) Unloading and keeping shape at T_{low}; (4) heating up to T_{high}; then start of next cycle. These tests consisted of loading the specimen to a strain (ε_m) at a constant crosshead speed of 5 mm/min at a temperature T_{high} (stage 1), and then cooling down to the temperature T_{low} while holding the same strain (ε_m (stage 2)). After 5 min at the temperature T_{low}, the specimen was unloaded (stage 3) and reached a strain ε_e. The unloaded specimen was immediately heated from T_{low} to T_{high} in 5 min (stage 4), which left a permanent strain ε_p. This four-stage thermo-mechanical cycle was repeated to a total of 4 cycles. The

fixed conditions of the cyclic test were: ε_m=100%; T_{high}=60 °C, T_{low}=20 °C, and ε_e (the strain after unloading) and ε_p (the permanent strain) were both recorded for each specimen.

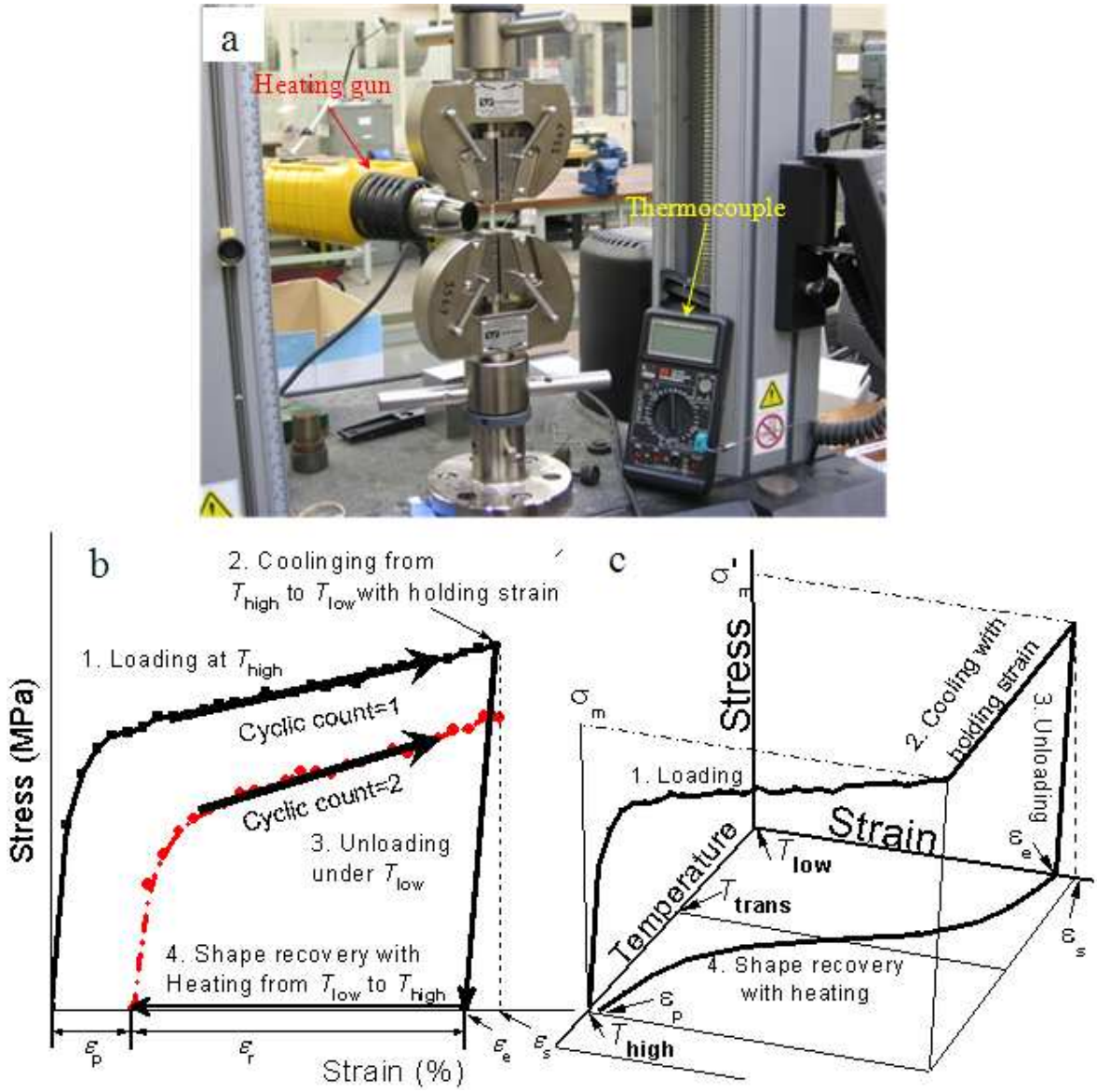

Figure 3.12 Thermal cycling tensile experimental set-up: (a) photography of set-up, (b) 2-D and (c) 3-D schematic drawings of cyclic tensile testing.

3.3.5.3 Electro-active shape recovery test

Microcantilevers made from the conductive nanocomposite (with dimensions shown in **Figure 3.13a**) for electrical actuating shape recovery testing were fabricated through laser cutting. The electro-active recovery set-up is shown in **Figure 3.13c**.

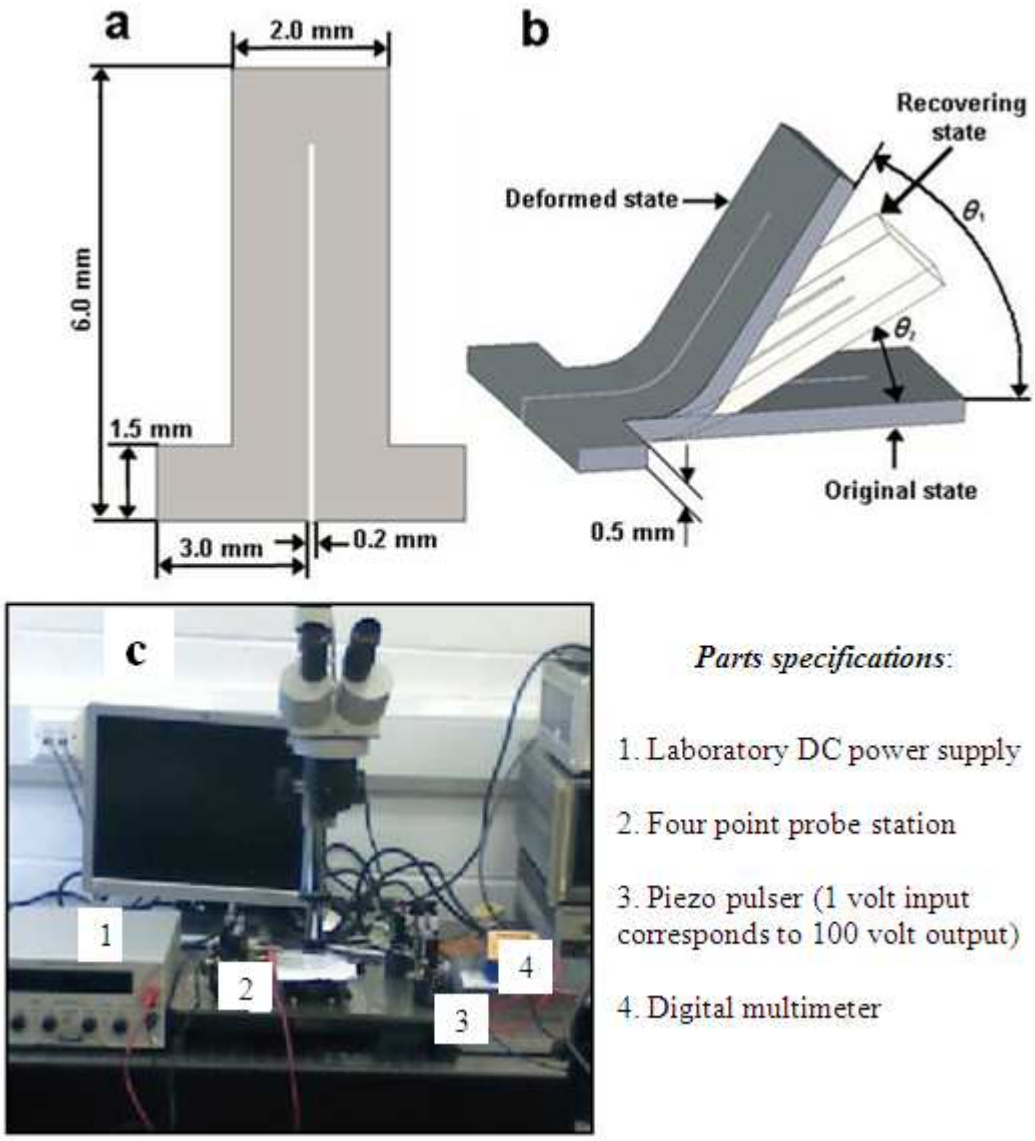

Figure 3.13 Schematic of (a) sample dimension, (b) recovery stages with marked angle and (c) the electro-active set-up

Recovery tests were performed using different electrical powers, and the sample temperatures were measured using an IR thermometer. The shape memory recovery rates (*RR*) were calculated based on the following equation:

$$RR = \frac{(\theta_1 - \theta_2)}{\theta_1} \times 100\% \tag{3.13}$$

where θ_1 is the initial bending angle of the cantilever and θ_2 the residual bending angle after shape recovery, as shown in **Figure 3.13**b. Lager samples with a similar shape in **Figure 3.13**a were also tested as shown in **Figure 3.14**a, the recovery was evaluated by pre-deforming the cantilever (**Figure 3.14**b). The shape memory recovery rates (*RR*) were calculated based on the following equation:

$$RR = \frac{(\theta_1^{'} - \theta_m)}{\theta_1^{'}} \times 100\% \qquad (3.14)$$

In particularize, the $\theta_1^{'}$ was be very close to 360°.

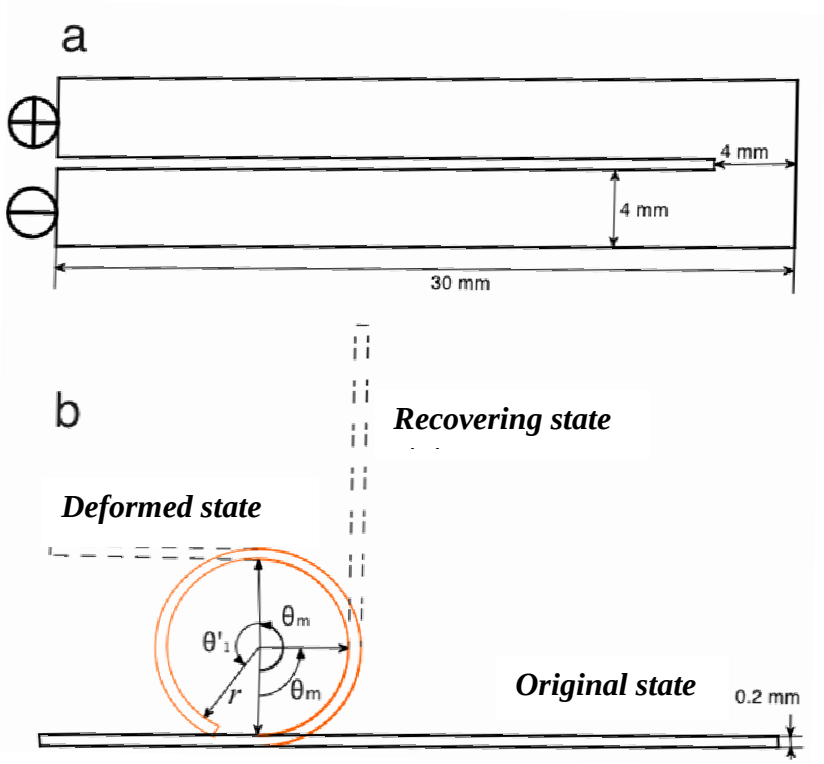

Figure 3.14 (a) Millimetre scale cantilever sample dimension and (b) recovery demonstration with each state as well as the marked angle

Chapter 4

NANOCLAY REINFORCED POLYURETHANE SHAPE MEMORY NANOCOMPOSITES

As mentioned in **Chapter 2**, one major disadvantage of SMPs is their low stiffness and strength compared to shape-memory alloys or ceramics, which dramatically limits the application of the SMPs. Accordingly, a great deal of current work focuses on searching for nano-size fillers to enhance the mechanical and shape-memory recovery properties of the SMPs [118,71,136,134,128]. In this chapter, attapulgite clay is studied with the purpose to enhance the mechanical properties of SMPU. The SMPU was chosen because of its availability and linear amorphous structure which allow correlating with available theoretical analyse [228,18, 149]. Nanocomposites based on the attapulgite clay and SMPU were fabricated through mechanical melting/mixing techniques. The main objectives were to examine how the clay enhances the strength of the polymer matrix, and understand the changes of physical/chemical properties during conditioned shape conversion.

4.1 Nano-clay powder characterization

Figure 4.1 shows an SEM image of the commercial attapulgite clay powder revealing a loose fibre bundle structure. The length of each fibre varies from sub-micrometre to a few micrometres and the diameter is in the order tens of nanometres. The TEM images in **Figure 4.2a** show that the commercial attapulgite particles are highly dispersed individual rods, without much aggregation. Selected area electron diffraction (SAED, not shown) reveals its amorphous nature, confirmed by the HR-TEM images in **Figure 4.2b** and **c**. The diameter of individual fibres is about 20–50 nm, whereas the average length is a few microns. The mean value of the aspect ratios of the fibres (l/d) is in the range of 40–100.

After heat treatment at 850 ºC for 2 hours, the attapulgite fibres reconstruct and combine together to form a bundled structure (see **Figure 4.3a**), which could no longer be broken even by ultrasonication for an extended time.

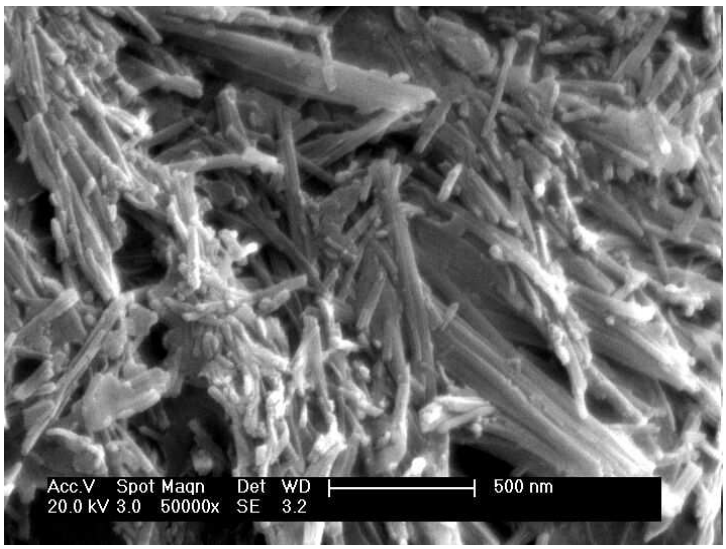

Figure 4.1 SEM observation of the commercial clay revealing a loose fibre bundle structure, with the length of fibres varying from submicrometre to few micrometers and the diameter about tens of nanometres.

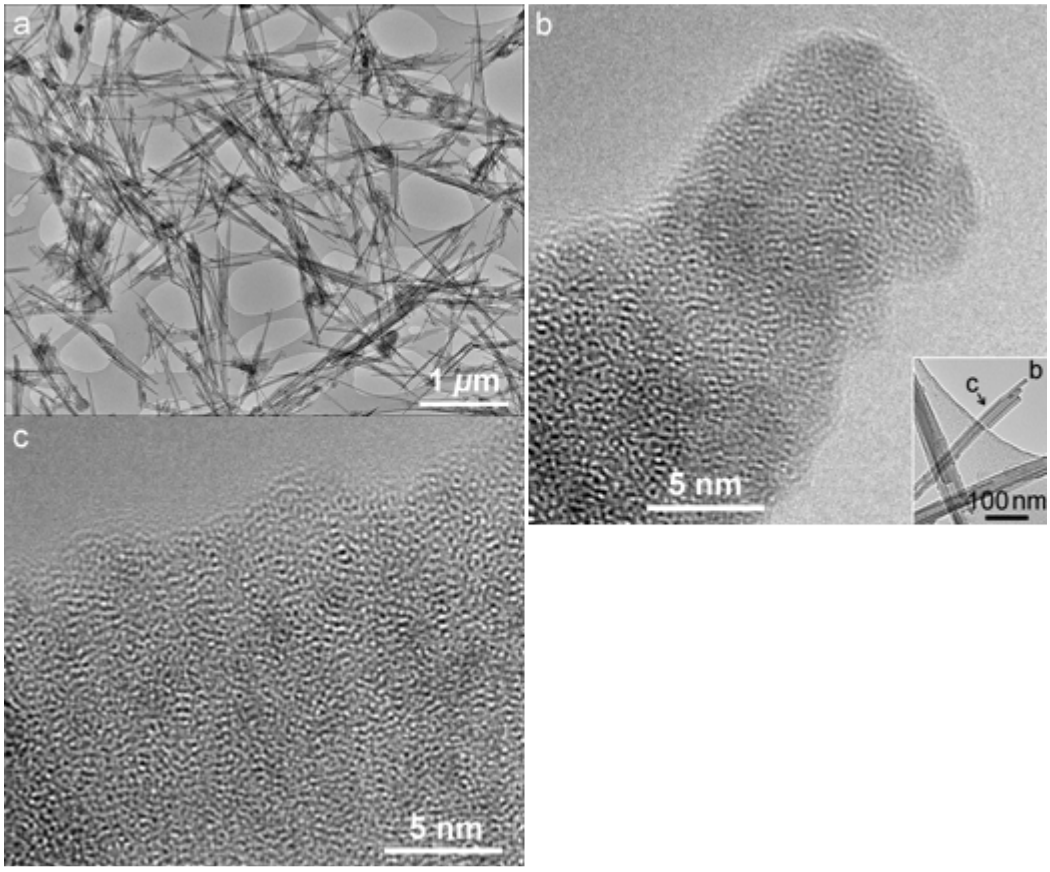

Figure 4.2 TEM observation of non-treated clay powder: (a) overview, (b) and (c) HR-TEM micrographs taken at the end and body of the clay fibre indicated in the inset.

The ring-like scattered diffraction spots reveal the nanocrystalline feature as shown by the inset SAED pattern of **Figure 4.3a**. The corresponding HR-TEM images in **Figure**

4.3b and **4.3c** confirm this new feature. Individual crystallites are embedded in the amorphous matrix with a separation of around 5 nm.

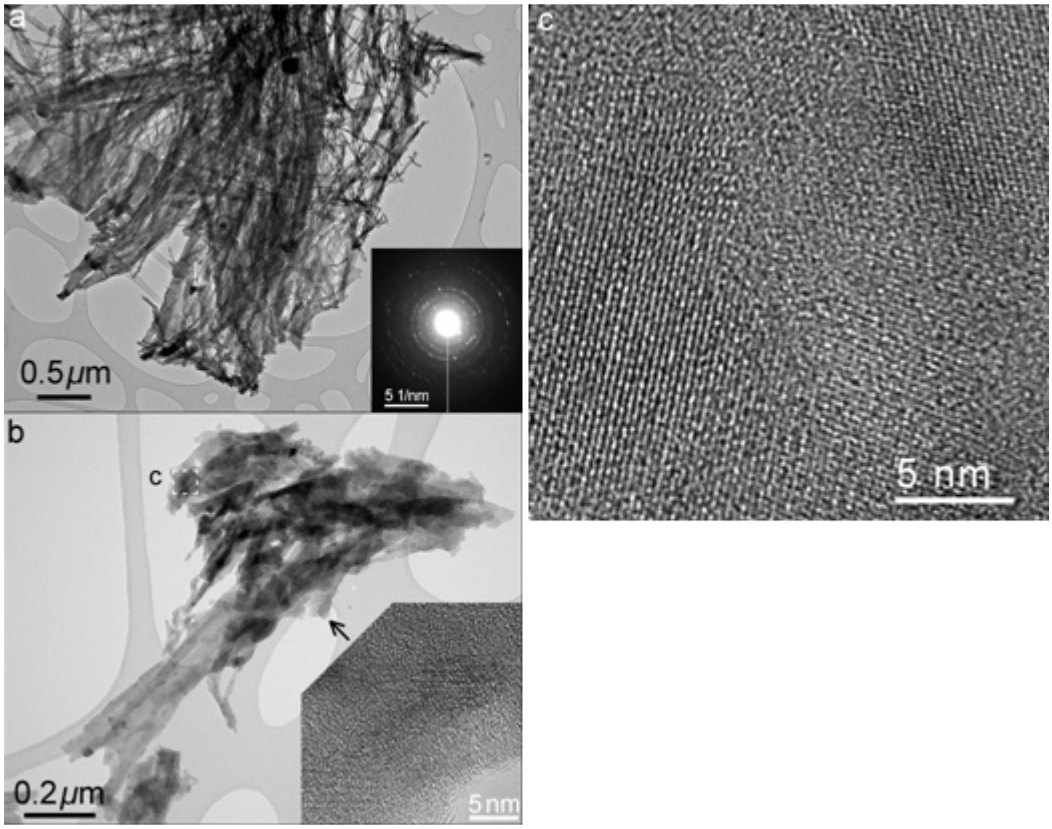

Figure 4.3 TEM observation of heat-treated clay powder: (a) overview and electron diffraction pattern, (b) and (c) HR-TEM micrographs taken at the indicated position of a clay cluster.

Figure 4.4 shows the FTIR results of the commercial and heat treated attapulgite powders. There are two types of molecules containing hydroxyl groups associated with the natural attapulgite. The peak at 3430 cm^{-1} corresponds to the hydroxyl stretching vibrations of the absorbed moisture [229]. The absorbance peak at 3552 cm^{-1} can be attributed to the anti-symmetric stretching modes of molecular water coordinated with the magnesium at the edges of the channel [230]. The peak at 1654 cm^{-1} is associated with the hydroxyl deformation mode of zeolitic water, and the peak at 984 cm^{-1} is the bending vibration of the OH groups [231].

In comparison with the spectrum of the commercial attapulgite powder, the FTIR spectrum of the heat-treated clay revealed a broadening of the peak at 3436 cm^{-1} whereas the 1654 cm^{-1} mode was lost. This suggests that heat treatment had removed most inter-fibrillar water, and reduced most of the –OH group content in the attapulgite.

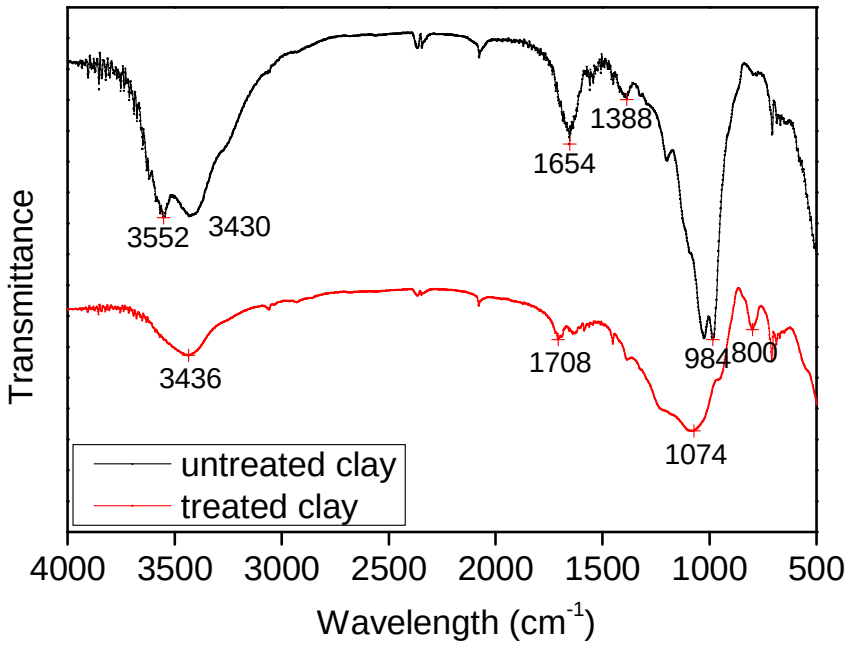

Figure 4.4 FTIR results for the commercial and heat-treated clay powders.

As shown in **Figure** 4.4, the decrease in –OH group content led to absorbance peaks at 1074 cm^{-1} and 984 cm^{-1} which can be attributed to the symmetric and anti-symmetric Si-O-Si stretching vibrations [232,233]. The peak at 800 cm^{-1} indicates the presence of Si-O-Al and O-Al bonds [233]. It should be pointed out that the peak at 3436 cm^{-1} is still pronounced but shifted from 3430 cm^{-1} after the heat treatment. This is due to the O-H bond being stretched after removing the interfibrillar water [234].

The TGA result of the commercial powder is shown in **Figure 4.5** and reveals a three-stage change during heating. The first stage, at a temperature of about 100°C, corresponds to the loss of moisture which may exist in attapulgite powder as free water. The second stage occurs at about 200°C when the zeolitic tube is destroyed, coinciding with the loss of hygroscopic water and zeolitic water [235]. The third stage, beyond 450 °C, is when the hydroxyl group is gradually reduced. The total weight loss is close to 15.84% for the untreated clay, whereas the heat treated clay did not show a significant drop in weight (see **Figure 4.5**) and re-absorption of water molecules after heat treatment was negligible.

In summary, thermal treatment removes water and most hydroxyl groups for the natural clay powders based on the thermal analysis and IR results. The treated clay powders become crystallized and exhibit a bundled structure as revealed by TEM.

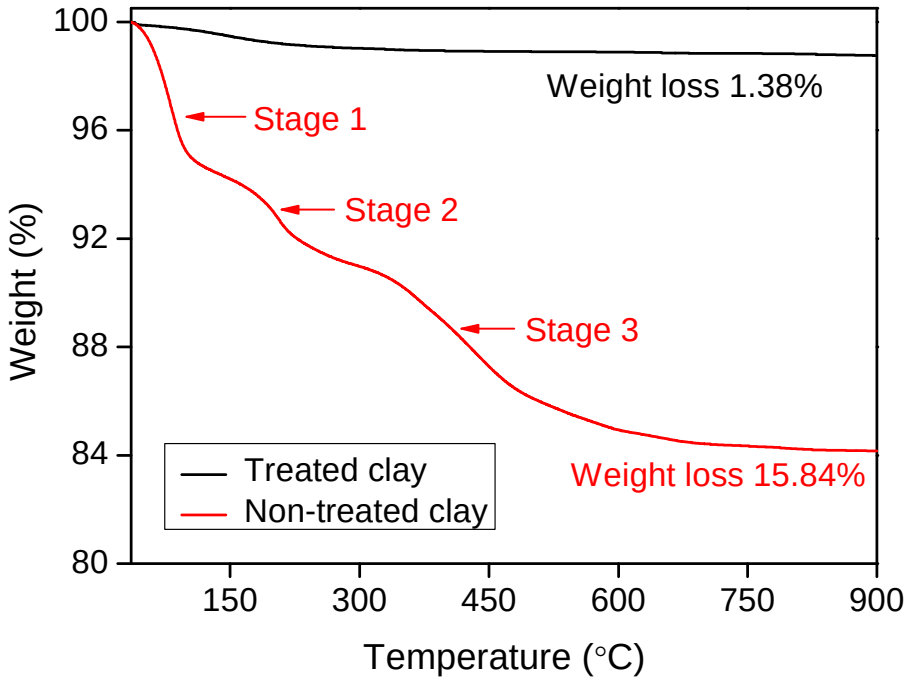

Figure 4.5 TGA analysis of clay powders showing the weight loss during heating for both the commercial and heat-treated clay powders.

4.2 Vickers microindentation and instrumented nanoindentation

Hardness measurements were carried out to samples using Vickers indentation and nanoindentation. **Figure 4.6** presents the microhardness data of the pure PU, treated and untreated clay reinforced composites as a function of applied normal load. Hardness of the PU-based shape memory materials decreases as a function of indentation load, especially at small loads. For ductile materials such as metals, hardness normally decreases with increasing indentation load, which is commonly called the indentation size effect (ISE) [[236]].

Several explanations have been offered for the origin of the ISE, including limitations in experimental conditions (low resolution of the objective lens, work hardening or softening generated during the surface preparation), intrinsic structural factors of the material such as work hardening during indentation, indentation elastic recovery, and grain size effect [[236,237,238]]. The pure PU sample shows the most significant decrease in hardness as a function of normal load (see **Figure 4.6**). This might be explained by the apparent elastic recovery of PU, which could "artificially" enhance the microhardness value at a low load due to shrinkage of the indentations. At a higher load, this artificial enhancing effect is not significant as the indention is quite large.

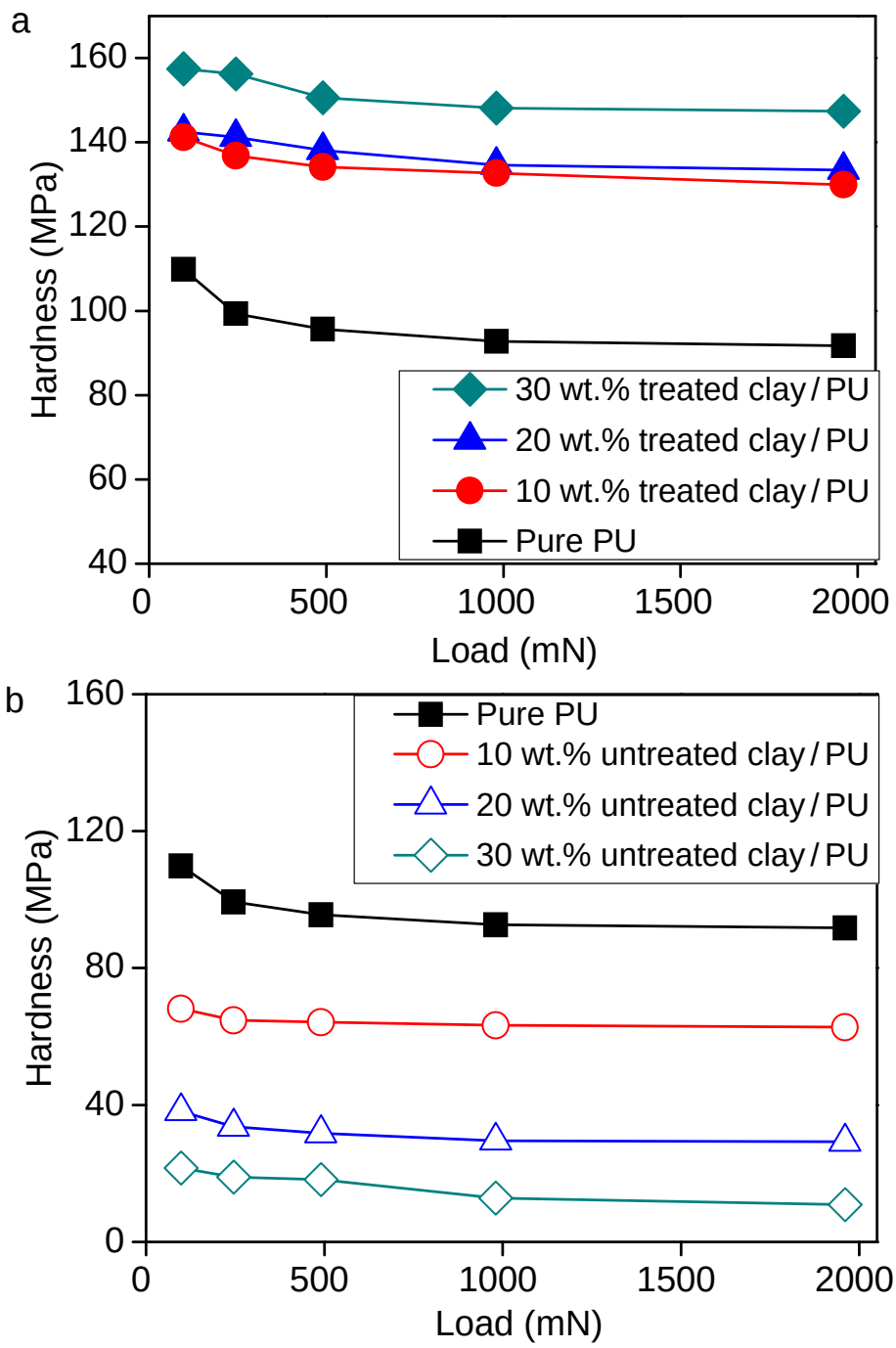

Figure 4.6 Hardness of pure PU and PU-based shape memory composites reinforced with (a) treated and (b) untreated clay powders.

Figure 4.7 summarizes the averaged hardness of the PU-based shape memory composites as a function of the content of heat-treated and untreated clay, measured at different indentation loads as indicated in **Figure 4.6**. Both **Figure 4.6** and **4.7** clearly show that, with addition of the heat-treated clay powder, the hardness of the composites significantly increases with the clay content. At 30 wt.% treated clay, the microhardness reaches a maximum value of about 160 MPa, which is nearly a 60% improvement over

the pure PU. On the contrary, adding untreated clay powder results in a tremendous decrease in hardness of the nanocomposites of up to nearly 85% at 30 wt.% clay.

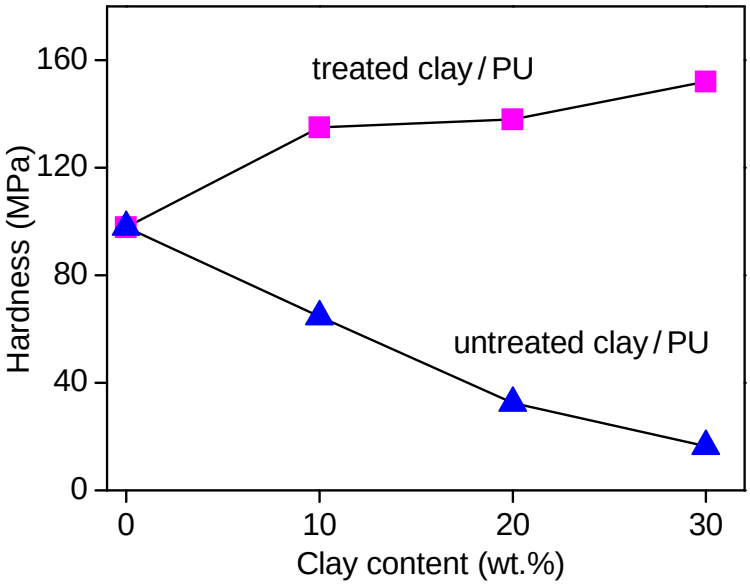

Figure 4.7 Averaged hardness of PU-based shape memory composites as a function of the content of untreated and treated clay powders.

Figure 4.8 generalizes the nanoindentation outcomes with AFM images. Typical loading–unloading curves for the nanoindentation of PU and its nanocomposites with treated clay are shown in **Figure 4.8a**. The indentation depth under a fixed load (400 mN) gradually decreases with increasing clay content, indicating an increase in the resistance to plastic deformation. A reduction of the strain recovery during unloading with the addition of nanofiller is also observed, because incorporating the nanofillers in the microstructure hampers the movement of molecular chains during deformation. **Figure 4.8b** illustrates the hardness profiles for the PU sample and its nanocomposites with treated clay as a function of indentation depth. With a shallow indentation depth, the hardness seems very high because of the indentation size effect (ISE), and this effect fades continuously with the penetration depth. The averaged hardness value increases by about 90 %, from 89 MPa to 166 MPa when the filler content is increased from 0 to 30 wt.%. The nanoindentation results also show a slight increase in improvement in yield stress with increasing filler content. **Figure 4.8c-d** show the surface morphology of indentation marks for the pure PU and nanocomposite (with 30 wt.% clay) from the nanoindentation test. For the pure PU, a pile-up of material can be observed indicating its soft nature, whereas, for the 30 wt.% nanoclay composite, the pile-up is severely restricted because of the increase in the mechanical strength of the nanocomposites.

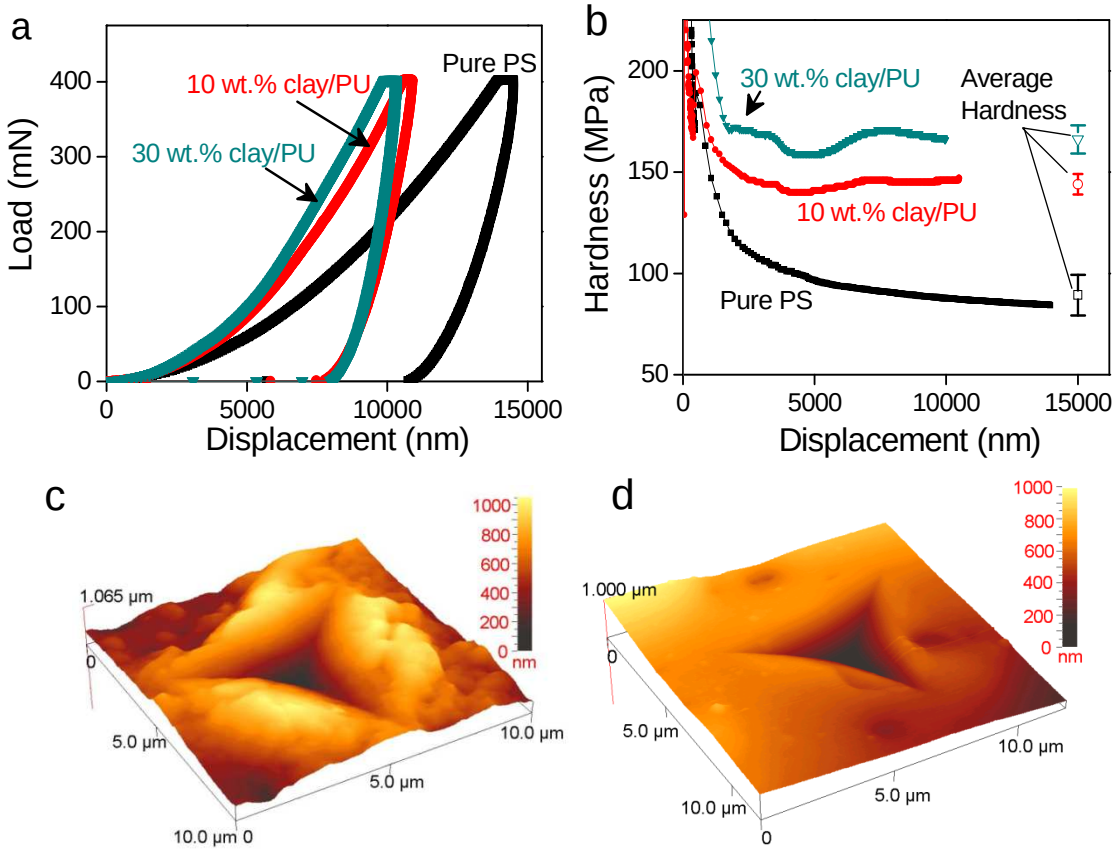

Figure 4.8 (a) Typical nanoindentation results of samples; (b) hardness versus indentation depth derived from nanoindentation tests; (c) AFM images for pile-up of materials for the pure PU sample; (d) AFM images of indentation mark on 30 wt.% treated clay/PU.

A comparison of hardness values from the nanoindentation and Vicker's microindentation is presented in **Figure 4.9**.

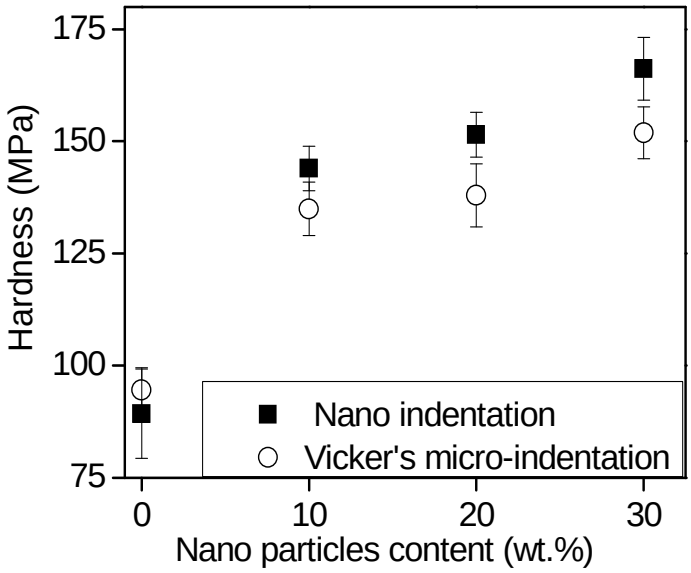

Figure 4.9 Comparison of hardness results from nanoindentation and Vickers micro-indentation tests.

The two measurements are comparable and indicate very similar trends in the relationship between the hardness and the content of clay fibers in the nanocomposites. Meanwhile, the results from nanoindentation are higher than vicker's indentation for the composites samples, because of the different testing theory and characterization location. This result is useful for industrial applications as it implies that the Vickers micro-indentation test can be used with equal effect to nanoindentation in evaluating polymer composites.

4.3 Thermal analysis and Microhardness-T_g relations

The DSC traces of the pure PU and the PU-based nanocomposites are listed in **Figure 4.10**. The glass transition temperature (T_g) is evident as a step in the DSC curves. The T_g of the nanocomposites decreases on addition of the untreated clay powder, but not when the heat-treated clay is incorporated. This decrease in T_g is attributed to the presence of moisture and excessive hydroxyl and other organic groups which exist in the non-treated clay powders and make it harder to obtain good interfacial bonding between polymer and nano-filler. Moisture also acts as plasticizer for the PU polymer causing a decrease in both the T_g and the strength of the polymer [28,85]. Because the T_g of the nanocomposites with the non-treated clay powder decreases below room temperature, the material becomes very soft during testing.

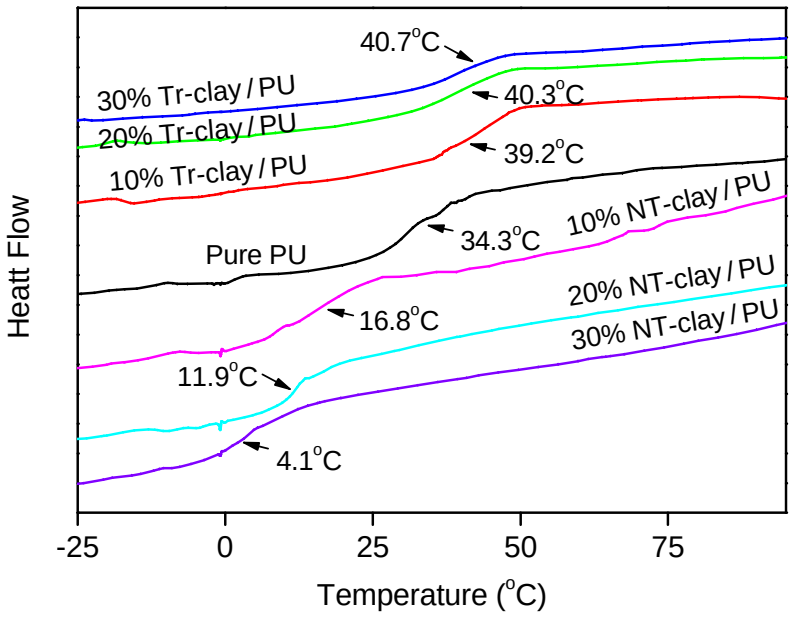

Figure 4.10 DSC analysis results of PU-based shape memory composites with the glassing temperature indicated for each composite.

In contrast, addition of the heat-treated nano-clay leads to an increase in the T_g of the nanocomposites by 5 °C compared to the pure PU. In the absence of a plasticizer, the addition of the nanofiller leads to restricted segmental motion of the polymer chains which raises the T_g [239,240].

Figure 4.11 shows the hardness results for PU and treated clay nanocomposites as a function of temperature. Here the logarithm of microhardness, ln H_v, is plotted against the temperature T to show the changes more conservatively. The hardness was found to decrease with temperature in the hybrid composite following a published exponential law [241,242], for the semi-crystalline or amorphous polymers:

$$H_v = H_{vo} \times \exp(-\beta T) \tag{4.1}$$

where H_{v0} is the hardness of the material at 0 K and β is the coefficient of thermal softening. **Equation (4.1)** can be changed into:

$$\ln H_v = \ln H_{vo} - \beta T \tag{4.2}$$

Statistical analysis on the relation between microhardness and T_g was performed and the results are described in **Figure 4.11**, i.e. ln(H_v) decreases linearly with temperature for all the samples.

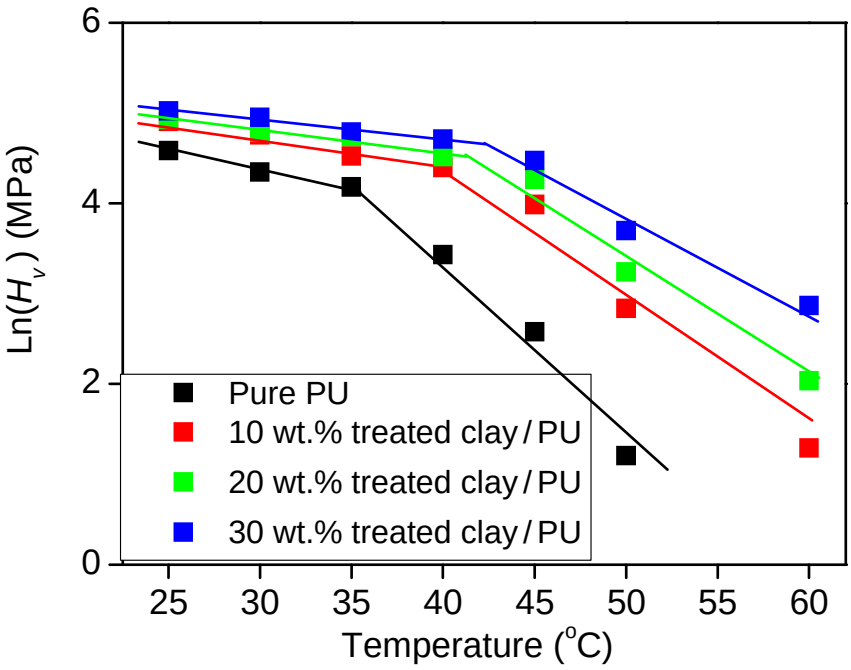

Figure 4.11 Microhardness of PU-based shape memory composites versus temperature.

However, there is an apparent discontinuity in the thermal expansion coefficient around T_g, although it becomes less apparent with increasing clay content. This implies that microhardness tests at different temperatures can be used as a tool to determine the T_g of the polymer and its nanocomposites. A continuous increase in T_g with filler content is also evident from **Figure 4.11**, which supports the DSC results in **Figure 4.10**.

Figure 4.12a shows the storage modulus (E') from the DMTA tests for the composites with different clay contents.

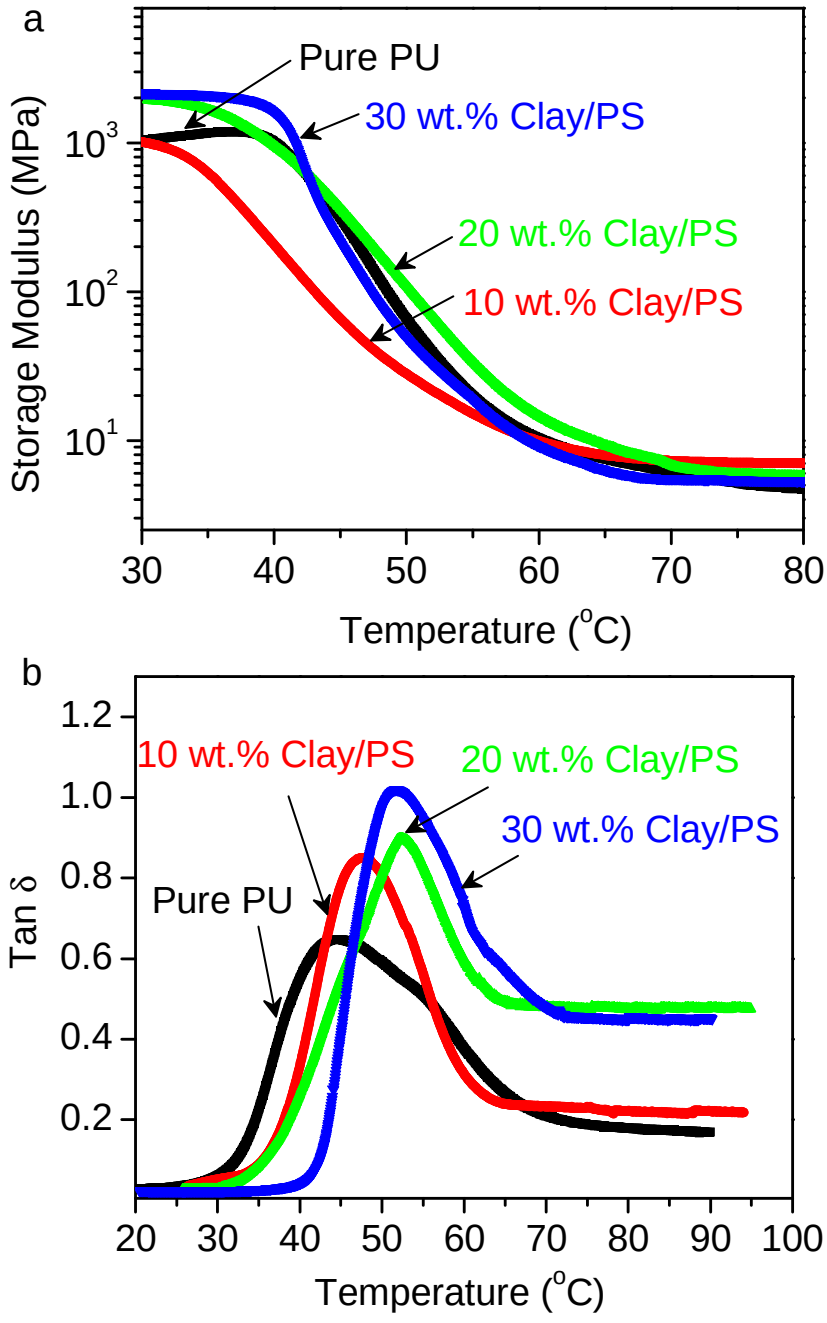

Figure 4.12 DMTA characterization on T_g of nanoclay based SMP composites (a) Storage modulus versus temperature curves; (b) *Tan δ* versus temperature results.

The storage modulus has a maximum value for the SMP nanocomposite with 30 wt.% clay, indicating that the stiffness of 30 wt.% clay/PS nanocomposite is the highest among all the tested samples. A sharp drop in modulus is observed above T_g within a narrow temperature range due to the softening effect of the polymer nanocomposite, which has already been reported [243].The *tan* δ curves shown in **Figure 4.12b** reveal that the transition temperatures of the nanocomposites increase with clay content. The nanocomposite with 30 wt.% clay also shows the highest *tan* δ value, which reveals its best energy absorption capacity among these samples [244]. It has been reported that the damping effect of the polymer depends strongly on the hard segment content, crystallization of the soft segment and cross-linking rate [245,246]. In this study, the best damping effect was achieved for the nanocomposites with 30 wt.% clay, because of the significant increase in the content of hard segments.

In brief, improvement in the thermal properties with the addition of nano-clay has been proved based on the T_g results based on the DSC tests and modulus results from the DMTA tests.

4.4 Shape recovery demonstration and thermal-mechanical cycling tests

Shape recovery speeds were measured by recording the recovery of an indentation mark using a Peltier heater with a maximum temperature of around 50°C. **Figure 4.13** and **Figure 4.14** show the fading of the indentations after temperature increase for the pure PU and PU nanocomposites containing 20 wt.% treated clay, respectively. The indentations gradually disappear upon heating, indicating a good self-healing performance. **Figure 4.13e** and **4.14e** also show the surface profiles of the indentations of these two samples. Prior to heating, pile-up around the indentations can be clearly observed, indicating the significant plastic deformation of the SMP and nanocomposites [247]. The real-time images indicate that the full recovery of pure PU took about 120 seconds while the same level of recovery in the composites sample took about 240 seconds. The nanocomposite samples are found to have a slower recovery speed than those of the PU at the same temperature, which is probably due to the increasing energy consumption in overcoming the clay barriers.

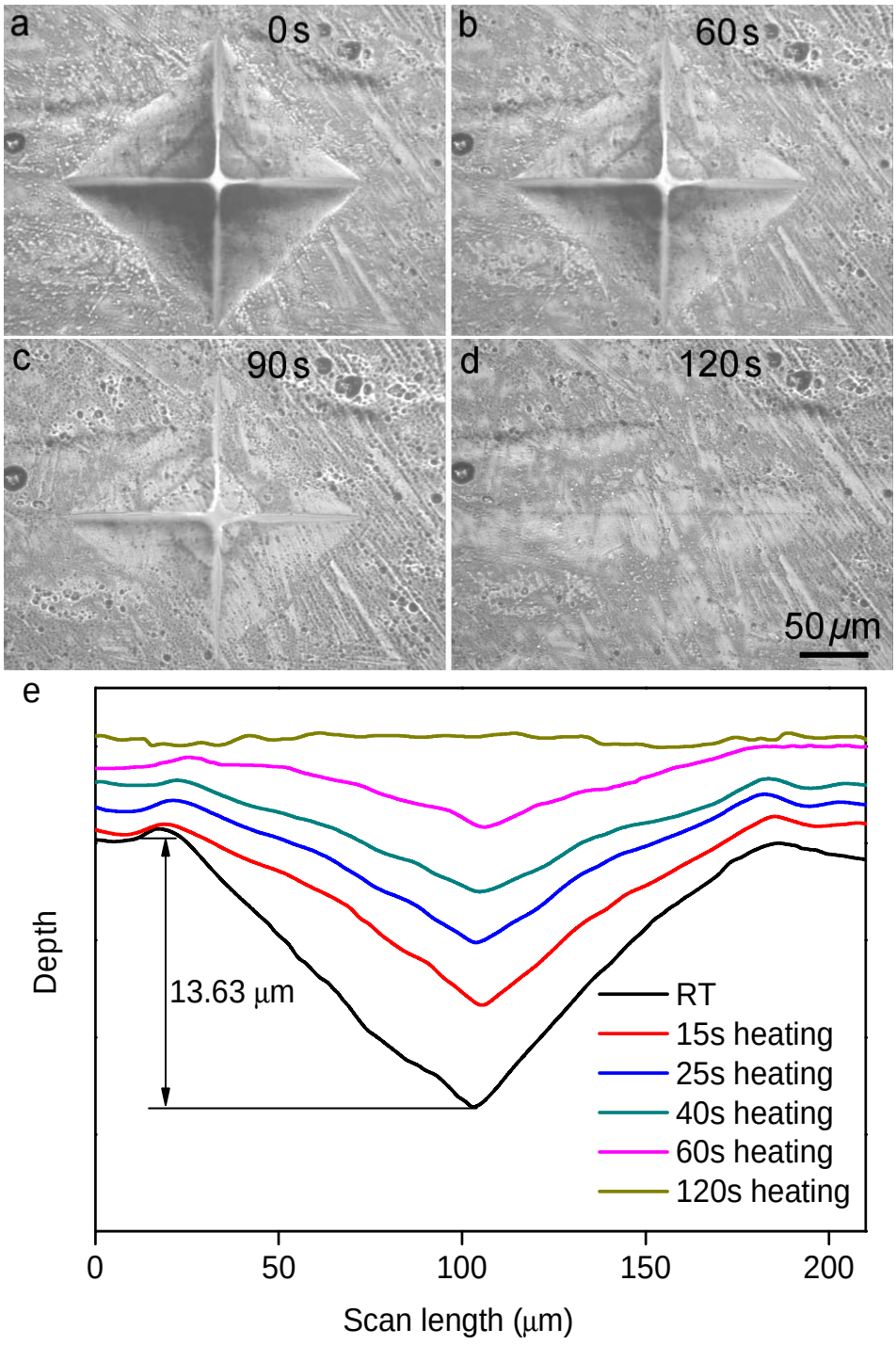

Figure 4.13 OM micrographs showing the evolution of the indentation on pure PU during heating at 50 °C for different time: (a) 0s, (b) 60s, (c) 90s and (d) 120s. (e) Profile evolution of the indentation heated for different duration times indicated.

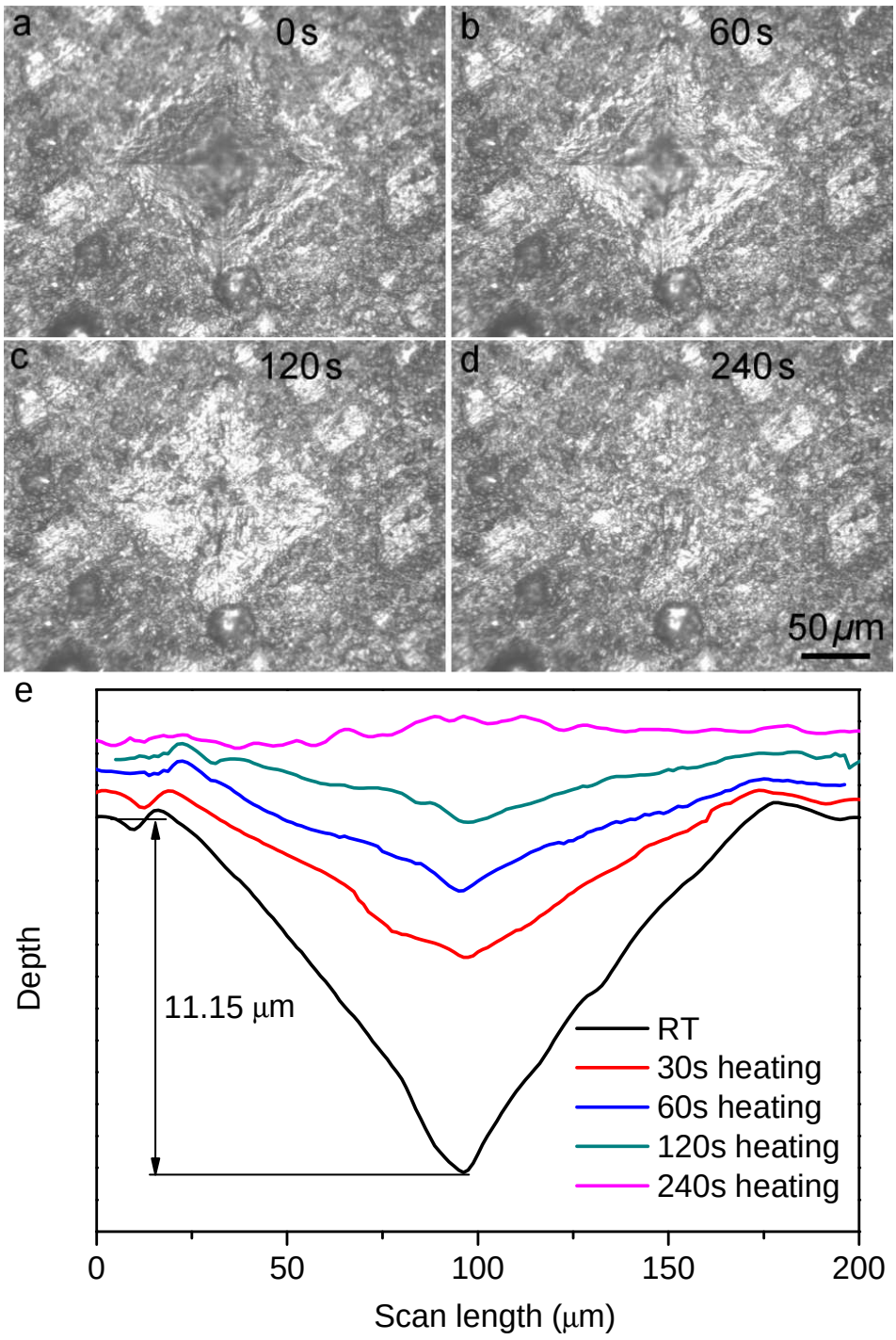

Figure 4.14 OM micrographs showing the evolution of the indentation on 20% treated clay/PU composite during heating at 50 °C for different time: (a) 0s, (b) 60s, (c) 120s and (d) 240s. (e) Profile evolution of the indentation heated for different times indicated.

In order to compare directly the shape memory efficiency of PU and clay/PU composites, two thin beams of the pure PU and 30 wt.% clay/PU composites, with a cross section area of 2×2 mm^2, were bent after heating to 80 °C, and the shape was fixed while cooling to room temperature (20 °C). The shape recovery was demonstrated on a hotplate with a surface temperature of 80 °C, which was designed to illustrate

remote recovery at a higher triggering temperature. The pure PU sample exhibited a prompt response, recovering its original shape within 30 s (see **Figure 4.15c**). The nanocomposite beam with the 30 wt.% clay showed a full shape memory recovery after 60 s (see **Figure 4.15d**).

Figure 4.15 Recoveries of shape memory samples heated on a hotplate with a surface temperature of 80 °C.

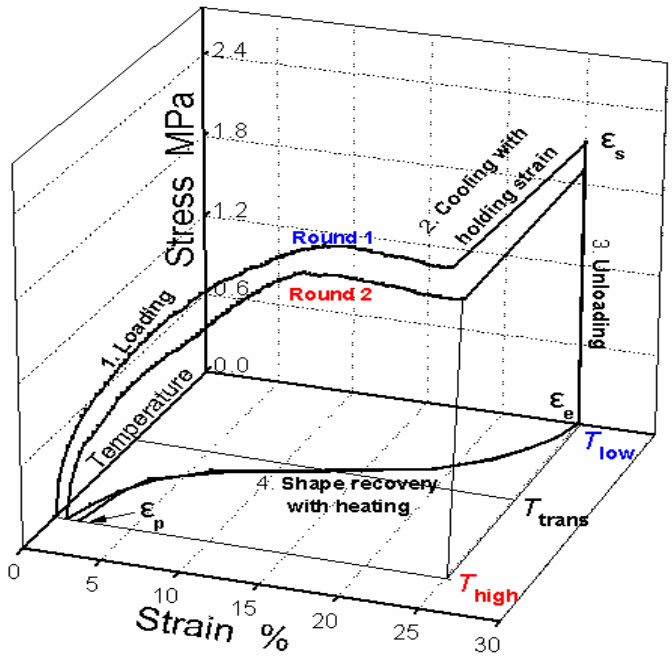

Figure 4.16 Typical thermal cyclic tensile results of 30 wt.% clay SMP nanocomposite.

The slow recovery of the nanocomposite sample is attributed to the incorporation of nano-fillers that hamper the movement of molecular chains, so that the shape memory effect is slightly delayed. **Figure 4.16** presents the thermal-mechanical cycling test of

the 30 wt.% clay composite. A good shape recovery was observed: the shape recovery rate is 99.2% in the first tensile cycle and 97% in the second. The maximum stress decreased by 8%, probably because some defects were generated and creep occurred during continuous loading at an air temperature of 60 °C.

4.5 Summary

Mechanical properties of the attapulgite clay reinforced polyurethane shape memory nanocomposites are strongly dependent on the pre-treatment of the nanopowders. The untreated commercial attapulgite clay resulted in a significant decrease in glass transition temperature and hardness of the nanocomposite due to the presence of moisture as well as the clay's amorphous structure and surface hydroxyl groups. The Vickers hardness of the nanocomposites composed of the heat treated clay powder was dramatically increased as a function of clay content, which is attributed to the homogeneous dispersion of the nano-fillers in the polymer matrix and strong filler–polymer interactions. Following heat treatment of the nano-powders, the loss of moisture and surface hydroxyl groups provided a crystallized and bundled structure.

Nanoindentation results showed that the average hardness value increased by about 90 %, from 89 MPa to 166 MPa when the content of nanoclay filler reached 30 wt.%. Improved interfacial bonding between the polymer and filler interface enhanced the mechanical properties of the nanocomposites. In comparison, untreated PU-clay nanocomposites showed a decrease in both the T_g and the strength of the nanocomposites. DMTA also showed an improvement in the thermo-mechanical properties of the nanocomposites by adding the nano clay fillers. Good shape memory effect was observed in the nano-composites: nearly 97 % recovery was obtained after two cyclic tensile tests. PU-based composites containing 30 wt.% treated clay nanoparticles exhibited the same capability of shape recovery as pure PU although recovery speed was slightly slower.Although a significant mechanical enhancement was observed in the composites examined in this chapter, it must be pointed out that the filler content is up to 30 wt.%. The concentration of the fillers is so high that there inevitably exist particle aggregations inside the composites. In the following chapter, a polystyrene based shape memory polymer with a range of low concentrations of nanofillers was used to study the effects of nanoparticles in matrix for the reinforcement of the mechanical properties and shape memory effect.

Chapter 5

THERMAL TRIGGERING OF POLYSTYRENE BASED SHAPE MEMORY NANOCOMPOSITES REINFORCED BY DIFFERENT NANOFILLERS

Apart from PU, Polystyrene (PS) based copolymers are the most commonly used for designing nanocomposites for good different purposes, because of their lower cost compared to the other polymers such as PMMA, PU and polycarbonate. Some studies have been carried out on the shape memory properties of PS-based SMPs [191,248,249,250], but the underpinning physical and mechanical enhancement mechanisms of the PS-based shape memory nanocomposites have not yet been evaluated. The chemical composition and molecular structure of the PS based copolymer used in this work are illustrated in **Figure 5.1**.

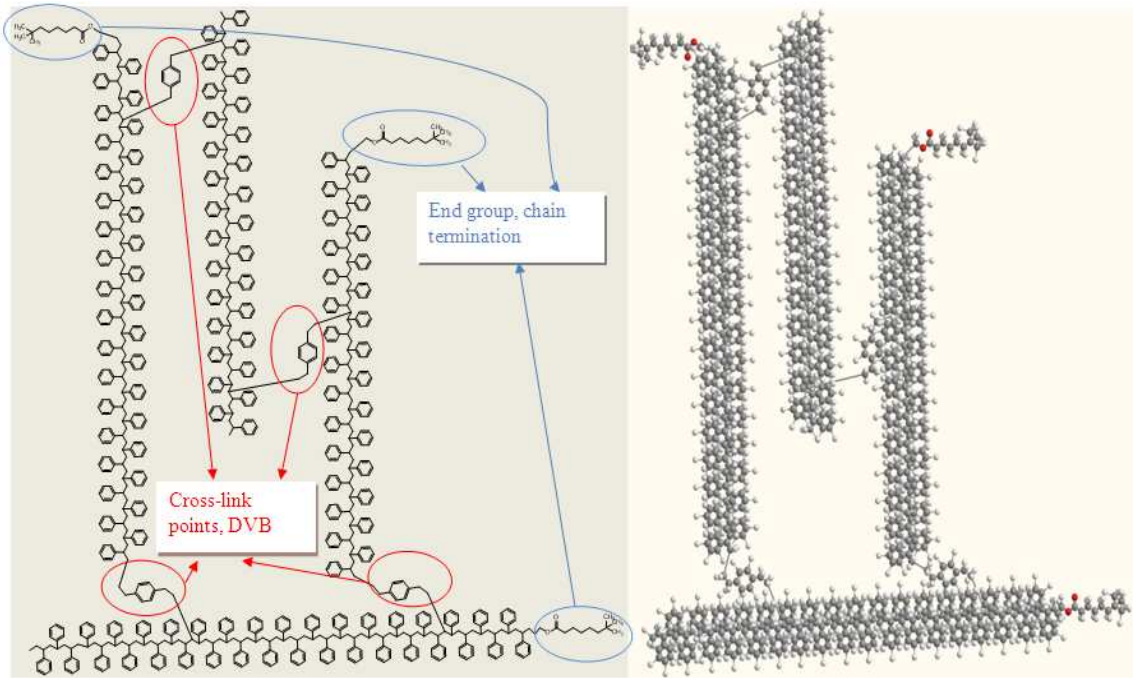

Figure 5.1 Schematic of chemical composition and molecular chain structure for shape memory PS-copolymer, (a) hard segment (crosslinking) network with addressed functional groups, (b) The ball-stick model on crosslinking molecular structure

Investigations of the thermal triggering of PS-based shape memory nanocomposites were performed using various nanofillers such as silica, Al_2O_3 and clay. The aims were to compare and study the factors which influence the nanopaticle enhancement efficiency on the matrix, as well as to examine the dispersion status of the particles.

5.1 Nanoparticle characterization

The geometries and dimensions of the nanofillers were studied in detail using TEM observation. **Figure 5.2** shows spherical Al_2O_3 particles of diameters ranging from 25 nm to 120 nm. According to supplier's information (also assessed in TEM) [200], the Al_2O_3 particles used in this study had a small diameter of 15 nm or less. The silica particles tend to aggregate due to their high surface energy (smaller average particle size) and surface hydroxyl groups, according to the supplier [200].

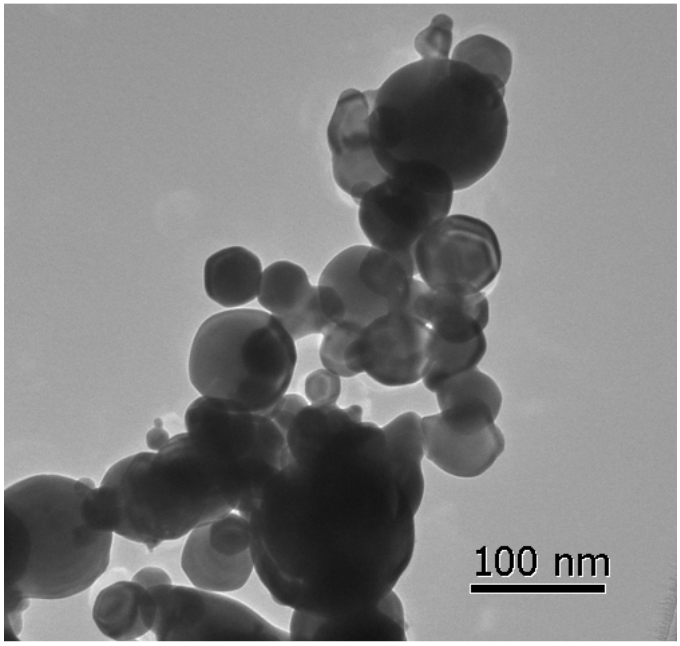

Figure 5.2 TEM micrograph showing the morphology of Al_2O_3 nanoparticles.

By noting the agglomeration states of the above two spherical inorganic nanoparticles, it was concluded that specific dispersing techniques would needed to ensure the separation of the nanoparticles clusters, especially for the silica. **Figure 5.3** presents TEM images of the as-received and heat treated clay powder. The nano-clay powder exhibits a fibre-like amorphous structure in the as-received state and becomes a 3-D bundled rod-structure after heat treatment at 850 °C for 2 hours [251]. The diffraction spots of selected area electron diffraction pattern reveal the nanocrystalline nature of the heat-treated clay as shown by the inset in **Figure 5.3**b.

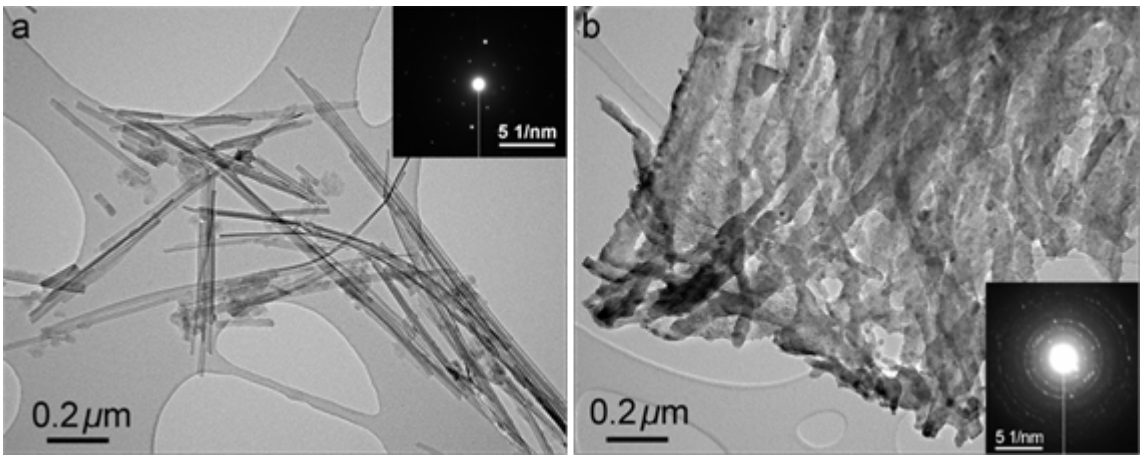

Figure 5.3 TEM images of (a) as-received, and (b) heat-treated clay powders, with selected area diffraction pattern shown in the inset.

Nano-particle identification by TEM offers a visual comparison between the different nanofillers which were employed in this work. Besides the direct geometry and dimension evaluation, the 'internal' state of the particles were also revealed, which could lead to a better understanding of the effects of the fillers on the mechanical properties of composites.

5.2 Macroscopic mechanical properties

Three kinds of nano-particles, as previously identified, were selected to fabricate the nanocomposites at different concentrations. Vickers indentation and uniaxial tensile testing were used to characterize the macroscopic mechanical properties. **Figure 5.4** shows the Vickers hardness readings for the three nanocomposites as a function of nano-filler content. A significant increase in hardness can be attributed to the addition of the nanoparticles. With the addition of 4 wt% of the nanoclay powder, the microhardness reaches a maximum value of about 75 MPa, which is nearly a 400% improvement over the pure PS. The Al_2O_3 nanoparticles show a similar hardness enhancement to that displayed in the nano-clay filled composites. The SiO_2 nanoparticles demonstrate the weakest enhancement effect: the hardness is only doubled when the SiO_2 content reaches 4 wt.%. It is also apparent that the hardening effect is much more pronounced with the first 0.5 wt.% addition and the improvement is less for all three reinforcement materials thereafter.

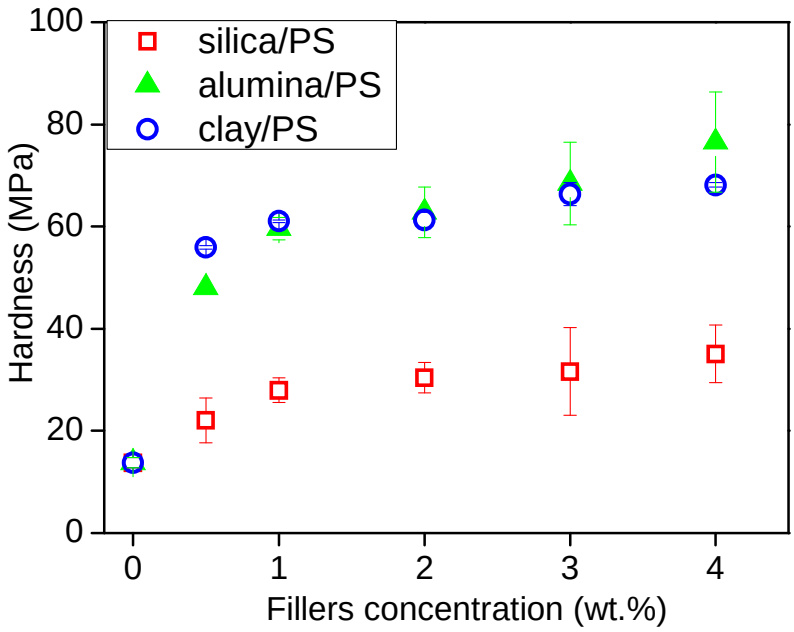

Figure 5.4 Vicker's hardness results for SMP nanocomposite operated with 25 g load and 20 s loading time.

The composites with 1 wt% of each of the nanofiller were selected for uniaxial tensile tests to compare their stress-strain behaviour at room temperature (~20 °C), with the typical stress-strain curves shown in **Figure 5.5b**. From the results of the maximum stress and strain shown in **Figure 5.5c**, the SiO_2/PS composites show a nearly 16% increase in the maximum strength, and the Al_2O_3/PS and clay/PS composites present much better enhancements of 100 % and 120 %, respectively. The Young's modulus values (shown in **Figure 5.5b**) measured from the tensile tests confirm that the clay/PS composites show the best enhancement, nearly 3 times of that of the pure PS.

Figure 5.6 shows the stress-strain relationships for the clay/PS nanocomposite as a function of clay content at room temperature. The tensile stress increases significantly with increasing clay content up to 1 wt.%, and then decreases dramatically upon further addition of nano-clay. For example, incorporation of only 1 wt.% clay results in a modulus that is almost three times that of the pure PS.

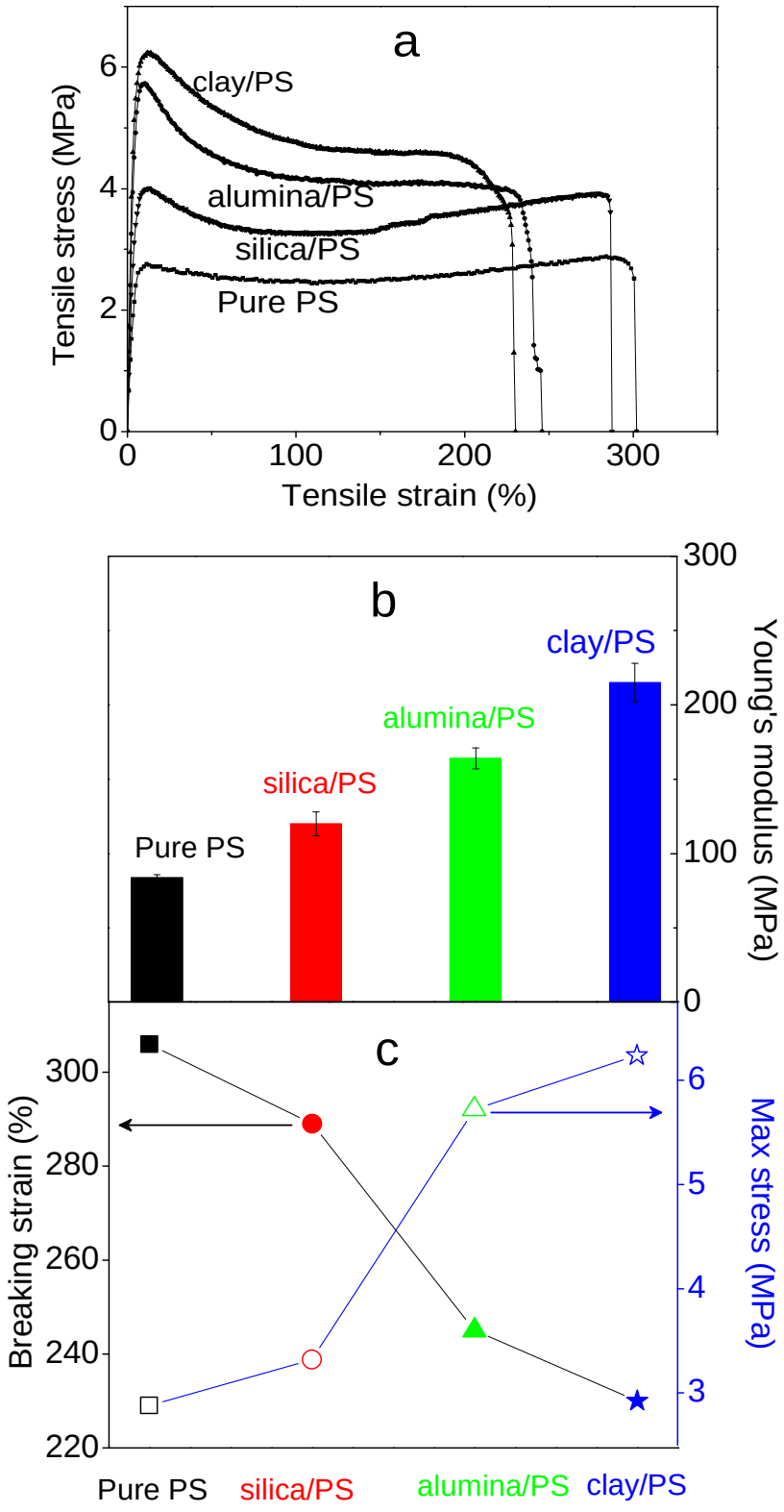

Figure 5.5 Uniaxial tensile results for SMP nanocomposite at room temperature: (a) Stress-strain curves; (b) typical Young's modulus from tensile test; (c) breaking strain and maximum stress.

Considering the geometry and dimensions indicated in the TEM images, such obvious enhancement could be attributed to the higher aspect ratio of rod fillers. This has been

explained by the effective load transfer along the fibre rod [252,253]. The decrease in this enhancement after adding more than 1 wt.% clay is likely to be due to an imperfect organic-inorganic interface and agglomeration of nanoparticles [254,243]. The current dispersion technique using ultrasonic stirring has limited efficiency for nanoparticle scattering inside the matrix when the concentration of the nanofiller is higher than 1 wt.%.

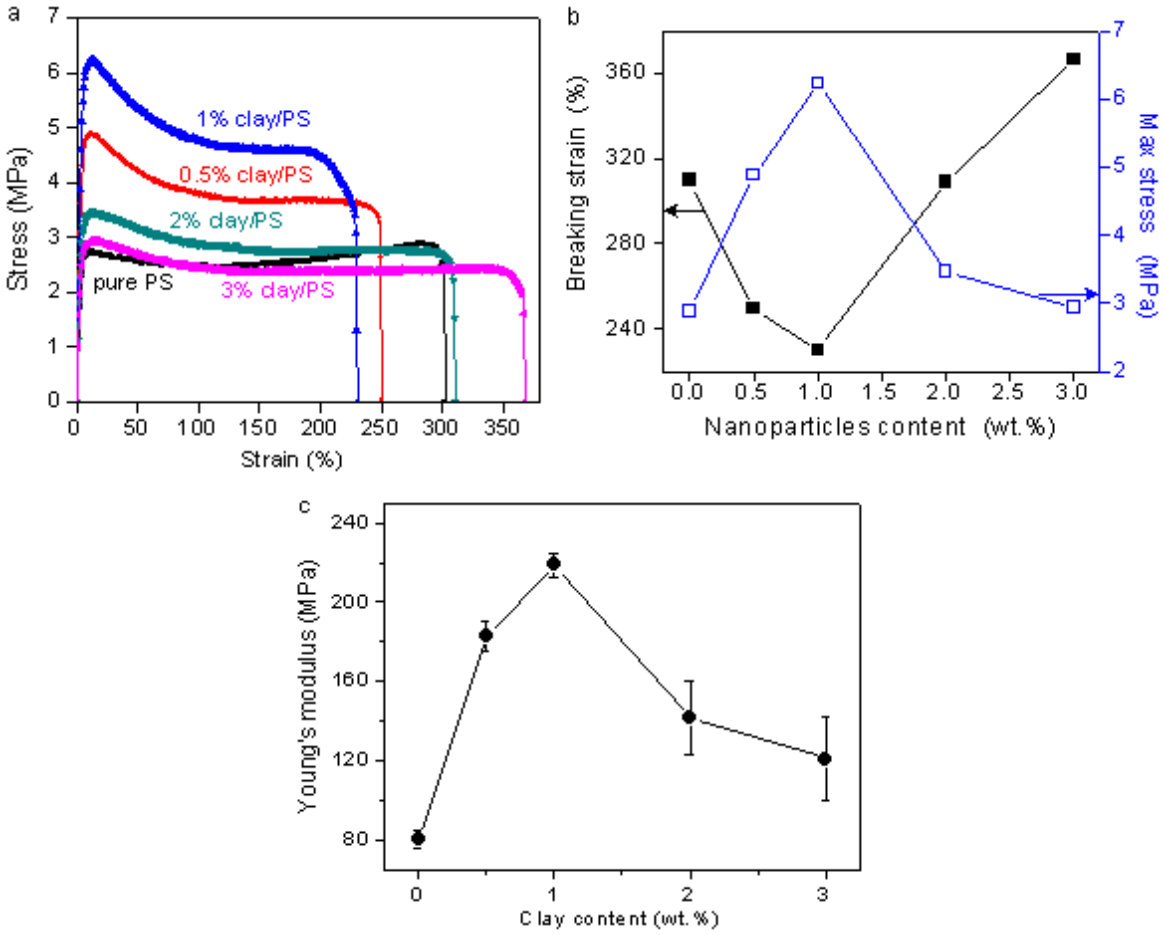

Figure 5.6 Tensile results for nanocomposites of clay/PS: (a) typical stress-strain curve; (b) breaking strain and maximum stress; (c) Young's modulus as a function of clay content.

Nanofillers dispersed in the polymer matrix reinforce the soft matrix through effective load capacity and transferability. When the aspect ratio of the particles equals unity (spherical nanoparticles), the composite modulus is dependent on a number of particle characteristics such as their modulus, density, the particle size and shape, the volume fraction and the nature of the interface. As the modulus and density of Al_2O_3 is larger than that of SiO_2, the enhancement effect for the Al_2O_3/PS sample is more significant as shown in **Figure 5.4** and **Figure 5.5**. The rod-like nanofillers may bridge more polymer

chains and afford more effective load transfer, leading to an improvement in strength. Upon adding a critical volume fraction of nano-rods (such as nano-clay), the nano-rods stretch and perturb the polymer matrix, and the polymer blend confines the nanorods, generating elongated domains that are reinforced by these fillers [255]. Nanofillers with rod-like structures, as compared with spherical nanoparticles, have been predicted to be better in homopolymer systems because the stress concentration is reduced and the load is transferred with more efficiency by the high aspect ratio and specific geometry of the fillers [256,257].

5.3 Thermal properties

The DSC results shown in **Figure 5.7** reveal that, with the addition of nanoparticles from 1 wt.% to 3 wt.%, the glass transition temperatures decrease slightly (less than 3 °C) for all specimens, which is acceptable given the improvement in mechanical strength.

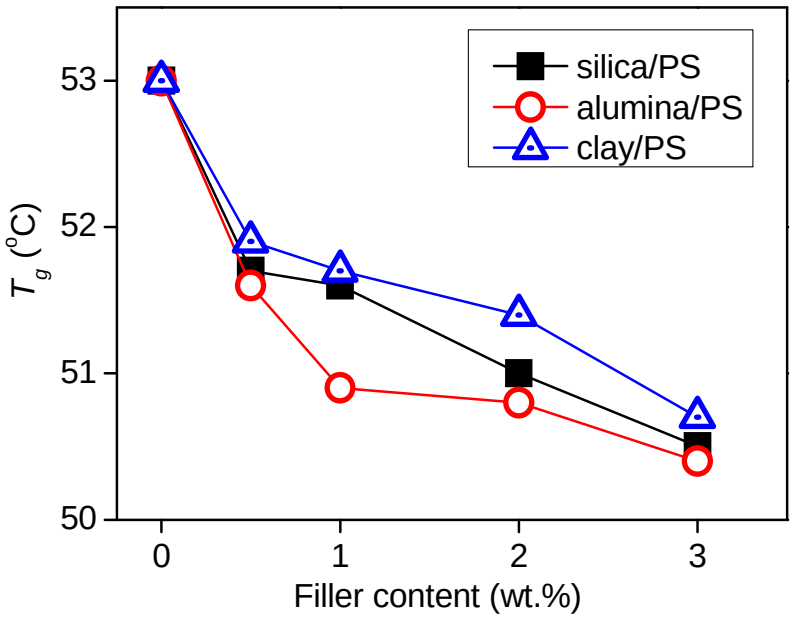

Figure 5.7 DSC monitoring on T_g of SMP nanocomposites

The ideal nanocomposite system assumes that the thermal property should be improved significantly with minor loading of nanoparticles, but passive influences such as filler aggregation, chain transfer, exceptional termination of chain growth, would result into a decrease in T_g. Similar explanations have been reported that a homogenous dispersion of nanoparticles in the polymer matrix is difficult to achieve without additional method

such as pre-dispersing solutions or surface treatment of the fillers by surfactant [258,20,259]. Aggregation of the nanofillers in the nanocomposites has been reported as a major factor leading to a decrease in the transition temperature [260]. The clay/PS composites show the smallest decrease in the transition temperature of the nanocomposites studied, which could indicate that the clay/PS composite system achieves the most uniform disperson of nanofiller. The DMTA results for this clay/PS nanocomposites (**Figure** 5.8**a)** show the storage modulus (*E´*) to have a maximum value at 1 wt.% clay, with the stiffness of 1 wt.% clay/PS nanocomposite being the highest of all the samples tested. A sharp drop in modulus is observed above T_g over a narrow temperature range, which has been frequently reported [243,261,262].

The *tan* δ curves in **Figure 5.8b** reveal that the transition temperatures of the nanocomposites increase slightly with addition of clay content, which matches what was observed in the DSC analysis. The nanocomposite with 1 wt.% clay also shows the highest *tan* δ value, which gives it the best energy absorption capacity among these samples [244]. The best damping effect was achieved with 1 wt.% clay, as the incorporation of nanofillers maximizes the hard segment content and creates numerous physical cross-linking points, which directly leads to higher energy consumption because molecular chain movement needs to overcome those obstructing effects. However, with 2 wt.% clay, probably due to the poor dispersion of nanofillers, the energy absorption during deformation is reduced, thus leading to a reduction in the damping effect. However, there are usually multiple factors which influence the mechanical properties and constitutive models of the polymer and its nanocomposites, which will be discussed in **Chapter 8**.

5.4 Thermal-mechanical cycling measurements

Cyclic tensile measurement was used quantify the shape memory effect for the clay/PS specimens, and the results are shown in **Figure 5.9**. When an external stress is applied to the SMP, soft/flexible segments will be preferentially extended in the stress direction compared with the hard/fixed segments. Both the cross-linking of the PS and nanofiller particles will act as hard/fixed segments.

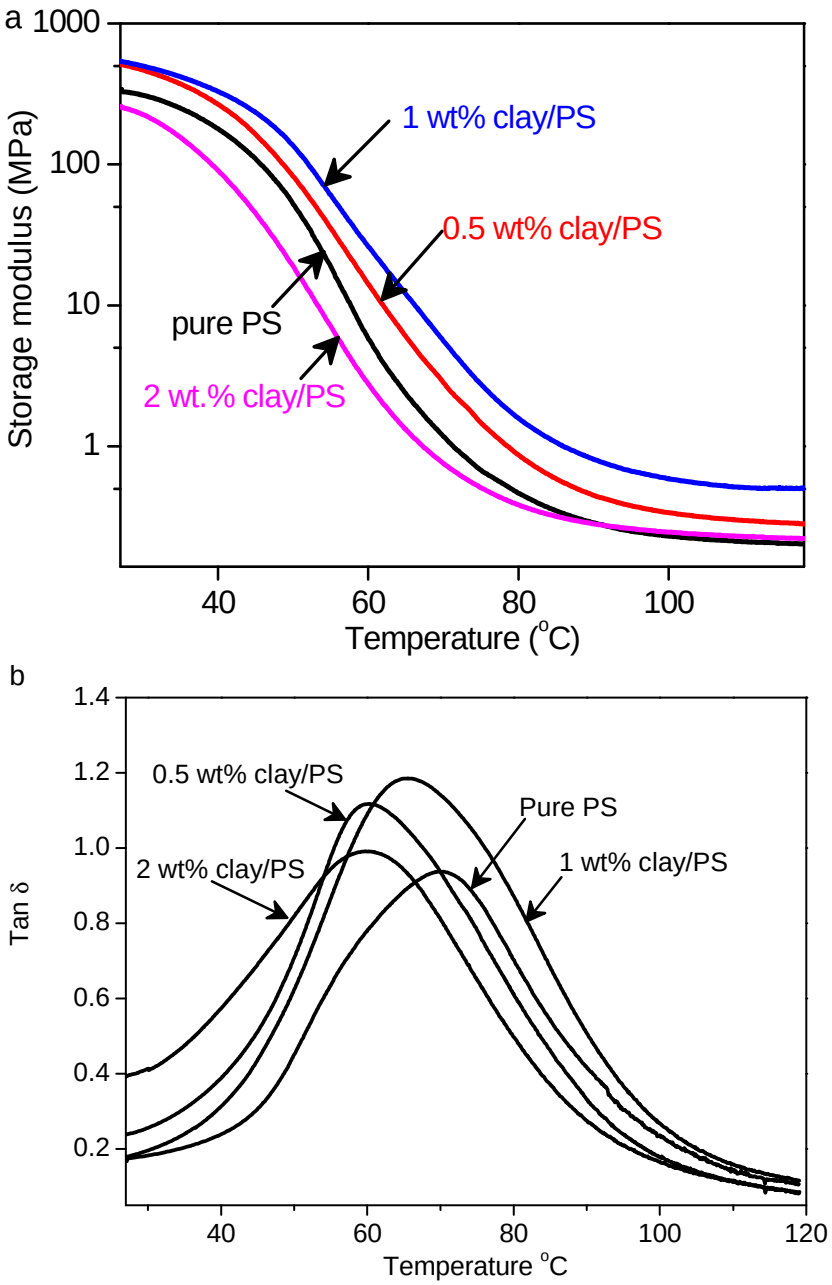

Figure 5.8 DMTA investigation on nanoclay based SMP composites (a) storage modulus versus temperature curves; (b) *Tan δ* versus temperature results.

As shown in **Figure 5.9**, the maximum stress of the pure PS (1.45 MPa) at 60 °C is about half of that at room temperature (**Figure 5.5a**). Similar behaviour was also repeatedly observed in all the nanocomposites. This is because the chains of shape memory polymers become flexible above the transition temperature, which results in a reduction of the maximum stress. The maximum stress of the 1 wt.% clay/PS nanocomposite is the highest among all samples, showing a good enhancement even at temperatures above T_{trans}. As the cyclic tensile fast proceeds, the residual strain ε_p increases (see **Figure 5.9**), which could be attributed to such possibilities as: (1) random

breaking of covalent cross-link bonds, (2) energy storage by the fillers [263], or (3) a blocking effect by incorporated nanofillers [254].

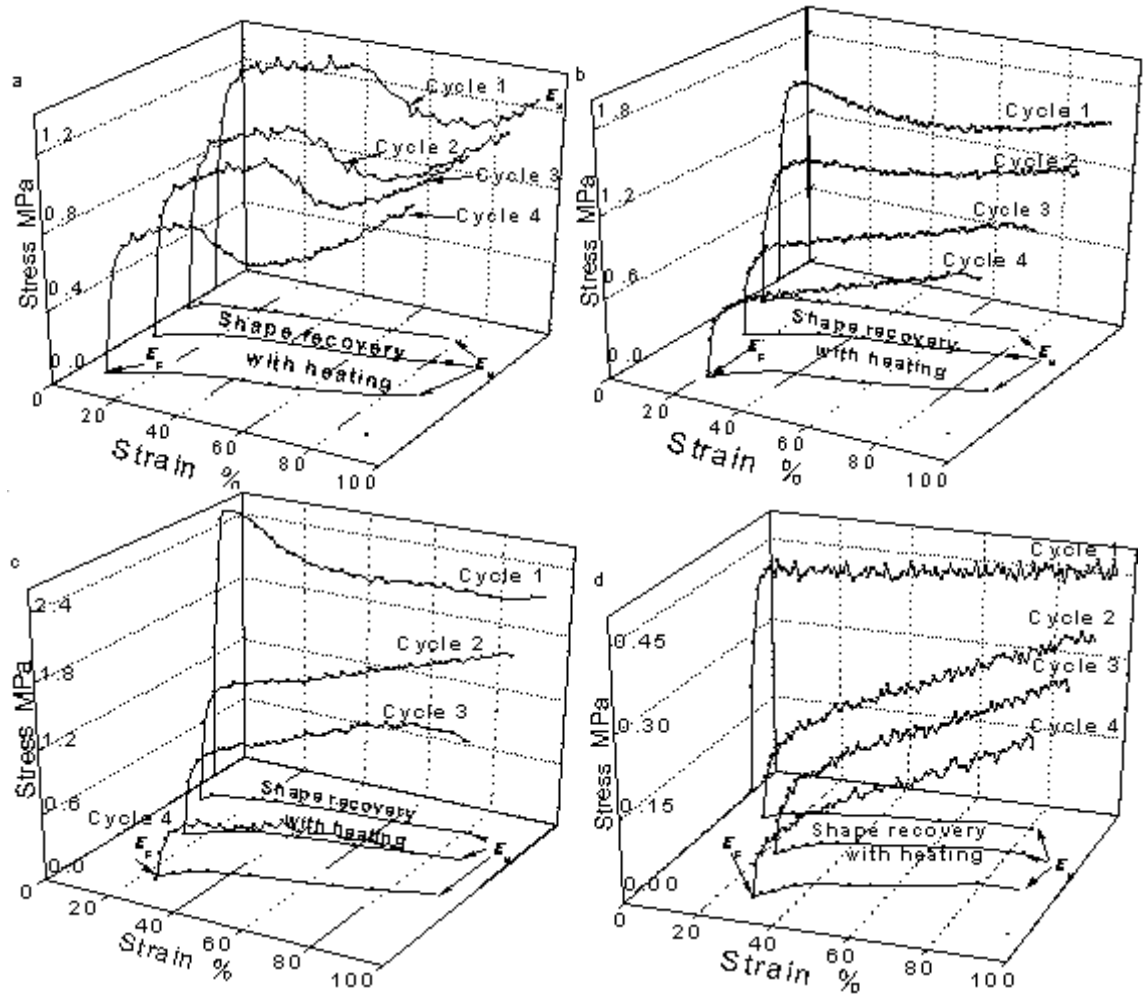

Figure 5.9 Thermal mechanical cyclic testing results: (a) pure PS; (b) 0.5 wt.% clay/PS composites; (c) 1 wt.% clay/PS composites; (d) 2 wt.% clay/PS composites.

The shape memory effect can be quantified using the strain recovery ratio as a function of cycle number *N*, defined by **Equation (5.1)** [259]:

$$R_r(N) = \frac{\varepsilon_e(N) - \varepsilon_p(N)}{\varepsilon_e(N) - \varepsilon_p(N-1)} \tag{5.1}$$

where $R_r(N)$ is the strain recovery ratio in the cycle number N, $\varepsilon_e(N)$ is the unloading strain at T_{low} in the cycle number N, and $\varepsilon_p(N)$ and $\varepsilon_p(N–1)$ are residual strains at cycle number N and N–1, respectively. All information can be directly obtained from the results of the cyclic tensile testing at a fixed temperature. T_{high} is identified with the T_g of the polymer, and T_{low} normally is room temperature (~20 °C).

Figure 5.10 summarizes the recovery ratio of the clay/PS composite SMPs from the thermal cycling tests. It has been found that the recovery rates of all the samples are above 85%, which represents good retention of shape recovery.

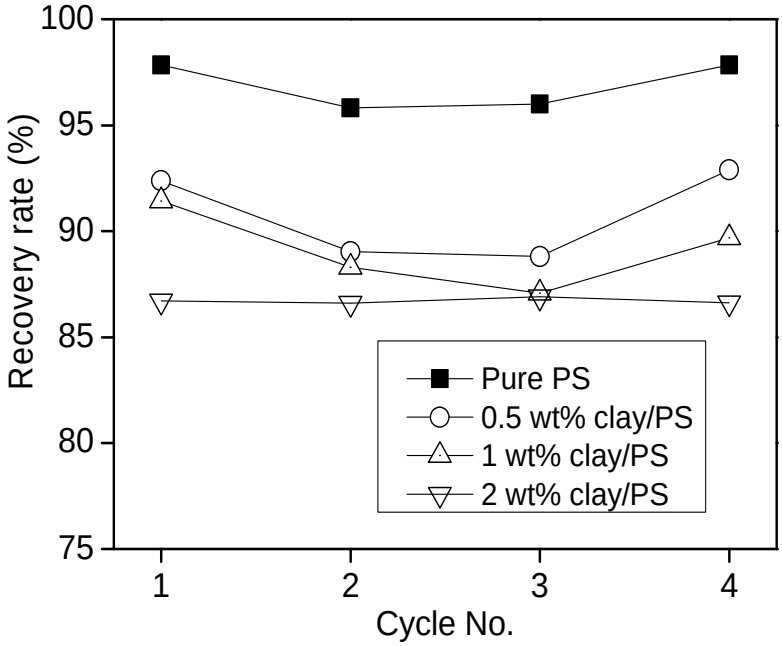

Figure 5.10 Recovery rate *versus* cycle number of pure PS and clay/PS samples

The recovery ratio for the 2 wt.% clay nanocomposite is nearly 15% lower than that of the pure PS, and this can be attributed to many factors such as increased energy consumption, the agglomeration of nanofillers in the polymer, and random breaking of the covalent cross-link bonds. There seems to be a slight decrease in the recovery rate with cycle number, but then a slight increase after two or three cycles, which is a typical "learning phase" seen in many SMPs [4,5]. After the first tensile cycle, some of the cross-link points will be broken in the SMP and composites, which could freeze the free movement of the molecular chains, thus causing reduction in the recovery rate in next cycle. Then the recovery strain becomes stable as more molecular chains function as flexible soft segments once they have been heated above T_g, thus gradually leading to an increase in the reversible recovery rate.

5.5 Shape recovery property

The PS and nanocomposite samples with a thickness of 0.6 mm and width of 10 mm were rolled after being heated to 90 °C, and the shape kept fixed during cooling to room

temperature (20 °C). The shape recovery test was carried out in hot water at 60 °C. The pure PS sample (see **Figure 5.11**) exhibited a prompt response in hot water and reached almost 90 % recovery within 20 s.

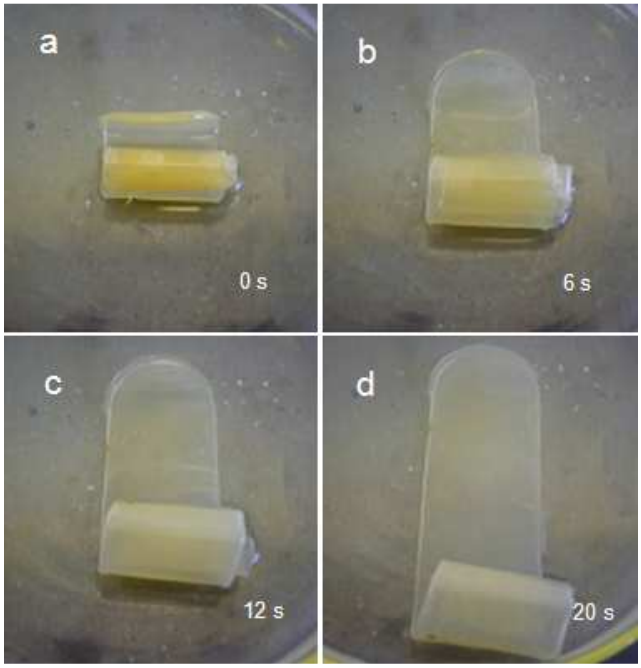

Figure 5.11 Recovery of a pure SMPS sheet in 60 °C hot water.

The 0.5 wt% clay/PS nanocomposites (in **Figure 5.12**) also showed good shape memory recovery but with a faster recovery speed (recovering within 16 s) than that of the pure PS. The reason could be that the T_{trans} of the nanocomposite SMPs decreases with addition of nanoclay filler. On the other hand, the 1 wt.% clay/PS sample (in **Figure 5.13**) shows a full recovery within 25 s, which is faster than that of the pure PS.

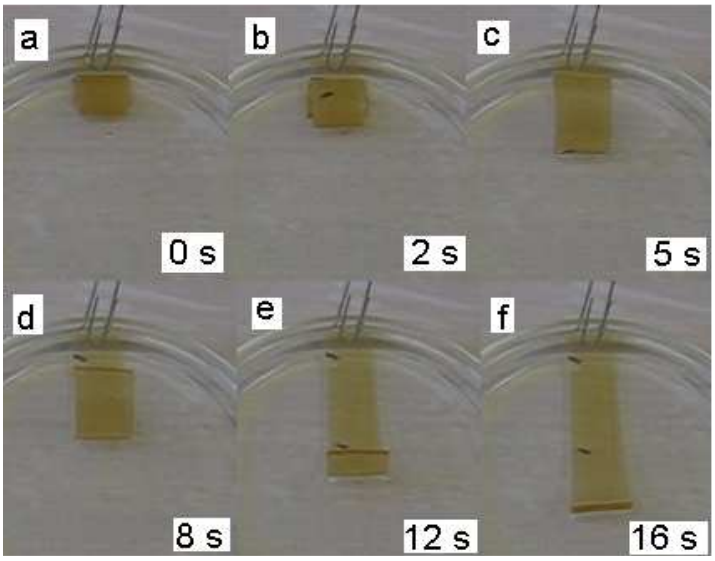

Figure 5.12 Recovery of 0.5 wt% clay/PS sheet in 60 °C hot water.

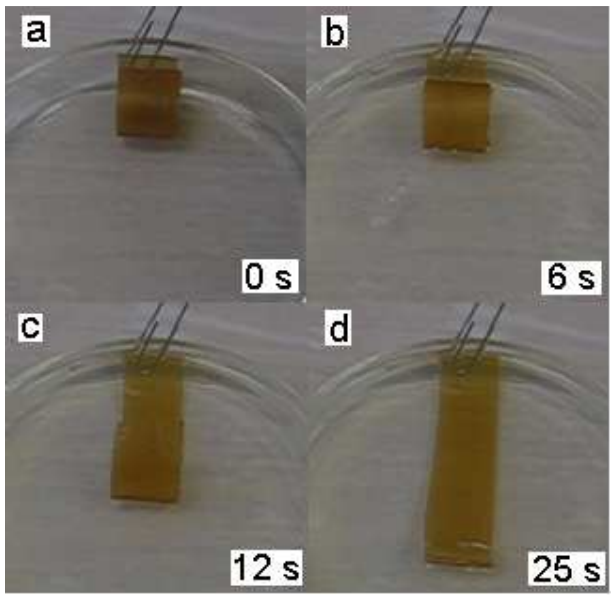

Figure 5.13 Recovery of 1 wt% clay/PS sheet in 60 °C hot water.

In **Figure 5.14**, demonstration of the shape recovery of the dyed PS nanocomposites with “h w u” characters was made on a hotplate at 80 °C. A full recovery was achieved in 2 min for the various degrees of deformation.

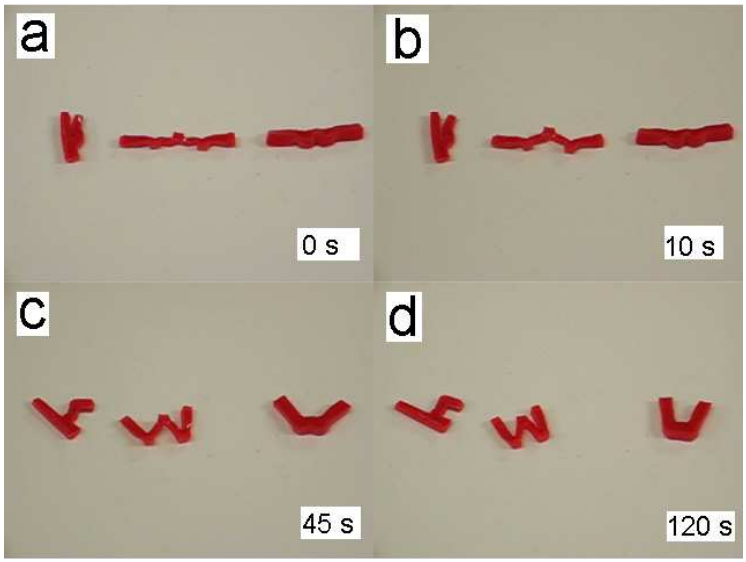

Figure 5.14 Demonstration of shape recovery with “h w u” characters designs on a hotplate surface of 80 °C

As a further assessment of the capacity of the materials, a micro-gripper based on the pure PS was manufactured using laser micromachining as shown in **Figure 5.15**. A good shape recovery of the gripper at 80 °C was demonstrated. The edge of pence coin is used as an indicator of scale showing its potential for biomedical or micro-assembly applications.

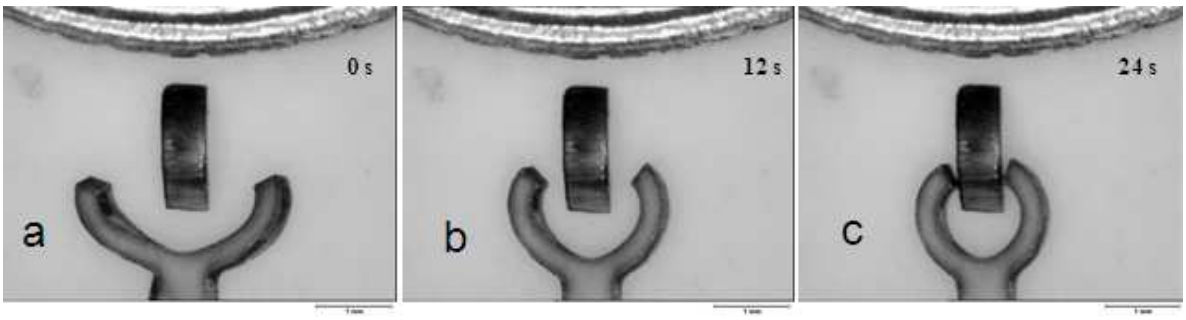

Figure 5.15 Shape recovery of a micro-gripper based on a pure PS copolymer (the edge of a five pence coin is also shown for comparison)

5.6 Summary

Shape memory nanocomposites were fabricated using chemically cross-linked PS copolymer as a matrix and different nanofillers (including alumina, silica and clay) as the reinforcing agents. Their mechanical and thermal properties and shape memory effects have been characterized. Nanofillers exhibit an effective enhancement in the strength and modulus of composite SMPs. Among the three types of nanofiller, the heat-treated nanoclay achieved the best improvement in strength. DMTA results indicated that the 1 wt% clay composites had the highest storage modulus and the best energy absorption capacity. Thermal cycling tests indicated that the recovery rates of all nanocomposite SMPs were above 85%, and good shape recovery ability was achieved. Shape recovery was demonstrated using different samples and designs. In brief, nanofillers provide significant reinforcement to the PS, and the nanocomposites exhibit better thermal and mechanical properties, including shape memory properties, than the unreinforced PS. Clay/PS composites showed a better performance than the other fillers. However, the shape memory was triggered here by thermal stimulus, which would be difficult to do in many biological applications such as bio-medical devices because the temperature of human body could trigger the recovery. Therefore, the following chapters will explore new methods of triggering the shape memory effect with high efficiency, enhancing the strength, and realizing uniform dispersion of nanoparticles.

Chapter 6

SPHERICAL CARBON NANOPARTICLE /POLYSTYRENE ELECTRO-ACTIVE NANOCOMPOSITES

Recently, various electrically actuated composites (EAPs) using addition of CNPs, CNFs, or CNTs into the polymer matrix have received great attention because these nanofillers improve both the mechanical and electrical properties [264,265]. SMP-based EAPs [264,266] with good dielectric permittivity could be appropriate materials for actuation in bio-robots [267], mini-pumps [268], and/or orthotic prosthetic assistance utilities [269,270] as they can change their shape in response to an electrical stimulus [271,272,273]. The SMP-based EAPs have many advantages such as low cost, light weight, high actuation strain (up to 200%) and controllable recovery time [251]. For current SMP systems, two methods are generally used to improve mechanical and shape recovery properties: i) trimming polystyrene molecular chains [248,250] with functional groups or ii) incorporating rigid micro- or nano-fillers into a polymer matrix [213]. Leng *et al.* [32] and Koerner *et al.* [140] investigated the electro-triggering shape memory effect for shape memory nanocomposites with carbon nano-fillers. So far, systematic studies on the dielectric permittivity and thermo-electrical property of PS-based SMP composites have rarely been reported, although results are crucial for MEMS applications such as actuators and sensors [272,274,275,276]. Therefore, this chapter will focus on the macro-/micro-mechanical properties, the dielectric and thermo-electric properties of CNP/PS nanocomposites, as well as the electro-active shape memory effects.

6.1 Microstructure and thermal properties

Figure 6.1 shows the fracture surface morphologies of composites with different CNP concentrations. The average size of individual CNPs below 100 nm, and the CNPs are uniformly distributed throughout the SMP matrix in all samples. The vein-type fracture patterns of the polymer matrix indicate a certain degree of plasticity in the matrix when fractured at the temperature of liquid nitrogen. Nanosized shallow dimples or voids are frequently observed between the vein-type features, where the CNPs are more exposed. Accordingly, it is considered that the CNPs serve as the source of nanovoid/dimple nucleation. The uniform dispersion of the nanosized CNPs in the styrene-based polymer

matrix was achieved via mechanical stirring in an ultrasonic bath, which forms a basis for better enhancement of mechanical properties of the composites.

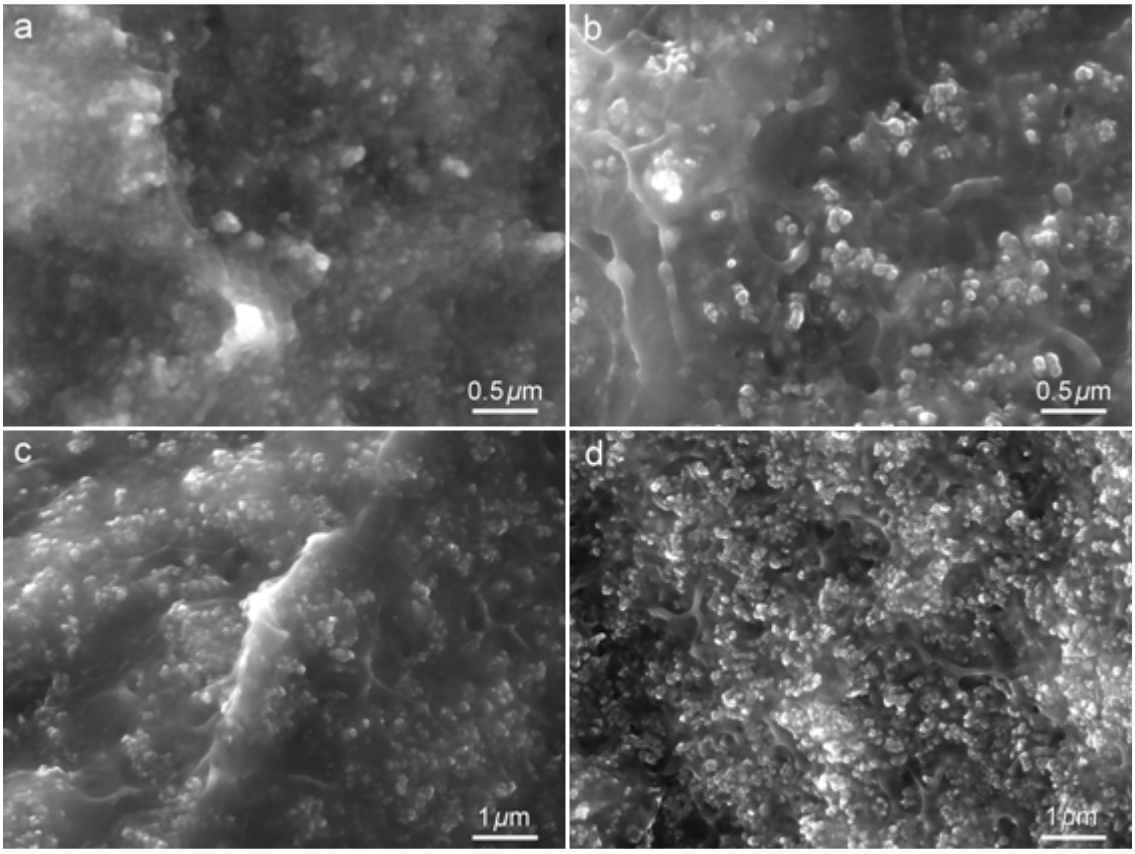

Figure 6.1 SEM images of the shape memory nanocomposites revealing the distribution of CNPs inside the PS matrix: (a) 1 wt.% CNP/PS,(b) 2 wt.% CNP/PS,(c) 3.5 wt.% CNP/PS, (d) 5.5 wt.% CNP/PS.

Thermo-mechanical properties of the CNP/PS nanocomposites were characterized by DMTA. The storage modulus-temperature plots for samples with different nanofiller concentrations are shown in **Figure 6.2**. The storage modulus of the composites at room temperature increases continuously as more CNPs are incorporated into the PS matrix. However, in every case, the storage modulus drops above 50 °C which is close to the glass transition temperature, T_g, of the shape memory composites [243]. The measured glass transition temperatures of the composites are between 60 and 75 °C. The *tan* δ curves presented in **Figure 6.2**b reveal that the glass transition temperatures of the composites increase substantially upon addition of CNP. The composite with 3.5 wt.% CNP has the highest *tan* δ value, which is the best energy absorption capacity or damping effect among all these samples. The damping effect is strongly dependent on the hard segments content, crystallization of soft segments, cross-linking rate and interface between fillers and matrix [244,245,277]. The damping effect of the composites

with 3.5 wt.% CNP content is more obvious than those with lower CNP contents. This can be explained by the significant enhancing effect of the CNP, and significant increase in interfacial boundaries over other polymer composites. Further increase in the CNP content might result in the particle agglomeration, which would reduce the energy absorption and damping.

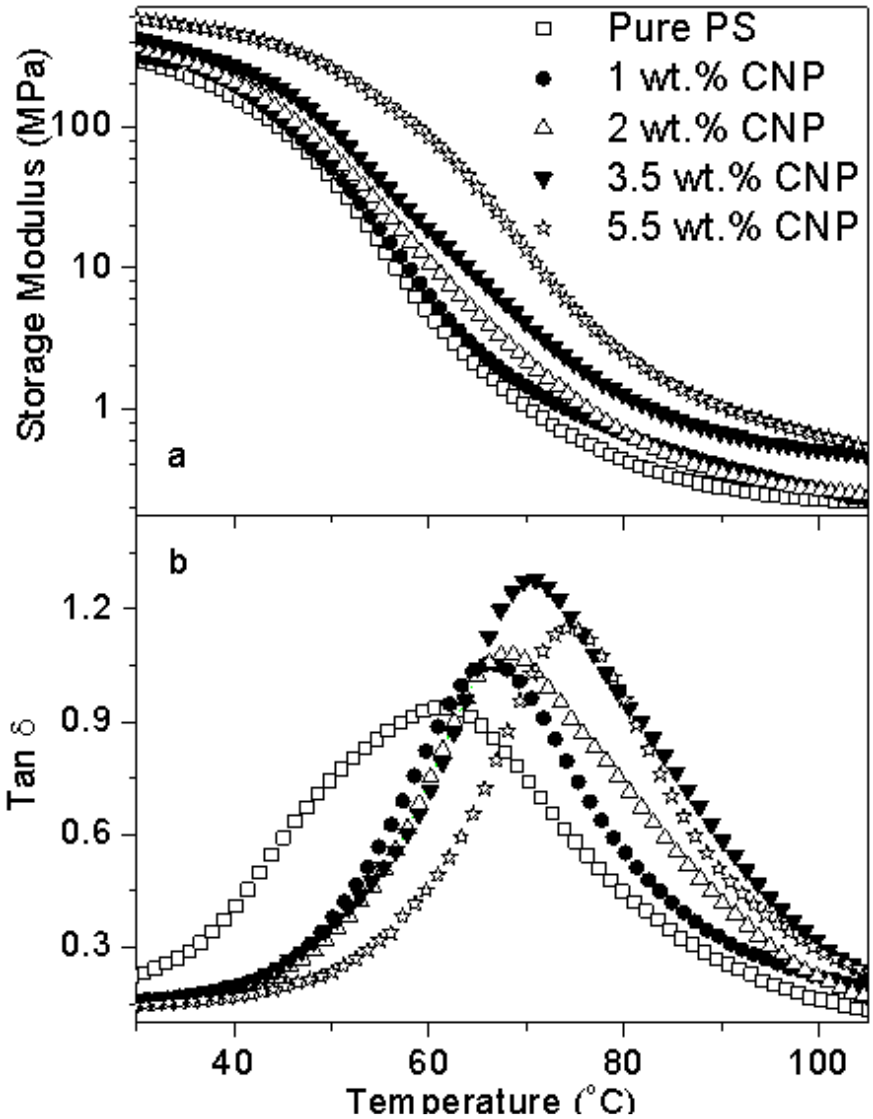

Figure 6.2 Plots of (a) the storage modulus and (b) tan δ as a function of temperature for all the nanocomposites.

6.2 Macro/nano-scale mechanical properties

Uniaxial tensile tests were performed to evaluate the macroscopic mechanical properties. **Figure 6.3**a presents the typical stress-strain curves for CNP/PS composites.

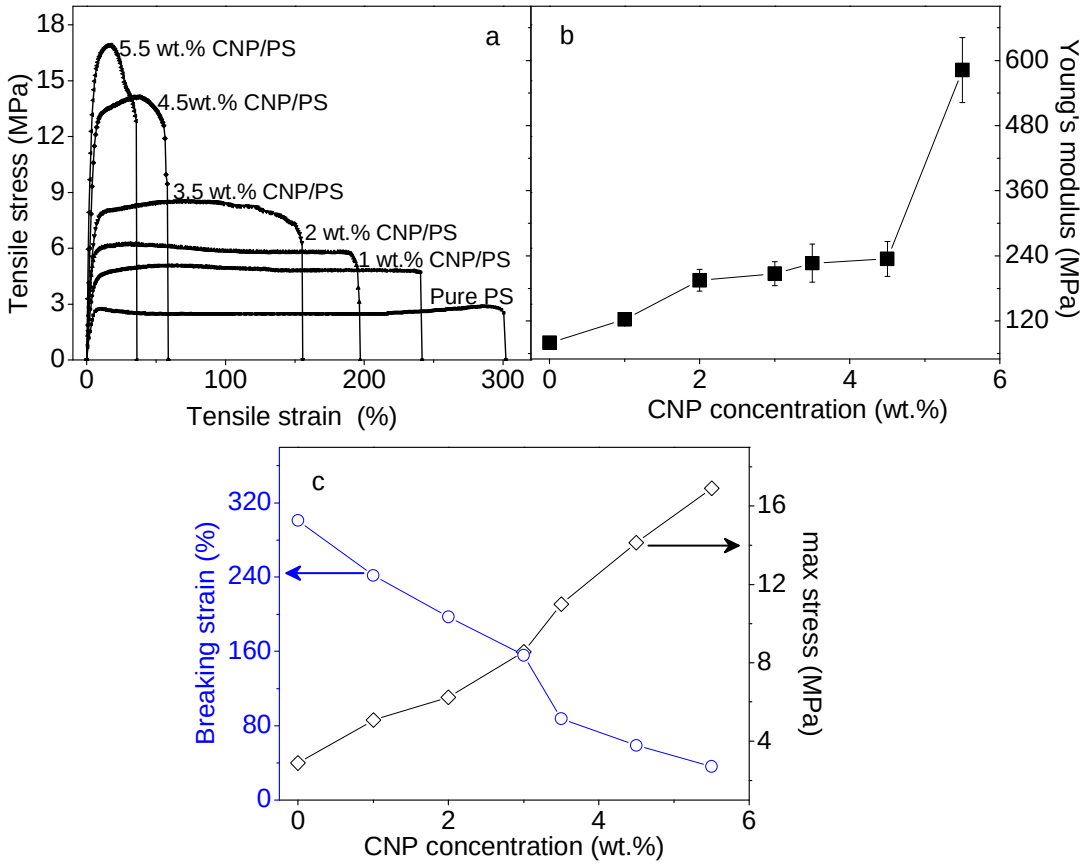

Figure 6.3 Uniaxial tension results for CNP/PS: (a) stress-strain curves, (b) Young's modulus and (c) max stress/breaking strain as a function of CNP concentrations

An increase in maximum stress and rapid decrease of the maximum strain can directly be seen associated with the addition of CNP. Moreover, the curves show an obvious drop after the peak stress while increase as the filler concentration increases, indicating more internal failure. Analysis of the stress-strain curve provides the Young's modulus (**Figure 6.3b**), maximum stress and strain as a function of CNP concentration. The results show that Young's modulus continues to increase as more CNPs are incorporated into matrix and the composites with 5.5 wt.% CNP achieve the highest Young's modulus, at nearly 8 times of that of pure PS. Detailed analysis results from stress-strain curves is presented in **Figure 6.3c**. As the CNP concentration increases to 5.5 wt.%, a significant improvement in the maximum stress is obtained and the value at 5.5 wt% CNP/PS is 4 times that of pure PS. Meanwhile, the breaking strain shows a continuous decrease from 300% to 30%.

Comparing with the tensile results in **Chapter 5** for various nanoparticles (at 1 wt.%), the Young's modulus and maximum stress of all the nanoparticles studied can be ranked

according to the following sequence: Clay/PS> Alumina/PS> CNP/PS> Silica/PS, whereas the breaking strains show a similar value of around 250 %. The maximum stress of the 1 wt.% clay/PS all show is the same as that of the 2 wt.% CNP/PS. The Young's modulus of the 1 wt.% clay/PS is same as that of the 4.5 wt.% CNP/PS. Considering the geometry differences between the clay and CNP, it can be concluded, that although the spherical CNPs achieved reinforce to the soft matrix because of its higher modulus and uniform dispersion, the enhancement is not as significant as that from the clay due to its lower capacity and load transfer. A detailed discussion is included in **Chapter 8**.

Typical force (P)-displacement (h) curves of the CNP/PS nanocomposites from the nanoindentation tests are presented in **Figure 6.4a**. A larger slope of dP/dh in the loading stages and a lower maximum penetration depth displacement is clearly obtained with the addition of carbon nano-particles. **Figure 6.4**b shows that the elastic modulus and hardness values derived from nanoindentation increase with CNP concentration. The nanocomposite of 5.5 wt.% CNP/PS showed a 3-fold increase in hardness and a 4-fold increase in modulus compared over those of the pure PS. Although the enhancement is evident, the values of elastic modulus from nanoindentaiton (1-6 GPa) are dramatically different from those obtained from the tensile tests (100-600 MPa). This could be explained by the different geometries of the two test methods. The tensile tests examine the uniaxial tensile deformation (Young's modulus) of the bulk material, whereas the nanoindentation is an approach to obtain the residual elastic modulus on a nano/micro meter scale under compressive loading. Generally, a material of this type will appear much harder in compression than in a tension.

The dissipation energy (DE) and dissipation energy ratio reveal the distribution of elastic-plastic regions in composites, and can be employed to study the dynamic response in composites. In this chapter, the values of DE and DE ratio were used to investigate the nanoparticle effect on elastic (soft)-viscos (hard) regions. **Figure 6.5** summarizes the calculated values of DE and DE ratio for the CNP/PS samples under various experimental conditions. As illustrated in **Figure 6.5a**, the DE value gradually increases with increasing load. It actually decreases up to 2 wt.% of CNPs, but increases dramatically up to 3 wt.%, which indicates that there is a marked increase in energy consumption at 3 wt.% CNP. As a reduction of DE is usually considered to be due to a reduction in plastic regions, it can be concluded that the incorporation of the CNPs

enhances the elastic regions and reduces the plastic region up to a concentration of 2 wt.%, i.e. that the material becomes brittle. The opposite situation was observed when the CNP concentration reaches 3 wt.%, which matches the enhancement analysis (**Figure 6.4**) for the change in elastic modulus.

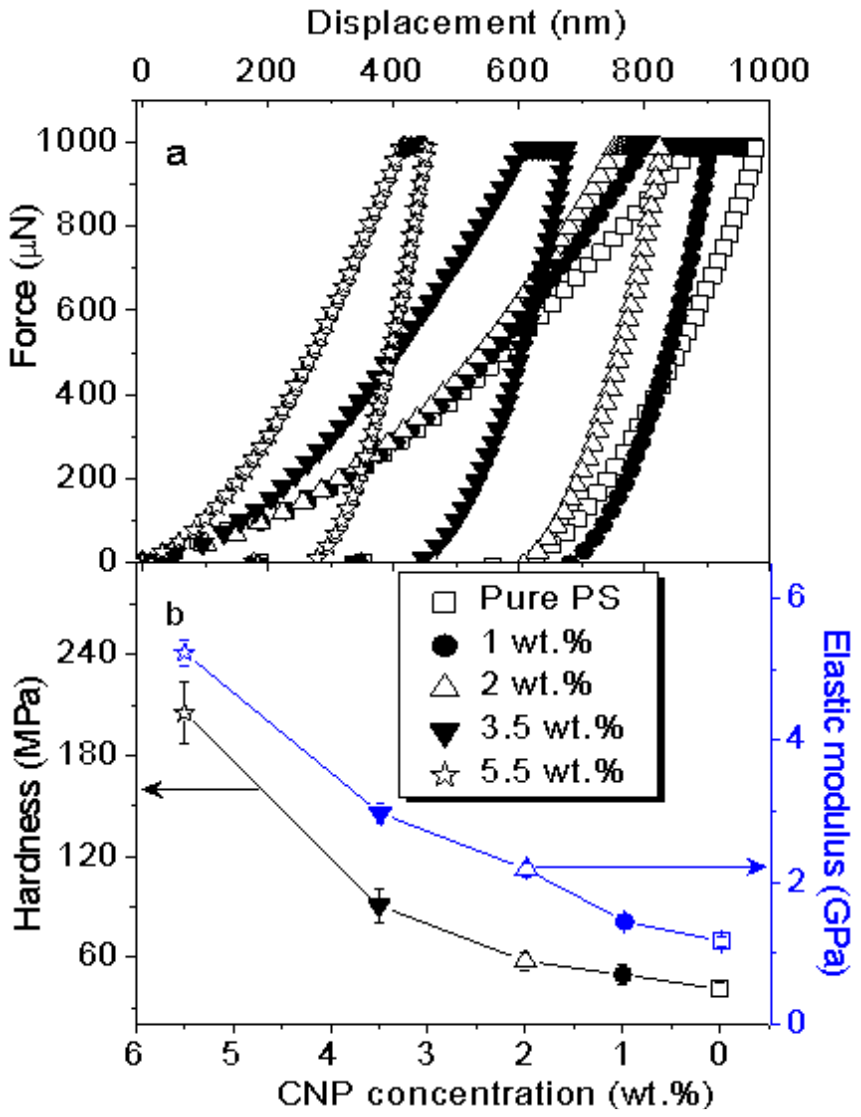

Figure 6.4 Nanoindentation results of PS and CNP/PS nancomposites as a function of CNP concentrations: (a) load-displacement curves and (b) hardness and elastic modulus

The results in **Figure 6.5b** indicate that the DE ratio tends to beome constant value when the applied load is above 1 mN. **Figure 6.5c-f** show the results for specimens tested with different holding times and loading rates at the max load of 1 mN. As seen in **Figure 6.5c** and **6.5d**, both DE and DE ratios increase when the holding time increases, however, the composites show smaller values of DE than those of the pure PS, indicating their better energy capacity with adding CNP. These phenomena can be understood as the longer the time, the more energy is dissipated in the composite system.

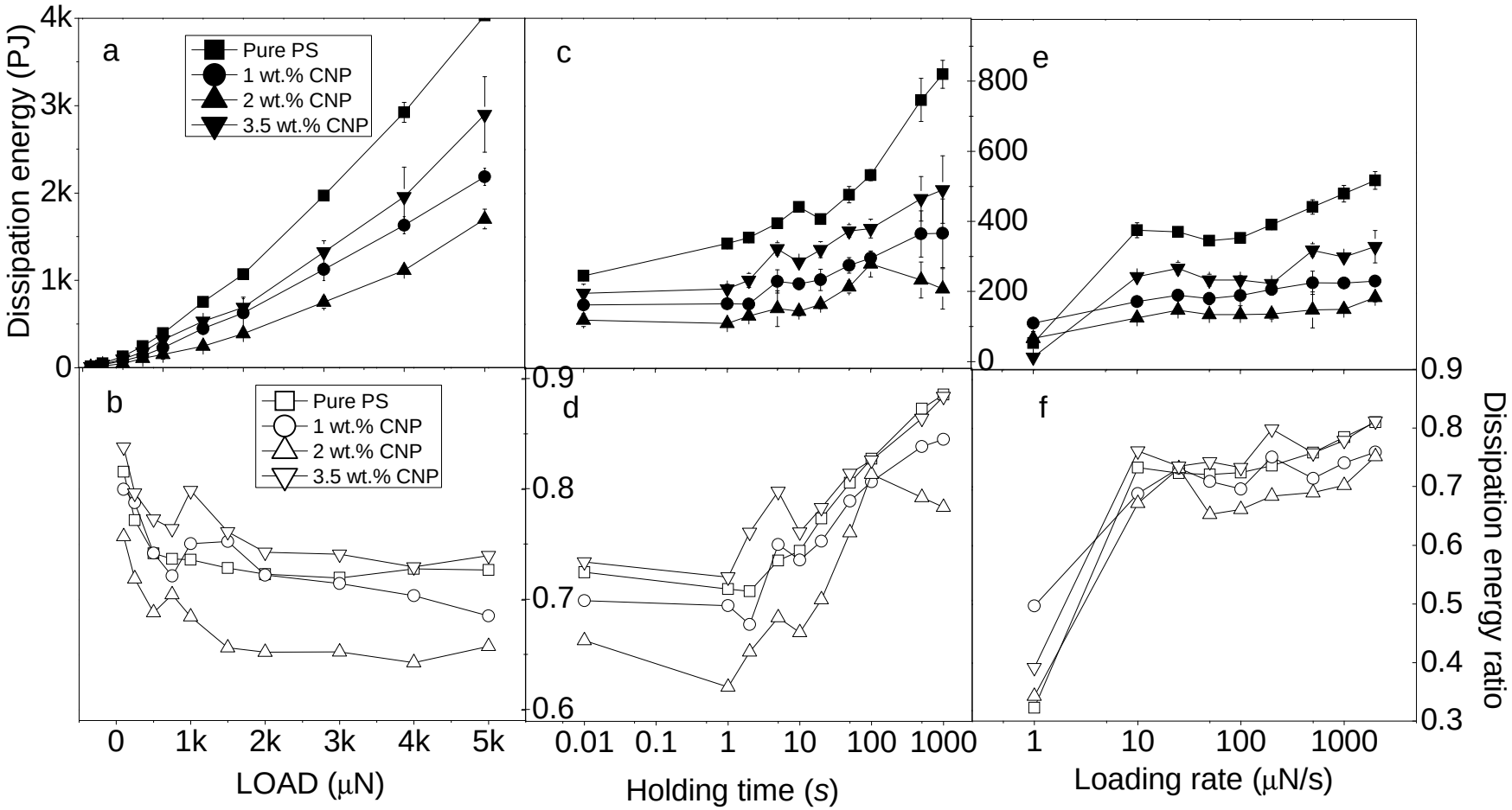

Figure 6.5 Energy analysis of the nanoindentation of CNP/PS composites with varied operational conditions: (a) Dissipation energy and (b) Dissipation energy ratio as a function of applied load; (c) Dissipation energy and (d) Dissipation energy ratio as a function of holding time on max load; (e) Dissipation energy and (f) Dissipation energy ratio as a function of loading rates.

Multiple molecular-level processes take place during this period, including debonding of the inorganic-organic interface, polymer relaxation, and creep. It should be noted that the 2 wt.% CNP/PS sample shows the lowest DE and DE ratio, which imply the best load/energy capacity of all samples. **Figure 6.5e** and **6.5f** show the values of DE and DE ratio as a function of loading rate. The pure PS has a gradually ascending trend with the loading rates, although the loading rate has little effect on the DE and DE ratio for the composites at loading rates above 10 μN/s. It must be pointed out that extremely low values for both DE and DE ratio were obtained at the loading rate of 1 μN/s, for each curve. The reason for this could be that, the elastic regions absorb and store the greater part of the input energy at loading rates as low as 1 μN/s with conformational changes of the flexible molecular chains in elastic region [278], and so release all (or most of) this reversible energy during the retrieving of the indentor. This result reveals the visco-elastic properties and energy capacity of elastic regions in thesis materials.

In summary, the nanoindentation results provide a mechanical assessment at the nano-/micro- scale. The modulus values for the composites are much larger than those of pure PS. Further analysis on the DE and DE ratio illustrate the dynamic energy absorption/conversion of the materials and their viscoelastic properties.

6.3 Conductivity and dielectric properties

Figure 6.6 displays the measured conductivity *versus* CNP concentration at room temperature. As the CNP content (φ_{CNP}) increases from 1 wt.% to ~3.5 wt.%, the measured conductivity dramatically increases from 1×10^{-8} to 10^{-2} S/cm, and then the rate of increase drops as the CNP concentration exceeds 3.5 wt.%. The conductivity at φ_{CNP} > 3.5 wt.% is large enough for electrical conduction for general microactuator usage.The observed conducting behaviour can be explained by the percolation which treats a polymer-based inorganic (Ξ_1)–organic (Ξ_2, $\Xi_2 << \Xi_1$) conducting system as a random mixture of resistors and capacitors, or conductors and insulators [279,280]. At a low concentration of conductive (CNP) phase, conduction is dominated by hopping conduction among the nanofillers with an electrical conductivity closer to that of an insulator [279,281]. The SMP composite becomes more conductive as the filler concentration is increased up to a critical value, the percolation threshold (φ_c), which depends on the filler and its dispersion in the matrix [282].

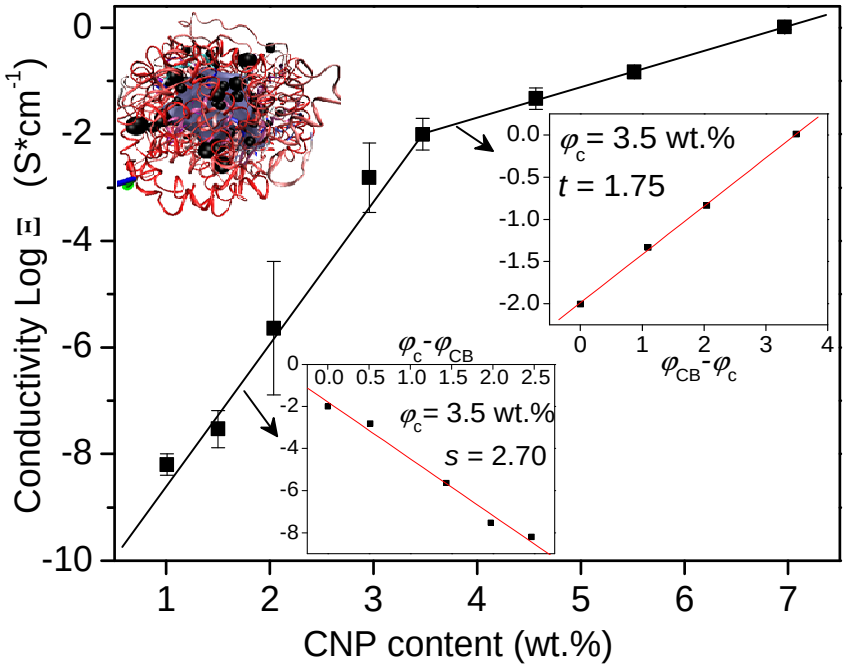

Figure 6.6 Conductivity of PS and nanocomposites as a function of CNP content; the insets show a 3-D illustration of the composites and the linear curve fitting needed for determining the threshold value.

Figure 6.6 clearly shows two regimes with different slopes, corresponding to "insulating behaviour" at φ_{CNP} < 3.5 wt.% and "conductive behaviour" at φ_{CNP} > 3.5 wt.%. To determine the threshold value φ_c of the SMP composites, the experimental conductivity σ was fitted based on the following power laws [279,283]:

$$\Xi(\varphi_{CB}) \propto (\varphi_c - \varphi_{CB})^{-s} \quad \text{for} \quad \varphi_{CNP} < \varphi_c \tag{6.1}$$

$$\Xi(\varphi_{CB}) \propto (\varphi_{CB} - \varphi_c)^{t} \quad \text{for} \quad \varphi_{CNP} > \varphi_c \tag{6.2}$$

Where t and s are the critical exponents in the conducting and insulating regions, respectively. Linear curve-fitting using the above equations gave φ_c = 3.5, t = 1.75, and s = 2.70 (see the inset charts in Figure 6.6). Previous work [284,285] were reported that a higher critical value of t > 2 for polymer/CNP systems and was explained by CNP aggregation and cluster-cluster structure causing less conductive efficiency. A better conductive efficiency was achieved in this work with the t value of 1.75, which is probably due to the better mixing of nanoparticles as a result of the additional ultrasonic agitation. Another explanation could be due to CNP aggregation at the interfaces between hard and soft segments [286]. The formation of aggregates and irregular dispersion of CNPs in the two-phase polymer system decreases the conductivity.

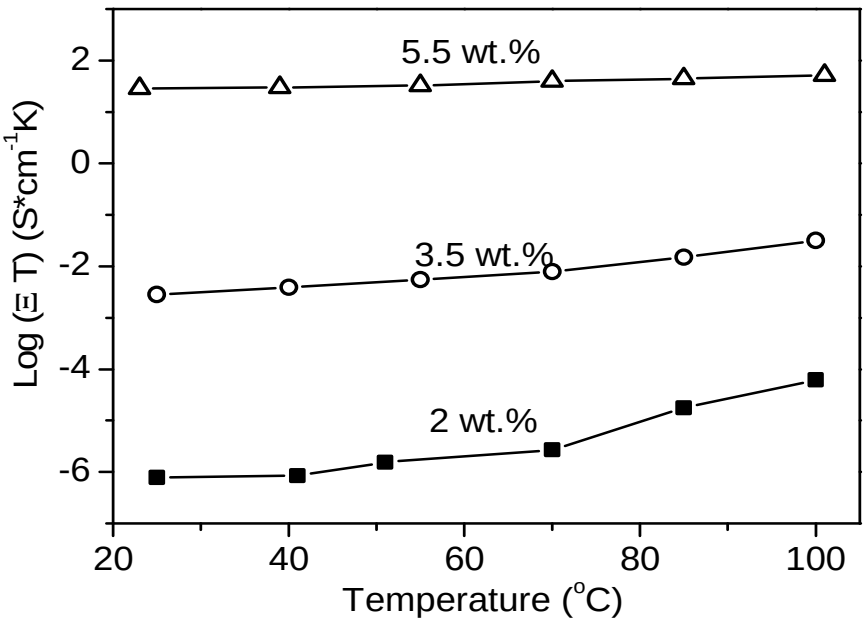

Figure 6.7 DC conductivity of CNP/PS nanocomposites as functions of temperature and CNP concentrations

Composites with different CNP contents were chosen for AC electrical testing, and the AC conductivity results are presented in **Figure 6.7** as a function of temperature. With increase in temperature, the measured conductivity gradually increases because the thermal energy increases the hopping conductivity in the composites [287]. As shown in **Figure 6.7**, the conductivity of the sample with 2 wt.% CNP approaches the percolation limit of an insulator-dominated state, and a further increase in temperature significantly increases the conductivity through enhanced hopping. When the CNP content is above φ_c, the CNP particles or clusters are almost linked with each other to a certain degree, forming a continuously distributed CNP network in the matrix.

6.4 Dielectric properties

The complex permittivity Ø represents the ability of the system to store charge at the interface under an applied electric field. Insulating polymers do not have an interface for charge storage and their dielectric constant is therefore small. With the addition of conductive particles, the interface between the polymers and conductive particles increases dramatically, leading to a higher dielectric constant for the composites. The dielectric permittivity and real part of the complex permittivity (Ø′) as a function of frequency for different CNP contents at room temperature are displayed in **Figure 6.8**. The dielectric constant increases from a value of around 2.75 for the pure PS [288] to

nearly 10^6 for the 3.5 wt.% CNP composite. The dielectric constants $\underline{\varepsilon}$ and $\underline{\varepsilon}'$ increase as the CNP concentration changes from 2 wt.% to 3.5 wt.%, and then decreases as the CNP concentration further increases to 5.5 wt.%. With such a high content of CNPs (>3.5 wt.%), the composite becomes a "metallic" type conductor which effectively loses its ability to store charge at the interfaces between the CNP particles and polymer.

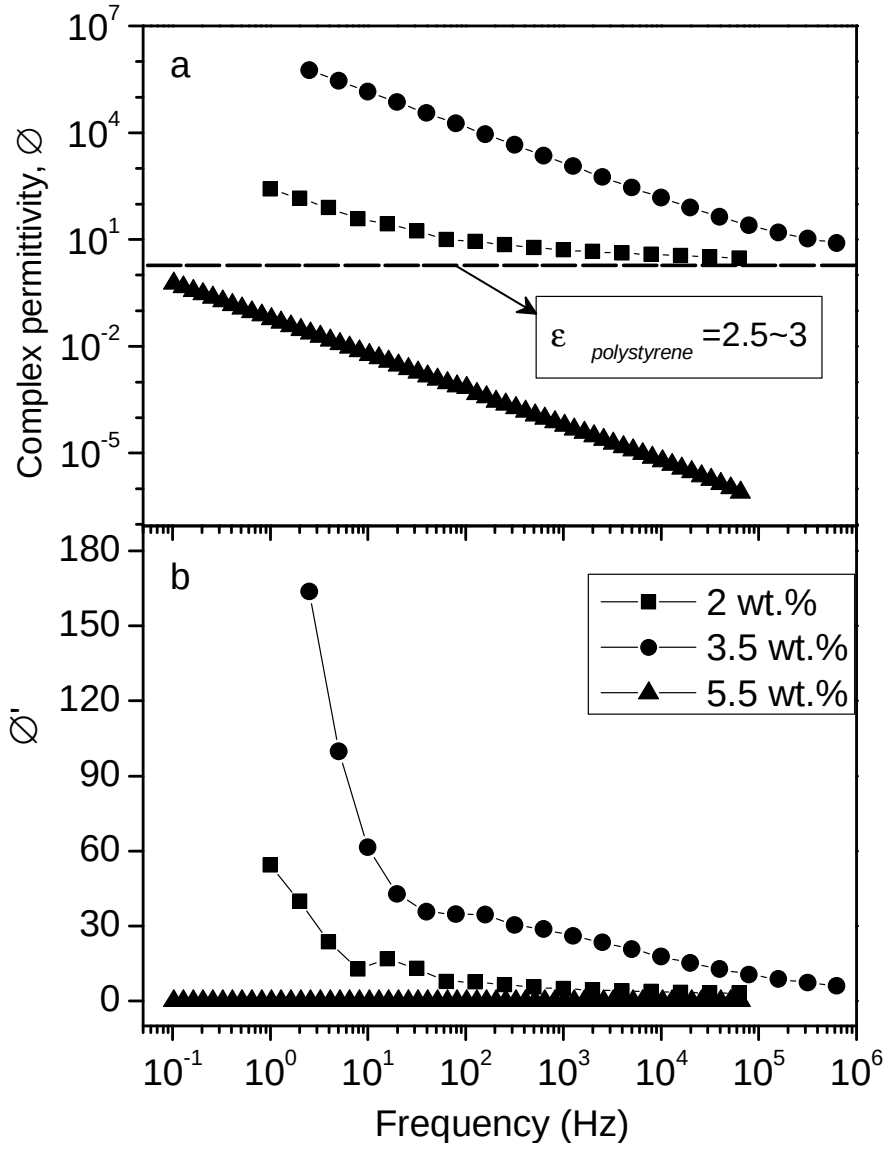

Figure 6.8 (a) Complex permittivity Ø and (b) real part of complex permittivity Ø′ for CNP/PS nanocomposites as a function of frequency at room temperature.

At CNP concentrations below φ_c, the relatively large distance between the conductive particles/clusters makes the composite behave as an insulator at low frequencies. The complex permittivity ε of the composite with 3.5 wt.% CNPs varies from 1×10^6 to around 3 as the frequency is increased to 100 kHz. Similarly, the composites with 2 and 3.5 wt.% CNPs showed a similar decrease in Ø with increasing frequency up to around 100 Hz. As the frequency increases further, the value of Ø gradually approaches a

constant value of 2.75, the dielectric constant of the pure polystyrene. Since the charges on the interfaces are unable to follow the changes of electrical field, the polymer matrix acts as a pure insulator. On the other hand, for the composites with 5.5 wt.% CNP, the CNP concentration is beyond the percolation threshold, and they are conductive due to an efficiency continuous electric path. The increase in frequency does not change the dielectric constant significantly with values of Ø< 1 and Ø′ nearly equal 0 efficiently, i.e. not much capability to store charge but a typical metallic conductor. The results show that the dielectric properties of these composites change significantly with the operational frequency, and this information is useful for microactuators which may be manipulated with various frequencies.

The temperature-dependence of the complex permittivity of PS/CNP composites is shown in **Figure 6.9a** at a fixed frequency of 1 kHz.

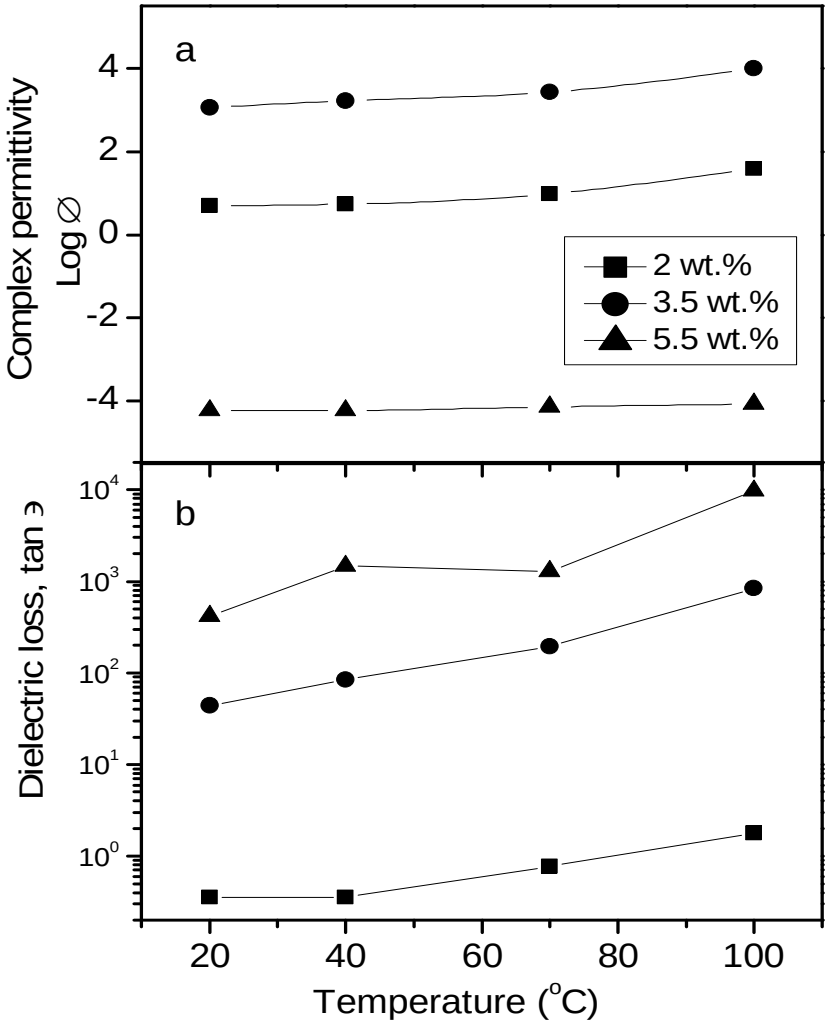

Figure 6.9 (a) Complex permittivity Ø and (b) dielectric loss, tan Ɜ, of the CNP/PS nanocomposites as a function of temperature (with a fixed frequency of 1 kHz)

The increase in complex permittivity $\underline{\varepsilon}$ of the composites with 2 wt.% and 3.5 wt.% CNP contents with temperature is attributed to the increased hopping effect at high temperatures. In contrast, the complex permittivity of the composite with 5.5 wt.% CNP remains almost constant. The dielectric loss, tan Э (tan Э = Ø″/Ø′, where the Ø″ is imaginary part of the complex permittivity) is related to the material conductivity, in that a material with a high value of tan Э is more conductive with less resistive loss. Therefore, the SMP with 5.5wt.% CNP, above the percolation threshold value, shows a higher tan Э than that with 2 wt.% (as shown in **Figure 6.9b**). On the other hand, as the temperature increases, both the content of conducting regimes (through the hopping effect) and the conductivity of the composites increase as shown in **Figure 6.9b**. At the same time, the electron tunnelling effect becomes significant [289], and also the tan Э value increases with temperature.

6.5 Electro-active recovery

In this section, the shape recovery and actuation of the CNP/PS nanocomposites will be examined. The composite with 3.5 wt.% CNP was selected to investigate the electro-active shape memory property using laser-cut cantilevers. **Figure 6.10** shows a typical recovery of a micro-cantilever at an applied voltage of 30 V, where the deformed cantilever showed a full recovery within 40 seconds.

Figure 6.11 compares the shape recovery ratio under various applied voltages using the method discussed in **Section 3.3.5.3**. With increasing voltage, time for full recovery of the deformed cantilever was reduced significantly, due to the higher input energy. The time for 95% recovery at 40 V is around 12 seconds, whereas 86 seconds are needed at 25 V for a similar recovery. Additionally, the maximum amount of recovery of the cantilever at 20 V is only 90%, indicating that this voltage of 20 V generated in sufficient power to achieve full recovery. In this work, the high electrical recovery efficiency was achieved when the voltage was equal to or above 25 V. Moreover, electrically triggering recovery seems to be more controllable because there is a good relationship between recovery time and recovery ratio when the voltage is 25 V or 30 V. For the higher voltages of 35 V and 40 V, the recovery is too fast to be controllable.

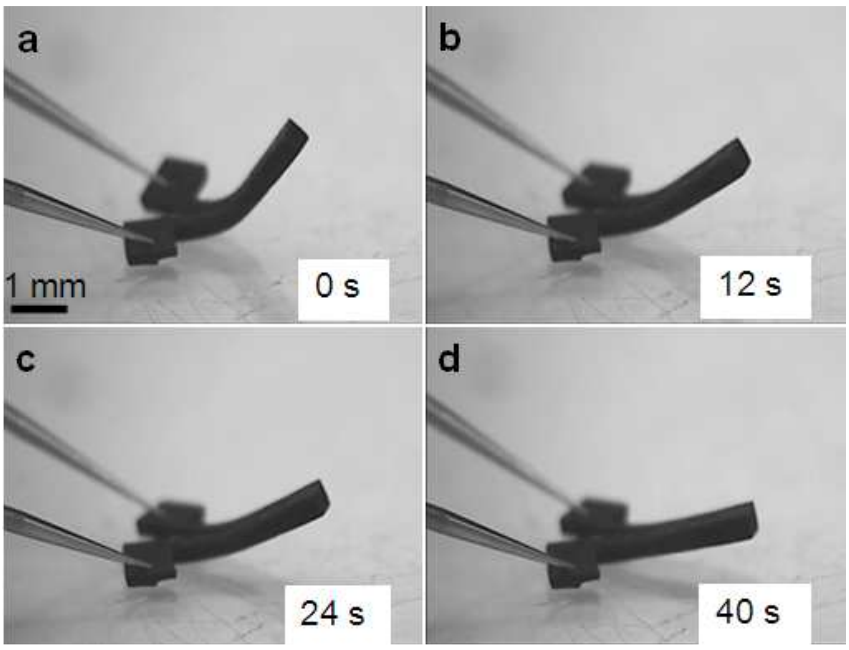

Figure 6.10 Electro-active shape recovery for a cantilever made of 3.5 wt.% CNP/PS nanocomposite applied with a voltage of 30 V, (a) pre-deformed shape, (b) after 50% recovery shape, (c) after 90% recovery, and (d) after full recovery.

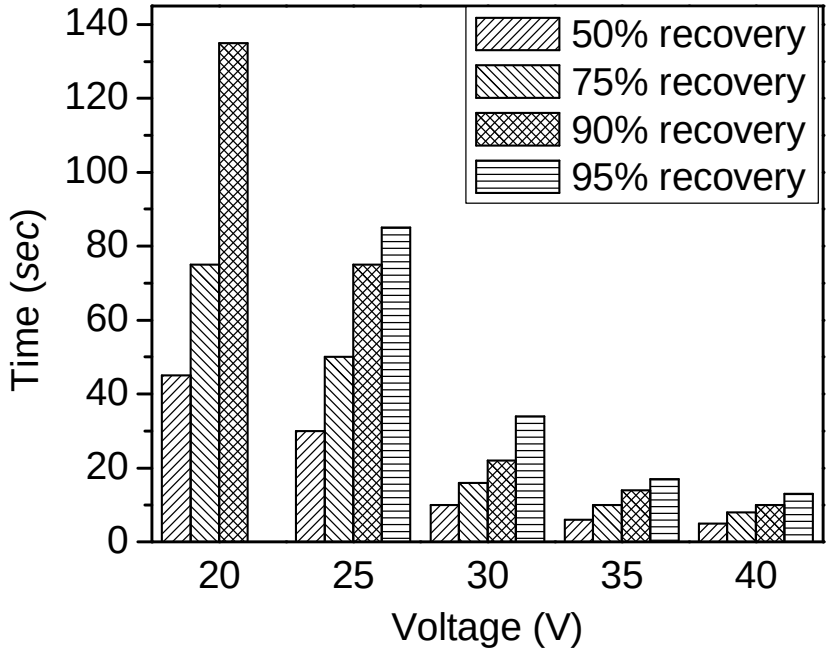

Figure 6.11 Electro-active shape recovery time as a function of voltage applied for the composites with 3.5 wt.% CNP.

Figure 6.12a presents results of the measured surface temperature (T) versus time (t) at different applied voltages, exhibiting a typical three-stage change. The first stage corresponds to the onset of the temperature increase, and the lower the power, the longer the time required for this onset. In the second stage, the temperature increases significantly with voltage, due to Joule heating. With further increase in holding time at

different voltages, there is a point of inflection in the curve and the gradient decreases, which can be attributed to the change of Columbic forces in the percolation conductive path across the polymer matrix [290] and thermal fluctuations due to the nonlinearity in Joule heating [291]. For the relationship of the current versus time as shown in **Figure 6.12b**, the electrical current does not show a large variation with changes in the applied voltage. However, the current increases significantly between 20 and 30 V, which is due to the decrease in sample resistivity caused by the Joule heating.

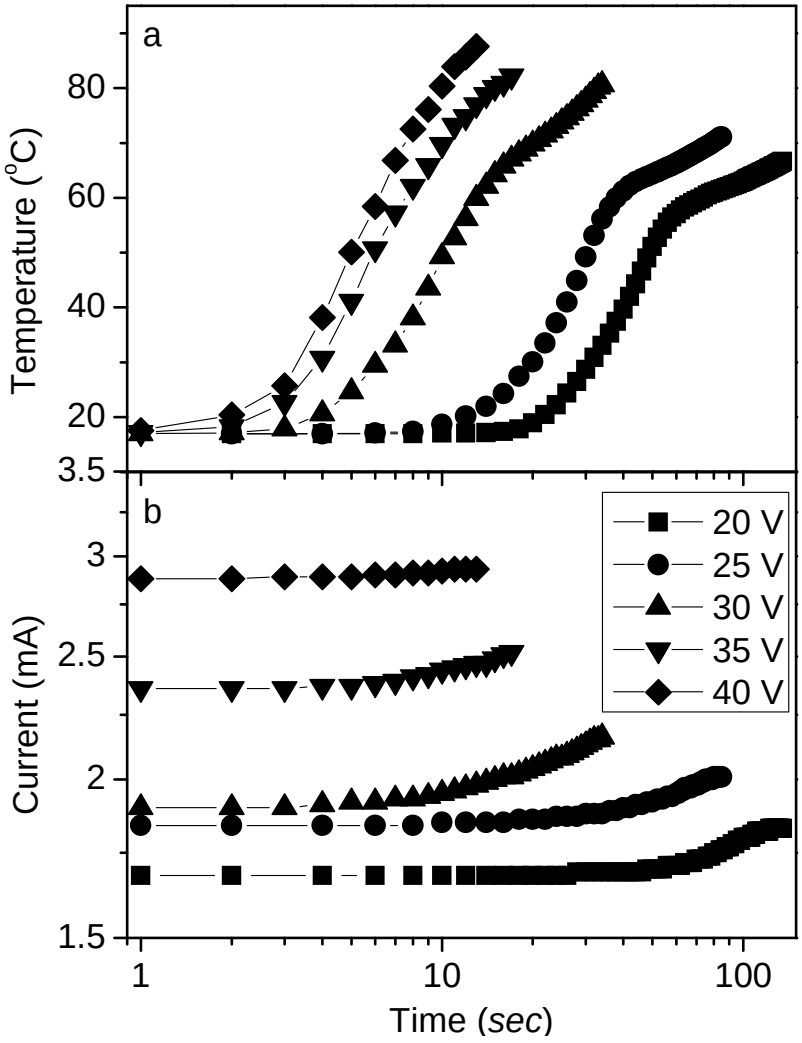

Figure 6.12 Electro-active shape recovery of microcantilever at different applied voltages: (a) temperature and (b) current of the samples as a function of time

Energy conversion during the electro-active recovery can be split into two parts, expressed in the following equation:

$$E_e = E_{rec} + Q_t \tag{6.3}$$

where E_e is the applied electrical power during testing, and E_{rec} and Q_t are the recovery energy and heat generation, respectively. In a static charging process (i.e. the cantilever

is not bent, and no shape recovery occurs during the electrical charging process), there is no recovery energy consumption, so the E_e is equal to that of Q_t. Due to the recovery of the deformed cantilever during the "shape recovery" process, part of the electrical energy will be consumed for shape recovery, also the heat generation effect will not be as significant as in the static charging process. **Figure 6.13** shows the measured sample temperature as a function of the applied electrical power. In the situation of static charging, the sample temperature increases significantly as a function of power, due to the Joule heating at the applied electrical power. The increase in thermal energy causes changes into paths through the conductive network by Columbic forces and the polymer network structure density in the matrix [291, 292], so leading to a nonlinear heat transfer between the matrix and surroundings. For the electro-recovery test, the surface temperatures of the cantilever vary with electrical power but are much lower than the static ones, clearly indicating that part of the input energy has been consumed in actuation.

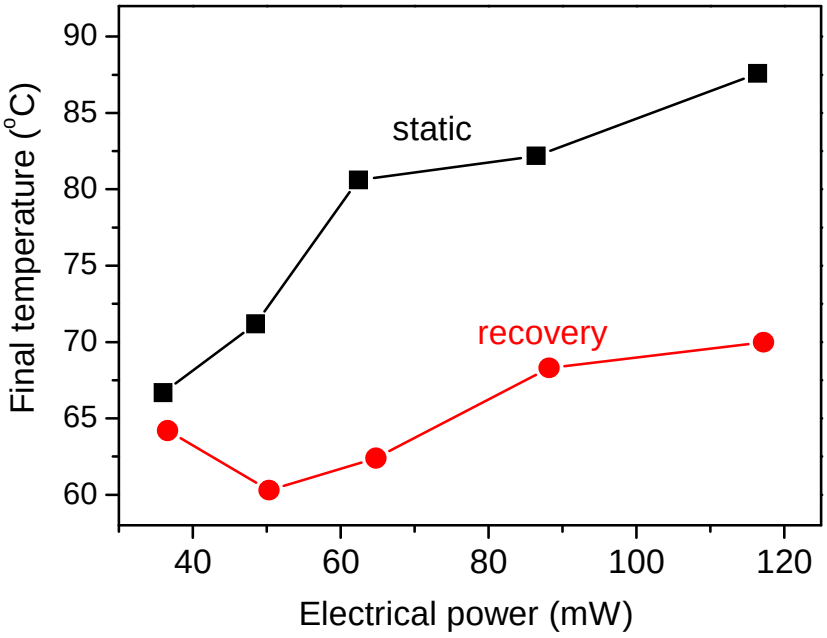

Figure 6.13 Temperature versus electrical power during static charging process (the cantilever was not deformed, and thus no shape recovery taken place during the charging process) and shape recovery charging process (the cantilever was bent and there was shape recovery of the structure during the charging process).

6.6 Summary

In conclusion, ultrasonic mechanical stirring was used in nanocomposite fabrication, and electro-active PS-based nanocomposites were successfully synthesised through incorporation of CNPs into the PS matrix. The mechanical and thermo-mechanical enhancements have been verified with the results from the tensile test, nanoindentation and DMTA tests, respectively. The electrical tests indicated that a two-phase conductive system was formed with a percolation threshold value of 3.5 wt%. The conductivity and dielectric constants changed dramatically as a function of frequency, temperature and CNP concentration. Measurement of dielectric constant and dielectric loss as a function of temperature and frequency manifested a stable thermal electrical performance from room temperature to 100 °C. Shape recovery results indicated that these smart nanocomposites could be potentially useful for microactuation applications. However, the enhancement to the SMP matrix using the CNPs was not as expected compared with the other nanoparticle filled composites investigated in **Chapter 5**. In the next chapter, the use of rod-type nanofillers, i.e. CNFs and CNTs, to improve both electrical and mechanical properties will be discussed.

Chapter 7

CARBON NANO FIBER/CARBON NANOTUBE - POLYSTYRENE SHAPE MEMORY NANOCOMPOSITES

Incorporating CNFs or CNTs into an SMP matrix has received great attention in the last few decades as it can effectively improve both the mechanical and functional properties of the polymer matrix. For example, Leng *et al.* [32] reported the novel infrared activating ability of shape memory nanocomposites with various carbon nano-fillers. Ni *et al.* [259] investigated the macroscopic mechanical enhancement and shape recovery ability for the CNF/CNT SMPU system by tensile testing. Gunes *et al.* [149] synthesized the SMPU based nanocomposites with CNP and CNF, and studied their electrical properties and electrical-active recovery. Detailed studies of the phenomenology and theory of remote triggering shape recovery in CNT/CNP-filled thermoplastic elastomer have been made by Koerner *et al.* [140].

Nanoindentation, as an adveanced surface micro/nano mechanical characterization technique, has been applied on SMPs for different research aims. For example, Wornyo *et al.* [226] used nanoindentation to investigate the deformation behaviour of diethylene glycol dimethacrylate and polyethylene glycol dimethacrylate shape memory copolymer networks with various organic components. Fulcher *et al.* [293] provided a detailed approach to the thermo-mechanical characterization on a thermosetting epoxy based SMPs using nanoindentation at different temperatures. Nelson *et al.* [294] reported the temperature-dependent nano-scale recovery of thermoset epoxy based SMPs using the tip of an AFM. So far, a lot of effort has been into the nanomechanics of polymer based nanocomposites, but few studies are available for SMP nanocomposites. In this chapter, PS based nanocomposites with well-dispersed CNFs and CNTs were prepared, and their nanomechanics and thermomechanics were studied using nanoindentation and cyclic thermo-mechanical tests.

7.1 Microstructure and thermal properties

SEM was used to study the distribution of the fillers inside the matrix. **Figure 7.1** shows the morphologies of the nanocomposites with 2 wt.% of carbon nano-fillers.

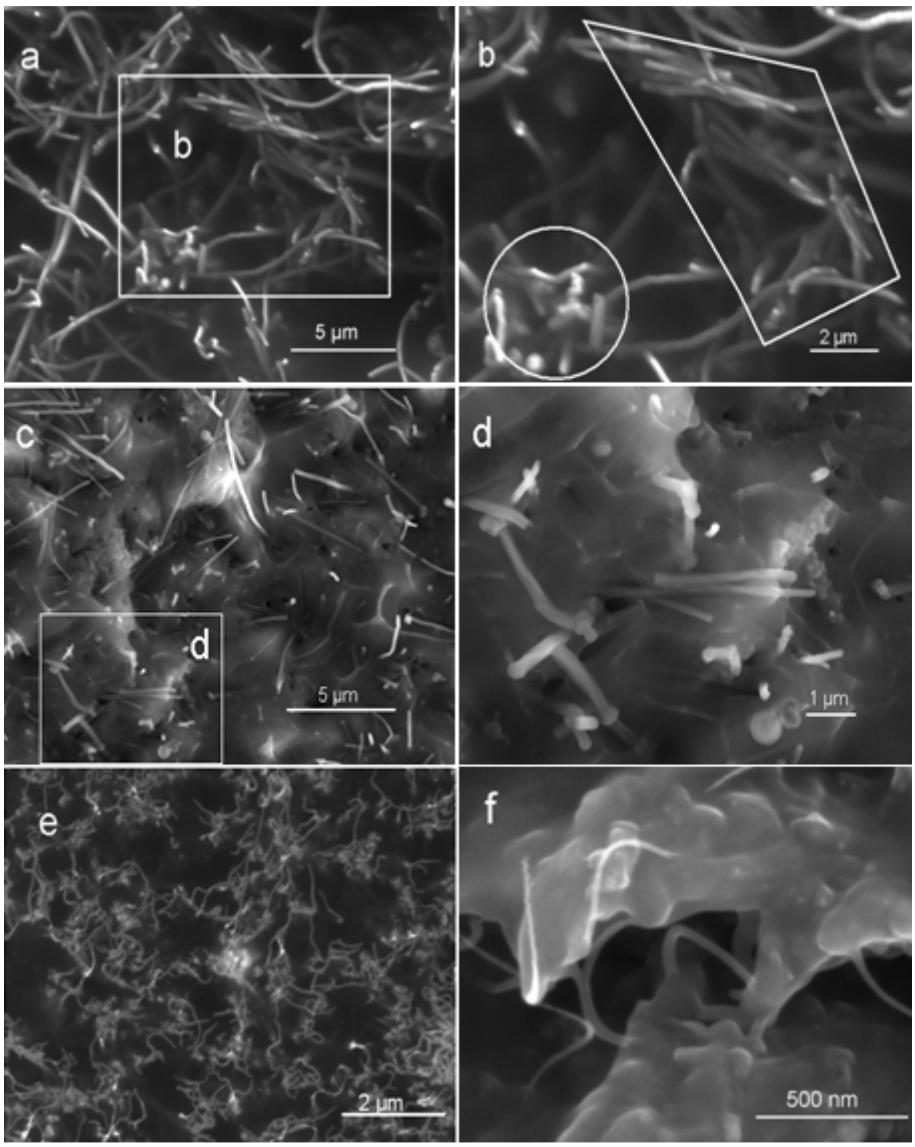

Figure 7.1 SEM images of the shape memory nanocomposites revealing the distribution of carbon nanofillers in the matrix (a) irregular distribution of 2 wt.% CNF/PS,(b) CNF knots and interlocks in a selected area,(c) Uniform scattering of MWCNT in 2 wt.% MWNT/PS, (d) Magnified image of selected area of fig.4c, (e) Uniform scattering of curly SWNT in 2 wt.% SWNT/PS, (f) SWNTs bridging a micro crack.

CNF rods with high values of *l*/*d* (above 100) are observed as irregular bundles (in **Figure** 7.1**b**) in the composites. Generally, rod like nanofillers tend to bundle together and cannot be easily separated due to surface polar groups and non-uniform growth as reported [295]. Such bundling of the CNF in the polymer matrix could dramatically reduce its effect by lowing the effective scattering volume of the nanofillers, leading to defect in microstructure (non-uniform organic-inorganic phase) and improving the load transfer efficiency. The SEM images of the MWNT/PS composites reveal a homogeneous dispersion of the MWNTs in the PS matrix (**Figure 7.1c**). Most CNTs are presented as separate single tubes. In **Figure 7.1d**, the MWNT rods can be seen to have

smaller diameters than the CNFs, and are randomly and uniformly distributed inside the polymer substrate. The good dispersion ensures a uniform composite structure with an effective load transfer. For the SWNT/PS composites, the SEM image of nanocomposite sample surface in **Figure 7.1e** indicate that the SWNTs exist as random curly wires in the matrix, with much smaller dimensions but scattering volume percentage compared with the CNFs and MWNTs. The SWNTs are distributed uniformly inside the matrix and they tend to form a continuous pattern as most of the SWNTs attach to each other. The magnified image from the fracture surface (**Figure** 7.1**f**) reveals clearly the bridging of several SWNTs inside a micro-crack, indicating a better stress distribution in the PS matrix, enhancing the load transfer from the matrix to the SWNTs during fracture, and limiting the propagation of micro-crack.

The DMTA results for all the samples are summarised in **Figure 7.2**, which shows the variation of storage modulus and *tan* δ as functions of nanofiller loading and temperature. The storage modulus E' of the nanocomposites at room temperature increases with nano-filler concentration, and a maximum storage modulus of 1.2 GPa is obtained for the 3 wt.% SWNT/PS nanocomposites. However, the storage modulus decreases rapidly over the glass transition temperature T_g due to the softening effect of the polymer [[243]]. The curves also show an increasing trend of T_g with nano-filler content, and the peak value of *tan* δ and the highest T_g are achieved at the composites with 2 wt% CNF/PS (**Figure 7.2**b) and 2 wt% SWNT/PS (**Figure 7.2**f), whereas for the MWNT/PS (**Figure 7.2**d), these best values are at 3 wt.% of the nanofillers. The measured glass transition temperatures of all the nanocomposites are between 60 and 75 ^{o}C, higher than that for the pure PS, which shows the improvement of thermal properties using nanofillers. For the CNF/PS and SWNT/PS nanocomposites, the transition temperature decreases with increase in the filler content up to 3 wt.%. As indicated from the SEM observations, more irregular dispersion or agglomeration of the CNF will cause more defects in the microstructure, thus deteriorating load transfer and restricting of the mobility of macromolecule chains in the system. The decrease of T_g in 3 wt% SWNT/PS can be attributed to the fact that the filler begins to aggregate as the volume concentration reaches the dispersion threshold with the currently used dispersion techniques.

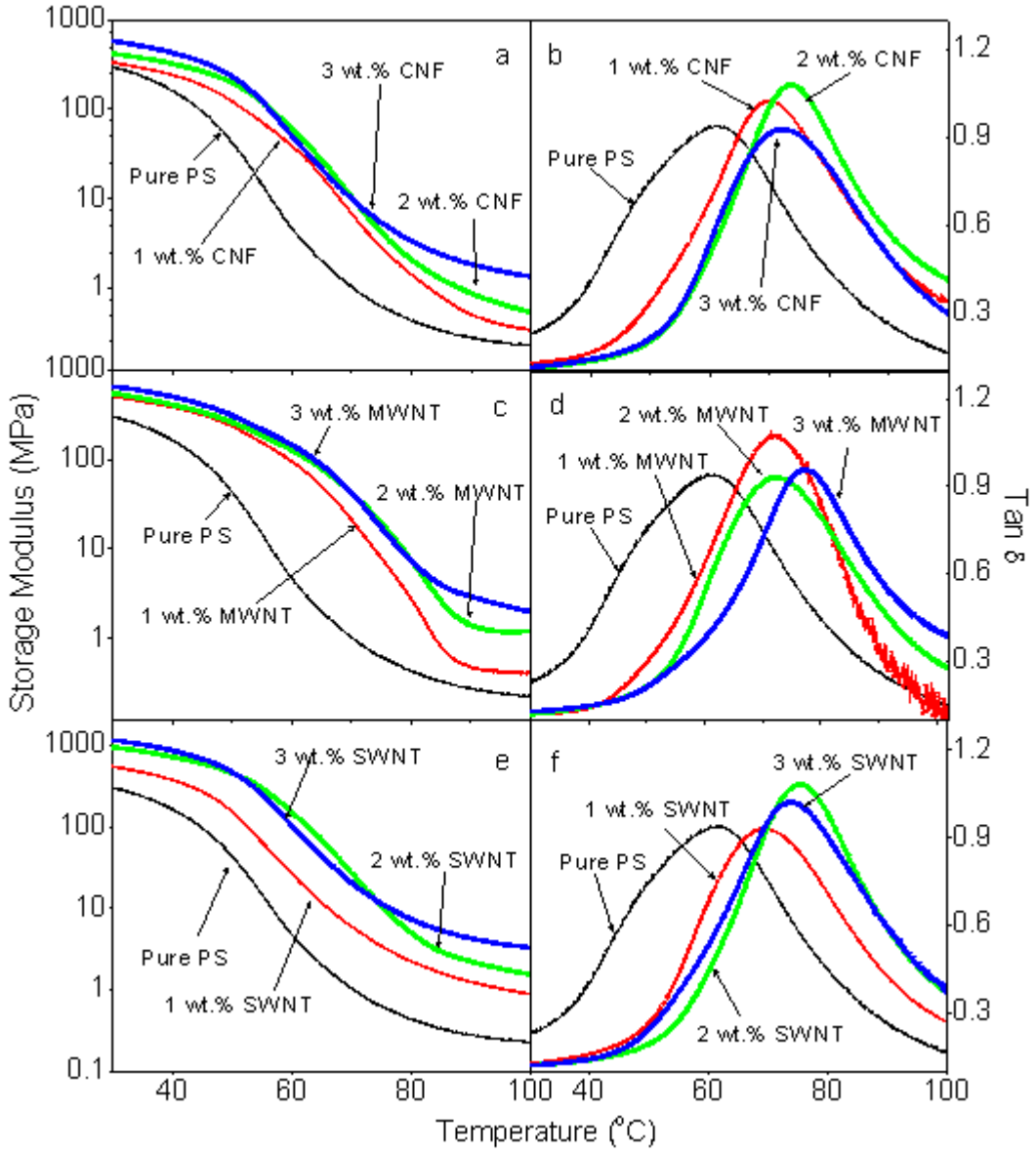

Figure 7.2 DMTA results for the nanocomposites with CNF and CNTs: (a) storage modulus for CNF/PS composites, (b) tan δ results for CNF/PS composites (c) storage modulus for MWNT/PS composites, (d) tan δ results for MWNT/PS composites (e) storage modulus for SWNT/PS composites, (f) tan δ results for SWNT/PS composites

Figures 7.2b, d and f reveal that the transition temperatures of the nanocomposites increase substantially with addition of the nanofillers. For the CNF/PS and SWNT/PS, both the T_g and *tan* δ values of the nanocomposites keep increasing up to 2 wt.%. This can be attributed to the increased physical cross linking points out filler-polymer interfaces and increased dissipation energy in the system at a higher filler concentration. In contrast, the values of *tan* δ decrease for the 3 wt.% CNF/PS and SWNT/PS nanocomposites, accompanied by a decrease in T_g, which is reflected in the values of storage modulus. The damping effect in the MWNT/PS is lower than that in the CNF/PS or SWNT/PS. This can be explained by the more significant effect of MWNTs

than CNF at lower volume fractions (**Chapter 3**) of MWNTs than that of SWNT, both of which could lead to the less internal interface defects and decreased values of *tan δ*.

The storage modulus in the rubbery state is an indication of interfacial strength between the organic phase and nanofillers. The interaction forces among the macromolecular chains become weak with increased temperature as the molecular chains have been thermo-activated and the strength of the polymer/nanofiller interface dominates the mechanical properties at a high temperature. According to rubber elasticity theory, the storage modulus in the rubbery state can be described as [226]:

$$E_R = 3kTv_c \qquad (7.1)$$

where k is Boltzmann's constant, T is the temperature corresponding to the DMA rubbery modulus, and v_c is the crosslink density. As shown in **Figures 7.2a**, **c** and **e**, the incorporation of the nano-fillers increases the modulus of the nanocomposites. For instance, the storage modulus is 1.2 MPa for the 3 wt.% CNF/PS, 1.9 MPa for the 3 wt.% MWNT/PS and 3.4 MPa for the 3 wt.% SWNT/PS. The SWNT/PS nanocomposite exhibits a larger E_R, 180% higher than that of the CNF/PS at the same weight percentage. Calculations of values of the v_c of all the nanocomposites were made and the results are plotted in **Figure 7.3** as a function of filler concentration.

The value of v_c consists of two parts, one due to chemical cross-linking (known as covalent bond) and one due to the physical cross-linking [226]. Since the chemical cross-linking points contributed by the curing agent are more or less the same for all the samples, the physical cross linking points are probably the dominant factor in changes to the storage modulus in the composites series. Physical cross-linking points can be generated by macromolecular chain knots, interfacial polar effects and hydro-bond. Normally, the physical cross linking points are considered weaker than covalent cross linking bond. However, in the nanocomposites, the larger areas of inorganic–organic interface offer many more positions for physical cross-linking points, which affects the material properties significantly [226]. The cross-linking rate in a macromolecular-nanofiller system is related to concentrations and surface properties of the nanofiller and degree of dispersion [226].

Figure 7.3 indicates that the values of v_c gradually increases with adding more fillers, and the SWNT/PS nanocomposite exhibits the highest values and rates of increase of the three concentrations, whereas v_c for the MWNT/PS nanocomposite shows a relatively linear increase with filler content. For the SWNT/PS samples, the smallest size and hence highest volume fraction (given the same weight fraction, as indicated in **Chapter 3**) increase the contact interfacial area between the nanofillers and the polymer matrix dramatically. The limited performance of the CNF/SMPS composites shown in **Figure 7.3**, is attributed to the aggregation of the CNFs dramatically reducing the effective dispersion volume [296] and load capacity [297], which significantly limit the inorganic-organic contact area and directly leads to the lowest values of v_c.

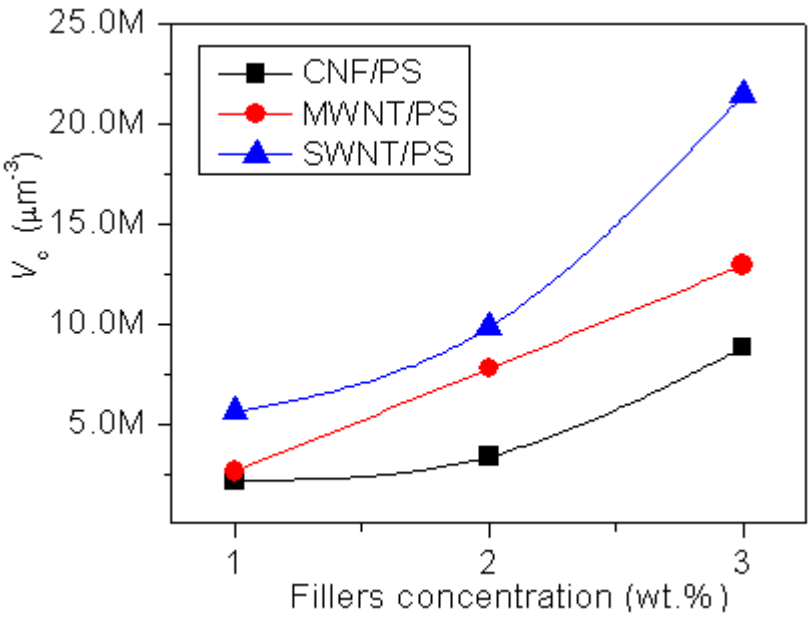

Figure 7.3 The calculation results of v_c as function of fillers concentration

7.2 Tensile testing results

Figures 7.4a-c present the typical stress-strain curves for all composites. The derived values of Young's modulus, maximum stress and strain of the specimens with different filler concentrations are shown in **Figures 7.4d-f**. The results indicate that the peak stress increases significantly with increasing nanofiller content, whereas the maximum strain decreases significantly. The SWNT/PS nanocomposites show the best improvement in modulus and maximum strength, and Young's modulus reaching nearly 800 MPa and the peak stress reaching 15 MPa when the SWNT concentration is 3 wt.%. However, the SWNT/PS nanocomposites also show the most rapid decrease in the

maximum strain, and the maximum strain is less than 20 % when the filler fraction is 2 wt.%. This shows that the toughness of the SWNT/PS is relatively poor. Compared with the SWNT/PS, the CNF and MWNT filled composites show moderate improvement of Young's modulus and the peak stress. As to the maximum strain, the MWNT/PS maintains a reasonable maximum strain of 50 % with increase in the filler fraction up to 3 wt.%.

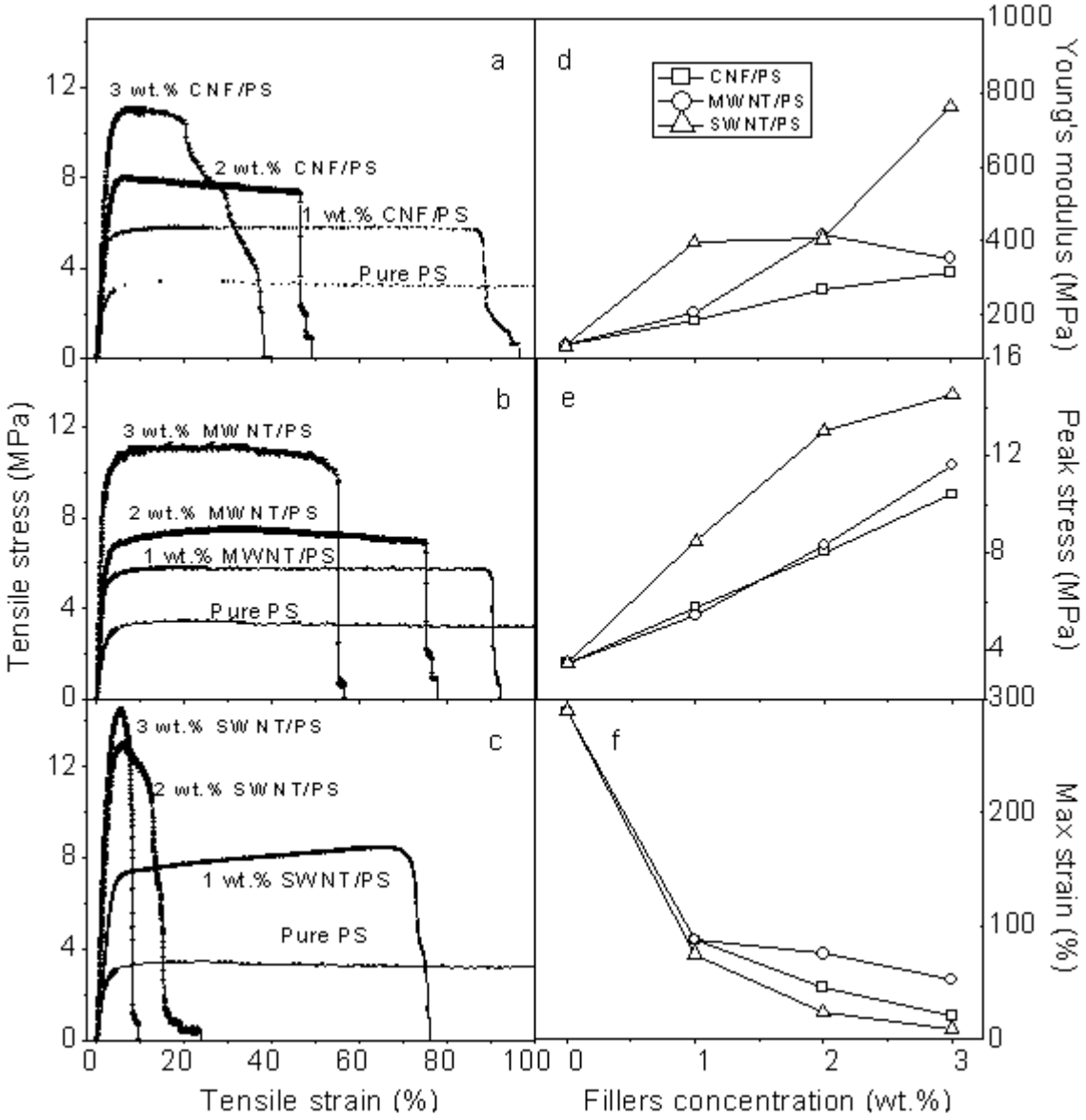

Figure 7.4 Uniaxial tensile results for CNF and CNTs filled composites: stress-strain curves for (a) CNF/PS composites, (b) MWNT/PS, (c) SWNT/PS; derived results as a function of filler concentration (d) Young's modulus, (e) peak stress and (f) maximum strain.

The cross section of samples after tensile testing was examined using SEM and images were shown in **Figure 7.5.** All the samples are very close to breaking, but not yet completely breaking. The PS fracture images in **Figure 7.5a** display a typical viscoelastic failure with polymer threads bridging a micro gap [298].

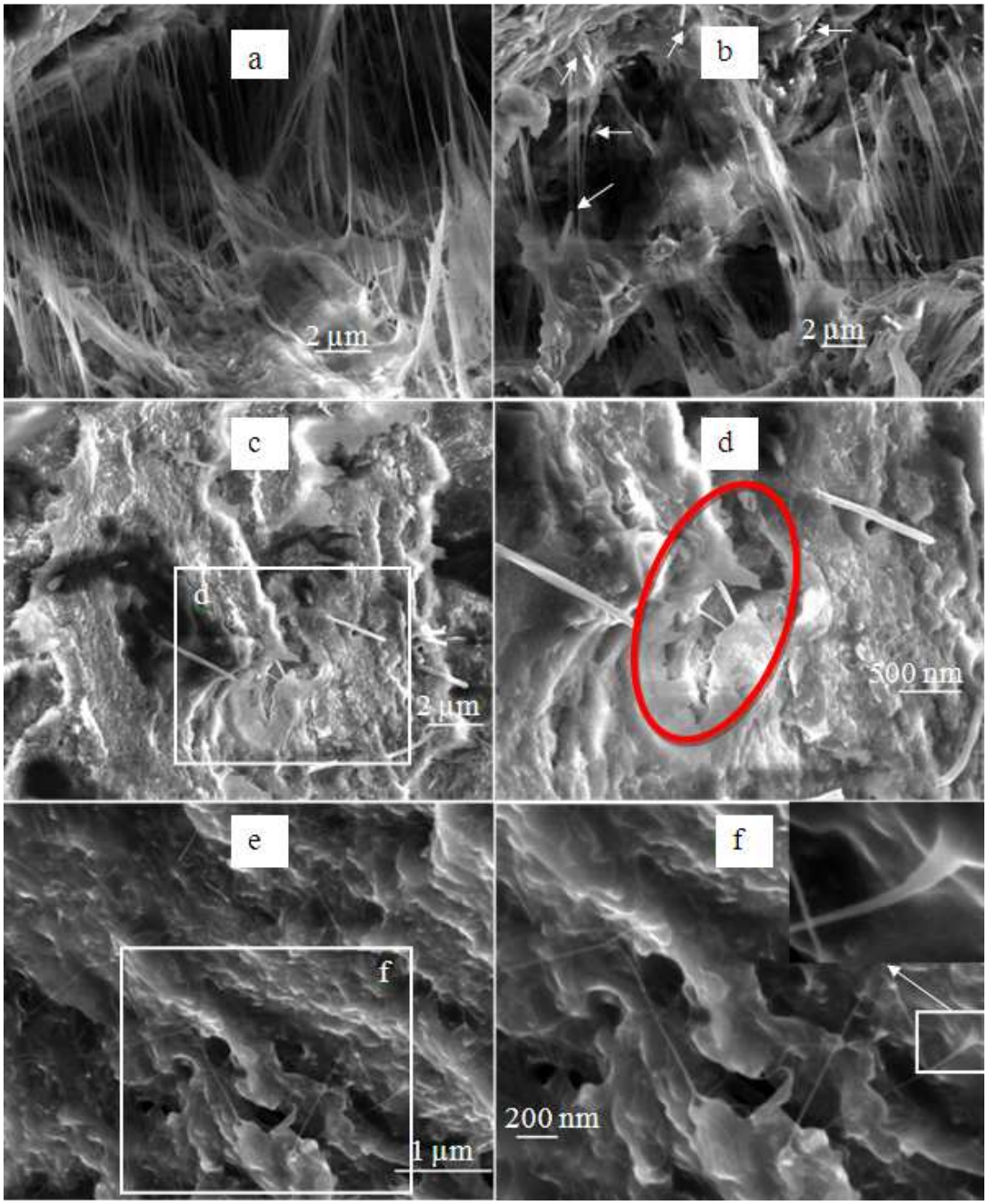

Figure 7.5 SEM images of cross-section for specimens almost broken revealing the material failure and filler effects, (a) Pure PS,(b) 2 wt.% CNF/PS,(c) 2 wt.% MWNT/PS, (d) The magnified image of selected area in (c), (e) 2 wt.% SWNT/PS, (f) stretched SWNTs bridging the nano-scale crack.

For the CNF/PS nanocomposites shown in **Figure 7.5b**, some threads can be seen in cracks, and CNF rods can be traced clearly. At this deformation strain (close to the breaking point), the CNFs don't contribute much on preventing fracture, as most of them are still embedded inside polymer which has limited load bearing capacity. For the MWNT/PS nanocomposite, an indication of brittle/rigid breaking of polymer can be observed on its surface (**Figure 7.5c**), indicating that it has already fractured. MWNTs pulled out from the polymeric matrices are visible and it can be assumed that most parts of the MWNT effectively contribute to the load transfer from matrix when cracks form. This assumption is confirmed by the higher magnification image shown in **Figure 7.5c**, which shows that two MWNTs bridging the micro-crack. For the SWNT/PS sample, the SEM images shown in **Figures 7.5e-f** reveal that the SWNT coil are fully extended to straight rods (**Figures 7.1e-f**). This clearly indicates that the stretching SWNTs strongly enhance the fracture resistance of the polymer. Moreover, the stretched SWNT rods are oriented along the best direction to prevent the crack growth. In **Figure 7.5f**, the inset image shows the end of a pulled-out SWNT. Clearly the SWNT was well bonded to the polymer, and has been pulled out from the polymer matrix, showing an effective contribution of the SWNTs in preventing the fracture failure of the polymer.

Many articles have reported the prediction and measurement of rod like fibre enhancement of polymeric substrates during tensile testing [299-301]. The flexibility and higher modulus of SWNTs will ensure that they have better performance on enhancing and toughening the polymers. The enhancement has been verified with partly of the stretching of coiled SWNTs.

7.3 Nano-indentation results

Figure 7.6 shows typical load-displacement curves of the pure PS and nanocomposites with 1 wt.% CNFs and CNTs obtained from the nanoindentation tests. Considering the radius of curvature of about 150 nm for the Berkovich tip, relatively smooth curves were obtained which would indicate there is no significant porosity or filler aggregation in the sample area tested [302]. The load-displacement curves for the CNT/PS sample show higher slopes (dP/dh) in the loading regime and lower h_{max} than those for the PS and CNF/PS, which indicates that the CNTs offer better mechanical enhancement of the soft polymer matrix than the CNFs do. The curve from the SWNT/PS displays the best

micro-mechanical enhancement as the smallest penetration depth was obtained with equivalent operational conditions. This could be explained by the fact that the SWNT has a much smaller diameter, larger surface area and volume fraction, offering superior load transfer and an effective enhancement in mechanical properties. From **Figure 7.6**, the dissipation energy can be calculated, and a simple comparison shows that the area beneath the CNT/PS curve is less than those of the pure PS and the CNF/PS.

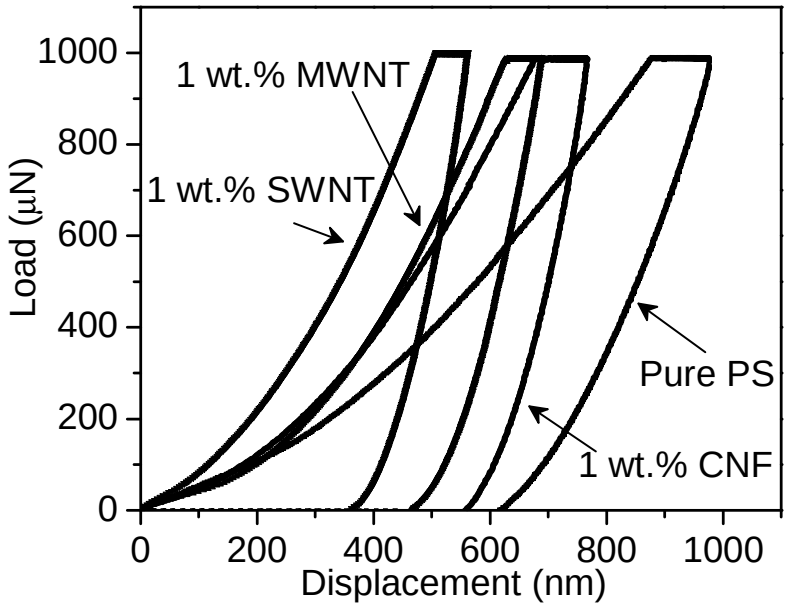

Figure 7.6 Representative load-displacement curves of samples with a peak load of 1 mN

Figures 7.7 and **7.8** summarise the calculated elastic modulus and hardness values for all the composites with the different concentrations of carbon filler as functions of load and holding time. The results shown in **Figure 7.7** indicate that the composites show improved micromechanical properties, either as elastic modulus or hardness. The indentation size effect is also clearly visible as both the hardness and modulus values decrease with increasing indentation load (or indentation depth), before reaching a plateau value. In order to avoid this ISE effect on modulus and hardness values, the data at the plateau stage were used for comparing. The nanoindentation results demonstrate that the enhancement is significantly dependent on nanofiller content as well as the specific filler type. As shown in **Figure 7.7**, the peak values for the CNF/PS and SWNT/PS samples were at about 2 wt.%. Meanwhile, the MWNT/PS sample achieve a maximum value at 1 wt.%, then shows a decrease in both the elastic modulus and hardness values. The sample with 2 wt.% SWNT/PS has a modulus of 4 GPa and hardness of 280 MPa, exhibiting the maximum reinforcement of all the specimens.

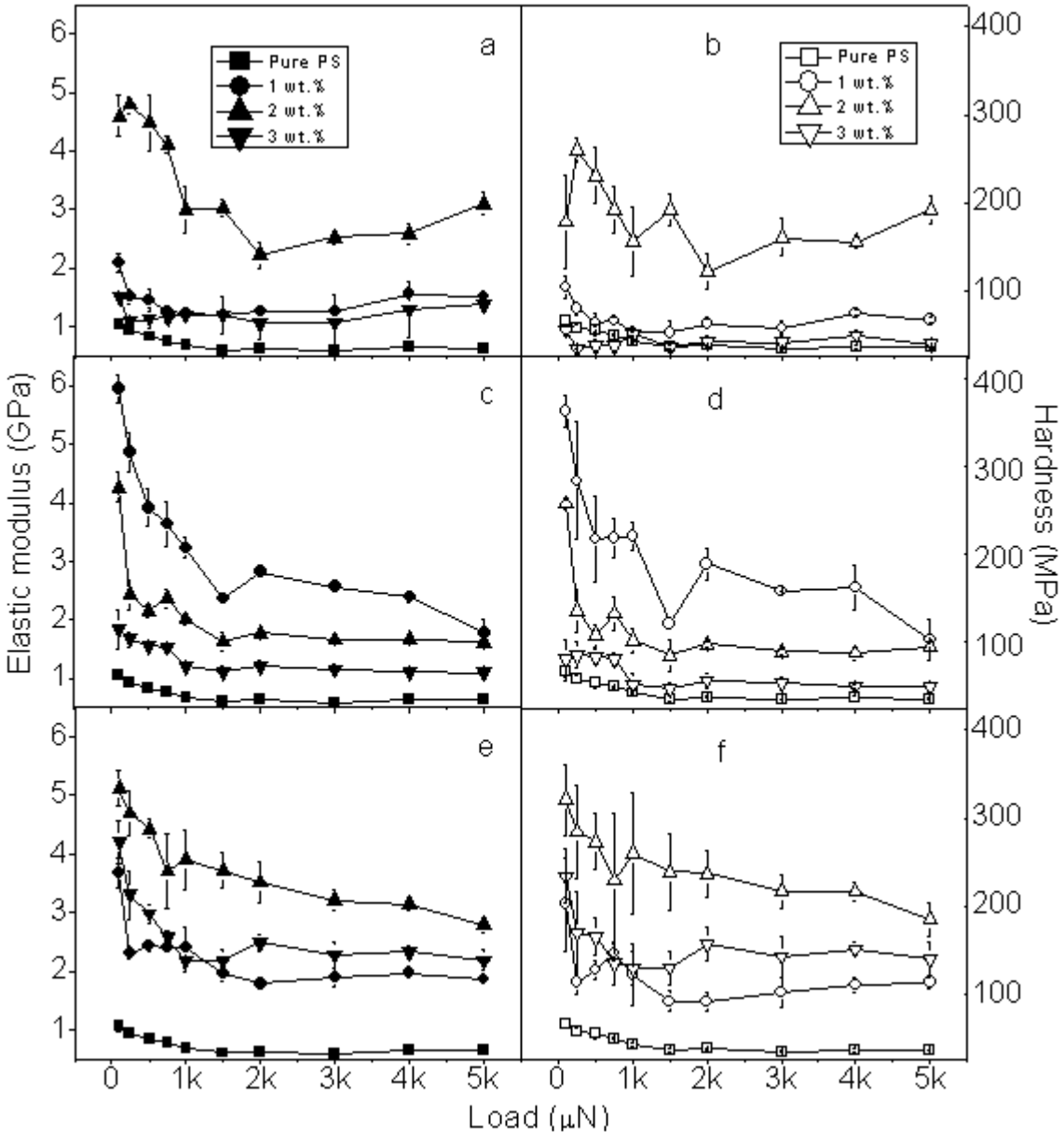

Figure 7.7 Elastic modulus and hardness results from nanoindentation tests as a function of maximum load: (a) elastic modulus and (b) hardness of PS and CNF/PS; (c) elastic modulus and (d) hardness of MWNT/PS; (e) elastic modulus and (f) hardness of SWNT/PS.

The 2 wt.% SWNT/PS sample was the most consistent strength as the modulus remains at 2.5 GPa even at the filler concentrations up to 3 wt.%, which is more than four times of that of pure PS. The values were scattered as the filler concentration is varied, as shown in the error bars. It should be noted that there is a sharp decrease in the modulus when the filler content increases from 2% to 3 wt.%, the value at 3 wt% being even lower than 1 wt.% with a large error range. This can be explained by the non-uniformity of the material and significant loss of efficiency by the aggregation of fibres as indicated in the SEM image shown in **Figure 7.1**. As explained before, the elastic modulus measured from the nanoindentation tests is much higher than that from the tensile tests.

This is because the testing methods are different, i.e. tension VS compression. Tensile tests should be more meaningful in comparing the mechanical properties, as most applications of composites involve tensile loading. The nanoindentation modulus are normally higher than those from the tensile tests, as these materials appear stronger in compression than that in tension since the interfacial peeling force are less prominent. Meanwhile, for most applications in MEMS and biomedical fields, there is a need to study functional properties of thin-films or structures in one dimension or at sub-micrometre scale. In those cases, nanoindentation was a role in measuring mechanical properties.

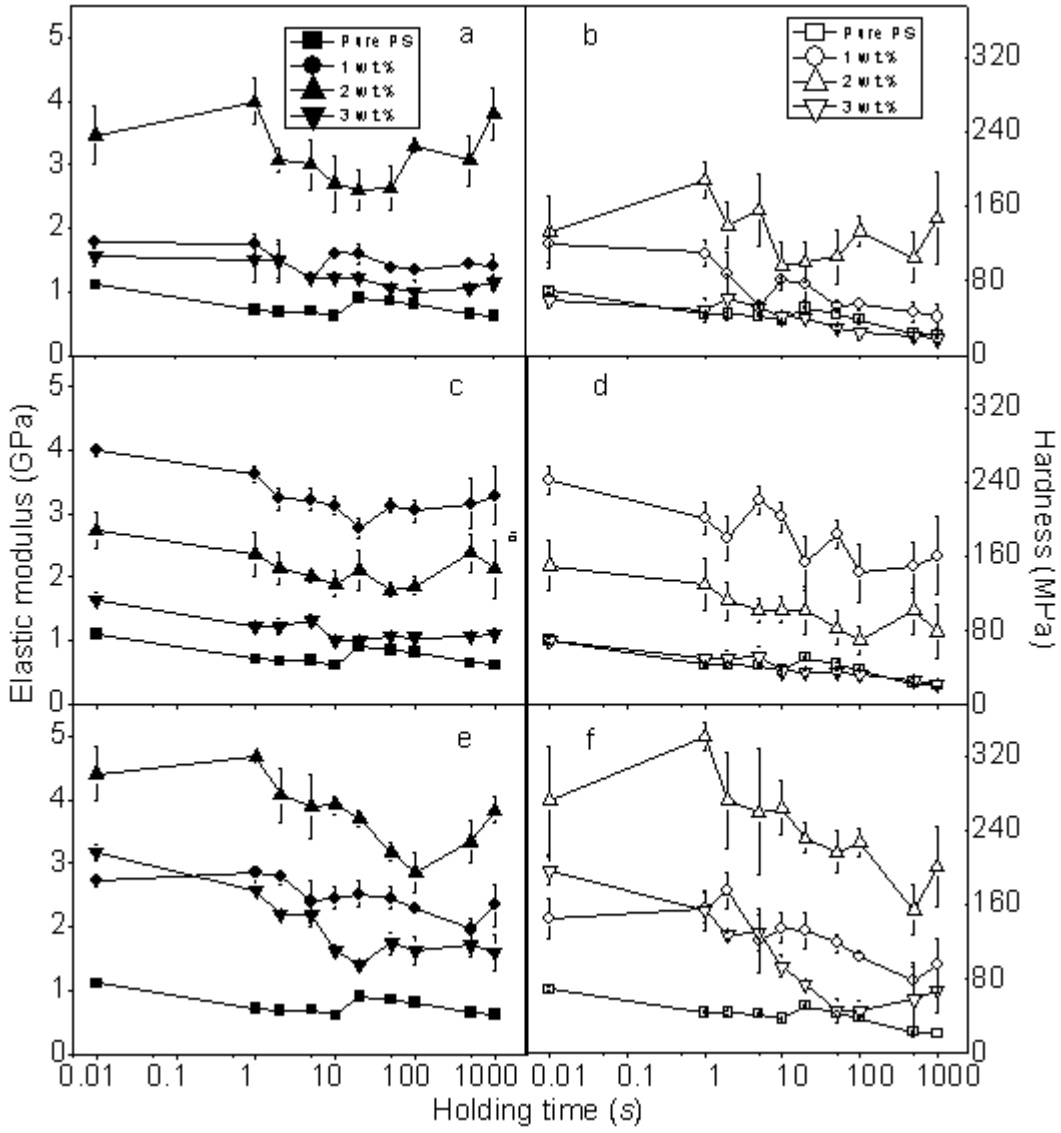

Figure 7.8 Elastic modulus and hardness results from nanoindentation tests as function of holding time: (a) elastic modulus and (b) hardness of PS and CNF/PS; (c) elastic modulus and (d) hardness of MWNT/PS composites; (e) elastic modulus and (f) hardness of SWNT/PS composites

The creep resistance of the nanocomposites was assessed by increasing the holding time at the maximum load during indentation, and the results are summarized in **Figure 7.8**. For the pure PS, both the modulus and hardness values gradually decrease, which is due to the creep of the soft molecular chains. For the composites, a decreasing trend can be observed in **Figure 7.8**, which is highly dependent on the nanocomposite composition and interface conditions. The significant decrease in modulus at higher loads for the composites can be explained by complete or partial breaking of the physical cross-link points between the inorganic-organic interfaces at very large applied forces. As shown in **Figures 7.8a**, **b**, **e** and **f**, the curves with larger variations in the modulus/hardness are those with higher values of strength. The most significant change occurs for the 2 wt.% SWNT/PS nancomposite, which has the highest values of hardness and modulus. In principle, the CNF should have large variation, as the indenter might be located on, or partly on, a CNF fibre due to its large size. The data for the MWNT/PS composites shown in **Figures 7.8c** and **d** display a similar pattern to that of the pure PS, and show more stable values than those of the CNF/PS. This could be explained by a better distribution of MWNT inside the PS substrate than that of the CNF. The SWNT/PS composites in **Figures 7.8e** and **f** show very large variation which can be explained as illustrated in **Figure 7.9**.

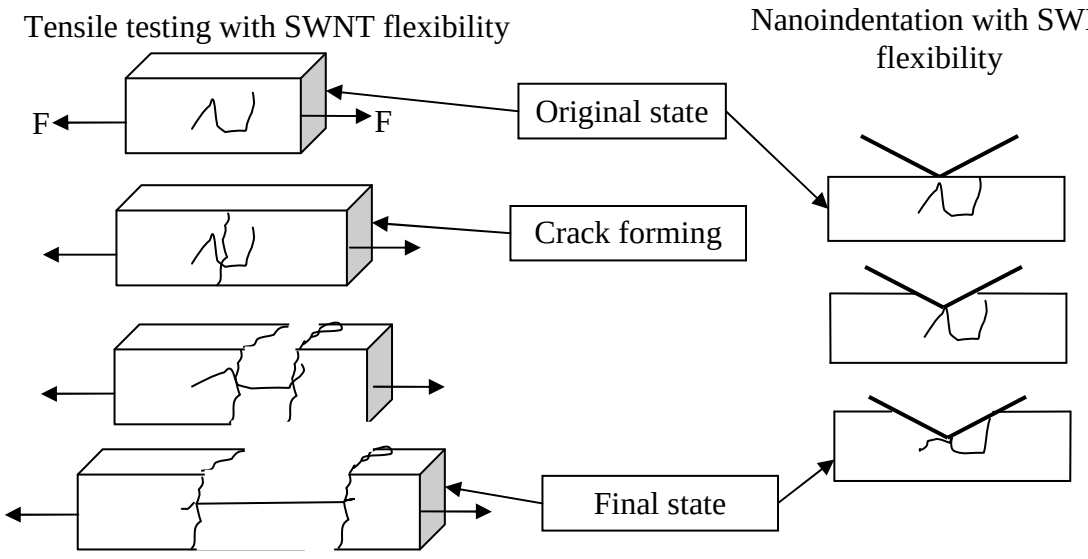

Figure 7.9 Schematic of SWNT behaviours in tension and indentation. The SWNT cords carry the load directly as the cracks reach them in the tensile test, while they can change the conformation with the first touch of the indenter tip leading to a load transfer.

The coiled CNTs in the PS matrix show a complicated performance under indentation, and its deformation can be accommodated by the polymer although the load might not be easily transferred to the individual CNTs. This is quite different to the situation in tensile testing when cracking has started, where the CNTs can provide bridging effect at the fracture surface as shown in **Figure 7.9**. **Figure 7.10** shows the calculated values of the dissipation energy (DE) and dissipation energy ratio (dissipation energy/total energy) for all the samples at different loads. The DE of the pure PS shows the highest value in all the DE charts as a function of load, which is due to the soft nature of the polymer.

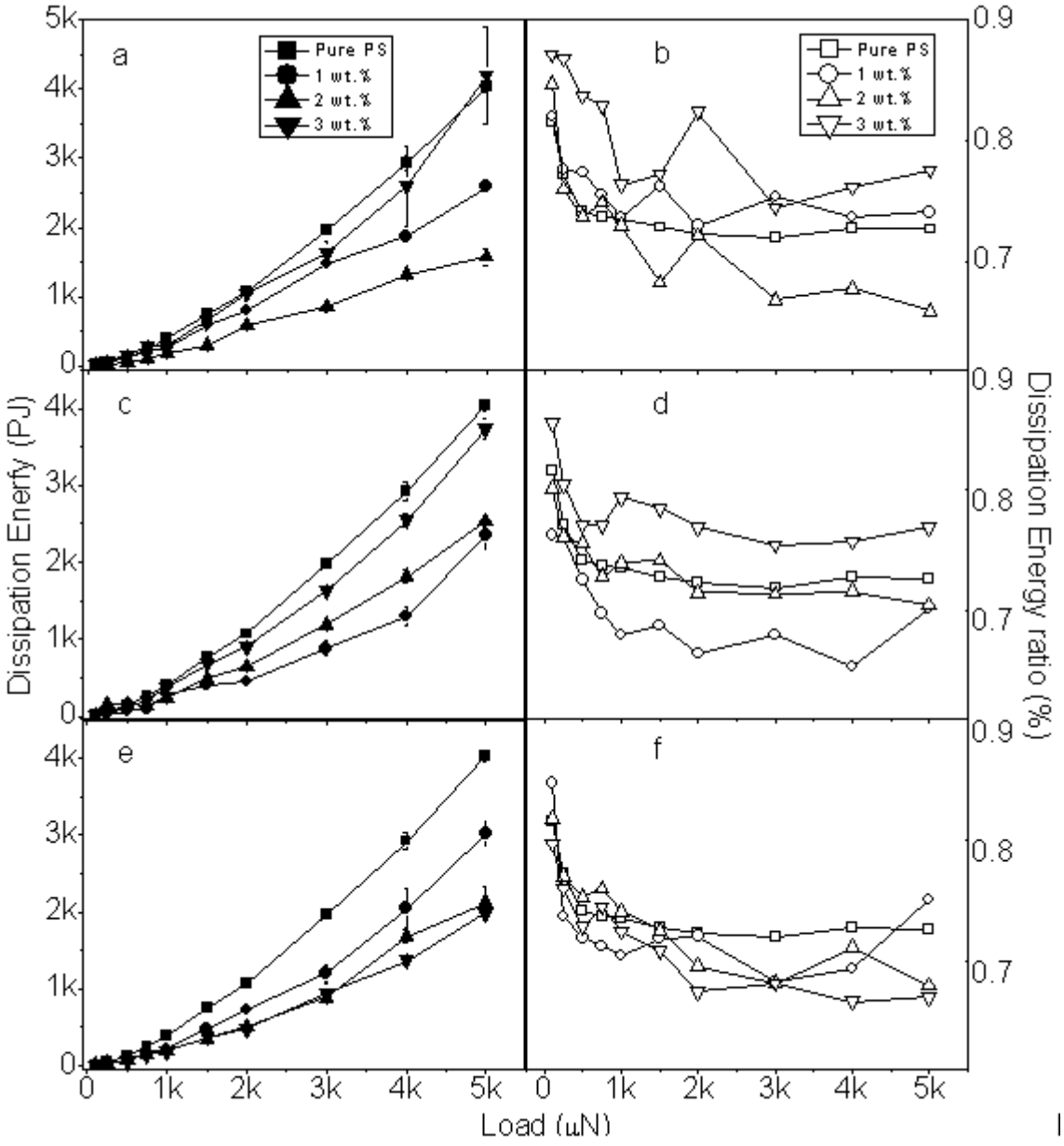

Figure 7.10 Energy analysis on the nanoindentation process as a function of maximum applied load: (a) Dissipation energy and (b) Dissipation energy ratio of PS and CNF/PS; (c) Dissipation energy and (d) Dissipation energy ratio of MWNT/PS composites; (e) Dissipation energy and (f) Dissipation energy ratio of SWNT/PS composites

For all the samples, as load increases, the DE results achieve to increase as the displacement increases. Meanwhile, the DE trends indicate some relationship to the elastic modulus as the DE decreases (corresponding to an increase in modulus). This can easily be understood because the material becomes stronger to resist the external force. The higher DE values in the lower load region might be caused by ISE as the calculation of DE ratio needs to consider the residual depth, which was not considered in the analysis. The DE ratio shows a decrease in the initial loading (< 1 mN) and then reaches a plateau when the applied load is above 1 mN, as shown in **Figures 7.10b**, **d** and **f**. Concerning the average value above 1 mN in those charts, the changes of the DE ratio show similar trends with modulus and hardness to those in **Figure 7.7**. Compared with the other two composites, the SWNT/PS presents stable and low DE values and DE ratios even when the filler concentration is as high as 3 wt.%, where the DE and DE ratios of CNF/PS and MWNT/PS are lower than those at 2 wt%. The results show that the SWNT/PS has the largest effect in strengthing the polymer.

The validation of the DE value and DE ratio as a function of holding time is shown in **Figure 7.11**. Both the DE and DE ratio increase with holding time. The composites show smaller values of DE than those of the pure PS, indicating a better performance of the nanocomposite to resist external forces. There are two different slopes for modulus against holding time for the pure PS as illustrated in **Figure 7.11a**, and the knee is at around 5 s. Pure PS has hard segments and soft segments, and theoretically, when the holding time is short, the load or stress is mainly applied to the soft segments which is manifest as a low DE. As the holding time increases, the molecular chains and structures extend under the applied force. Moreover, temporary alignment of nanoparticles, small area aggregation and partial breaking of the physical cross linking points in the composite system could lead to a significant increase in the DE and DE ratio.

The DE ratios in **Figures 7.11b**, **d** and **f** reveal a similarly ascending trend with holding time to those of the DE results. The DE ratios reach a stable region when the holding time is longer than 10 seconds for all the samples. The trend of changing DE ratio with holding time is similar to those for hardness/modulus in **Figure 7.8**, which implies that the DE ratio is related to the enhancement effect, which might need more work to verify. The SWNT/PS also exhibits the most stable and low DE/DE ratio of all samples as indicated in **Figures 7.8e-f**.

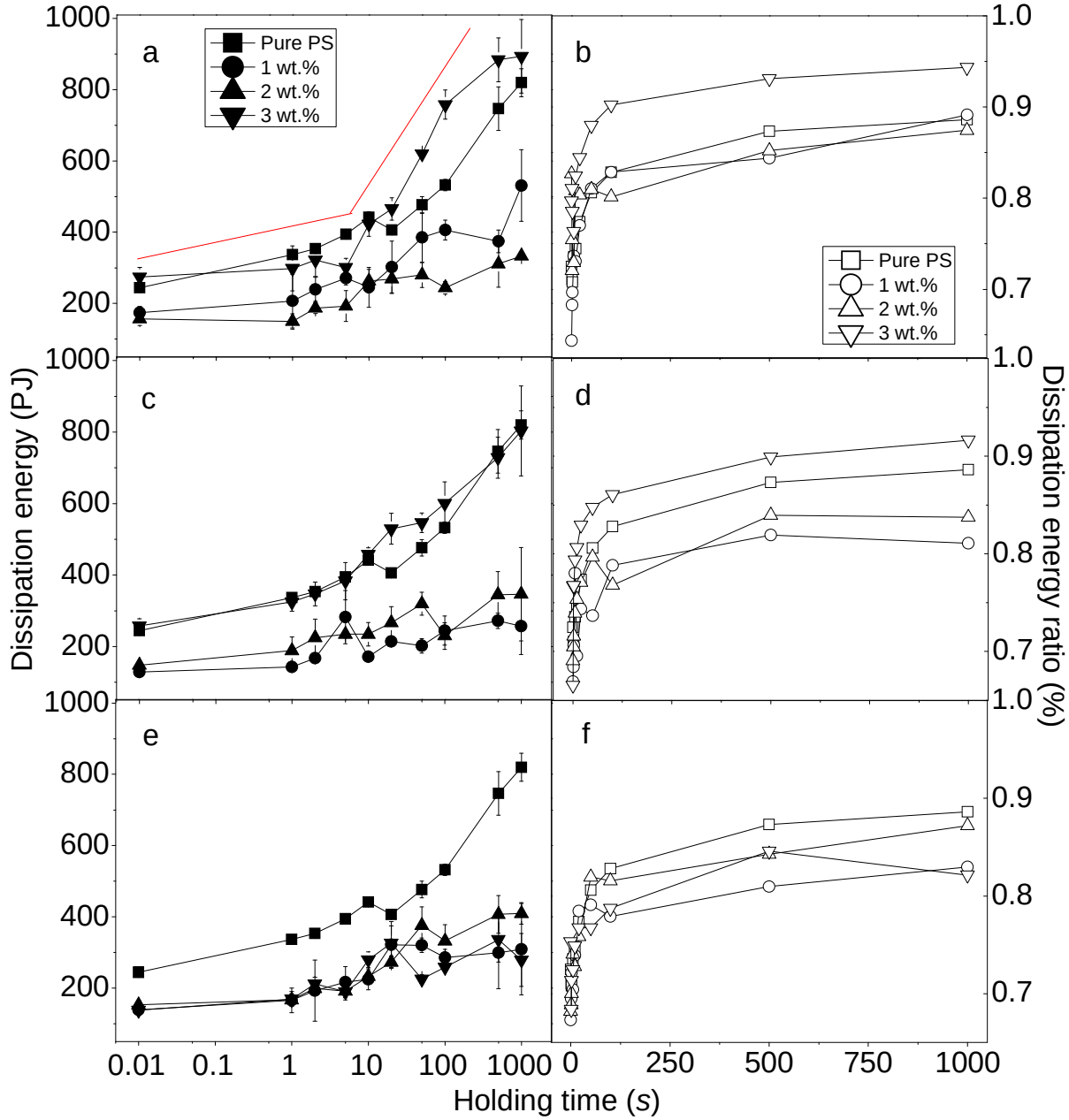

Figure 7.11 Energy analysis of the nanoindentation process as a function of holding time at maximum load: (a) Dissipation energy and (b) Dissipation energy ratio of PS and CNF/PS; (c) Dissipation energy and (d) Dissipation energy ratio of MWNT/PS composites; (e) Dissipation energy and (f) Dissipation energy ratio of SWNT/PS composites

The results for the DE and DE ratio with holding time are useful as they reveal the viscoelastic properties of the material as influenced by the hard segment (plastic) to soft segment (elastic) composition. Analysis on the DE and DE ratio with changing holding time can reveal the dynamic energy absorption of materials under external applied force.

Results for the DE as a function of loading rate are shown in **Figure 7.12**. The DE values for the pure PS have been discussed in **Chapter 6**.

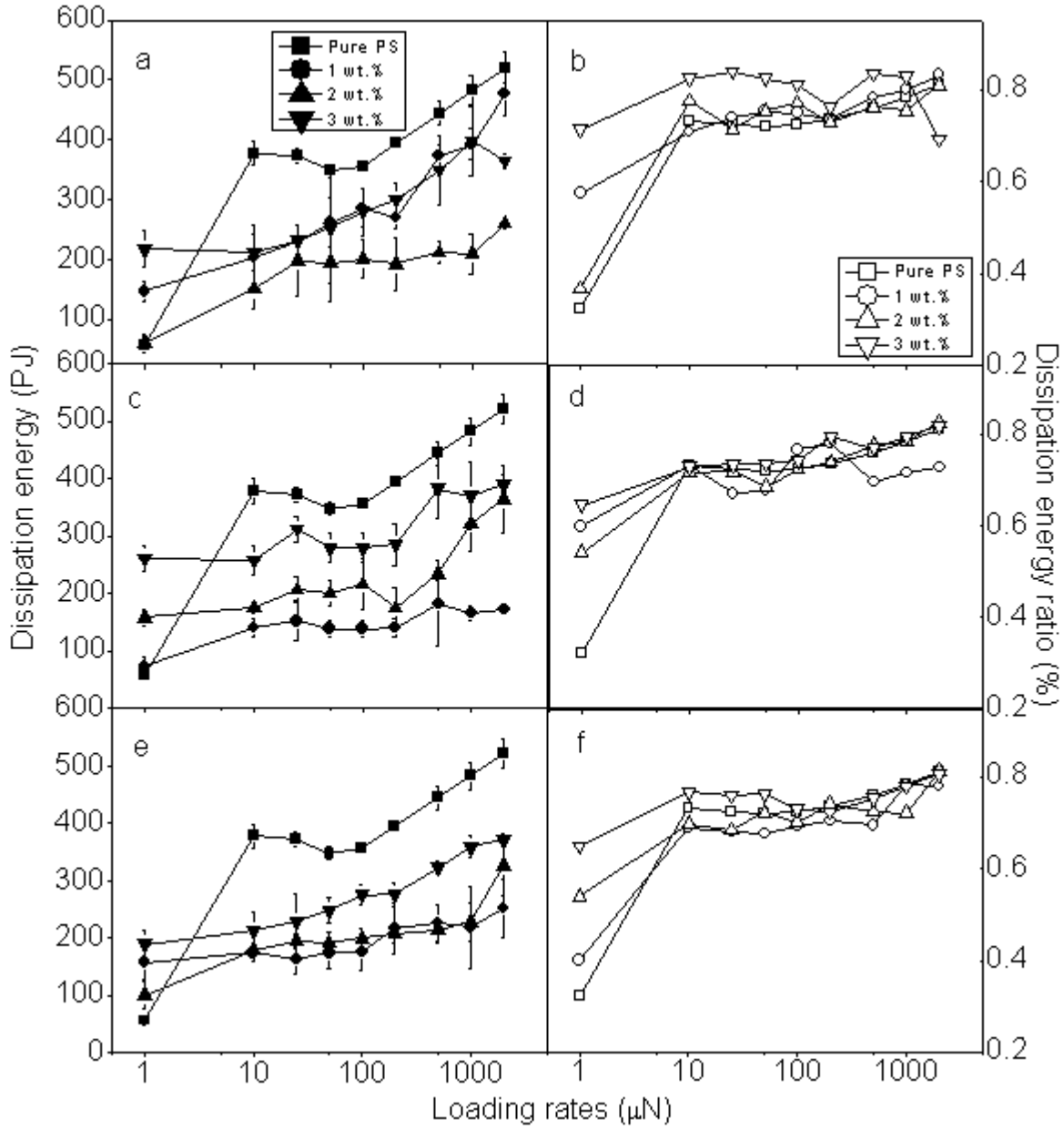

Figure 7.12 Energy analysis of the nanoindentation process as a function of loading rate: (a) Dissipation energy and (b) Dissipation energy ratio of PS and CNF/PS; (c) Dissipation energy and (d) Dissipation energy ratio of MWNT/PS composites; (e) Dissipation energy and (f) Dissipation energy ratio of SWNT/PS composites

For the composites, a similar trend can be seen, in that the DE values increase with loading rate, for example, an increase of 200%-350% for the CNF/PS with increase of the loading rates is shown in **Figure 7.12a**. For the MWNT/PS and SWNT/PS, its loading rate was a minor influence on the DE and DE ratio, and the increase of the DE is as little as 100%, however, for the SWNT/PS. The SWNT/PS samples behave more

stably with loading rate, and also show the lowest DE values compared with the other nanofillers. For the DE ratios shown in **Figures 7.12b**, **d** and **f**, the results indicate a similar trend when the loading rate is higher than 10 μN/s. A narrow range of 0.7-0.8 for the DE values was obtained for all the samples. However, the DE ratios at the lowest loading rate did vary which suggests the differences in the viscoelastic properties and energy capacity of elastic regions.

In summary, the analysis of the DE and DE ratio provide detailed information of the sample responses to the external forces under the imposed conditions. The DE values are affected dramatically by the applied load which increases the energy input. The addition of nanoparticles made the materials more able to resist the external force, and the relationship follows the same trend as that of the elastic modulus. The DE ratio reaches a plateau when the applied load is above 1 mN, in a similar way to the hardness value. The dependency of DE/DE ratio on the holding time/loading rates reveal the viscoelastic behaviour of the materials. The DE values indicate the viscous component of the matrix, and DE ratios fall in the range of 0.7-0.9, which is considered as an indication of the viscous/elastic ratio.

7.4. AFM profiling

The AFM was employed to identify the morphologies of the nano-indentations and deformed surfaces of the samples. **Figure 7.13** shows AFM images of the pure PS and nanocomposites with 1 wt.% carbon nanofillers after nanoindentation. A smaller indentation mark was observed for the nanocomposite samples compared with that of the pure PS, and the SWNT/PS nanocomposite presents the smallest permanent depth of all three samples. 3-D AFM images are also shown in **Figure 7.13**, which clearly reveal the pile-up at the edges of the indentation mark on the nanocomposite surfaces, whereas pile up was not observed on the pure PS sample. For indentation deformation of elastic–plastic materials, there are two typical phenomena, pile-up and sink-in, both of which can affect the indentation results dramatically.

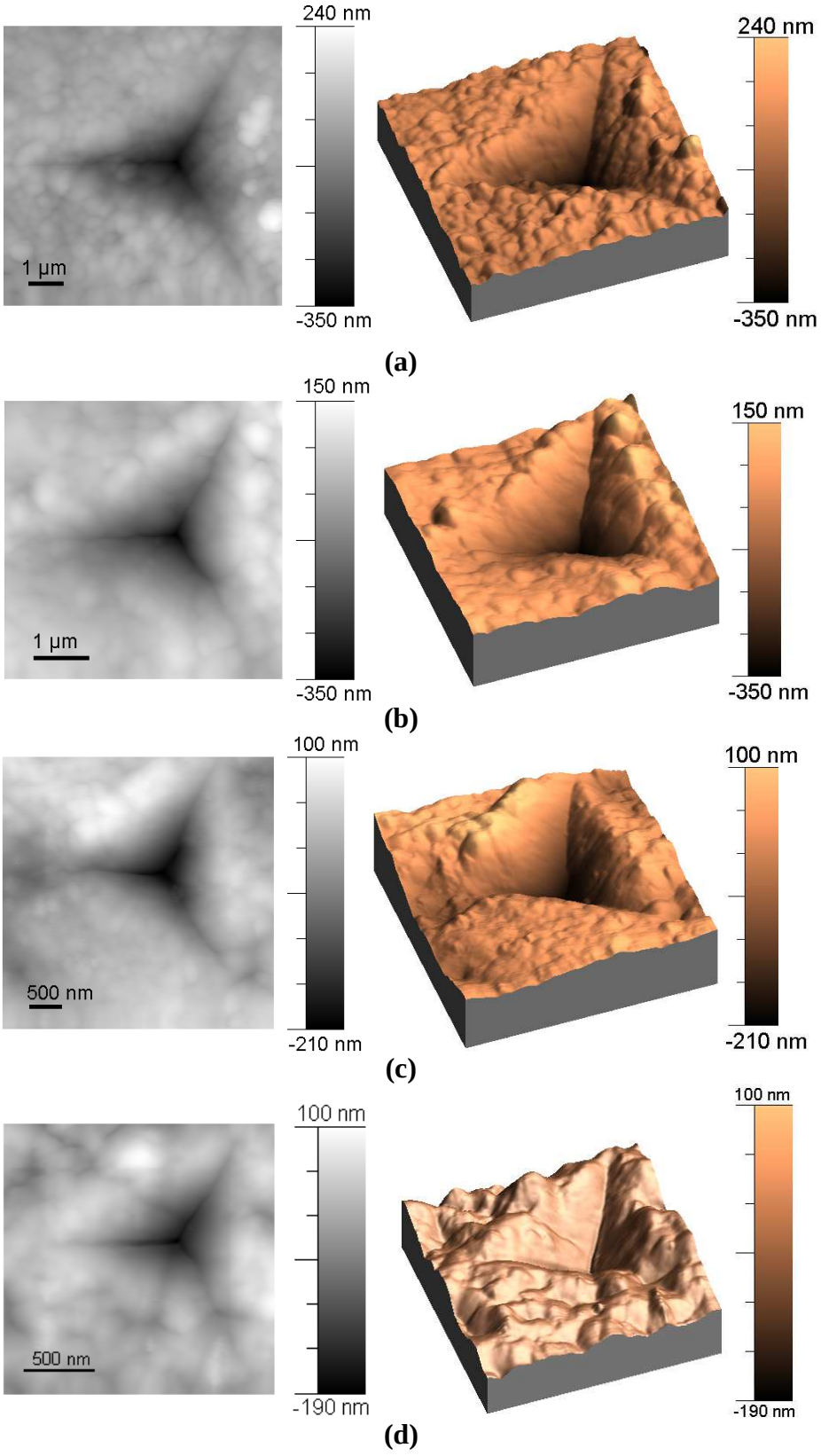

Figure 7.13 2D and 3D AFM surface deformation morphologies with nanoindentation marks: (a) pure PS, (b) 1 wt.% CNF/PS,(c) 1 wt.% MWNT/PS,(d) 1 wt.% SWNT/PS

The effect normally depends on the mechanical properties, namely the elastic modulus, yield stress and strain-hardening exponent of the materials [303,304]. The strain-hardening

exponent or the plastic ratio of the pure polymer is normally too small to show an apparent pile-up. Similar experimental work has been previously carried out based on the nanoindentaion of polymer substrates [305,306,307]. Two key parameters derived from the nanoindentation results are normally used to discuss the pile-up or sink-in effects on indentation modulus and hardness [305,306]. The first one is the threshold value of E/σ_Y = 90 [305] which determines the material deformation [306,307]. The materials will pile-up after indentation if the E/σ_Y ratio is greater than this critical value, otherwise, materials will show 'sink-in' after indentation. Above the critical E/σ_Y ratio, the pile-up effect is dependent on the strain-hardening exponent and the significance of pile-up is considered to increase as E/σ_Y increases [224,306]. For nanoindentation of polymer based composites with a Berkovich tip, corrected equations for the yield strength σ_Y and pile-up effect are [224,308,309]:

$$\sigma_Y = 0.25 P_{\max} c^{-2} \tag{7.2}$$

$$\ln\left(\frac{h_e}{h_{\max}}\right) = -b \ln\left(\frac{E}{\sigma_Y}\right) + a \tag{7.3}$$

$$h_e = h_{\max} - h_p \tag{7.4}$$

where c is the plastic zone size as seen in **Figure 7.14b**, a and b are constants related to the strain-hardening exponent, and h_e is the elastic recovery depth.

A second widely used parameter is the $h_p/h_{\max}$ ratio, which is a convenient and experimentally measurable quantity for identifying the expected indentation behaviour of a given material [306]. The $h_p/h_{\max}$ ratio is related to the work-hardening during nanoindentation by a Berkovich tip. Oliver and Pharr [224] showed that significant pile-up was detected when $h_p/h_{\max}$ is close to 1, and also suggested that pile-up is not significant if the $h_p/h_{\max}$ ratio is below 0.7 which is expected to be a constant regardless of penetration depth. They also suggested that it is impossible to predict if work-hardening of a material is based solely on the load–displacement data from an experimental point of view [224]. Therefore, in an indentation experiment, care must be taken when $h_p/h_{\max} > 0.7$, as the use of $h_p/h_{\max}$ can lead to large errors in the contact area. On the other hand, when the pile-up is small (i.e. $h_p/h_{\max} < 0.7$), as suggested by other researcher [224], the contact area given by the method ($h_p/h_{\max}$) matches very well with the true contact area obtained from finite element analyses, independent of the work-hardening characteristics.

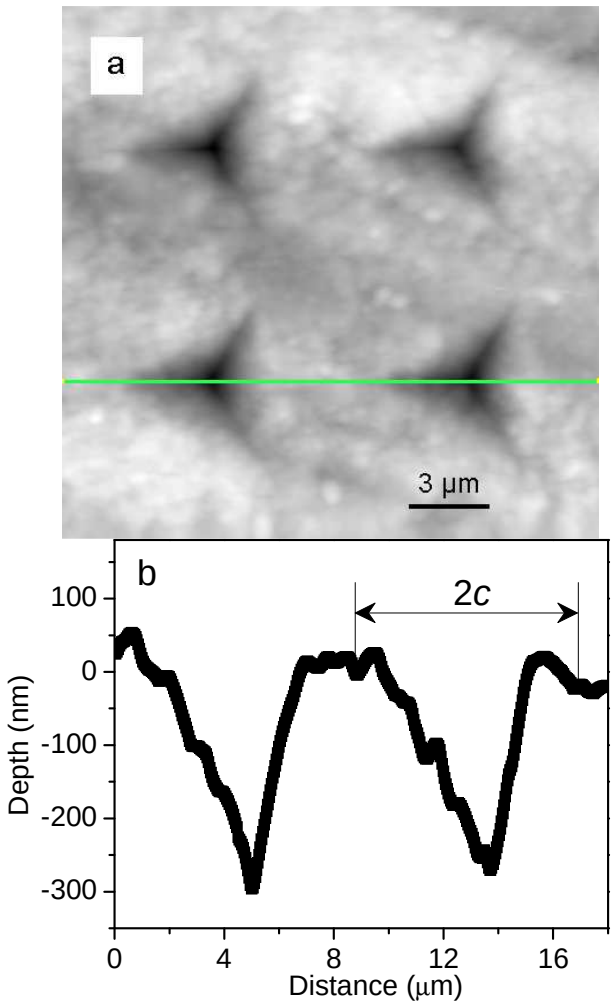

Figure 7.14 (a) AFM topographical image of a 2 × 2 array of indents created on a SMPS surface at a load of 2 mN, (b) Surface profile of two indents along the line drawn in the topographical image shown in (a) with the plastic deformation zone on one of the indents.

Figure 7.15a statistically summarises the calculated E/σ_Y values under different indentation loads for all the samples. A highly uniform distribution of E/σ_Y results is observed and only a few data points are out of the threshold range. The points beyond the range are the 2 wt.% CNF/PS composites under 100 µN, and 3 wt.% CNF/PS under 5 mN. Meanwhile, the h_p/h_{max} ratio results (in **Figure 7.15b**) showed that the pile-up effect does not affect most of the nanoindentation results, because the calculated results are in the range below 0.7 [224]. The h_p/h_{max} of 3 wt.% CNF/PS composites at all loads are close to or beyound the boundary (h_p/h_{max}=0.7), as are the 2 wt.% CNF/PS composites under 100 µN. Similar results are seen in **Figures 7.16a** and **c**, where the analysis was carried out on the E/σ_Y values with variation both of the holding time and loading rate. Investigation of the h_p/h_{max} values versus h_c indicates a similarity of the calculated data as all of these data fall in range of 0.5, which implies that the pile-up

effect would not affect validation of the modulus and hardness in nanoindentation measurement [224].

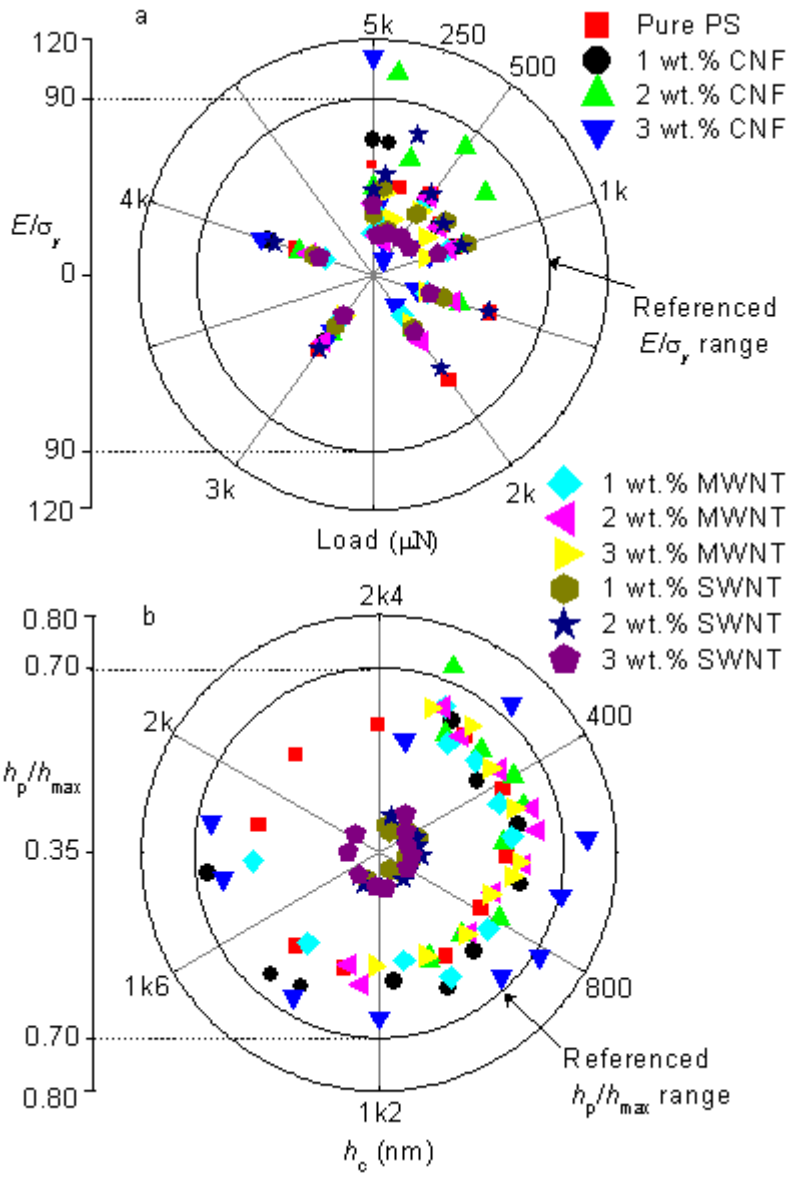

Figure 7.15 Statistical diagrams of the calculated results distribution with various maximum loads: (a) E/σ_y versus load, (b) h_p/h_{max} as a function of h_c

In summary, the analysis of the values of E/σ_Y and h_p/h_{max} from both the nanoindentation and AFM results show that nearly all of the results fall within the reference region (marked in **Figures 7.15** and **7.16**). Considering the microstructural analysis results from SEM and DMTA, the high h_p/h_{max} ratio for the 3 wt.% CNF/PS can be explained by the increase in local CNF alignment as indicated in **Section 7.1**, which could act as work hardening components and the failure of the knots during nanoindentation when higher content of CNF filler was used. The anomalous results for 2 wt.% CNF/PS composites could be due to tip self-similarity under low load [303].

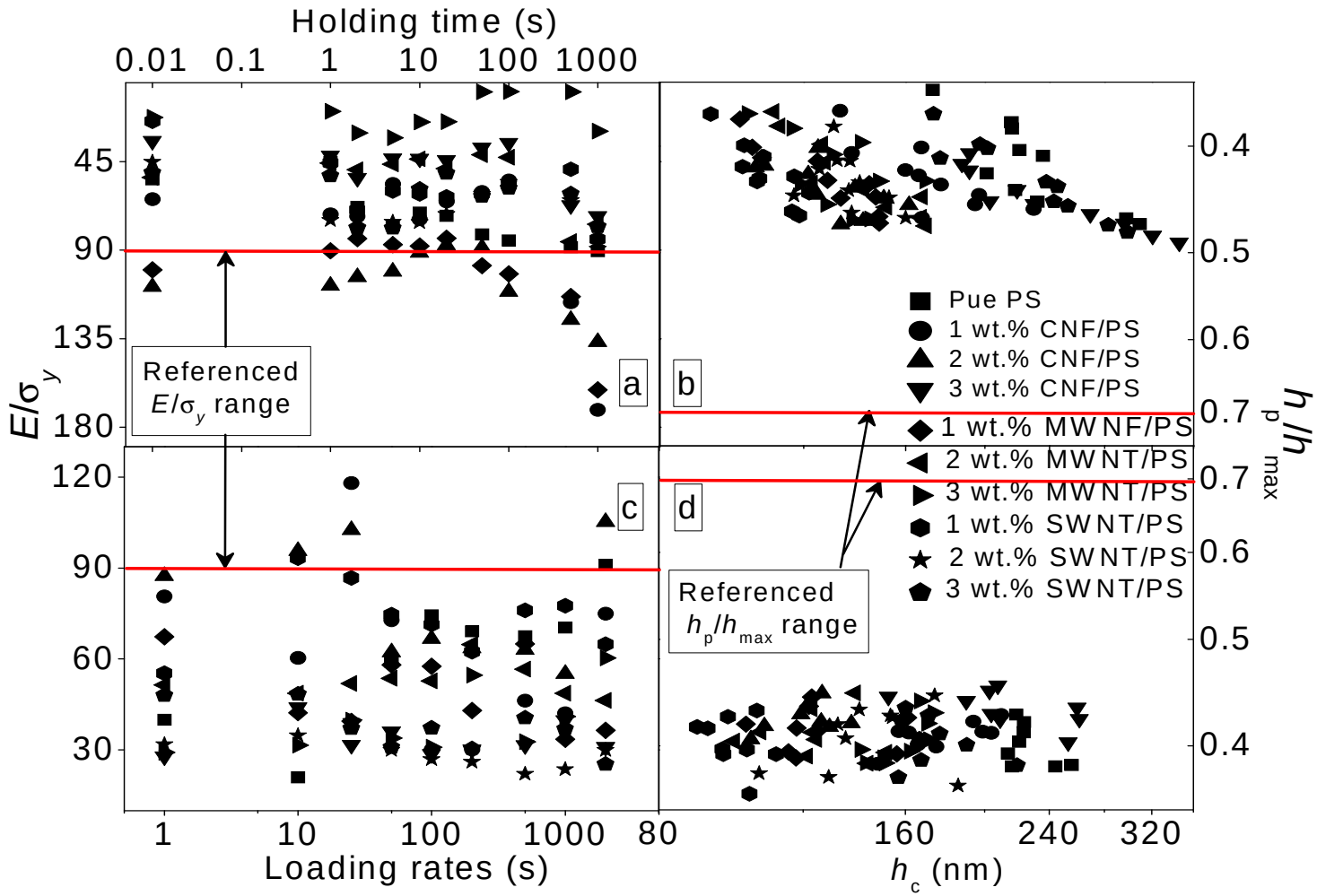

Figure 7.16 Statistical analysis of the calculated result distribution of: (a) E/σ_y versus load under controlling of holding time, (b) h_p/h_{max} as a function of h_c under controlling of holding time, (c) E/σ_y versus load with different loading rates, (d) h_p/h_{max} as a function of h_c with different loading rates.

7.5 Conductivity and the percolation threshold

Figure 7.17 displays the measured conductivity *versus* concentration for the nano-carbon fillers at room temperature. Reasonable improvements in conductivity are exhibited by all the samples, and the conductivity dramatically increases from 1×10^{-10} to 10^{-2} S/cm when the filler content is increased from 0.5 wt.% to around 5 wt.%.

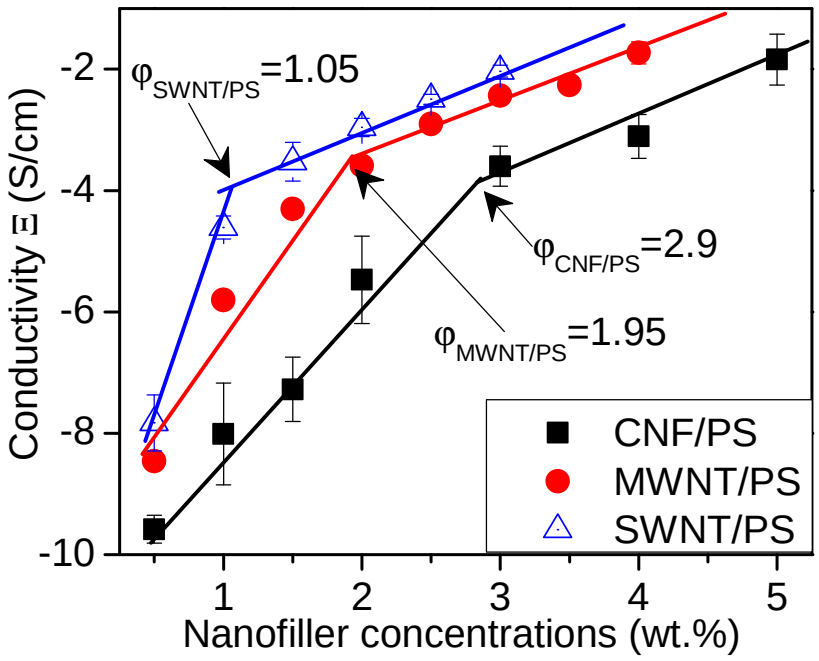

Figure 7.17 Conductivity results for nanocomposites as a function of nano-carbon filler concentration; the linear curve fitting determines the percolation threshold values for the composite samples.

The dependent of a percolation network is observed for each curve as discussed in **Chapter 6**. The results indicate that the ranking for the increase in conductivity is as follows: SWNT/PS>MWNT/PS>CNF/PS, which is very similar to the ranking for the mechanical enhancement. As previously addressed in **Chapter 6**, the two regions with different slopes in **Figure 7.17** correspond to an "insulating region" and a "conductive region". Linear fitting of the data in **Figure 7.17** reveals common threshold value for all composites, i.e. φ_{CNF} is 2.9 wt.%, φ_{MWNT} is 1.95 wt.% and φ_{SWNT} is 1.05 wt.%. This means that the SWNT shows the highest conductive enhancing capability with the lowest threshold value. One possible reason for this could be the good dispersion and higher volume fraction for the SWNT with the same weight concentration as seen in the SEM images, which facilitates for formation of conducting networks.

7.6 Thermal-mechanical properties

Figures 7.18a-d summarize the cyclic tensile curves for the pure PS, and the nanocomposites with 1 wt.% of CNF, MWNT, and SWNT, respectively. The values of yield/peak stresses decrease dramatically compared with those at room temperature which is due to the activation of molecular chains by the thermal stimulus. The initial strain for each curve increases with tensile cycle number (**Figures 7.18a-d**). This can be explained by: (1) random breaking of covalent cross linking bonds, (2) energy storage by the fillers [21], (3) a blocking effect by incorporated nanofillers [254].

Figures 7.18a-d also indicate that the pure polymer achieves the best repeatability of the stress-strain curves, whereas the nanocomposites have much larger variation in the yield/peak strength and strain. This can be explained by the physical cross linking points in the inorganic-organic interfaces breaking down as the composites are stretched. Those physical cross linking points [310,137], which are formed during fabrication, provide an enhancement of the matrix to supplement chemical cross-linking. There are various physical forces involved in this process, such as Van de Waals forces, hydrogen bonds, and electrostatic forces. However, these forces are weaker than the covalent chemical ones, and can be destroyed easily and never be restored during the tensile tests.

The recovery ratios for all the samples tested are summarized in **Figure 7.19**. The recovery rates of the pure PS are above 95% for all the cyclic tests. The CNF composites exhibit a rapid decrease in the recovery ratio as the nanofiller loading increases, with only 55% strain recovered in the 3 wt.% CNF/PS. This is probably due to microstructural failure, brought about by the brittle nature of the CNFs, as the interlocking bundled structure breaks down during cycling tensile loading leading to unrecovered strain and permanent defects in the microstructure. The MWNT nanocomposites perform better than the CNF ones, as their recovery rates are above 90% for concentrations of 1 wt.% and 2 wt.%, and at 3 wt.%, a recovery rate above 80% is maintained. The cyclic tensile tests identify that the MWNT/PS composites have better shape recovery than the CNF ones due to their better load transfer. Similar results, with high recovery rates, are exhibited by the SWNT/PS composites in **Figure 7.19c**. Rates above 80% were achieved after 4 cycles with good repeatability at different filler concentrations.

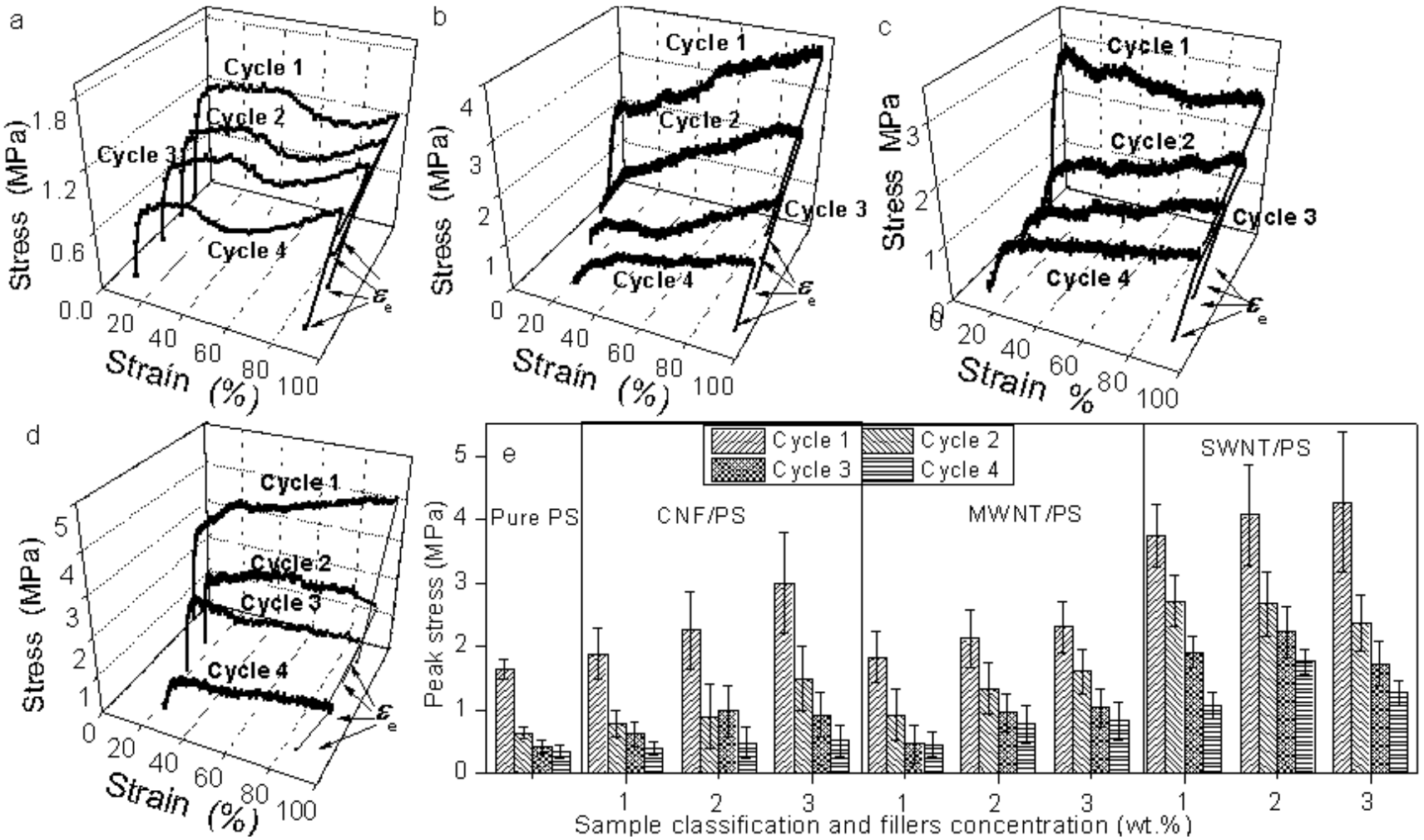

Figure 7.18 Thermal mechanical cyclic testing results: (a) PS; (b) 1 wt.% CNF/PS composites; (c) 1 wt.% MWNT/PS composites; (c) 1 wt.% SWNT/PS composites; (e) peak strength in each thermal tensile cycle

Moreover, the SWNT/PS composites show a typical 'learning' behaviour as explained previously. This seems to start at a low recovery rate, but then slightly increase after two or three cycles which is very common in shape-memory polymers [4,5]. It turns out that the SWMT/PS composites have stable recovery rates during cyclic testing.

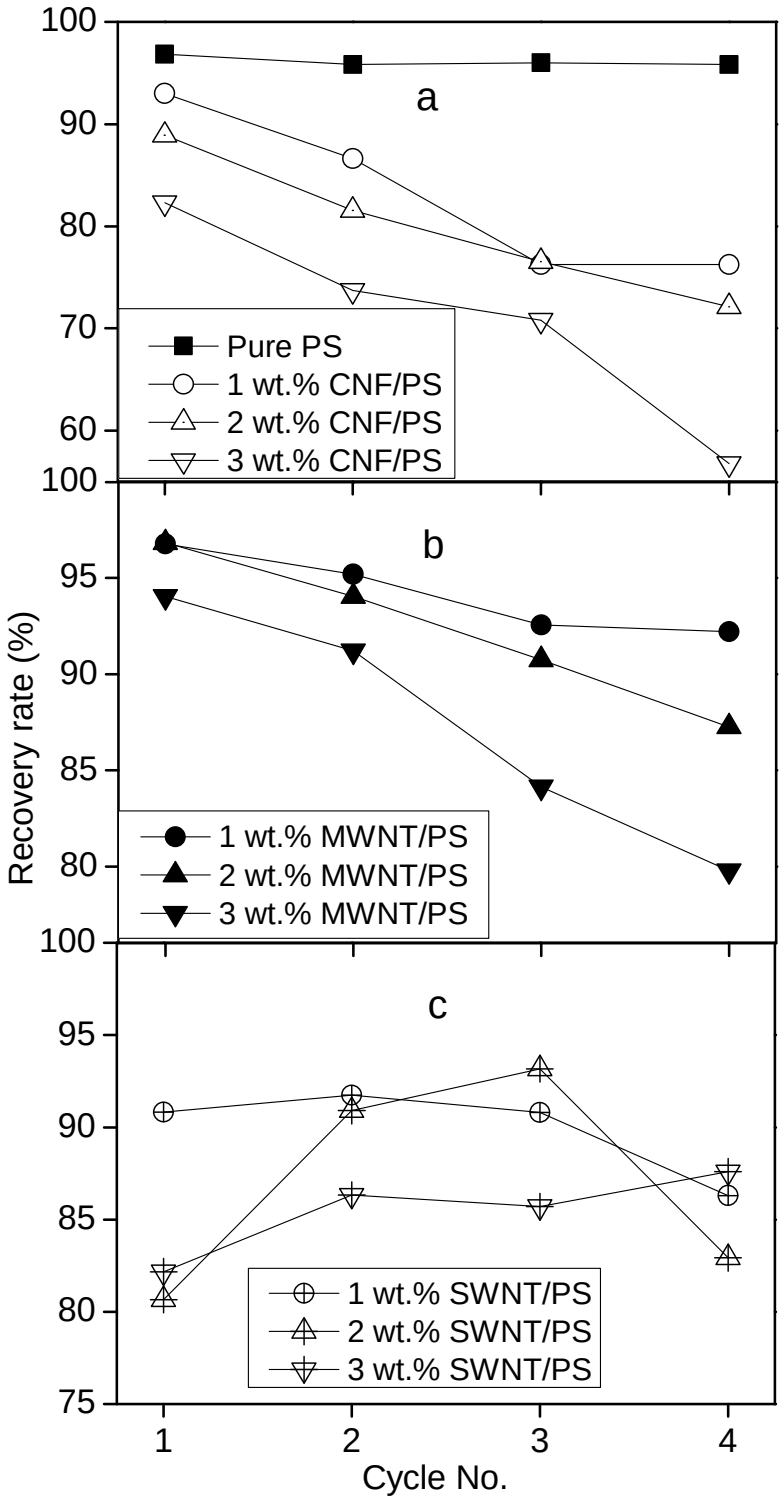

Figure 7.19 Recovery rate dependence with tensile cycle number for (a) Pure PS and CNF/PS composites, (b) MWNT/PS composites, (c) SWNT/PS composites

7.7 Shape recovery demonstration

In this section, demonstration of the shape recovery of the nano-carbon filled composites will be designed under thermal and electrical triggering. Specimens of thickness 0.2 mm, width 10 mm and length 50 mm were rolled after heating to 90 °C, and their shapes were kept fixed during cooling to room temperature (20 °C). The shape recovery test was carried out on a hot plate with a surface temperature of 80 °C. The composites tested had 2 wt.% and 3 wt.% filler concentrations, as the conductivity results indicated that the percolation threshold was in this region, making it a practical range for shape recovery comparison or application design. The shape recovery during heating is shown in **Figures 7.20** and **7.21**.

The 2 wt.% SWNT exhibited a prompt response on the hotplate surface and almost reached 100% recovery within 20 s, which is half the time for the CNF/PS. The 2 wt% MWNT/PS nanocomposites also showed good shape recovery with a faster recovery speed (recovering within 26 s). Meanwhile, further additions of the nanofiller up to 3 wt% reduced the shape recovery efficiency as indicated in **Figure 7.21**. All the 3 wt% samples presented slower recovery speeds than the samples with 2 wt.% filler, but the 3 wt.% SWNT/PS nanocomposite still behaved best as it achieves the fastest full recovery speed. Several reasons could be responsible for the acceleration of recovery time by adding nanofillers. Firstly, it could be that the addition of the nanofillers improves the thermal conductivity and leads to a faster thermal transfer in composites, which effectively accelerates the recovery especially at high volume fractions of the SWNT. Secondly, the introduction of nanofiller induces chain transfer and decreases the molecular weight. This could significantly reduce the activation energy for chain movement and so increase the recovery speed under the same thermal conditions.

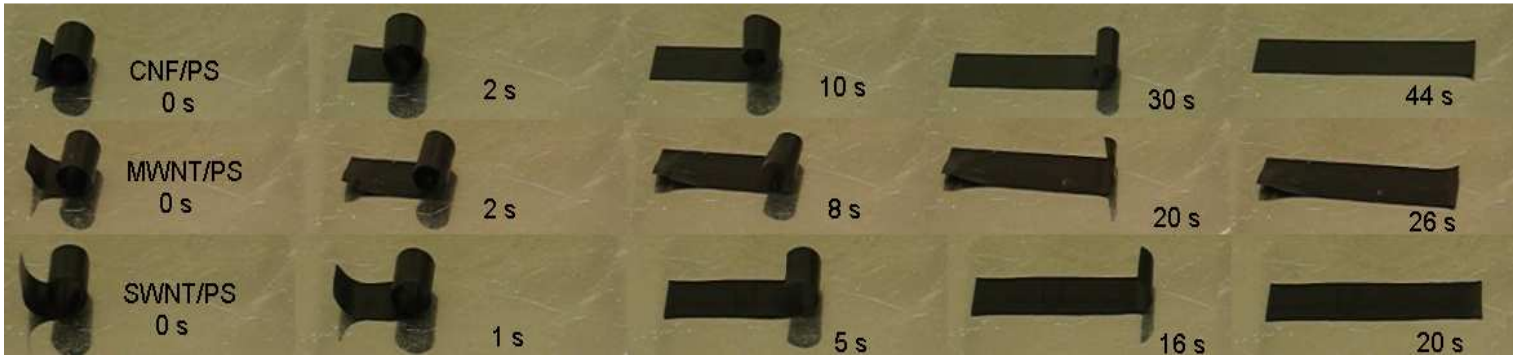

Figure 7.20 Recovery of 2 wt.% nano-carbon based SMP composite sheet on a hotplate with surface temperature of 20 °C above specimen's T_g.

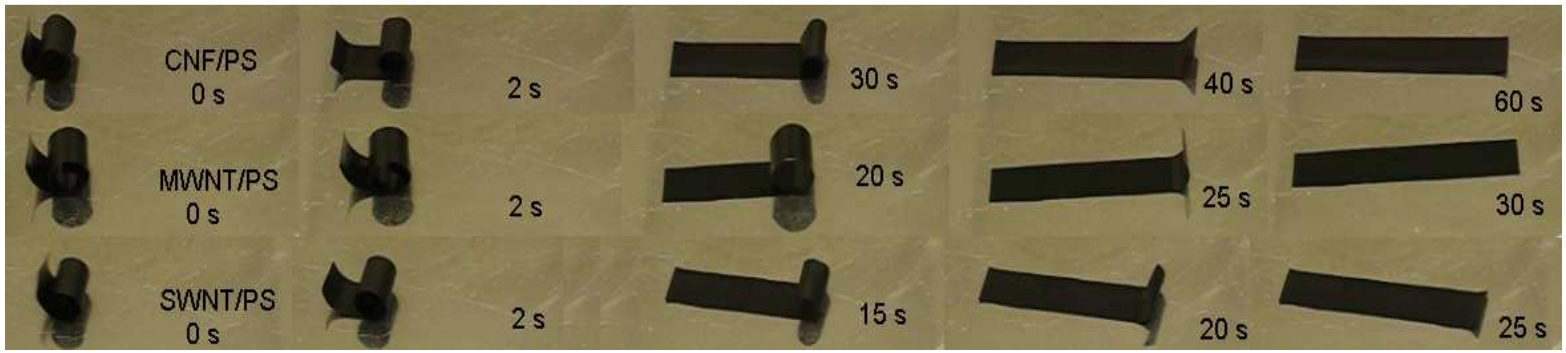

Figure 7.21 Recovery of 3 wt.% nano-carbon based SMP composite sheet on a hotplate with surface temperature of 20 °C above specimen's T_g.

To demonstrate electrically triggered recovery, the sample dimension was enlarged. A composite film of thickness 0.2 mm, width 10 mm and length 40 mm was trimmed into a 'U' shape. Pre-deformation of the sample was performed by rolling it at 90 °C and then keeping the shape fixed during cooling down to room temperature (20 °C). The shape recovery test was performed using a DC power supply at voltages up to 30 V.

Two different pre-deformations, A and B (**Figures 7.22a** and **b**), were adopted to reveal the recovery efficiency under levels of deformation. The results are summarized in **Figures 7.23** and **7.24**. The 2 wt.% SWNT/PS sample showed a full recovery in 25 s for the deformation A, whereas it took 35 seconds for full recovery of deformation B. As it is presented, the recovery speed did not change significantly as there were only 10-second variations between deformation stages A and B. This is probably attributable to the differences in the length of the deformed part (highlighted in **Figure 7.22**).

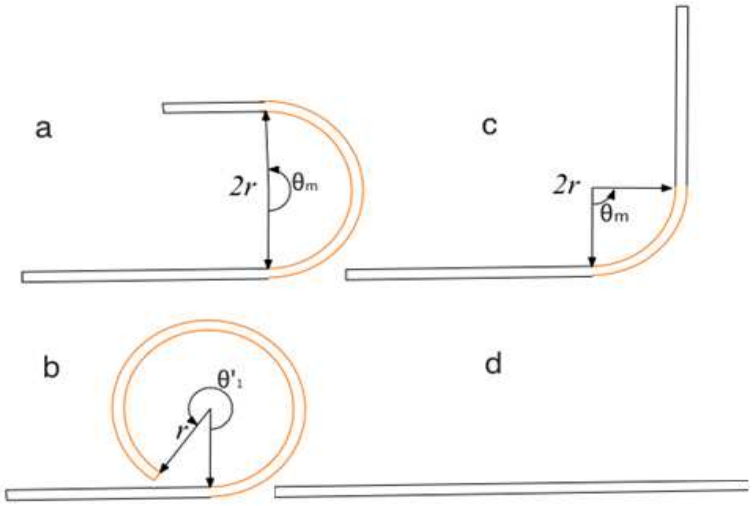

Figure 7.22 Schematic diagram of sample pre-deformation and shape recovery under electrical triggering.

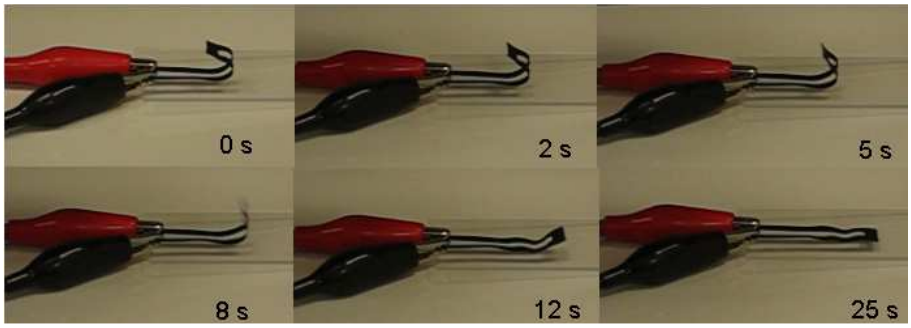

Figure 7.23 Electrically triggered recovery of 2 wt.% SWNT/PS with applied voltage of 30 V for deformation A.

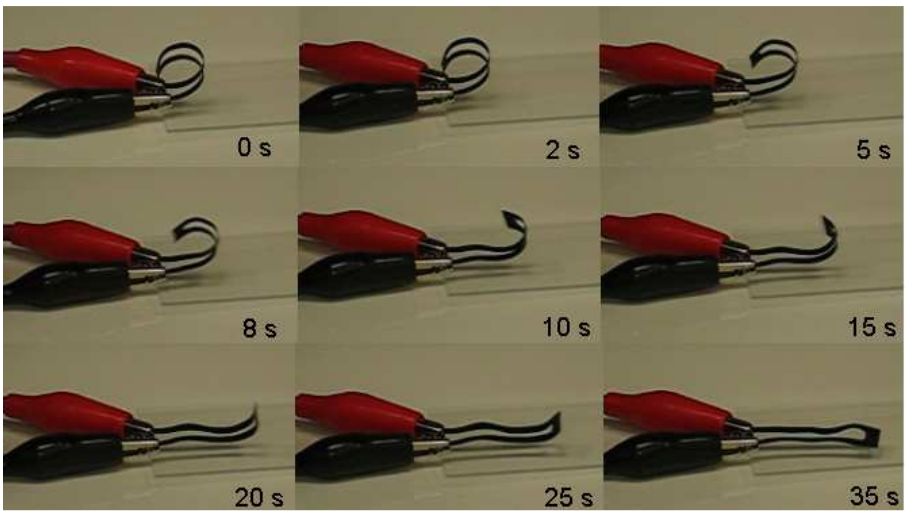

Figure 7.24 Electrically triggered recovery of 2 wt.% SWNT/PS with applied voltage of 30 V for deformation B.

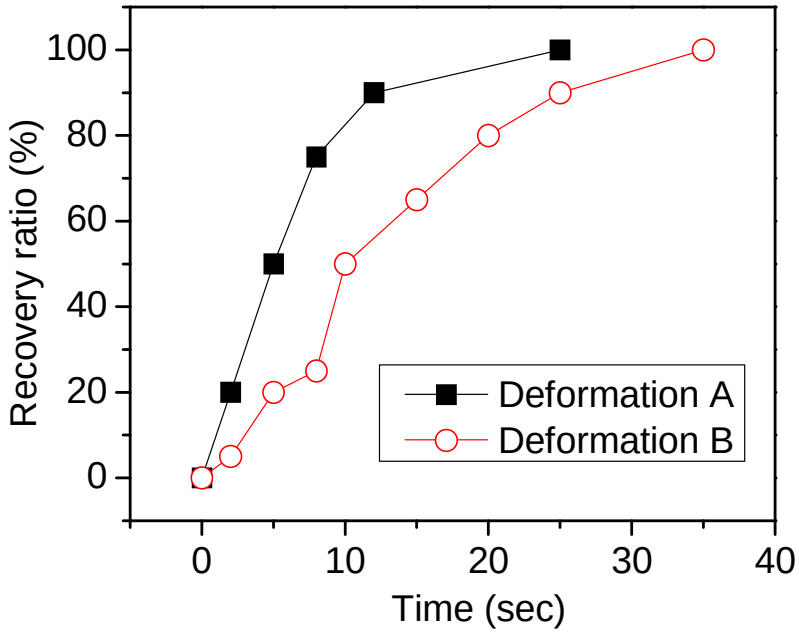

Figure 7.25 Calculated results of electrical triggering recovery ratio for 2 wt.% SWNT/PS with applied voltage of 30 V with different deformation levels

For deformation A, the deformed part is only 1/4 of the whole specimen, whereas nearly the whole specimen contributes to the recovery for the deformation B. Using **Equation (3.14)**, the calculated results of recovery ratio are plotted in **Figure 7.25**. Similar trends can be observed for deformation A and B, and the initial recovery of deformation B seems slower than that of deformation A. The reason is that a longer time is needed to accumulate enough electrical energy to recover from the larger deformation.

7.8 Demonstration of the shape recovery of a stent

The previous results have significant ramifications toward the understanding of the recovery behaviour of SMPS and CNT/PS nanocomposites under electro-actuation and cycling tensile. Although a number of previous studies have examined the unconstrained strain recovery behaviour of SMPs as it has been explored in literature review chapter, many applications require recovery under stress or strain constraint due to external conditions. Moreover, the key points would depend more on the practical application condition and specific design. The results herein provide a foundation for understanding the recovery behaviour of SMPs and SMP nanocomposites as a function of constraint with a design of biological stent.

The SMPS and 2 wt.% SWNT/PS were used to fabricate various designs of stent having different tube diameters with and without uniformly distributed holes of diameter 2 mm (**Figures 7.26a-c**). The fabricated stents were deformed as shown in **Figure 7.26d**, and were then put into hot water at a temperature of 80 °C to demonstrate the shape recovery effect. The recovery records are shown in **Figures 7.26e-g**. The SMPS stent with the holes showed faster recovery and larger recovery rate than the solid one, and the stents made from the 2 wt.% SWNT/PS composites had the fastest recovery of all the three devices tested. It achieved nearly the same recovery ratio as the pure SMPS stent within 10 s. The reasons for the faster recovery speed of composites could be the introduction of inorganic fillers improves the thermal conductive of the substrate. This prelimary work has shown the potential applications of SMP nanocomposites in microsurgery applications, and future work will be focused on the effects of the diameter and wall thickness of the stent on its shape recovery expansion.

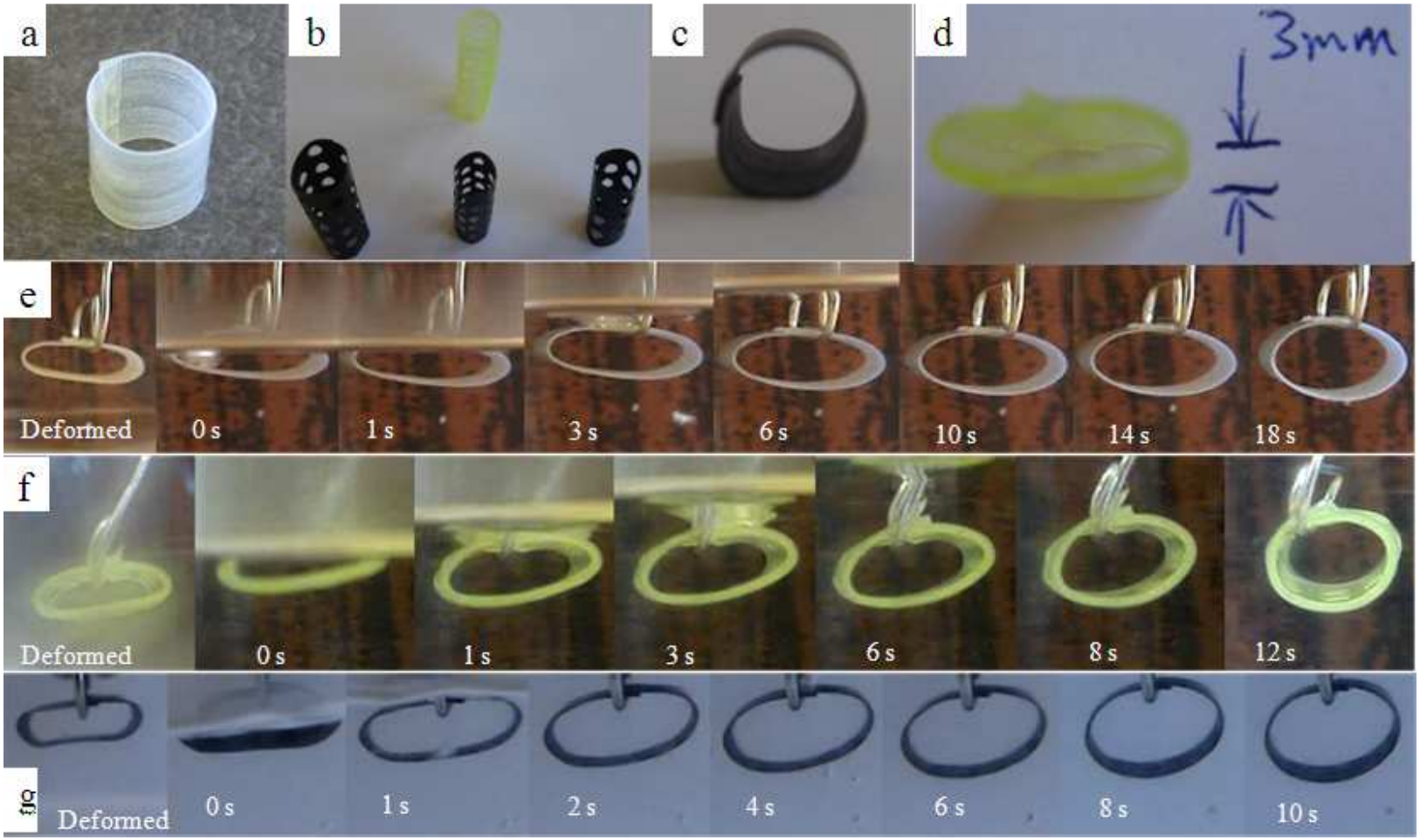

Figure 7.26 Design and recovery of stent in hot water at a temperature of 20 °C above the specimen's T_g, (a) stent (diameter=10 mm) of pure SMPS without holes, (b) stents of SMPS and 2 wt.% SWNT/PS with perforations,(c) stent of 2 wt.% SWNT/PS without holes, (d) deformed shape of stent,(e) recovery of stent for SMPS without holes, (d) recovery of SMPS stent with perforations of diameter=1.5 mm, (e) recovery of 2 wt.% SWNT/PS with perforations of diameter=1.5 mm.

7.9 Summary

Mechanical and thermal property enhancements have been verified from the DMTA tests, and the CNT/PS composites showed superior thermal properties. The SWNT/PS sample displayed the highest storage modulus and T_g. Elastic modulus and hardness results from the nanoindentation tests showed the enhancement of carbon nano-fillers, and the 2 wt.% SWNT/PS composites achieved the best nanomechanical properties among all the samples. The AFM images and surface profiles on nanoindentations showed the existing of pile-ups for some samples. The calculated E/σ_Y and h_p/h_{max} ratios showed that the pile-up effect would not significantly affect the nanoindentation results. Thermal cycling results indicated that the recovery rate was reduced by adding nanofillers to the polymer. The SWNT/PS nanocomposites exhibited the highest recovery rate and peak strength, which indicates that a better organic-inorganic interface and uniformity were achieved. The SWNT/PS sample presents the fastest recovery speed and a good recovery for different pre-deformation conditions. Stents were made using the SMPS and the nanocomposites to demonstrate a microsurgical application. The stent made from the 2 wt.% SWNT/PS composites showed a fast recovery speed and good recovery ratio.

Chapter 8

DISCUSSION

This chapter discusses the experimental results in two board areas. The first area is about the effect of nanoparticle on soft polymer matrices. A number of models are introduced and modified to fit the SMP nancomposite systems studied, indicating a consideration of size effects and geometry of the nanoparticles. The second area focuses on the shape memory mechanisms and constitutive models of the SMPs and SMP nanocomposites.

8.1 Dimensional effects of nanofillers on mechanical enhancement

8.1.1 *Composite system and model selection*

8.1.1.1 Composite system validation

As described in **Chapters 5** and **6**, the macroscopic tensile tests on the composites with the spherical nanofillers of Al_2O_3, SiO_2 and CNP showed that the enhancement effect was dominated by the characteristics of the embedded particles, such as their modulus and density, as well as their mass fraction. The Nano-Al_2O_3/polymer gave a higher Young's modulus than composites using the other spherical particles.

For a given mass fraction, rod-like nanofillers can bridge more polymer chains and provide more effective load transfer, leading to an improved strength. Upon adding a critical volume fraction of the nano-rods (such as nano-clay, CNF or CNTs), the nano-rods are stretched and thus perturb the polymer matrix, and the polymer blends confine the nanorods, generating elongated domains that are reinforced by these fillers [311]. Nanofillers with rod-like structures, have been predicted to be better than spherical nano-particles at reinforcing homopolymer systems because the stress concentrations are reduced and the stress is transferred by the high aspect ratio and specific geometry of the fillers [256]. For instance, there is a remarkable improvement in mechanical properties of SMPs reinforced with 1 wt.% clay as shown in **Chapter 5**, compared with the spherical fillers. In this work, no specific techniques was adopted to improve the interface between inorganic and organic phases, although only low particle concentrations were introduced into the polymeric matrix (less than 4 wt.%). In the

following, it is assumed that there is an 'ideal contact' at the interfaces between the polymer and nanoparticles.

8.1.1.2 Model selection for size effect

A refined *Takayanagi* two-phase model consideration of the interface was used to predict the particle size effect [312]. The equations in the Takayanagi model were modified to suit the different particle geometries such as spherical fillers [**Equation (8.1)**] and rod fillers [**Equation (8.2)**] [312].

$$\frac{1}{E_c}=\frac{1-\sqrt{[(r+\tau)/r]^3\phi_f}}{E_m}+\frac{\sqrt{[(r+\tau)/r]^3\phi_f}-\sqrt{\phi_f}}{\{1-\sqrt{[(r+\tau)/r]^3\phi_f}\}E_m+\sqrt{[(r+\tau)/r]^3\phi_f}(k\text{-}1)\ E_m/\ln k}+$$
$$\frac{\sqrt{\phi_f}}{\{1-\sqrt{[(r+\tau)/r]^3\phi_f}\}E_m+\{\sqrt{[(r+\tau)/r]^3\phi_f}-\sqrt{\phi_f}\}(k+1)E_m/2+\sqrt{\phi_f}E_m} \quad (8.1)$$

$$\frac{1}{E_c}=\frac{1-\sqrt{[(r+\tau)/r]^2\phi_f}}{E_m}+\frac{\sqrt{[(r+\tau)/r]^2\phi_f}-\sqrt{\phi_f}}{\{1-\sqrt{[(r+\tau)/r]^2\phi_f}\}E_m+\sqrt{[(r+\tau)/r]^2\phi_f}(k\text{-}1)\ E_m/\ln k}+$$
$$\frac{\sqrt{\phi_f}}{\{1-\sqrt{[(r+\tau)/r]^2\phi_f}\}E_m+\{\sqrt{[(r+\tau)/r]^2\phi_f}-\sqrt{\phi_f}\}(k+1)E_m/2+\sqrt{\phi_f}E_m} \quad (8.2)$$

where E_c and E_m represent the Young's modulus of the composite and matrix, r is the radius for spherical and rod fillers, τ is the interface thickness, k is the interfacial constant ($1< k< (E_f/E_m)$), and ϕ_f is the volume fraction of filler (vol%), which was calculated from:

$$\phi_f=\frac{1}{1+(M_m/\rho_m)\times(\rho_f/M_f)} \quad (8.3)$$

where M_m and ρ_m denote the mass and bulk density of matrix, M_f and ρ_f represent the mass and density of fillers.

For the current system, the value of τ was set at 6 nm and k=4 as indicated in the work of other researchers [312].The *Takayanagi* model has proved effective in predicting the particle size effect, especially for those fillers with regular geometry such as spherical and rod fillers [312].

8.1.1.3 Elastic models for fibre aspect ratio effect

Both the Halpin and Tsai model and the Mori and Tanaka model will be applied in this work. The modified Halpin and Tsai [165, 166] model is expressed as:

$$\frac{E_c}{E_m} = \frac{1+\zeta\eta\phi_f}{1-\eta\phi_f} \quad \textbf{(}8.4\textbf{)}$$

where ζ is a shape parameter, determined by filler geometry and loading direction, and η is given [165, 166] by

$$\eta = \frac{E_f / E_m - 1}{E_f / E_m + \zeta} \quad \textbf{(}8.5\textbf{)}$$

where E_f is the Young's modulus of the filler. Following the work from Halpin and Kardos [166], a shape parameter of ζ =2(l/d) will be used in this study, and l/d is aspect ratio.

The Mori and Tanaka model refined by Tandon and Weng [167, 168] can be expressed as:

$$\frac{E_{11}}{E_m} = \frac{A}{A+\phi_f(A_1+2\upsilon_m A_2)} \quad (8.6)$$

$$\frac{E_{22}}{E_m} = \frac{2A}{2A+\phi_f(-2\upsilon_0 A_3+(1-\upsilon_m)\ A_4+(1+\upsilon_m)\ A_5 A)} \quad \textbf{(}8.7\textbf{)}$$

where E_{11} is the longitudinal modulus and E_{22} is the transverse modulus, υ_0 is the Poisson's ratio of the matrix, A_1, A_2, A_3, A_4, A_5, and A are functions of the Eshelby's tensor, related to the properties of the filler and the matrix [161]. **Equations (8.6)-(8.9)** account for the effect of filler shape, for example, rod-like, plate-like or disc-like.

The Mori and Tanaka model was modified by Fornes and Paul [169] who suggested equations for random orientation of fibres in all three orthogonal directions:

$$E_{ran-3D}^{fibers} = 0.184E_{11} + 0.816E_{22} \quad \textbf{(}8.8\textbf{)}$$

$$E_{ran-3D}^{plateles} = 0.49E_{11} + 0.51E_{22} \quad \textbf{(}8.9\textbf{)}$$

In the following section, the Halpin & Tsai model [**Equations (8.4) ~ (8.5)**] and Mori & Tanaka model [**Equations (8.6) ~ (8.9)]** will be applied to the composites modulus with different fillers.

8.1.2 *Modelling inputs*

For the theoretical analysis in this section, the matrix and filler materials were assumed to be linear elastic and isotropic. **Table 8.1** lists the physical details of all the nanoparticles, which will be used as the input data for the models. The values for the polystyrene modulus were taken from the experimental data listed in **Chapter 5**. Some of the input data in **Table 8.1** are assumed as average values based on the technical information from the supplier, with consideration of the non-uniformity of particle dimensions and aggregation.

Table 8.1 Polymer matrix and nanoparticles features for computational modelling

Name	**Bulk density, g/cm^3**	**Poisson's ratio**	**Young's modulus, GPa**	**Average size, nm**
Polystyrene	1.05	0.35	0.09	N/A
Al_2O_3	0.9	0.2	300	~80
Silica	1.35	0.2	70	~25 nm
CNP	0.1	0.2	100	~50 nm
CNF	0.3	0.2	200	Φ=100 nm , l=5 μm
MWCNT	0.22	0.2	400	Φ=80 nm , l=8 μm
SWNT	0.15	0.16	600	Φ=10 nm , l=1 μm
Attapulgite clay	0.65	0.2	150	Non-treated Fibre,Φ=20 nm , l=3 μm; treated platelets *Thickness* =20 nm , l=3 μm;

8.1.3 *Theoretical modelling*

8.1.3.1 Particle size effect

Particle size effect was predicted by the modified multi-phase enhancement model [**Equation (8.1)**], considering the matrix properties, rigid filler properties, and the interface connection. **Figure 8.1** displays the calculated values for the polymer/spherical filler composite.

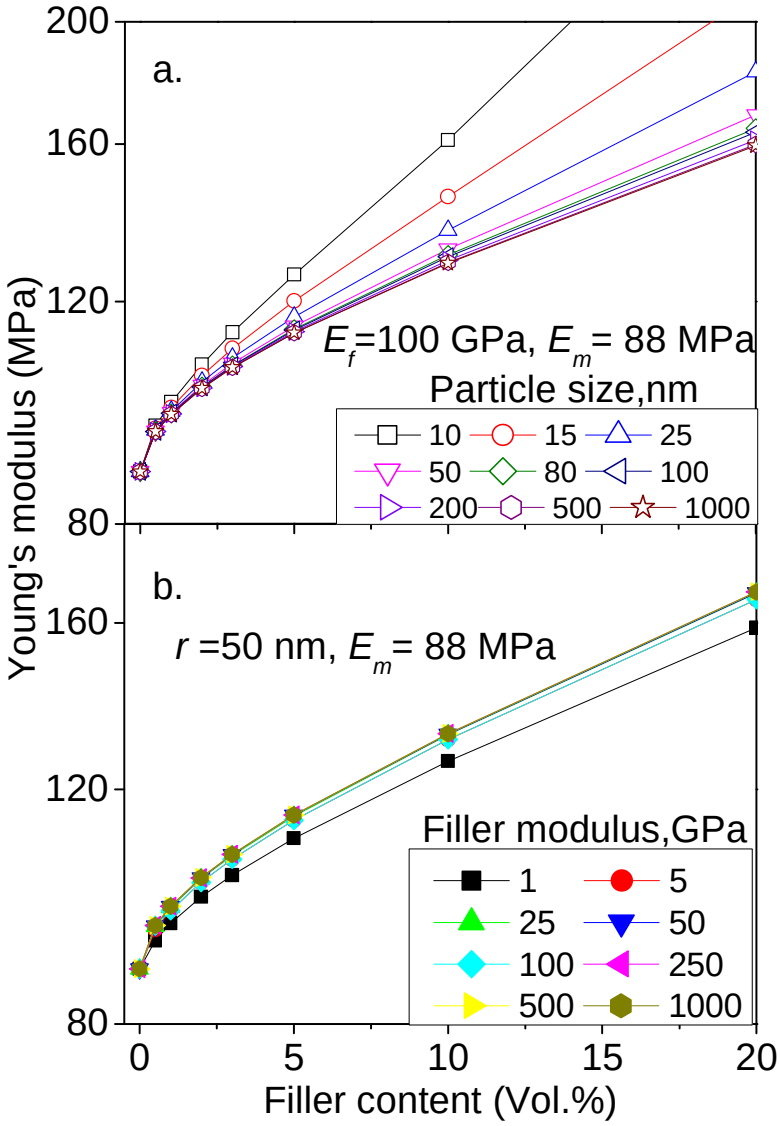

Figure 8.1 Multi-phase modelling for polymer nanocomposites reinforced with spherical fillers, (a) particle size effect and (b) effect of filler modulus.

The predicted modulus increases as the volume fraction increases for both the particle size effect (**Figure 8.1a**) and filler modulus effect (**Figure 8.1b**). As indicated in **Figure 8.1a**, the smaller the filler particle, the higher the modulus increment for a given volume fraction, although, there is a turning point at r = 50 nm. A clear trend for the calculated modulus of composites can be observed with the particles size above 50 nm, which agrees with the data reported in references [157,313], and the particle size of 50 nm is the threshold value for this composite system.

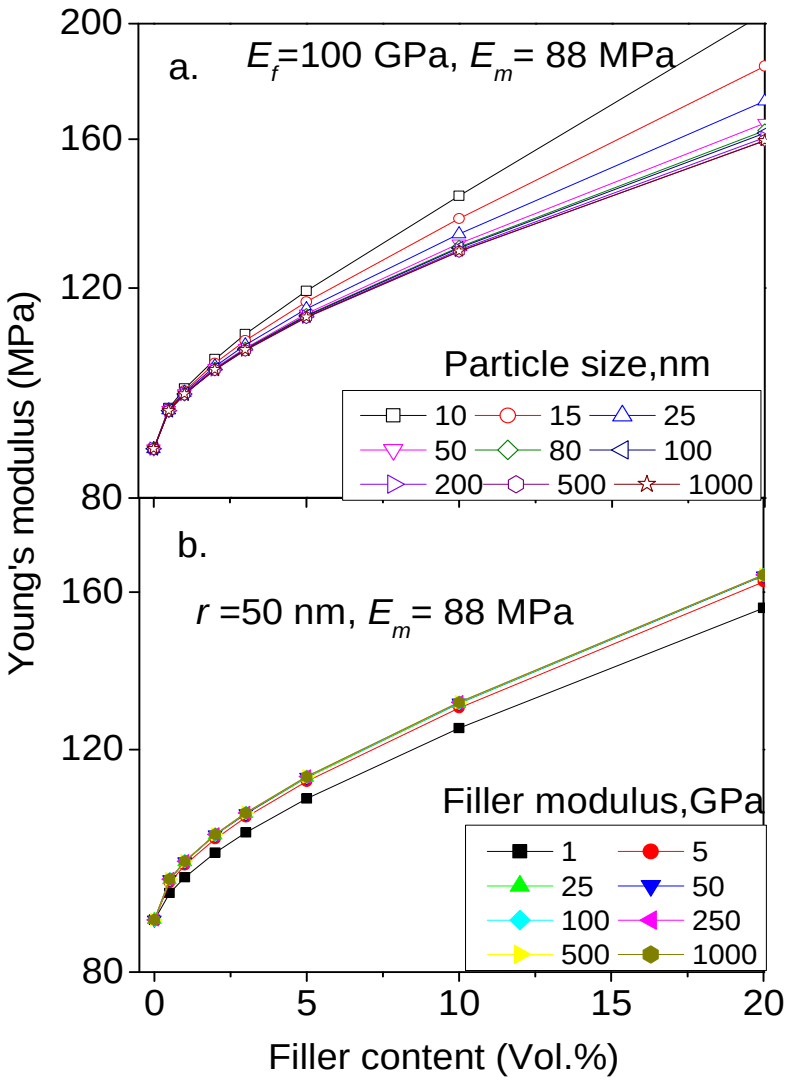

Figure 8.2 Multi-phase modelling for polymer nanocomposites reinforced with rod fibre, (a) particle size effect and (b) effect of filler modulus.

The effect of the filler's modulus on enhancement is presented in **Figure 8.1b**, and there is no dramatic effect of filler modulus between 1 and 1000 GPa. Considering the rate of increase of composite modulus with volume fraction (**Figure 8.1b**), the filler modulus has a rather weaker effect. The same model was applied to the rod filler/PS system and the results are presented in **Figure 8.2**. A similar trend is observed for the effect of particle size, and the plot shows a lower increment of the modulus compared with the spherical filler for the same volume fraction below the percolation value. **Figure 8.2b** reveals the same phenomenon for the changes of modulus with filler content to that shown in **Figure 8.2b**.

8.1.3.2 Effect of aspect ratio on composite modulus

The modelling results with the Halpin–Tsai and Mori–Tanaka theories are shown in **Figure** 8.3, which predicts the reinforcement on the soft polymer matrix as a function of volume fraction of filler. Using the input parameters listed in **Figure 8.3**, rod fillers are predicted to have a more significant enhancement than spherical ones, and the modulus is expected to increase with aspect ratio from the predictions of both the theories. However, the Haplin-Tsai model predicts a smaller increase of the modulus with the rod filler aspect ratio, especially at a high aspect ratio. The modelling Mori-Tanaka theory shows higher values of modulus than those from the Halpin-Tsai theory. This is because the Mori-Tanaka model considers the load transfer to be improved due to the aspect ratio of fillers [167, 168, 169].

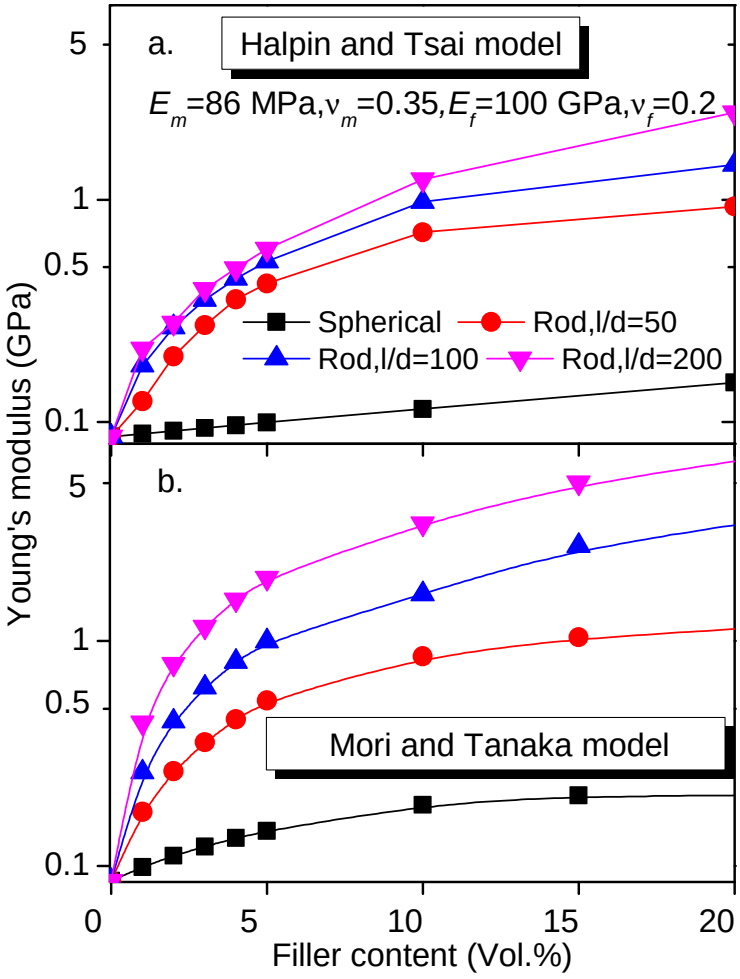

Figure 8.3 Calculated modulus *versus* filler content for SMPS nanocomposites reinforced with spheres and rods, (a) Halpin– Tsai equations and (b) Mori–Tanaka theory.

The effects of filler modulus and aspect ratio on reinforcement are exhibited in **Figures 8.4a-b**. The combination of both high modulus and high aspect ratio leads to different levels of reinforcement. As expected, increasing the aspect ratio results in good reinforcement for a given filler modulus and concentration. Likewise, increasing the filler modulus also improves the reinforcement especially when the aspect ratios are larger than 20–30.

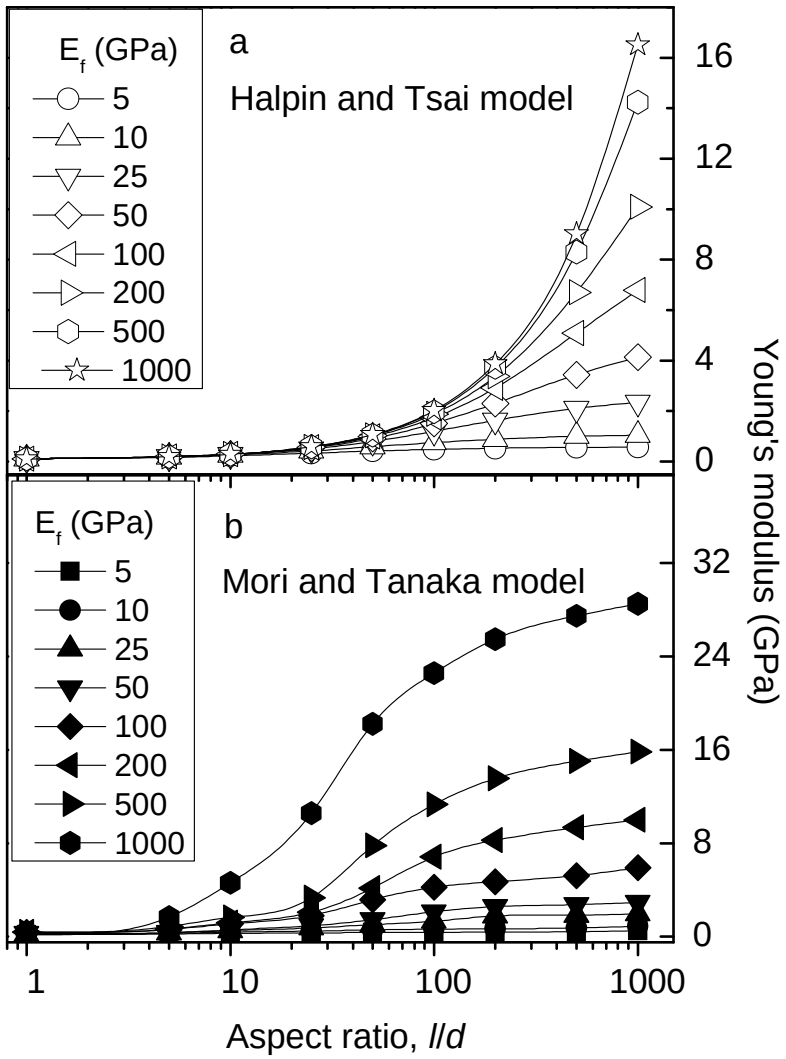

Figure 8.4 Modelling results from (a) Halpin– Tsai equations and (b) Mori–Tanaka theory as functions of aspect ratio and filler modulus.

It is important to note that the Halpin–Tsai equations do not predict much on effect of filler geometry because **Equations (8.5) and (8.6)** do not reflect the aspect ratio particularly strongly. The Mori–Tanaka theory, on the other hand, gives different reinforcement trends, as shown in **Figure 8.4b**, and the predicted enhancements are much higher than those from the Halpin–Tsai equation at the same aspect ratio.

The theoretical modelling results suggest that, if the filler modulus is high, it will have a pronounced effect in improving the nanocomposite stiffness as demonstrated in **Figure 8.3**. The Halpin–Tsai equation calculates less of an effect of aspect ratio whereas, the Mori–Tanaka theory seems to be more sensitive to filler geometry as indicated in **Figures 8.3** and **8.4**. For a given filler modulus and aspect ratio, the Mori–Tanaka model predicts considerably greater unidirectional reinforcement than does the Halpin–Tsai equation. Each theory, however, conveys to the rule of mixtures for very high filler aspect ratios. Overall, the trends in **Figure 8.3** and **8.4** demonstrate considerable potential for improvement in nanocomposite stiffness by increasing the aspect ratio of the fillers, whether from improvements in individual filler dispersion, or from adding high aspect ratio filler.

8.1.4 *Comparison of experimental and theoretical results*

In this section, a comparison is made between theoretical data and the experimental from the tensile tests shown in **Chapters 5 to 7**.

8.1.4.1 Size effect of nanoparticles

The particle size effect for the spherical fillers on Young's modulus of the composites is shown in **Figure 8.5**, which compares the predictions of the multi-phase model with the experimental results. It is clearly that the experimental data exhibit a similar trend to the modelling results. The model predicts that all curves should have a similar rate increase as the particle size is in a range of 50 nm-80 nm for the three spherical fillers used. A slight change in the particle size would not to be expected to cause a marked variation on the composite modulus until the particle size is less than 25 nm, below which a dramatic influence is expected. Smaller particles have a larger total surface area for a given particle loading, so that the strength of the composite increases through more efficient load transfer. Although the experimental data matched the prediction in trend, most of the measured data are below the theoretical ones. The reason for this is that the theoretical analysis assumes ideal dispersion with perfect surface contact for the reinforcement, which is hard to achieve in practice. When the filler loading is above 0.1 vol.%, the dispersion of filler cannot be considered to be perfect [314]. For most of the composites tested, the particles tend to aggregate due to their high surface energy.

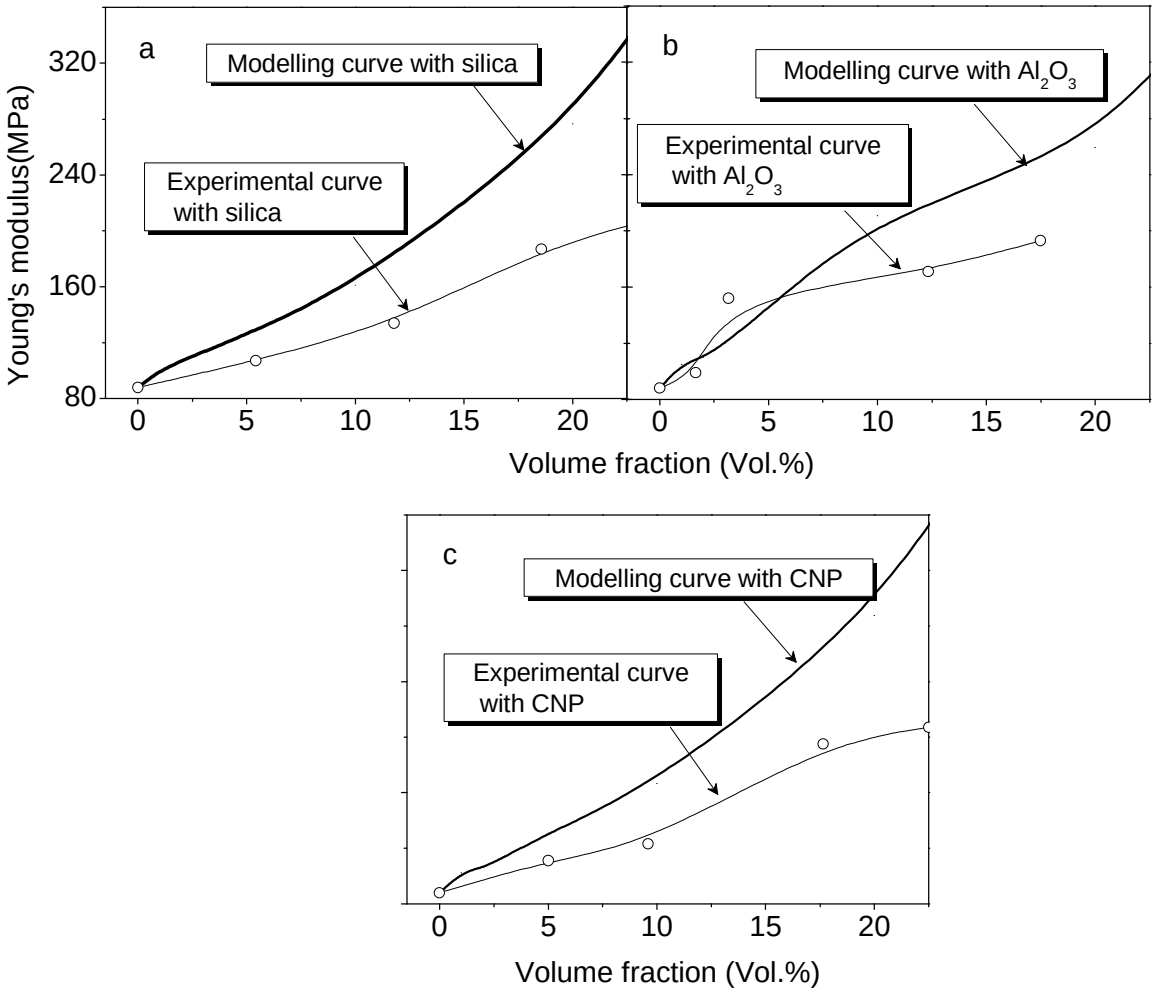

Figure 8.5 Modelling and experimental results for composites with different spherical fillers, (a) Silica/SMPS composites, (b) Al_2O_3/SMPS composites and (c) CNP/SMPS composites.

However, it is noting that, for the Al_2O_3 particles at, or below 3 vol.%, the composite modulus is comparable to the theoretical one. The CNPs were the highest surface energy because of their smaller size. When the volume fraction is increased above 15 vol.%, the composite strength increases only slowly as the particles tend to agglomerate.

Figure 8.6 summarizes the modelling and experimental results of the rod filler reinforced composites. The experimental data demonstrate higher values than predicted, contrary to what was found for spherical particle reinforcement. For the rod fillers with larger diameters, CNF and MWNT, there is no obvious correlation between the experimental data and the theoretical predictions. For the smaller sized rod fillers, SWNT and clay, the theoretical curves reveal a similar trend but the values are much smaller than the measured ones. This could be attributed to neglecting the rod filler

orientation in the multi-phase model, which effect plays a more important role in rod filler reinforcement in composites than the particle size or filler modulus.

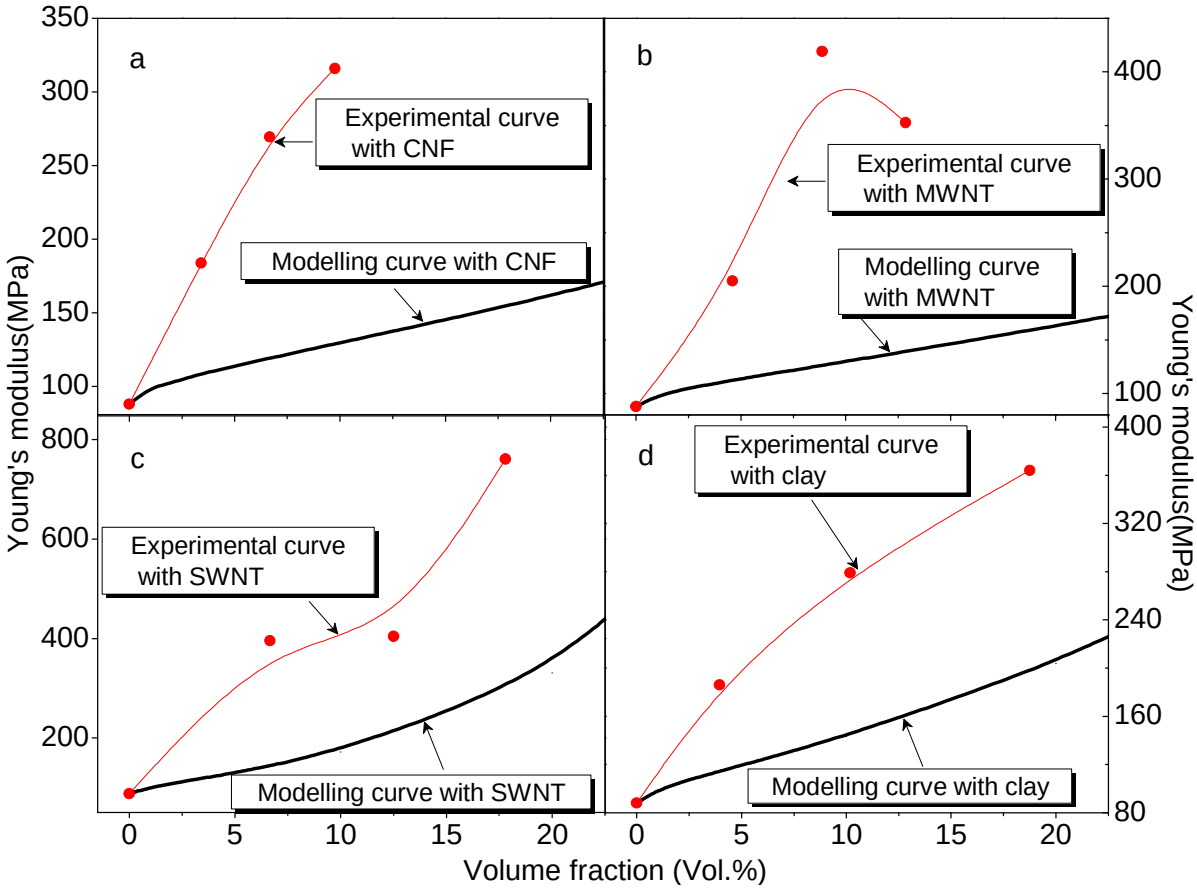

Figure 8.6 Theoretical modelling and experimental results for composites with rod fillers, (a) CNF/PS composites, (b) MWNT/PS, (c) SWNT/PS and (d) Clay/PS.

The modified multi-phase model was used to predict the particle effect on the composite modulus. For the spherical fillers, the modelling results clearly show that the particle size has a significant effect on the strength of particulate-filled polymer composites, which generally increases with decreasing size. The size effect plays a more important role than the filler modulus in reinforcement. Meanwhile, the experimental results proved that the modified multi-phase model is ineffective when applied to predict the modulus if rod particle filled system, because it takes less account of on the filler aspect ratio.

8.1.4.2 Effect of filler aspect ratio

Figure 8.7 compares the calculated and measured modulus for the SMP nanocomposites studied at 1 wt.% filler. Both the Halpin-Tsai and Mori-Tanaka models make a reasonable estimate of the nanoparticle reinforcement for all of the applied spherical fillers, except for silica. For the silica/PS system, the considerable difference between the calculated and measured Young's modulus can be attributed to the agglomeration of the nanofiller caused by hydro-groups on the particle surface, and this effect has been reported by other researchers [315, 316].

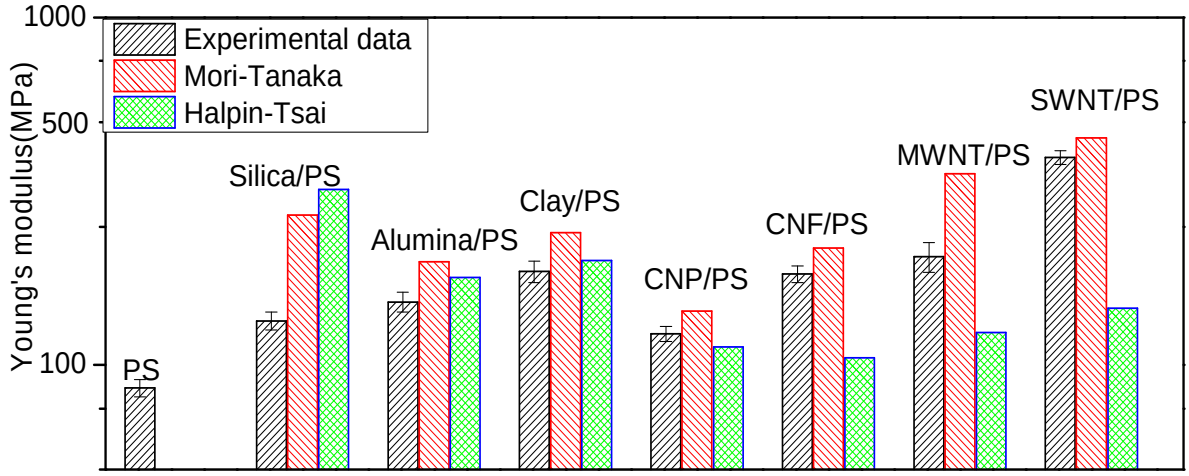

Figure 8.7 Comparison of predicted Young's modulus with experimentally measured data for 1 wt.% filler/SMPS nanocomposite.

As to the rod filler/polymer composite system, the Mori-Tanaka model predicts the observed filler enhancements, but considerably over-estimates the modulus values. The Halpin-Tsai model mostly showed a significant under-estimate of the modulus. The better prediction of the Mori-Tanaka model is attributed to its consideration of the aspect ratio and the effect of volume fraction. For the MWNT filled composites, the experimental results are dramatically different from the prediction from the Mori-Tanaka model, which could be due to the low effective volume fraction due to aggregation or impurity of the MWNTs. It is also interesting to compare experimental data to the model predictions based on particle aggregation morphology, since the actual composites contain a certain amount of aggregrated filler as a result of limitations of the dispersing technique and higher particle surface energy.

Figure 8.8 compares the modelling and experimental data for the modulus of the nano carbon filled composites at different concentrations, and reveals how effective the two theories are in predicting the effects of geometry, aspect ratio and modulus of the nanofillers.

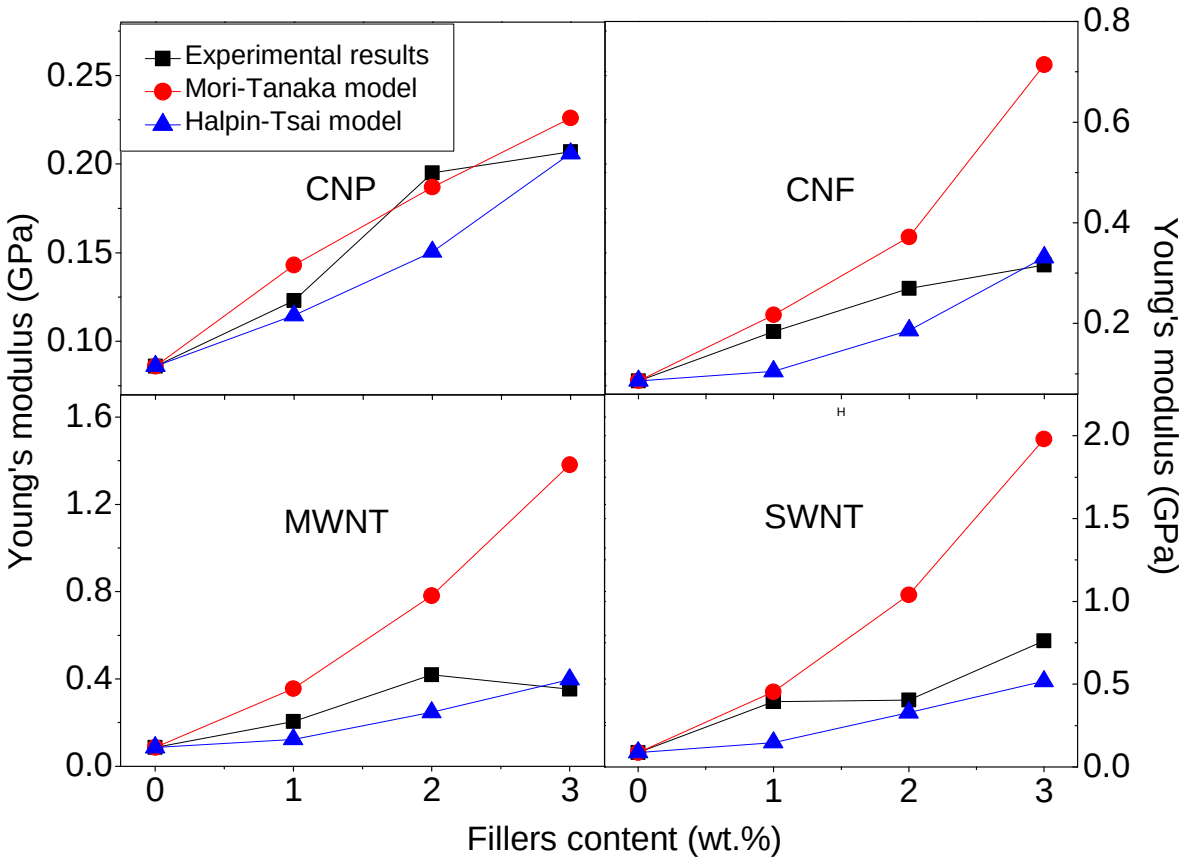

Figure 8.8 Comparison of predicted Young's modulus for composites with carbon nanofillers with experimentally measured data.

The models predict the observed changes of the nanocomposite stiffness and demonstrate that significant reinforcement could be achieved by using fillers either with higher volume fractions, or with larger aspect ratio. However, the Halpin–Tsai equation slightly underestimates the measured data with less effect of aspect ratio. The Mori–Tanaka theory matches the experimental values well at the filler contents less than 1 wt.%, and then tends to over-estimates the modulus compared with experiment which could be attributed to the filler distribution, non-uniformity of geometry, or aggregation. Any of these could dramatically reduce the load transfer capability of the filler, and lead to internal defects (such as stress concentrations and crack) and decrease the macroscopic modulus. The SWNT/PS composites showed higher measured modulus than the other fillers for the same weight percentage and more stable increase of

modulus with filler content, which could be attributed to the high modulus of SWNT, higher aspect ratio (*l/d* ~ 100), and higher volume fraction (lower bulk density). The TEM observation of the treated clay (**Figure 4.3**) indicates that the rod-like clay form a plate-like structure after heat treatment. Accordingly, the modified Mori–Tanaka model suggested by Fornes and Paul [**Equation (8.9)**] was adopted to predict the reinforcement by the treated clay. **Figure 8.9** shows the calculated results of the Young's modulus of composites with different shapes of filler based on **Equations (8.8)** and (**8.9)** (Mori-Tanaka model).

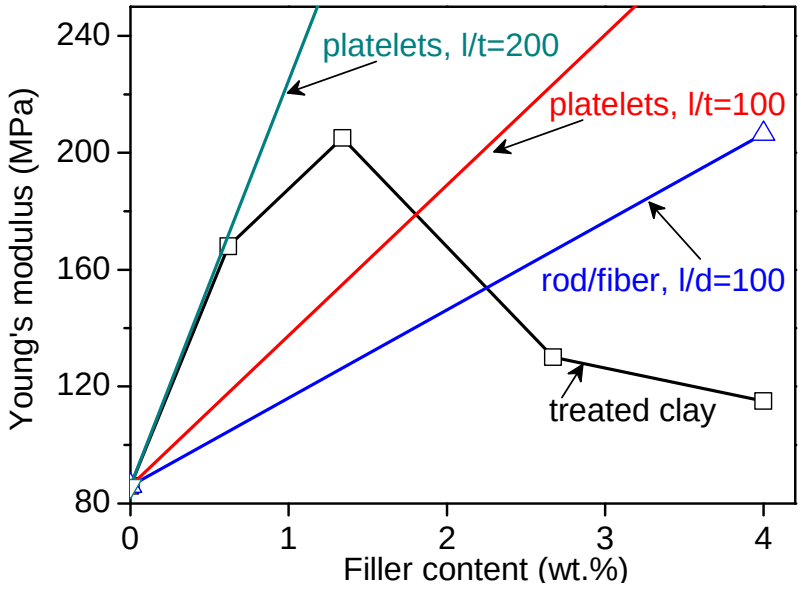

Figure 8.9 Predicted of Young's modulus of treated clay nanocomposite SMPs compared with experimental data

Of the three forms considered, platelet filler with l/d=200 fit the initial increment of modulus best. These platelet filler show good reinforcement because of their high aspect ratio and multi-directional load transfer [311, 317]. The deviation from the predicted curve at higher filler contents (beyond 1 wt.%) may be due to the increased agglomeration for their higher volume fractions.

Using the Halpin–Tsai and Mori–Tanaka models, the calculated outputs shown in **Figure** 8.1**–8.4** reveal that the composite modulus can be significantly affected by physical factors such as filler modulus, aspect ratio, geometry, and volume fraction of the filler. Those results also reflect how the size, geometry, stiffness, or dispersion of the particles influence the composite, modulus by load transfer from the matrix to filler. Rigid fillers are naturally resistant to strain due to their high modulus. When a relatively

softer macromolecular matrix is reinforced with these types of fillers, the polymer, particularly that adjacent to the filler particles, becomes highly restrained mechanically. This enables a significant proportion of an applied load to be carried by the filler, assuming that the contact between the two phases is adequate without any specific treatment. Logically, the higher the filler modulus is, the greater the restraint encountered by the matrix and, thus, the greater the stress transfer. However, some unavoidable phenomena often occur with passive influences such as filler aggregation and significant phase separation of the large contact interface. On the other hand, introducing fillers with high aspect ratio can reduce this effect by increasing the amount of stress transferred to the filler geometrically, which was shown by the theoretical results. Furthermore, the enhancement of a layered platelet shape was also confirmed from the results of the treated clay composites. The aspect ratio and geometry of the nanofillers play a more important role in reinforcing the polymer matrices than the particle size and stiffness of the individual particles.

8.2 Thermally triggered shape memory mechanism and viscoelastic constitutive model

The constitutive model presented in this section is the incorporation of the nonlinear Adam–Gibbs model of structural relaxation into a continuum finite-deformation thermal visco-elastic model [318, 319]. To convey this model simply, the effects of heat conduction and pressure on the structural relaxation and any inelastic behaviour of the material have been neglected. Descriptions and identifications of the current SMP system are presented in the first part of this section, and then the model and parameter determination are introduced in details. Thirdly, theoretical modelling of the viscoelastic and shape recovery behaviour of SMPS and nanocomposites is carried out. Finally, the simulation and experimental results are compared.

8.2.1 *SMP system identification and model approaches*

As scoped in the literature review (**Chapter 2**), the thermally activated shape recovery of amorphous SMPs is dramatically dependent on the chain mobility induced by the glass transition (i.e. $T_{trans} = T_g$), which is considered to be the threshold factor for the

free movement of molecular chains. This chain mobility is the ability of the chain segments to rearrange locally to bring the macromolecular structure and stress response to equilibrium. Generally, most amorphous polymers demonstrate a certain degree of shape memory behaviour which can be explained by this segmental movement theory [261, 320, 321]. Cross-linking methods are adopted to achieve better mechanical properties, higher recoverability and more programmable shape conversion as described in **Chapter 2**. The defined cross-linking includes not only the chemical cross-linking network, but also physical crosslinking joints, and junction forces from macromolecular chain entanglements [228,118,322].

Improving cross-linking leads to a higher strength but less flexibility as the large number of cross-linking points limits the molecular chain mobility permanently. In cross-linking SMP systems, the cross-linking density is strictly limited and the shape memory effect is caused by the transition of a cross-linking polymer from a state dominated by entropic energy (rubbery state) to a state dominated by internal energy (glassy state) as the temperature decreases [323-325]. At temperatures above the T_g, individual macromolecular chains undergo large random conformational changes, which are constrained by the cross-linking sites formed during material processing [324, 325]. Deforming the material reduces the possible configurations and hence the configurational entropy of the macromolecular chains, leading to the well-known entropic behaviour of elastomers. After the removal of the external load at a temperature above T_g, the tendency of the material to increase its entropy will recover the undeformed (processed) shape defined by the spatial arrangement of crosslinking sites [326]. However, this shape recovery can be interrupted by lowering the temperature below T_g. Therefore, the mobility of macromolecular chains is significantly reduced by the reduction in free volume, and the conformational change of individual macromolecules becomes increasingly difficult. Instead, cooperative conformational change of neighboring chains becomes dominant, and deformation thus requires much higher energy [327, 328]. Therefore, the removal of the mechanical load at temperatures below T_g only induces a small amount of shape recovery, most parts of deformation incurred at the temperature above T_g is restored. The shape memory effect is invoked as the temperature increases above T_g, where the individual macromolecular chains become active again and the shape recovery mechanism described above is permitted. In this sense, shape memory effect is simply a temperature-delayed recovery [68, 329].

Also, it is necessary to identify the polymer system before modelling as there is dramatic variation in the recovery mechanisms for different types of SMPs.

In this project, the amorphous PS system consists of cross-linked network (hard segments) and amorphous long PS chains (soft segments) as explained in **Chapter 5**. Shape recovery mechanism with hard and soft segments is illustrated in **Figure 8.10** and **8.11**.

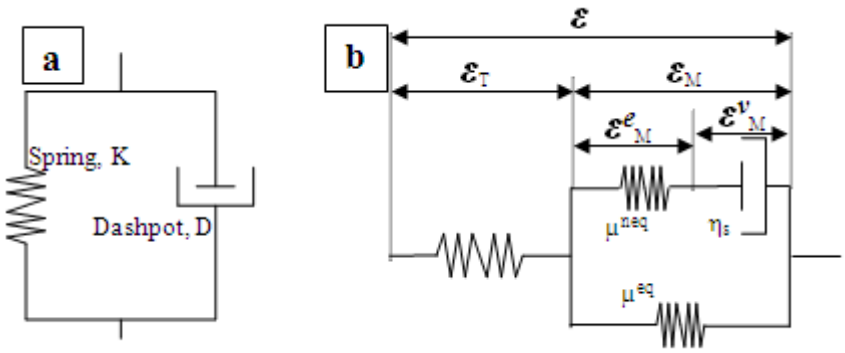

Figure 8.10 (a) 1-D viscoelastic model, (b) viscoelastic model with thermal component and mechanical component.

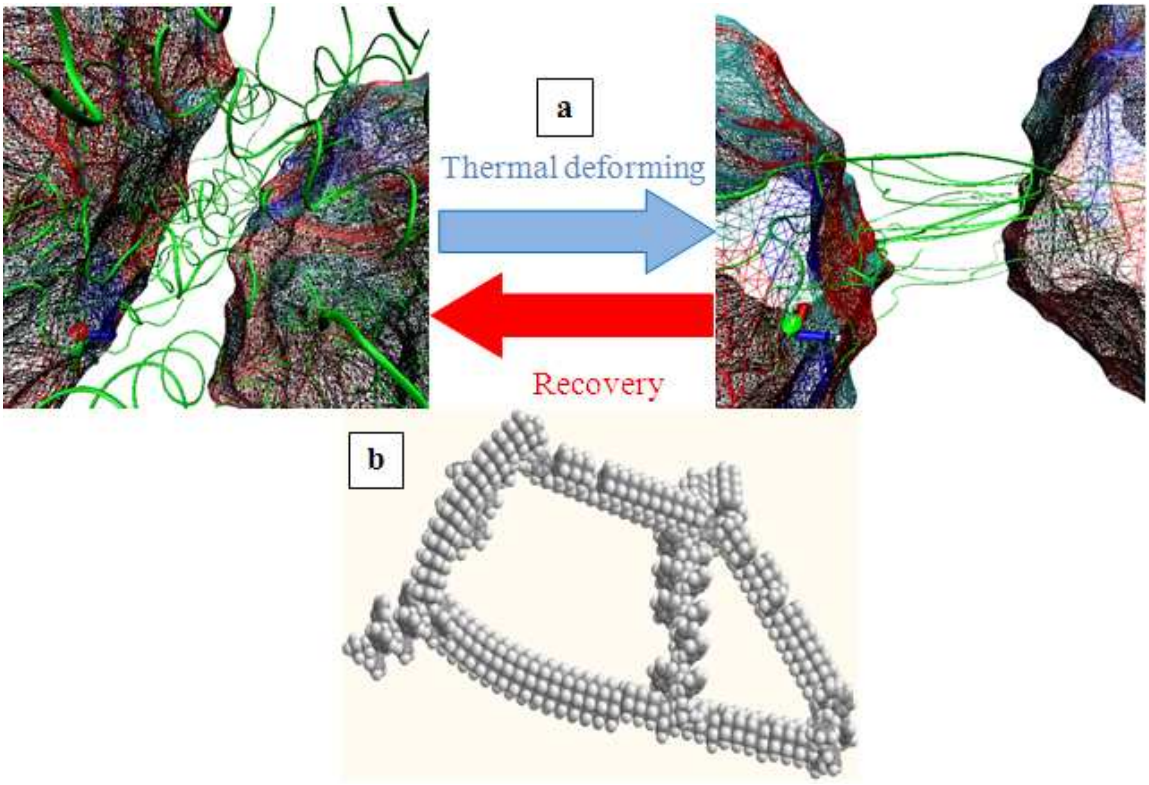

Figure 8.11 Illustrations of SMP structures and theoretical models, (a) 3-D schematic of hard-soft segment movement during the shape recovery procedure, (b) cell of hard segment with cross-link point.

The function of each part is shown in 3D alongside typical 1-D multi-component models which were widely used to model amorphous SMPs [10330]. In contrast to the above theory on cross-linking SMPs as presented in **Figure 8.11**, the shape change of cross-linked PS is almost entirely achieved by the chain mobility of soft segments which changes more almost instantaneously with temperature. Below the T_g, the structure is changed by the elimination of the chain mobility and reduced thermal energy from relaxation to equilibrium. This effectively freezes the structure in a nonequilibrium configuration and allows the material to store a deformed shape [176,6]. Reheating to above T_g restores the mobility and allows the structure to relax again to an equilibrium configuration and the material to recover its permanent shape.

A kinematic and constitutive model for pure amorphous SMP has been explored by Nguyen *et al.* [49, 50], generated from a constitutive model of the large strain time-dependent behaviour of elastomers [318, 319]. The finite-deformation continuum constitutive model is proposed for the thermoviscoelastic behaviour of the current amorphous SMP system, incorporating the Adam–Gibbs theory of structural relaxation in the glass transition region, and is based on the several reported constitutive models [49,331].

8.2.2 *Kinematic model*

The model in **Figure 8.11c** describes thermoviscoelastic behaviour in a polymeric system with finite deformation [49, 50]. The assumptions were made by a series of multiplicative decompositions of the deformation gradient, first into thermal and mechanical components, then into elastic and viscous mechanical components. The sequence of deformation maps produced by the successive decompositions of the deformation gradient is illustrated in **Figure 8.12**.

The constitutive relations for the mechanical stress and thermal deformation were split into equilibrium and nonequilibrium parts. The analogous scheme in **Figure 8.12** describes the various components; Ω_0 (the thermodynamic equilibrium configuration) with the assumption that it restricts the initial state of the material to be in the rubbery state (Ω'_T), where relaxation events occur nearly instantaneously.

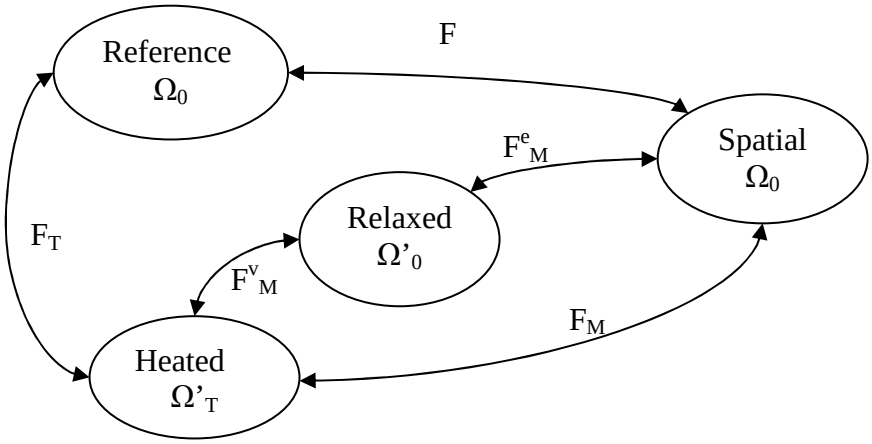

Figure 8.12 An analogous decomposition scheme for the deformation gradient to define the heated, Ω'_T, and the stress-free, Ω'_M, intermediate configurations [49, 50].

The relevant definitions and mathematical derivatives are summarized as follows [49,50]:

The deformation gradient tensor: $F = \text{Grad } x = \frac{\partial x}{\partial X}$ (8.10)

$$F = F_M F_T \tag{8.11}$$

Where Grad x is a continuous one-to-one mapping of the reference position **X** to the deformed position in **Equation (8.10)**. **Equation (8.11)** reflects the multiplicative split of the deformation gradient into thermal (F_T) and mechanical (F_M) components [332,333,334]. There is also an assumption that the thermal deformation is isotropic, which allows the thermal deformation gradient to be expressed as:

$$F_T = \Theta_T^{1/3} I \tag{8.12}$$

where Θ_T=det(F_T) is the thermal volumetric deformation. To model the stress relaxation response, F_M is split further multiplicatively into elastic (F^e_M) and viscous (F^v_M) components:

$$F_M = F^e_M F^v_M \tag{8.13}$$

where F^v_M is a mapping from $\mathbf{\Omega'_T}$ to a stress-free intermediate configuration $\mathbf{\Omega'_M}$. As explained [335], such nonequilibrium processes could consist of numerous states, and also **Equation (8.12)** can be described practically as

$$F_M = F^e_{Mi} F^v_{Mi}, \; i=1,2,3,4...q \tag{8.14}$$

Even so, it is considered helpful only to have one stress relaxation process to simplify the model. Since amorphous polymers exhibit extensive various volumetric and

deviatoric behaviour, F_M is also multiplicatively decomposed into volumetric Θ_M and deviatoric components $\overline{F_M}$ [336,337].

$$\overline{F_M} = \Theta_M^{-1/3} F_M \tag{8.15}$$

where Θ_M=det(F_M) is the mechanical component volumetric deformation. The total volumetric deformation is fallen as $\Theta = \Theta_T \Theta_M$. There is an assumption that the stress relaxation response is purely deviatoric such that the volumetric response caused by mechanical deformation is time-independent [50]. This can be easily understood and a good approximation for most polymers can be achieved since these exhibit only small changes in the bulk modulus, usually about a factor of two, over a wide range of time and frequency. Meanwhile, the shear modulus can vary by orders of magnitudes over the same time and frequency range. This assumption fulfills the isochoric flow assumption results for F_M^e and F_M^v in the following relation [50]:

$$\Theta_M^v = 1, \Theta_M = \Theta_M^e, \overline{F_M} = \overline{F_M}^e F_M^v \tag{8.16}$$

The left and right Cauchy-Green deformation tensors (C_M and b_M) are defined for the mechanical deformation and its components as [49,50]:

$$C_M = F_M F_M^T, C_M^e = F_M^e F_M^{eT}, C_M^v = F_M^v F_M^{vT},$$

$$b_M = F_M F_M^T, b_M^e = F_M^e F_M^{eT}, b_M^v = F_M^v F_M^{vT} \tag{8.17}$$

Combining **Equations (8.15)** and (**8.17)**:

$$\overline{C_M} = \Theta_M^{-2/3} C_M, \ \overline{C}_M^e = \Theta_M^{e(-2/3)} C_M^e, \ \overline{b_M} = \Theta_M^{-2/3} b_M, \ \overline{b}_M^e = \Theta_M^{e(-2/3)} b_M^e \tag{8.18}$$

Finally, the rate of the viscous deformation tensor C_M^v in $\mathbf{\Omega}_0$ can be expressed as an objective rate in the spatial configuration [49]:

$$\pounds_v b_M^e = F_M (\dot{C}_M^{v-1}) F_M^T \tag{8.19}$$

where the operator $\pounds_v(\cdot)$ is the Lie time derivative.

8.2.3 *Constitutive relations*

The modelling of thermo-viscoelastic behaviour and temperature dependence of the stress relaxation response of SMPs are based on the rheological model in **Figure 8.11c** and the analogous decomposition illustration displayed in **Figure 8.12**. When the temperature is much larger than T_g, the viscosity is so small that the effects of visco-

elasticity are negligible. Consequently, the rheological model can be reduced to the equilibrium spring in series with the temperature element. This situation corresponds to the mobile rubbery state, where stress relaxation can occur quickly to prevent the development of large non-equilibrium stresses [338]. As the temperature is lowered and the material begins to enter the glass transition region, the dashpot in the Maxwell element stiffens and the non-equilibrium spring becomes progressively engaged in the mechanical response [338], i.e. viscoelastic stress relaxation becomes dominant. Decreasing the temperature to below the T_g causes the dashpot to stiffen further and the material to build up more non-equilibrium stress. The ability to build up large non-equilibrium stress allows the glassy material to exhibit a dramatically stiffer stress response than the rubbery material [174, 339, 340]. This process continues until the non-equilibrium stress exceeds the yield strength of the non-equilibrium spring, then the resulting viscous flow causes the dashpot to soften [50]. In the following sections, detailed relations will be presented with each analogous decomposition part according to **Figure 8.12**.

8.2.3.1 Thermal strains and structural relaxation (thermal spring part)

An internal variable approach [49,50] was adopted to describe the non-equilibrium structure of the polymer in the formulation of the free energy density. The internal variable fictive temperature, T_f, was introduced as it is already used in modelling the annealing of glass, is such that the non-equilibrium structure at T_f is in equilibrium. In the current polymer system, T_f is T_g [341, 342], as illustrated in **Figure 8.13**. The evolution towards the equilibrium state consists of multiple non-equilibrium states, and can be described by the following nonlinear rate equation, inspired by the Kovacs-Aklonis-Hutchinson-Ramos (KAHR) model for structural relaxation [343-345]:

$$\frac{\partial \delta_i^{-neq}}{\partial t} = -\frac{1}{\tau_{Ri}(T,\delta)}(\delta^{neq} - \Delta a_i (T - T_0)),$$

$$\delta_i(0,T) = 0, \Delta a_i = a_r - a_g, \delta = \sum_i^N \delta_i, \; i=0,1,2,3\ldots.\text{p} \tag{8.20}$$

where δ^{neq} is the stress in the non-equilibrium state, τ_{Ri} is a temperature/structure dependent characteristic know as structural relaxation time, and $\Delta\alpha_i$ is a parameter characterizing the structural relaxation spectrum, α_r and α_g are the thermal expansion coefficients for the rubbery and glass states, respectively. To simplify the model, we

considered only one non-equilibrium state is considered. The fictive temperature T_f can be expressed as [346]:

$$T_f = \frac{1}{a_r - a_g}\delta + T_0 \tag{8.21}$$

To describe the temperature and structure dependence of the characteristic structural relaxation time, the Hodge-Scherer nonlinear extension of the Adam-Gibbs model in terms of the equivalent Williams−Landel−Ferry (WLF) constants was introduced.[49,347,348]

$$\tau_R(T, T_f) = \tau_R \exp\left[-\frac{C_1}{\log e}\left(\frac{C_2(T - T_f) + (T_f - T_g^{ref})}{T(C_2 + T_f - T_g^{ref})}\right)\right] \tag{8.22}$$

where T_g^{ref} is the T_g measured from coefficient of thermal expansion experiments with a specific cooling rate, C_1 and C_2 are the WLF parameters obtained from DMTA tests. Similarly, only one of the non-equilibrium states is considered to simplify the model.

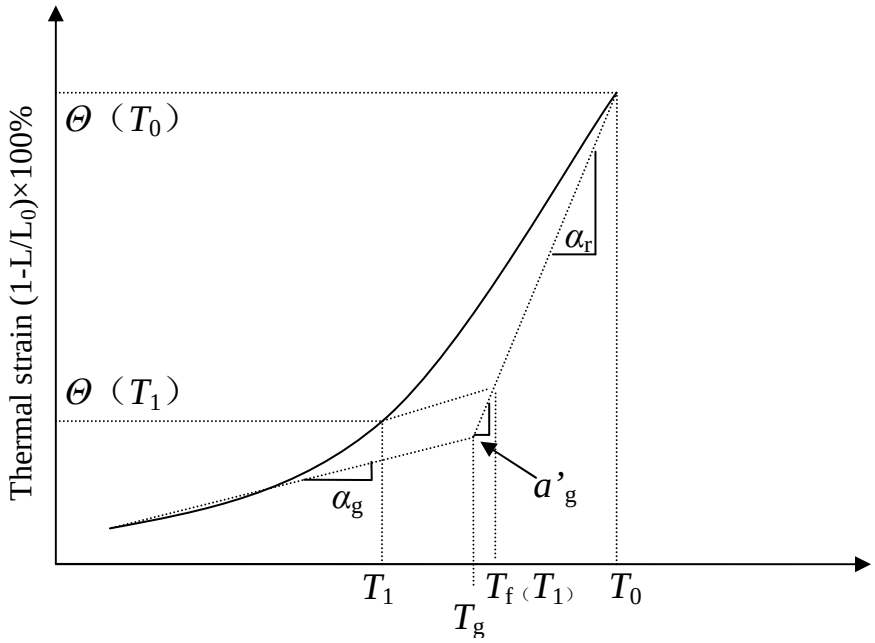

Figure 8.13 Illustration of the volumetric deformation dependency with temperature from T_0 to T_1, T_g is determined by the intersection of the high temperature line, with slope α_r, and low temperature line, with slope α_g. The determination of fictive temperature (T_f) at T_1 is also demonstrated, and the limiting value of T_f is T_g [341, 342].

8.2.3.2 Stress-strain relations for pure SMP (mechanical part)

Constitutive relationships between the stress and strain for the equilibrium behaviour of elastomeric materials are often expressed in terms of strain energy density, *U*, which is

expressed as a function of deformation and material properties [318, 319, 349, 350]. As introduced in S**ection 8.1.2**, the deformation gradient will now be considered and further developed using stretch invariant based strain energy density functions and the Mullins–Tobin concept of hard/soft domains will also be used [59]. The stretch invariants are given as [59, 60]:

$$I_1 = \lambda_1^2 + \lambda_2^2 + \lambda_3^2, \qquad I_2 = \lambda_1^2\lambda_2^2 + \lambda_2^2\lambda_3^2 + \lambda_1^2\lambda_3^2, \qquad I_3 = \lambda_1^2\lambda_2^2\lambda_3^2, \tag{8.23}$$

Where the λ_i are the principal stretches. This investigation only considers I_1 since it is the strongest [351]. The stress-strain relationship under uniaxial tension in the rubbery state of the SMP ($T>T_g$) can be represented by the Arruda and Boyce network model with Langevin chain statistics [319, 350, 352]:

$$\sigma_r = \frac{\mu}{3}\frac{\sqrt{N}}{\lambda_{chain}} \mathrm{L}^{-1}\left(\frac{\lambda_{chain}}{\sqrt{N}}\right)\left(\lambda^2 - \lambda^{-1}\right), \quad \lambda_{chain} = \sqrt{\frac{\left(\lambda^2 + 2\lambda^{-1}\right)}{3}} \tag{8.24}$$

This model is based on the statistics of the underlying macromolecular network where N is the number of "rigid links" between two crosslinking points (and/or strong physical entanglements), λ is the macroscopic axial stretch, σ_r is the true stress, λ_{chain} is the stretch on each chain in the eight chain network, μ is the modulus of the material, the function L^{-1} is the inverse Langevin function, constant relative to the energy of the undeformed chain. The effective chain stretch is given by [59, 60]

$$\mathrm{L}(\beta) = \coth\beta - \beta^{-1} \tag{8.25}$$

For SMP composites, the stress-strain relationships vary considering the different aspect ratios of fillers and reinforcing theories as discussed in **Chapter 2**. The stress-strain equation can be expressed incorporating filler enhancement (i.e. **Equations (8.4)-(8.9)**) [60, 61] as:

$$\sigma_r^{\text{fillers}} = \frac{\phi_s X\mu}{3}\frac{\sqrt{N}}{\Lambda_{chain}} \mathrm{L}^{-1}\left(\frac{\Lambda_{chain}}{\sqrt{N}}\right)\left(\lambda^2 - \lambda^{-1}\right), \tag{8.26}$$

where the ϕ_s is the volume fraction of soft segments, Λ is the applied stretch (the average stretch in the matrix), and X is a amplification factor which depends on filler volume fraction and distribution. The detailed definitions are given as [351]

$$X = 1 + 3.5\left(1-\phi_s\right) + 18\left(1-\phi_s\right)^2, \qquad \Lambda_{\text{chain}} = \sqrt{\frac{X}{3}\left(\lambda^2 + 2\lambda^{-1} - 3\right) + 1} \tag{8.27}$$

The hard and soft segment domains within the polymeric material during the shape deformation/recovery cycle stretch the hard/soft domain configuration [318, 319, 351]. The

volume fraction of the soft domains ϕ_s is changed by adding the nanofillers, and the soft segment contact evolves with deformation as initially occluded regions of soft domains are gradually released. **Equation (8.26)** takes the filler effects into consideration with including the amplification factor and amplified stretch which involve the volume fraction.

8.2.3.3 Viscoelastic relations (mechanical dashpot part)

The molecular processes of viscoelastic flow for finite strain rates and temperatures below T_g in glassy polymers have been attributed to the local intermolecular resistance to segmental rotation and the network resistance to molecular alignment [353-356]. The Eyring relationship [321, 357, 358] has been used to describe the temperature-dependent and stress-activated nature of the viscoelastic flow process.

$$\dot{\gamma}^v = \dot{\gamma}_0 \exp\left(\frac{-E_0}{kT}\left(1-\left(\frac{\bar{\Gamma}}{s_y}\right)\right)\right), \tag{8.28}$$

where $\dot{\gamma}^v$ represents the viscoelastic shear strain rate, $\dot{\gamma}_0$ is a pre-exponential constant, $\bar{\Gamma}$ is the equivalent shear stress, s_y is the yield (activation) stress, which represents the resistance to viscoplastic shear deformation in the material, and E_0 is an activation energy. Further modifications to the equation were proposed, introducing a Taylor expansion, an Arrhenius temperature dependence and the Schere-Hodge relations (**Equation (8.22)**), so that, the viscoelastic flow for the glass transition and rubbery temperature regions can be expressed as [49]

$$\dot{\gamma}^v = \dot{\gamma}_0 \exp\left[\frac{C_1}{\log e}\left(\frac{C_2(T-T_f)+(T_f-T_g^{ref})}{T(C_2+T_f-T_g^{ref})}\left(1-\left(\frac{\bar{\Gamma}}{s_y}\right)\right)\right)\right], \tag{8.29}$$

To model the dashpot softening response, the phenomenological evolution equation used by the referencing model [359] was proposed for the yield strength,

$$\dot{s} = h_0\left(1-\frac{s_y}{s_{yss}}\right)\dot{\gamma}^v, s_y(t=0)=s_{y0} \tag{8.30}$$

Where s_{yss} is the steady-state yield strength, s_{y0} is the initial yield strength, and $s_{yss} < s_{y0}$. When the temperature is raised in the sample (initial stage of recovery), the viscoelastic stress is low and tends to resist the flow as the polymer sample responds to

the internal recovery stress to restore the sample towards its original shape. The stress-strain response can be expressed as [49]:

$$\sigma' = \sigma_r + \sigma_v = 0, \tag{8.31}$$

For Pure SMP $$\sigma' = 0 = \eta(T)\,\dot{\gamma}^{v}\mathrm{t} + \frac{\mu}{3}\frac{\sqrt{N}}{\lambda_{chain}}\mathrm{L}^{-1}\left(\frac{\lambda_{chain}}{\sqrt{N}}\right)\left(\lambda^2 - \lambda^{-1}\right) \tag{8.32}$$

For SMP nanocomposites $$\sigma' = 0 = \eta(T)\,\dot{\gamma}^{v}\mathrm{t} + \frac{\phi_s X\mu}{3}\frac{\sqrt{N}}{\Lambda_{chain}}\mathrm{L}^{-1}\left(\frac{\Lambda_{chain}}{\sqrt{N}}\right)\left(\lambda^2 - \lambda^{-1}\right) \tag{8.33}$$

where η is the viscosity which can be expressed as [49].

$$\eta(T) = \eta_{Sg}^{ref}\,\dot{\frac{Q_s}{T}}\frac{s}{s_y}\exp\left[-\frac{C_1}{\log e}\left(\frac{C_2(T - T_{\mathrm{f}}) + (T_{\mathrm{f}} - T_g^{\mathrm{ref}})}{T(C_2 + T_{\mathrm{f}} - T_g^{\mathrm{ref}})}\right)\right]\left[\sinh\left(\frac{Q_s}{T}\frac{s}{s_y}\right)\right]^{-1}, \tag{8.34}$$

where η_{Sg}^{ref} is the characteristic shear viscosity, s is the flow stress, and Q_{S} is an activation constants. Considering, **Equation (8.29)**, then

$$\eta(T)\,\dot{\gamma}^{v} = \dot{\gamma}_0\,\eta_{Sg}^{ref}\frac{Q_s}{T}\frac{s}{s_y}\exp\left[\frac{C_1}{\log e}\left(\frac{C_2(T - T_{\mathrm{f}}) + (T_{\mathrm{f}} - T_g^{\mathrm{ref}})}{T(C_2 + T_{\mathrm{f}} - T_g^{\mathrm{ref}})}\right)\frac{\overline{\Gamma}}{s_y}\right]\left[\sinh\left(\frac{Q_s}{T}\frac{s}{s_y}\right)\right]^{-1} \tag{8.35}$$

Then, the **Equation (8.34)** can be written:

For Pure SMP

$$\sigma' = 0 = \mathrm{t}\,\dot{\gamma}_0\,\eta_{Sg}^{ref}\frac{Q_s}{T}\frac{s}{s_y}\exp\left[\frac{C_1}{\log e}\left(\frac{C_2(T - T_{\mathrm{f}}) + (T_{\mathrm{f}} - T_g^{\mathrm{ref}})}{T(C_2 + T_{\mathrm{f}} - T_g^{\mathrm{ref}})}\right)\frac{\overline{\Gamma}}{s_y}\right]\left[\sinh\left(\frac{Q_s}{T}\frac{s}{s_y}\right)\right]^{-1} + \frac{\mu}{3}\frac{\sqrt{N}}{\lambda_{chain}}\mathrm{L}^{-1}\left(\frac{\lambda_{chain}}{\sqrt{N}}\right)\left(\lambda^2 - \lambda^{-1}\right) \tag{8.36}$$

For SMP nanocomposites

$$\sigma' = 0 = \mathrm{t}\,\dot{\gamma}_0\,\eta_{Sg}^{ref}\frac{Q_s}{T}\frac{s}{s_y}\exp\left[\frac{C_1}{\log e}\left(\frac{C_2(T - T_{\mathrm{f}}) + (T_{\mathrm{f}} - T_g^{\mathrm{ref}})}{T(C_2 + T_{\mathrm{f}} - T_g^{\mathrm{ref}})}\right)\frac{\overline{\Gamma}}{s_y}\right]\left[\sinh\left(\frac{Q_s}{T}\frac{s}{s_y}\right)\right]^{-1} + \frac{\phi_s X\mu}{3}\frac{\sqrt{N}}{\Lambda_{chain}}\mathrm{L}^{-1}\left(\frac{\Lambda_{chain}}{\sqrt{N}}\right)\left(\lambda^2 - \lambda^{-1}\right) \tag{8.37}$$

8.2.4 *Model inputs*

All the relevant definitions and data sources are given in **Table 8.2**, along with references. are also attached. A complete list of the modelling input values is given in

Table 8.3. Some data entries have been simplified according to the references and sources in **Table 8.2** to fit the often purpose constitutive model.

Table 8.2 Parameters of the preliminary thermoviscoelastic constitutive model

Parameters	Keynotes	Resources or references
T_g^{ref}	Referenced glass transition temperature	DSC/DMTA
a_r	Thermal expansion coefficients of rubber state	Fit result from DSC/DMTA data
a_g	Thermal expansion coefficients of glassy state	Fit result from DSC/DMTA data
C_1	WLF parameters	Fit result from DSC/DMTA data
C_2	WLF parameters	Fit result from DSC/DMTA data
ϕ_s	Soft segment volume content	Nanoindentation
μ	Shear modulus	Calculation from experimental
N	Number of statistical link	Calculation from experimental
$\overline{\Gamma}$	the equivalent shear stress, $\overline{\Gamma}=\delta/\sqrt{3}$	Tensile
E_g	Glass state modulus	Tensile/DMTA
h_0	Rubber state modulus	Tensile/DMTA
$\dot{\gamma}_0$	Material constant	As indicated in Ref.[49,318]
η_{Sg}^{ref}	Material constant	As indicated in Ref.[49]
$Q_S/\ s_y$	Ratio of the activation constants and the yielding strength	Calculation as indicated in Ref.[49]
s_{yss}/s_{y0}	The ratio of steady-state yielded and initial yielding strength of the material	uniaxial and thermal cyclic tensile

8.2.5 *Comparison of constitutive modelling and experimental results*

The constitutive relations were determined using the data listed in **Table 8.3** and the algorithm described by **Equations (8.20)**-(**8.37)** in **section 8.2.3**, and then used to simulate the dynamic thermal-mechanical response of the nanocomposites (**Equations (8.32)** and **(8.33)**). The thermo-viscoelastic model was also used to reproduce the shape memory behaviour of the nanocomposites (**Equations (8.36)** and (**8.37)**) in a condition of isothermal recovery with a fixed pre-stretch strain and at a constant temperature.

Table 8.3 Input values for the constitutive model for different samples

Parameters	Pure	CNP			CNF			MWNT			SWNT		
(Unit)	SMP	1 wt.%	2 wt.%	3 wt.%	1 wt.%	2 wt.%	3 wt.%	1 wt.%	2 wt.%	3 wt.%	1 wt.%	2 wt.%	3 wt.%
T_g^{ref} (°C)	53	59.5	61.5	63	65	72	70	69	68	72	67	72.5	70
a_r ($\times 10^{-4}$°C^{-1})	6.84	6.62	6.24	5.92	5.73	5.34	5.43	5.62	5.41	5.21	5.69	5.23	5.17
a_g ($\times 10^{-4}$°C^{-1})	2.92	2.98	3.12	3.2	3.35	3.76	3.61	3.43	3.71	3.89	3.25	3.92	4.01
C_1	12.7	10.6	10.2	10.1	9.7	9.6	9.7	9.7	9.6	9.3	9.7	9.8	7.6
C_2 (°C)	49.8	31.3	32.1	31.7	27.7	25.3	25.5	27.5	25.9	26.3	27.3	24.4	19.6
N	13	26	34	36	14	21	26	19	24	30	27	32	40
$\overline{\Gamma}$ (MPa)	1.7	2.9	3.6	4.7	3.5	4.6	6.4	3.5	4.6	6.9	4.8	7.1	8.5
E_g (MPa)	3	5	6.2	8.1	6	8	11	6	8	12	8.4	12.3	14.7
μ (MPa)	330	330	330	330	330	330	330	330	330	330	330	330	330
h_0 (MPa)	0.2	0.2	0.2	0.2	0.2	0.2	0.2	0.2	0.2	0.2	0.2	0.2	0.2
$\dot{\gamma}_0$ (s^{-1})	1.7	14.1	33.6	97.6	30.	89.5	335.5	30.0	89.5	453.3	106.1	508.2	1044.0
η_{Sg}^{ref} (MPa/s)	15000	15000	15000	15000	15000	15000	15000	15000	15000	15000	15000	15000	15000
Q_S/ s_y (K/MPa)	100	100	100	100	100	100	100	100	100	100	100	100	100
s_{yss} / s_{y0}	0.6	0.4	0.34	0.35	0.31	0.29	0.22	0.33	0.26	0.2	0.44	0.34	0.29

8.2.5.1 Thermal visco-elastic properties

Figure 8.14 plots the storage modulus obtained from both the experimental data and simulation results for the pure PS.

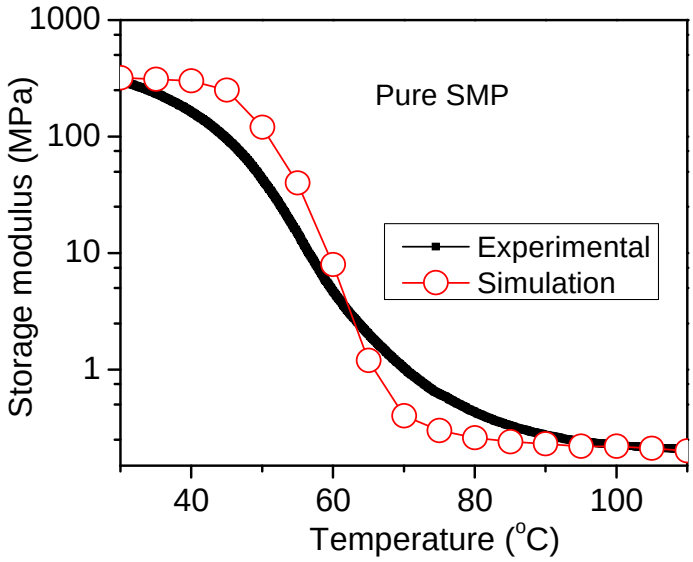

Figure 8.14 Storage modulus comparison for pure SMPS from simulation and experiment.

The storage modulus (~300 MPa) measured by the DMTA is a value between the Young's modulus (88 MPa from uniaxial tensile experiments) and nanoindentation elastic modulus (~1 GPa). These differences can be attributed to the different testing methods and their related theories. In this section, the glassy/rubbery storage moduli were used to compare with the theoretical analysis results, as they showed a consistent change with temperature, especially when the temperature is around T_g. The changes in modulus when the temperature crossing T_g obtained from experimental results are much lower than those from the theoretical analysis because the model considered an ideal system without internal defects and other imperfections. The practical system is much more complicated, and many possible factors could lead to a reduction of the modulus when the temperature increases, such as high distribution of molecular weight and non-uniformity of cross-linking points.

Theoretical analysis was also carried out for the nano-carbon filled composites, by inputting data for the composite materials into **Equations (8.32)-(8.33)**, and the comparisons between the simulation and experiment are made in **Figure 8.15**. Apart from the similar phenomena in **Figure 8.14** as explained before, it is also observed that the differences between simulation and experiment are not as significant for the CNT filled composites,

especially for the CNT/PS with filler concentration above 1 wt.%. This is because the model considers the enhancement effect from the nanofillers as shown in **Equations (8.6)** and (**8.9)**, and also the multiple effects of the filler aspect ratio and the filler volume fraction. From **Figure 8.15**, it can be seen that the theoretical results show good consistency with the experimental results for the composites with rod like nano-carbon fillers (b_2, b_3, c and d series), especially when the temperature is higher than T_g (viscoelastic state).

8.2.5.2 Shape recovery behaviour

The shape memory behaviour of the materials was simulated using **Equations (8.36)-(8.37)**, which describe the time-dependent thermoviscoelasticity of SMPs and nanocomposites. The analysis of shape recovery assumed the conditions of 100% pre-deformation strain and a constant heating temperature of 80 °C. All relevant parameters are shown in **Table 8.3**, and some numerical conversions were processed through **Equations (8.20)-(8.30)**. **Figure 8.16** compares the theoretical and experimental strain recovery ratios of pure SMPS. From **Figure 8.16**, it is observed that about 97% of the pure polymer strain can be recovered within 22 seconds, while a complete recovery fallen as long as 26 sec.

The curves of the recovery ratios vs. time exhibit similar patterns, showing a good match between the simulation results and the experimental ones. However, the experimental results show a consistently longer recovery time. The discrepancy may be due to stress relaxation of the sample during recovery which could slow down the recovery process [176], and this has not been considered in the theoretical analysis. It has been reported [360] that samples stretched at a higher temperature show a higher onset temperature for recovery, because the shape recovery is a complicated procedure containing different chain movements with different energy levels.

The agreement between the theoretical and experimental results presented in **Figure 8.16** is qualitatively adequate for the pure SMP, but not sufficiently good to explain the recovery behaviour of the composites with different particles. The same assumption was made with the conditions of 100% pre-deformation strain under heating to a constant temperature of 80 °C.

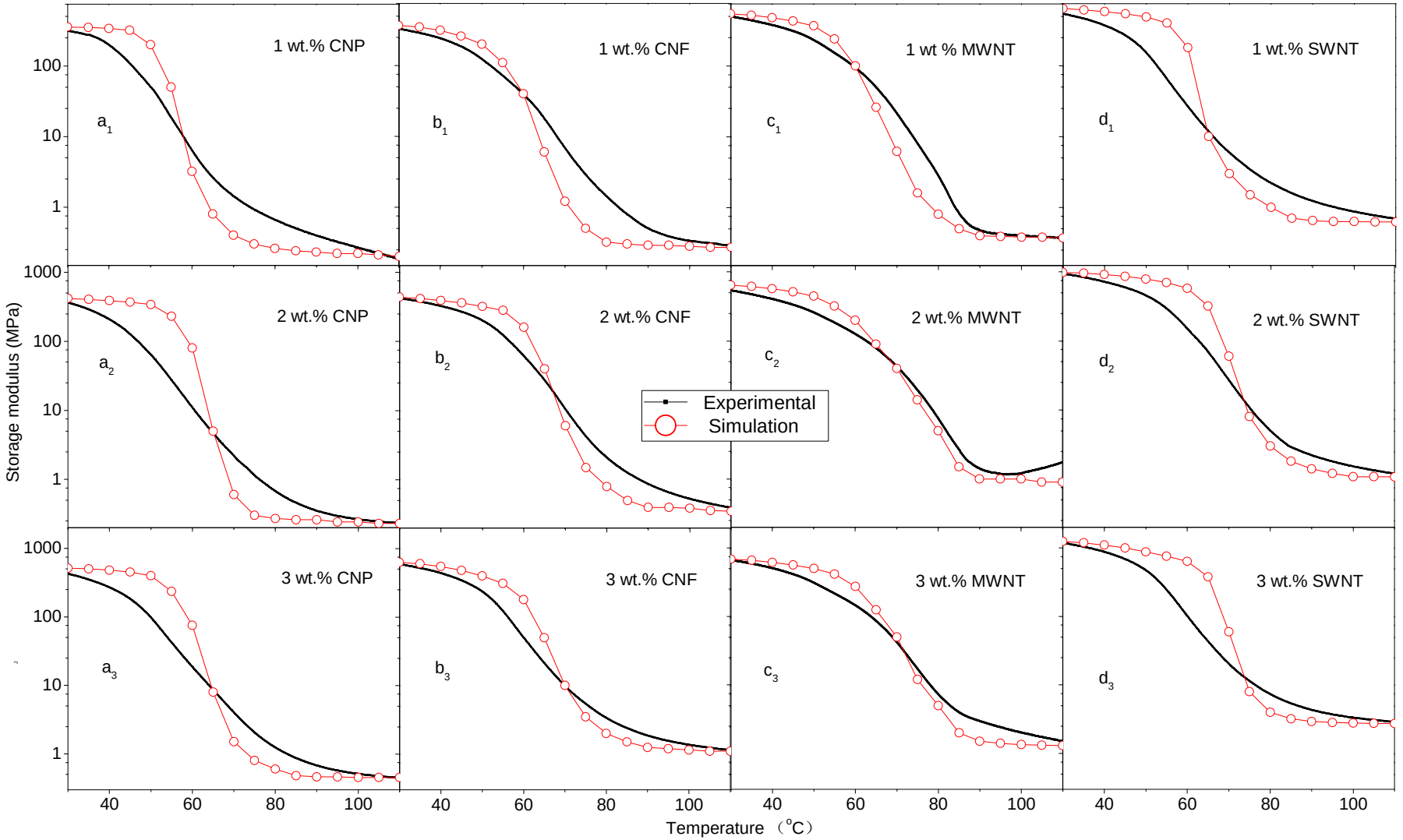

Figure 8.15 Comparison of simulated and experimental storage modulus results for nano-carbon filled composites

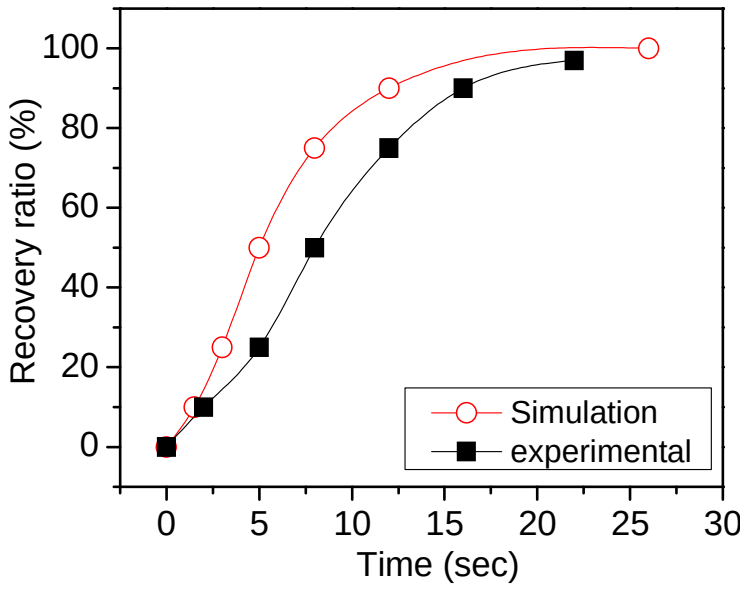

Figure 8.16 Comparison of recovery results from experimental and simulation for pure SMPS. The pre-deformation ratio is 100 % and the test/simulation temperature is 80 °C.

The theoretical simulation inputs were either obtained directly from **Table 8.3**, or numerically generated by **Equations (8.20)-(8.30)**, and then imported into **Equation (8.36)**. The selected samples were the composites with 2 wt.% CNP, CNF, MWNT and SWNT, respectively, and the results are shown in **Figure 8.17**. **Figure 8.17** shows quite different information for different samples. Reasonable agreements between the theoretical and experimental results was obtained for the 2 wt.% CNP/PS and MWNT/PS samples. When the deformation occurs early, the composite needs absorb enough thermal energy to resist the recoverable elastic entropic force of the network elements. Afterwards, the recovery accelerates and rapidly relieves most strains. Towards the end of the process, recovery becomes quite slow as the internal stress has been completely released. In this case, the experimentally measured non-isothermal recovery and the values from the theoretical prediction are in good agreement. There are always some minor unrecoverable strains in the experimental results generated during the pre-deformation such as unrecoverable chain stretch, chain breaking and movement of hard segments.

Theoretical predictions show that the higher the volume fraction of filler that the composite contains, the longer the time is needed for a full recovery. However, the experimental results showed a much faster recovery than the theory predicts for the 2 wt.% CNP/PS, MWNT/PS, SWNT/PS composites. The reasons are unclear and need to be investigated in future work.

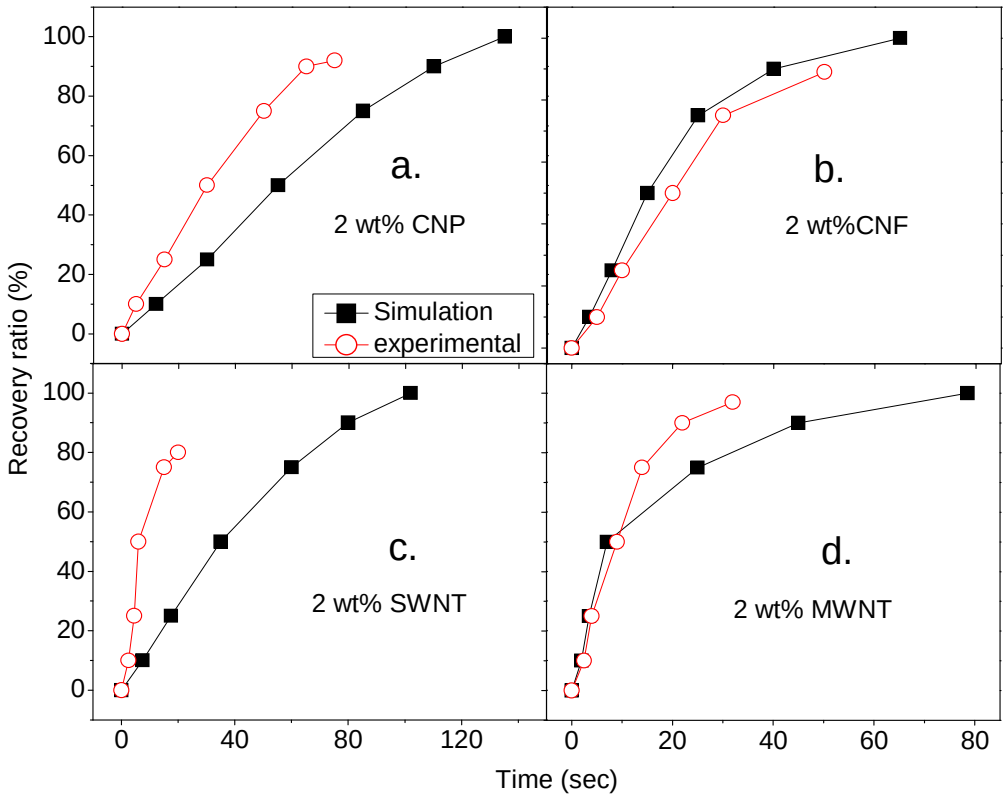

Figure 8.17 Comparison of recovery results from experiment and simulation for shape memory nanocomposites with 2 wt.% nanofillers, the pre-deformation ratio is 100 % and test/simulation temperature is 80 °C.

8.3 Summary

Theoretical analyses based on the experimental results were presented in this chapter. Size effect and geometry factors were considered as two dominant factors in predicting the efficiency of nanofiller enhancement. A modified Takayanagi two-phase model with taking in account the interface effect was modified to investigate the nanoparticle size effect. The elastic theories based on the Halpin–Tsai and Mori– Tanaka models were employed to understand better on the reinforcement brought about by the high aspect ratio nanoparticles. Theoretical modelling of the aspect ratio effect on the particle enhancement efficiency revealed a significant effect in improving the nanocomposite stiffness. The Halpin–Tsai equation proved less effective than the Mori–Tanaka one when calculating the reinforcement for fibres with various aspect ratios. With fixed modulus and aspect ratio of the nanofillers, the Mori–Tanaka model predicted that unidirectional reinforcement was considerably greater than that by the Halpin–Tsai model. Each theory, however, does converse to the same value for very high filler aspect ratios, corresponding to the rule of mixtures. Overall, both the theoretical and

experimental results demonstrate considerable potential for improvement in nanocomposite stiffness by increasing the aspect ratio of the nanofillers, whether from improvements in individual filler dispersion, or synthesis of higher aspect ratio fillers.

The constitutive relationships of the amorphous SMPs and nanocomposites were derived based on the literature survey and detailed kinematic equations. A multi-component model was adopted and modified to fit the SMPs studied and their nanocomposite systems. Moreover, elastic theory was embedded in the relationship to improve the modelling of thermoviscoelastic and shape recovery behaviour of the SMP nanocomposites. For both the SMP and its nanocomposites, the numerical simulation results for thermoviscoelastic behaviour agreed with the experimental ones. A significant decrease in modulus was indicated by the simulation results, due to its assumption of the transformation of the molecular chains. Thermally triggered shape recovery simulations were also performed by calculating the recovery time. A good match between the simulation results and the experimental ones was obtained. The experimental results showed longer recovery time due to relaxation as that was not taken into account in the theoretical equations. For nanocomposites, the simulation of shape recovery sometimes give contradictory results against the experimental results, which show faster recovery than the simulated ones. The reasons for this are unclear and need to be investigated in future work.

Chapter 9

CONCLUSIONS

Since the project contents cover a range of academic disciplines including polymer chemistry, mechanical engineering and chemical engineering, the main conclusions are classified into four categories.

For smart shape memory polymer/nanocomposites fabrication:

1. SMPs and their nanocomposites were fabricated by polymerization, which offers a better chance to fulfil the best properties such as higher strength and conductivity, through adding functional nanoparticles into the matrix.

2. The nanoparticles affect the material properties dramatically according to their physical properties such as modulus, particle shape, dimensional size, surface features. Moreover, the reinforcing effects of nanoparticles are highly dependent on the fabrication technique, as the dispersion state of nanoparticles will affect the particles enhancement of the matrix more than the particle physical properties.

3. The wet-chemical synthesis method was identified as an effective way of achieving the uniform distribution of nanofillers in the SMPS matrix.

For the physical performance of the fabricated materials:

1. Mechanical and thermal properties of SMPU were strongly reinforced by the treated attapulgite clay. The hardness-temperature analysis showed that Vickers microindentation could be used to detect the T_g of SMPs or composites empirically. A good shape memory effect was observed in the nanocomposites. PU-based composites containing 30 wt.% treated clay nanoparticles exhibited the same capability of shape recovery as pure PU although the recovery speed was slightly slower.

2. Improvements of mechanical and thermal properties and shape memory effects were observed by introducing three different nanofillers (alumina, silica and clay) into the SMPS matrix. The nanocomposites with heat-treated nanoclay achieved the best

improvement of all aspects tested. Thermal cycling tests indicated that the recovery rates of all nanocomposite SMPs were above 85%, and good shape recovery ability was achieved.

3. The mechanical and thermo-mechanical results from the tensile, nanoindentation and DMTA tests revealed enhancements of electro-active PS-based nanocomposites with incorporation of CNPs into the PS matrix. The electrical tests indicated that a two-phase conductive system was formed with a percolation threshold value of 3.5 wt%. The conductivity and dielectric constants changed dramatically as a function of frequency, temperature and CNP concentration. Shape recovery results indicated that these smart nanocomposites had potential application in microactuation.

4. The SWNT/PS sample displayed the highest storage modulus and Tg. Elastic modulus and hardness results from the nanoindentation tests proved the enhancement by carbon nano-fillers. The 2 wt.% SWNT/PS composites achieved the best mechanical properties among all the samples with nanometre localisation. Thermal cycling results indicated that the recovery rate of the polymer was reduced with the addition of nanofillers. Shape recovery demonstrations were performed under different triggering conditions, thermal stimulus and electro-active. The SWNT/PS sample presented the fastest recovery speed and a good recovery at different pre-deformation conditions. Stent demonstrations were performed with specific designs on pure SMPS and 2 wt.% SWNT/PS samples, and all the devices exhibited recovery under the test conditions. The stents made from the composites gave the fastest recovery speed as well as the best recovery ratio, which implied the possibility of applying these materials in such designs for various purposes, with an effective expansion function.

For the shape memory effect and demonstration of potential applications:

1. Embedding nanoparticles could decrease the shape memory efficiency on the same time as bringing strong enhancement to the soft matrix.

2. The shape recovery demonstrations were carried out on various designs such as grippers, stents and cantilevers, showing the possibility of applying the shape memory nanocomposites in some fields. Biological stent models were manufactured with pure

SMPs and nanocomposites, and the expansion behaviours caused by the shape recovery action of the materials were demonstrated and evaluated.

3. Electrical triggering shape recovery was demonstrated with CNP/PS cantilevers, and successful electro-shape recovery was achieved.

For the theoretical analysis:

1. A modified multi-phase model was used to predict the composite modulus as a function of particle size. The modelling results clearly showed that the particle size played a more important role than the filler modulus in reinforcement for the spherical particulate-filled polymer composites. For the composite system based on the rod particles, the modified multi-phase modelling results did not show consistency with the experimental results because of its limited expressing on the filler aspect ratio effect. Discussion of the aspect ratio effect on nanofiller enhancement was based on the Halpin–Tsai and Mori–Tanaka models. The calculated outcomes revealed that the composite modulus could be significantly affected by physical factors such as modulus, aspect ratio, geometry, and volume fraction of the filler. Both the modelling and experimental results showed that introducing fillers with high aspect ratio lead to more effective enhancement by increasing the amount of stress transferred to the filler. The enhancement from the layered platelet particles was also modelled and compared with results from the treated-clays to expand the discussion of geometrical effects 3-D. The aspect ratio and geometry of the nanofillers play a more important role in reinforcing the polymers than the particle size and stiffness of the individual particles.

2. Constitutive models for the thermo-viscoelastic behaviour and shape memory recovery were built for the nanocomposites based on a multi-component model and the composite elastic theory. The numerical simulations results for thermo-viscoelastic property agreed with the experimental ones. A significant decrease in modulus was seen from the simulation results, due to its assumption of ideal transformation of the molecular chains. Thermal triggering of the shape recovery was simulated through the calculation of the recovery time under the given conditions. The experimental results showed longer recovery time than the simulation. For the nanocomposites, the simulation of shape recovery time revealed confusing results compared with the experimental ones, a matter which needs to be investigated in future work.

Chapter 10

FUTURE WORK

This research work has shown that the SMP material properties can be modified through incorporating functional nanoparticles to meet the requirements of a specific application. Successful demonstrations of micro-devices and their fabrication under various external triggering conditions have been performed. However, there are some remaining questions:

a. Two way recovery is still unavailable as triggering factors such as thermal could only start recovery in a one-way cycle.

b. The precise control of multi step recovery needs to be improved as there was a poor relationship between the control input and the recovery level.

c. The available current control methods (thermal or electrical) both have great limitations, especially in some critical applications such as in human body. Advanced remote triggering methods need be proposed and validated.

For future work, the investigation of SMPs or its nanocomposites would be continued for application in the related areas of Bio-MEMS or bio-medical devices. Aiming to work out commercial application in the biological field, some further efforts needs to be made in the following directions:

- Novel shape memory polymer systems should be developed using biocompatible polymers especially biocompatible SMPU or its copolymers.
- New functional nanoparticles should be applied to introduce new triggering possibilities for the nanocomposites, for example magnetic nanofillers, UV sensitive fillers, fillers with chemical groups with responding to pH values.
- Other application fields should be explored with new models and integrated systems, such as bio-robotic parts.
- The constitutive model should be used and imported into the materials database of Finite Element Analysis (FEA) software and tested, as the properties of SMPs and their nanocomposites have not been developed for FEA yet.

BIBLIOGRAPHY

1. M. Behl and A. Lendlein, Triple-shape polymers, *Journal of Materials Chemistry*, 20, 3335-3345 (2010).
2. M. Behl, M. Y. Razzaq and A. Lendlein, Multifunctional Shape-Memory Polymers, *Advanced Materials*, 22, 3388-3410 (2010).
3. A. Lendlein, J. Zotzmann, Y. K. Feng, A. Alteheld and S. Kelch, Controlling the Switching Temperature of Biodegradable, Amorphous, Shape-Memory Poly(rac-lactide)urethane Networks by Incorporation of Different Comonomers, *Biomacromolecules*, 10, 975-982 (2009).
4. M. Behl and A. Lendlein, Shape-memory polymers, *Materials Today*, 10, 20-28 (2007).
5. A. Lendlein, H. Jiang, O. Junger and R. Langer, Light-induced shape-memory polymers, *Nature*, 434, 879-882 (2005).
6. K. Gall, C. M. Yakacki, Y. P. Liu, R. Shandas, N. Willett and K. S. Anseth, Thermomechanics of the shape memory effect in polymers for biomedical applications, *Journal of Biomedical Materials Research Part A*, 73A, 339-348 (2005).
7. K. Gall, M. Mikulas, N. A. Munshi, F. Beavers and M. Tupper, Carbon fiber reinforced shape memory polymer composites, *Journal of Intelligent Material Systems and Structures*, 11, 877-886 (2000).
8. K. Gall, M. L. Dunn, Y. P. Liu, G. Stefanic and D. Balzar, Internal stress storage in shape memory polymer nanocomposites, *Applied Physics Letters*, 85, 290-292 (2004).
9. K. Gall, D. L. MeDowelf, M. A. Di Prima, M. Lesniewski, T. Sanderson and D. Campbell, Cyclic and monotonic behaviour of epoxy shape memory polymer foam, *Advances in Heterogeneous Material Mechanics 2008*, 819-819 (2008).
10. H. Tobushi, H. Hara, E. Yamada and S. Hayashi, Thermomechanical properties in a thin film of shape memory polymer of polyurethane series, *Smart Materials & Structures*, 5, 483-491 (1996).
11. H. Tobushi, K. Okumura, M. Endo and S. Hayashi, Thermomechanical properties of polyurethane shape-memory polymer foam, *Shape Memory Materials and Its Applications*, 394-3, 577-580 (2001).
12. H. Tobushi, K. Okumura, S. Hayashi and N. Ito, Thermomechanical constitutive model of shape memory polymer, *Mechanics of Materials*, 33, 545-554 (2001).
13. H. Tobushi, S. Hayashi, K. Hoshio, Y. Makino and N. Miwa, Bending actuation characteristics of shape memory composite with SMA and SMP, *Journal of Intelligent Material Systems and Structures*, 17, 1075-1081 (2006).
14. H. Tobushi, K. Hoshio, S. Hayashi and N. Miwa, Shape memory composite of SMA and SMP and its property, *Engineering Plasticity and Its Applications from Nanoscale to Macroscale, Pts 1 and 2*, 340-341, 1187-1192 (2007).
15. H. Tobushi, S. Hayashi, Y. Sugimoto and K. Date, *Thermec 2009, Pts 1-4*, 2009.
16. Q. H. Meng, J. L. Hu, Y. Zhu, J. Lu and B. H. Liu, Biological Evaluations of a Smart Shape Memory Fabric, *Textile Research Journal*, 79, 1522-1533 (2009).
17. Q. H. Meng and J. L. Hu, A review of shape memory polymer composites and blends, *Composites Part a-Applied Science and Manufacturing*, 40, 1661-1672 (2009).
18. S. J. Chen, J. L. Hu, C. W. Yuen and L. K. Chan, Novel moisture-sensitive shape memory polyurethanes containing pyridine moieties, *Polymer*, 50, 4424-4428 (2009).
19. Q. H. Meng and J. L. Hu, Self-organizing alignment of carbon nanotube in shape memory segmented fiber prepared by in situ polymerization and melt spinning, *Composites Part a-Applied Science and Manufacturing*, 39, 314-321 (2008).

20. Q. Meng, J. Hu and S. Mondal, Thermal sensitive shape recovery and mass transfer properties of polyurethane/modified MWNT composite membranes synthesized via in situ solution pre-polymerization, *Journal of Membrane Science*, 319, 102-110 (2008).
21. Q. H. Meng, J. L. Hu, Y. Zhu, J. Lu and Y. Liu, Polycaprolactone-based shape memory segmented polyurethane fiber, *Journal of Applied Polymer Science*, 106, 2515-2523 (2007).
22. Q. H. Meng, J. L. Hu, Y. Zhu, J. Lu and Y. Liu, Morphology, phase separation, thermal and mechanical property differences of shape memory fibres prepared by different spinning methods, *Smart Materials & Structures*, 16, 1192-1197 (2007).
23. J. L. HU, *Shape memory polymers and textiles*, CRC press (2007).
24. H. Huang, Z. P. Mao and W. D. Yu, Temperature-sensitive Composite Membranes with "Double Switch" on Water Vapor Permeability, *Textile Bioengineering and Informatics Symposium Proceedings, Vols 1 and 2*, 286-291 (2008).
25. W. M. Huang, B. Yang, N. Liu and S. J. Phee, Water-responsive programmable shape memory polymer devices, *International Conference on Smart Materials and Nanotechnology in Engineering, Pts 1-3*, 6423, S4231-S4231 (2007).
26. W. M. Huang, C. W. Lee and H. P. Teo, Thermomechanical behaviour of a polyurethane shape memory polymer foam, *Journal of Intelligent Material Systems and Structures*, 17, 753-760 (2006).
27. B. Yang, W. M. Huang, C. Li, L. Li and J. H. Chor, Qualitative separation of the effects of carbon nano-powder and moisture on the glass transition temperature of polyurethane shape memory polymer, *Scripta Materialia*, 53, 105-107 (2005).
28. B. Yang, W. M. Huang, C. Li and J. H. Chor, Effects of moisture on the glass transition temperature of polyurethane shape memory polymer filled with nano-carbon powder, *European Polymer Journal*, 41, 1123-1128 (2005).
29. B. Yang, W. M. Huang, C. Li, C. M. Lee and L. Li, On the enects of moisture in a polyurethane shape memory polymer, *Smart Materials & Structures*, 13, 191-195 (2004).
30. J. S. Leng, D. W. Zhang, Y. Liu, K. Yu and X. Lan, Study on the activation of styrene-based shape memory polymer by medium-infrared laser light, *Applied Physics Letters*, 96 (2010).
31. J. S. Leng, X. L. Wu and Y. J. Liu, Infrared Light-Active Shape Memory Polymer Filled with Nanocarbon Particles, *Journal of Applied Polymer Science*, 114, 2455-2460 (2009).
32. J. S. Leng, H. B. Lv, Y. J. Liu and S. Y. Du, Synergic effect of carbon black and short carbon fiber on shape memory polymer actuation by electricity *Journal of Applied Physics*, 105, 104917 (2009).
33. J. S. Leng, X. Lan, Y. J. Liu and S. Y. Du, Electroactive thermoset shape memory polymer nanocomposite filled with nanocarbon powders, *Smart Materials & Structures*, 18 (2009).
34. H. B. Lv, Y. J. Liu, D. X. Zhang, J. S. Leng and S. Y. Du, Solution-responsive shape-memory polymer driven by forming hydrogen bonding, *Multi-Functional Materials and Structures, Pts 1 and 2*, 47-50, 258-261 (2008).
35. H. B. Lv, J. S. Leng and S. Y. Du, Electro-induced shape-memory polymer nanocomposite containing conductive particles and short fibers - art. no. 69291L, *Behaviour and Mechanics of Multifunctional and Composite Materials 2008*, 6929, L9291-L9291 (2008).
36. J. S. Leng, H. B. Lv, Y. J. Liu and S. Y. Du, Synergic effect of carbon black and short carbon fiber on shape memory polymer actuation by electricity, *Journal of Applied Physics*, 104, 104917 (2008).

37. J. S. Leng, H. B. Lv, Y. J. Liu and S. Y. Du, Water-driven programable polyurethane shape memory polymer: Demonstration and mechanism, *Applied Physics Letters*, 92, 114105 (2008).
38. J. S. Leng, H. B. Lu, Y. J. Liu and S. Y. Du, Conductive nanoparticles in electro activated shape memory polymer sensor and actuator, *Proc. SPIE*, 6931, 693109 (2008).
39. W. Small, E. Gjersing, J. L. Herberg, T. S. Wilson and D. J. Maitland, Magnetic resonance flow velocity and temperature mapping of a shape memory polymer foam device, *Biomedical Engineering Online*, 8, 42-50 (2009).
40. G. M. Baer, T. S. Wilson, W. Small, J. Hartman, W. J. Benett, D. L. Matthews and D. J. Maitland, Thermomechanical Properties, Collapse Pressure, and Expansion of Shape Memory Polymer Neurovascular Stent Prototypes, *Journal of Biomedical Materials Research Part B-Applied Biomaterials*, 90B, 421-429 (2009).
41. W. Small, P. R. Buckley, T. S. Wilson, J. M. Loge, K. D. Maitland and D. J. Maitland, Fabrication and characterization of cylindrical light diffusers comprised of shape memory polymer, *Journal of Biomedical Optics*, 13 (2008).
42. T. S. Wilson, J. P. Bearinger, J. L. Herberg, J. E. Marion, W. J. Wright, C. L. Evans and D. J. Maitland, Shape memory polymers based on uniform aliphatic urethane networks, *Journal of Applied Polymer Science*, 106, 540-551 (2007).
43. W. Small, T. S. Wilson, P. R. Buckley, W. J. Benett, J. A. Loge, J. Hartman and D. J. Maitland, Prototype fabrication and preliminary in vitro testing of a shape memory endovascular thrombectomy device, *Ieee Transactions on Biomedical Engineering*, 54, 1657-1666 (2007).
44. G. M. Baer, W. Small, T. S. Wilson, W. J. Benett, D. L. Matthews, J. Hartman and D. J. Maitland, Fabrication and in vitro deployment of a laser-activated shape memory polymer vascular stent, *Biomedical Engineering Online*, 6, 43-50 (2007).
45. G. Baer, T. S. Wilson, D. L. Matthews and D. J. Maitland, Shape-memory behaviour of thermally stimulated polyurethane for medical applications, *Journal of Applied Polymer Science*, 103, 3882-3892 (2007).
46. W. Small, T. S. Wilson, W. J. Benett, J. M. Loge and D. J. Maitland, Laser-activated shape memory polymer intravascular thrombectomy device, *Optics Express*, 13, 8204-8213 (2005).
47. D. J. Maitland, T. Wilson, D. L. Schumann and G. Baer, Laser-activated shape memory polymer microactuators for treating stroke, *2002 Ieee/Leos Annual Meeting Conference Proceedings, Vols 1 and 2*, 359-360 (2002).
48. H. J. Qi, T. D. Nguyen, F. Castro, C. M. Yakacki and R. Shandas, Finite deformation thermo-mechanical behaviour of thermally induced shape memory polymers, *Journal of the Mechanics and Physics of Solids*, 56, 1730-1751 (2008).
49. T. D. Nguyen, H. J. Qi, F. Castro and K. N. Long, A thermoviscoelastic model for amorphous shape memory polymers: Incorporating structural and stress relaxation, *Journal of the Mechanics and Physics of Solids*, 56, 2792-2814 (2008).
50. T. D. Nguyen, C. M. Yakacki, P. D. Brahmbhatt and M. L. Chambers, Modeling the Relaxation Mechanisms of Amorphous Shape Memory Polymers, *Advanced Materials*, 22, 3411-3423 (2010).
51. A. Olander, AN ELECTROCHEMICAL INVESTIGATION OF SOLID CADMIUM-GOLD ALLOYS, *Journal of the American Chemical Society*, 54, 3819-3833 (1932).
52. J. M. L.C. Chang and T.A. Read, *Trans. AIME*, 191, 47-52 (1951).
53. R. M. Genevray, *The Martensitic Transformation in Muntz Metal.* , MIT, 1953.
54. C. W. Chen, On a mechanism of high temperature intercrystalline cracking, *J. Met. Trans. AIME*, 209, 829-835 (1957).
55. Srinivasan AV and McFarland DM, *Shape Memory Alloys in Smart Structure*, Cambrige University Press (2001).

56. W. J. B. Frederick E. Wang, and Stanley J. Pickart Crystal Structure and a Unique``Martensitic"Transition of TiNi, *Journal of Applied Physics*, 36, 3232-3239 (1965).
57. F. El Feninat, G. Laroche, M. Fiset and D. Mantovani, Shape Memory Materials for Biomedical Applications, *Advanced Engineering Materials*, 4, 91-104 (2002).
58. K. Otsuka and X. Ren, Recent developments in the research of shape memory alloys, *Intermetallics*, 7, 511-528 (1999).
59. B. Y. Li, L. J. Rong, Y. Y. Li and V. E. Gjunter, A recent development in producing porous Ni-Ti shape memory alloys, *Intermetallics*, 8, 881-884 (2000).
60. T. Duerig, A. Pelton and D. Stöckel, An overview of nitinol medical applications, *Materials Science and Engineering A*, 273-275, 149-160 (1999).
61. S. Shabalovskaya, J. Anderegg and J. Van Humbeeck, Critical overview of Nitinol surfaces and their modifications for medical applications, *Acta Biomaterialia*, 4, 447-467 (2008).
62. M. Behl and A. Lendlein, Actively moving polymers, *Soft Matter*, 3, 58-67 (2007).
63. A. Lendlein and M. Behl, Shape-Memory Polymers for Biomedical Applications, *Smart Materials & Micro/Nanosystems*, 54, 96-102 (2009).
64. A. Lendlein and S. Kelch, Degradable, multifunctional polymeric biomaterials with shape-memory, *Functionally Graded Materials Viii*, 492-493, 219-223 (2005).
65. A. Lendlein and S. Kelch, Shape-memory polymers, *Angew Chem Int Ed Engl*, 41, 2035-2057 (2002).
66. Z. Yuan, B. Ji and L. B. Wu, Synthesis and Thermal Induced Shape Memory Properties of Biodegradable Segmented Poly(Ester-Urethane)S, *Acta Polymerica Sinica*, 153-158 (2009).
67. Y. L. Wang, Y. G. Li, Y. F. Luo, M. N. Huang and Z. Q. Liang, Synthesis and characterization of a novel biodegradable thermoplastic shape memory polymer, *Materials Letters*, 63, 347-349 (2009).
68. A. T. Neffe, B. D. Hanh, S. Steuer and A. Lendlein, Polymer Networks Combining Controlled Drug Release, Biodegradation, and Shape Memory Capability, *Advanced Materials*, 21, 3394-3398 (2009).
69. T. Xie and I. A. Rousseau, Facile tailoring of thermal transition temperatures of epoxy shape memory polymers, *Polymer*, 50, 1852-1856 (2009).
70. V. A. Beloshenko and Y. V. Voznyak, Shape memory effect in the epoxy polymer composites with aggregated filler, *Polymer Science Series A*, 51, 416-423 (2009).
71. I. S. Gunes, F. Cao and S. C. Jana, Evaluation of nanoparticulate fillers for development of shape memory polyurethane nanocomposites, *Polymer*, 49, 2223-2234 (2008).
72. T. Pretsch, I. Jakob and W. Muller, Hydrolytic degradation and functional stability of a segmented shape memory poly(ester urethane), *Polymer Degradation and Stability*, 94, 61-73 (2009).
73. V. Lorenzo, A. Diaz-Lantada, P. Lafont, H. Lorenzo-Yustos, C. Fonseca and J. Acosta, Physical ageing of a PU-based shape memory polymer: Influence on their applicability to the development of medical devices, *Materials & Design*, 30, 2431-2434 (2009).
74. Y. Liu, A. Chung, J. L. Hu and J. Lv, Shape memory behaviour of SMPU knitted fabric, *Journal of Zhejiang University-Science A*, 8, 830-834 (2007).
75. J. D. Merline, C. P. R. Nair, C. Gouri, T. Shrisudha and K. N. Ninan, Shape memory characterization of polytetra methylene oxide/poly (acrylic acid-co-acrylonitrile) complexed gel, *Journal of Materials Science*, 42, 5897-5902 (2007).

76. Z. G. Wei, R. Sandstrom and S. Miyazaki, Shape memory materials and hybrid composites for smart systems: Part II Shape-memory hybrid composites, *Journal of Materials Science*, 33, 3763-3783 (1998).
77. J. D. Merline, C. P. R. Nair, C. Gouri, G. G. Bandyopadhyay and K. N. Ninan, Polyether polyurethanes: Synthesis, characterization, and thermoresponsive shape memory properties, *Journal of Applied Polymer Science*, 107, 4082-4092 (2008).
78. H. J. Yoo, Y. C. Jung, N. G. Sahoo and J. W. Cho, Polyurethane-carbon nanotube nanocomposites prepared by in-situ polymerization with electroactive shape memory, *Journal of Macromolecular Science Part B-Physics*, 45, 441-451 (2006).
79. J. W. Xu, W. F. Shi and W. M. Pang, Synthesis and shape memory effects of Si-O-Si cross-linked hybrid polyurethanes, *Polymer*, 47, 457-465 (2006).
80. H. T. Zhuo, J. L. Hu and S. J. Chen, Electrospun polyurethane nanofibres having shape memory effect, *Materials Letters*, 62, 2074-2076 (2008).
81. S. J. Chen, J. L. Hu, Y. Q. Liu, H. M. Liem, Y. Zhu and Y. J. Liu, Effect of SSL and HSC on morphology and properties of PHA based SMPU synthesized by bulk polymerization method, *Journal of Polymer Science Part B-Polymer Physics*, 45, 444-454 (2007).
82. Y. Zhu, J. L. Hu, K. W. Yeung, H. J. Fan and Y. Q. Liu, Shape memory effect of PU ionomers with ionic groups on hard-segments, *Chinese Journal of Polymer Science*, 24, 173-186 (2006).
83. W. M. Huang, N. Liu, X. Lan, J. Q. Lin, J. H. Pan, J. S. Leng, S. J. Phee, H. Fan, Y. J. Liu and T. H. Tong, Formation of Protrusive Micro/nano Patterns atop Shape Memory Polymers, *Advanced Materials Science and Technology*, 614, 243-248 (2009).
84. G. H. Pan, W. M. Huang, Z. C. Ng, N. Liu and S. J. Phee, The glass transition temperature of polyurethane shape memory polymer reinforced with treated/non-treated attapulgite (playgorskite) clay in dry and wet conditions, *Smart Materials & Structures*, 17, 045007 (2008).
85. B. Yang, W. M. Huang, C. Li and L. Li, Effects of moisture on the thermomechanical properties of a polyurethane shape memory polymer, *Polymer*, 47, 1348-1356 (2006).
86. W. M. Huang, B. Yang, L. An, C. Li and Y. S. Chan, Water-driven programmable polyurethane shape memory polymer: Demonstration and mechanism, *Applied Physics Letters*, 86, 114105 (2005).
87. P. D. Fallon, A. P. Gerratt, B. P. Kierstead and R. D. White, Shape Memory Alloy and Elastomer Composite MEMS Actuators, *Nsti Nanotech 2008, Vol 3, Technical Proceedings*, 470-473 (2008).
88. H. B. Lu, K. Yu, Y. J. Liu and J. S. Leng, Sensing and actuating capabilities of a shape memory polymer composite integrated with hybrid filler, *Smart Materials & Structures*, 19, 065104 (2010).
89. J. E. Manzo and E. Garcia, The Smart Joint: Model and Optimization of a Shape Memory Alloy/Shape Memory Polymer Composite Actuator, *Smasis2008: Proceedings of the Asme Conference on Smart Materials, Adaptive Structures and Intelligent Systems - 2008, Vol 1*, 577-583 (2009).
90. P. Il Hyun and et al., Development and application of conducting shape memory polyurethane actuators, *Smart Materials and Structures*, 15, 1476 (2006).
91. Y. C. Jung, N. S. Goo and J. W. Cho, Electrically conducting shape memory polymer composites for electroactive actuator, *Smart Structures and Materials 2004: Electroactive Polymer Actuators and Devices (Eapad)*, 5385, 230-234 (2004).
92. Q. G. Meng, J. L. Hu and Y. Zhu, Properties of shape memory polyurethane used as a low-temperature thermoplastic biomedical orthotic material: influence of hard segment content, *Journal of Biomaterials Science-Polymer Edition*, 19, 1437-1454 (2008).

93. P. R. Buckley, G. H. McKinley, T. S. Wilson, W. Small, W. J. Benett, J. P. Bearinger, M. W. McElfresh and D. J. Maitland, Inductively heated shape memory polymer for the magnetic actuation of medical devices, *Ieee Transactions on Biomedical Engineering*, 53, 2075-2083 (2006).
94. A. Lendlein, J. Canisius, J. Schulte and K. Kratz, Shape memory polymers as stimuli-sensitive implant materials for medical applications, *SMST-2003: Proceedings of the International Conference on Shape Memory and Superelastic Technologies*, 563-572 (2004).
95. S. K. Lee, S. J. Lee, H. J. An, S. E. Cha, J. K. Chang, B. Kim and J. J. Pak, Biomedical applications of electroactive polymers and shape memory alloys, *Smart Structures and Materials 2002: Electroactive Polymer Actuators and Devices (Eapad)*, 4695, 17-31 (2002).
96. X. J. Yu, S. B. Zhou, X. T. Zheng, Y. Xiao and T. Guo, Influence of in Vitro Degradation of a Biodegradable Nanocomposite on Its Shape Memory Effect, *Journal of Physical Chemistry C*, 113, 17630-17635 (2009).
97. Y. S. Wong, Y. Xiong, S. S. Venkatraman and F. Y. C. Boey, Shape memory in un-cross-linked biodegradable polymers, *Journal of Biomaterials Science-Polymer Edition*, 19, 175-191 (2008).
98. A. Lendlein and S. Kelch, Shape-memory polymers as stimuli-sensitive implant materials, *Clinical Hemorheology and Microcirculation*, 32, 105-116 (2005).
99. Q. Meng and J. Hu, A review of shape memory polymer composites and blends, *Composites Part A: Applied Science and Manufacturing*, 40, 1661-1672 (2009).
100. W. M. Huang, B. Yang, Y. Zhao and Z. Ding, Thermo-moisture responsive polyurethane shape-memory polymer and composites: a review, *Journal of Materials Chemistry*, 20, 3367-3381 (2010).
101. H. Q. a. P. T. M. C. Liu, Review of progress in shape-memory polymers, *Journal of Materials Chemistry*, 17, 1543-1558 (2007).
102. H. Y. Luo, Y. Liu, Z. J. Yu, S. Zhang and B. J. Li, Novel Biodegradable Shape Memory Material Based on Partial Inclusion Complex Formation between alpha-Cyclodextrin and Poly(epsilon-caprolactone), *Biomacromolecules*, 9, 2573-2577 (2008).
103. H. Y. Lee, H. M. Jeong, J. S. Lee and B. K. Kim, Study on the shape memory polyamides. Synthesis and thermomechanical properties of polycaprolactone-polyamide block copolymer, *Polymer Journal*, 32, 23-28 (2000).
104. F. L. Ji, J. L. Hu, T. C. Li and Y. W. Wong, Morphology and shape memory effect of segmented polyurethanes. Part I: With crystalline reversible phase, *Polymer*, 48, 5133-5145 (2007).
105. H. Liem and L. Y. Yeung, Segment self-orientational behaviour in shape memory polymer thin films probed by Raman spectroscopy, *Journal of Applied Polymer Science*, 105, 765-770 (2007).
106. S. Mondal and J. L. Hu, Studies of shape memory property on thermoplastic segmented polyurethanes: Influence of PEG 3400, *Journal of Elastomers and Plastics*, 39, 81-91 (2007).
107. G. Rabani, H. Luftmann and A. Kraft, Synthesis and characterization of two shape-memory polymers containing short aramid hard segments and poly(epsilon-caprolactone) soft segments, *Polymer*, 47, 4251-4260 (2006).
108. A. Kraft and G. Rabani, Thermally induced shape-memory effect in segmented copolymers containing polycaprolactone soft segments and aramid hard segments, *Polymeric Materials Science and Engineering*, 90, 27 (2004).
109. A. Kraft, G. Rabani, C. Schuh, K. Muller and M. C. Lechmann, Shape-memory polymers containing aramid hard segments and polycaprolactone soft segments, *Polymeric Materials Science and Engineering*, 230, 539 (2005).

110. H. Zhang, H. T. Wang, W. Zhong and Q. G. Du, A novel type of shape memory polymer blend and the shape memory mechanism, *Polymer*, 50, 1596-1601 (2009).
111. G. M. Zhu, S. G. Xu, J. H. Wang and L. B. Zhang, Shape memory behaviour of radiation-crosslinked PCL/PMVS blends, *Radiation Physics and Chemistry*, 75, 443-448 (2006).
112. H. M. Jeong, J. H. Song, S. Y. Lee and B. K. Kim, Miscibility and shape memory property of poly(vinyl chloride)/thermoplastic polyurethane blends, *Journal of Materials Science*, 36, 5457-5463 (2001).
113. G. Zhu, G. Liang, Q. Xu and Q. Yu, Shape-memory effects of radiation crosslinked poly(epsilon-caprolactone), *Journal of Applied Polymer Science*, 90, 1589-1595 (2003).
114. P. T. Mather, X. F. Luo and I. A. Rousseau, Shape Memory Polymer Research, *Annual Review of Materials Research*, 39, 445-471 (2009).
115. F. K. Li and R. C. Larock, New soybean oil-styrene-divinylbenzene thermosetting copolymers. v. shape memory effect, *Journal of Applied Polymer Science*, 84, 1533-1543 (2002).
116. Y. Kagami, J. P. Gong and Y. Osada, Shape memory behaviours of crosslinked copolymers containing stearyl acrylate, *Macromolecular Rapid Communications*, 17, 539-543 (1996).
117. M. K. Jang, A. Hartwig and B. K. Kim, Shape memory polyurethanes cross-linked by surface modified silica particles, *Journal of Materials Chemistry*, 19, 1166-1172 (2009).
118. I. S. Gunes and S. C. Jana, Shape memory polymers and their nanocomposites: A review of science and technology of new multifunctional materials, *Journal of Nanoscience and Nanotechnology*, 8, 1616-1637 (2008).
119. C. S. Zhang, Q. Q. Ni, S. Y. Fu and K. Kurashiki, Electromagnetic interference shielding effect of nanocomposites with carbon nanotube and shape memory polymer, *Composites Science and Technology*, 67, 2973-2980 (2007).
120. M. Y. Razzaq, M. Anhalt, L. Frormann and B. Weidenfeller, Thermal, electrical and magnetic studies of magnetite filled polyurethane shape memory polymers, *Materials Science and Engineering a-Structural Materials Properties Microstructure and Processing*, 444, 227-235 (2007).
121. G. Vialle, M. Di Prima, E. Hocking, K. Gall, H. Garmestani, T. Sanderson and S. C. Arzberger, Remote activation of nanomagnetite reinforced shape memory polymer foam, *Smart Materials & Structures*, 18, 115014 (2009).
122. C. N. R. Rao and A. K. Cheetham, Science and technology of nanomaterials: current status and future prospects, *Journal of Materials Chemistry*, 11, 2887-2894 (2001).
123. R. J. Aitken, M. Q. Chaudhry, A. B. A. Boxall and M. Hull, Manufacture and use of nanomaterials: current status in the UK and global trends, *Occupational Medicine*, 56, 300-306 (2006).
124. S. Iijima and T. Ichihashi, Single-shell carbon nanotubes of 1-nm diameter, *Nature*, 363, 603-605 (1993).
125. T. W. Ebbesen, H. J. Lezec, H. Hiura, J. W. Bennett, H. F. Ghaemi and T. Thio, Electrical conductivity of individual carbon nanotubes, *Nature*, 382, 54-56 (1996).
126. P. G. Collins, M. S. Arnold and P. Avouris, Engineering Carbon Nanotubes and Nanotube Circuits Using Electrical Breakdown, *Science*, 292, 706-709 (2001).
127. J. Hu, M. Ouyang, P. Yang and C. M. Lieber, Controlled growth and electrical properties of heterojunctions of carbon nanotubes and silicon nanowires, *Nature*, 399, 48-51 (1999).
128. K. Gall, M. L. Dunn, Y. P. Liu, D. Finch, M. Lake and N. A. Munshi, Shape memory polymer nanocomposites, *Acta Materialia*, 50, 5115-5126 (2002).

129. J. W. Cho and S. H. Lee, Influence of silica on shape memory effect and mechanical properties of polyurethane-silica hybrids, *European Polymer Journal*, 40, 1343-1348 (2004).
130. V. Beloshenko and Y. Voznyak, Shape memory effect in the epoxy polymer composites with aggregated filler, *Polymer Science Series A*, 51, 416-423 (2009).
131. H. G. Jeon, P. T. Mather and T. S. Haddad, Shape memory and nanostructure in poly(norbornyl-POSS) copolymers, *Polymer International*, 49, 453-457 (2000).
132. N. Liu, Q. Xie, W. M. Huang, S. J. Phee and N. Q. Guo, Formation of micro protrusion arrays atop shape memory polymer, *Journal of Micromechanics and Microengineering*, 18 (2008).
133. M. L. Auad, V. S. Contos, S. Nutt, M. I. Aranguren and N. E. Marcovich, Characterization of nanocellulose- reinforced shape memory polyurethanes, *Polymer International*, 57, 651-659 (2008).
134. F. Cao and S. C. Jana, Nanoclay-tethered shape memory polyurethane nanocomposites, *Polymer*, 48, 3790-3800 (2007).
135. M. S. Kim, J. K. Jun and H. M. Jeong, Shape memory and physical properties of poly(ethyl methacrylate)/Na-MMT nanocomposites prepared by macroazoinitiator intercalated in Na-MMT, *Composites Science and Technology*, 68, 1919-1926 (2008).
136. S. Rezanejad and M. Kokabi, Shape memory and mechanical properties of cross-linked polyethylene/clay nanocomposites, *European Polymer Journal*, 43, 2856-2865 (2007).
137. F. Li, L. Qi, J. Yang, M. Xu, X. Luo and D. Ma, Polyurethane/conducting carbon black composites: Structure, electric conductivity, strain recovery behaviour, and their relationships, *Journal of Applied Polymer Science*, 75, 68-77 (2000).
138. J. S. Leng, X. Lan, H. B. Lv, D. W. Zhang, Y. J. Liu and S. Y. Du, Investigation of mechanical and conductive properties of shape memory polymer composite (SMPC) - art. no. 65262V, *Behaviour and Mechanics of Multifunctional and Composite Materials 2007*, 6526, V5262-V5262 (2007).
139. J. S. Leng, W. M. Huang, X. Lan, Y. J. Liu and S. Y. Du, Significantly reducing electrical resistivity by forming conductive Ni chains in a polyurethane shape-memory polymer/carbon-black composite, *Applied Physics Letters*, 92, 204101 (2008).
140. H. Koerner, G. Price, N. A. Pearce, M. Alexander and R. A. Vaia, Remotely actuated polymer nanocomposites - stress-recovery of carbon-nanotube-filled thermoplastic elastomers, *Nature Materials*, 3, 115-120 (2004).
141. X. Lan, Y. J. Liu, H. B. Lv, X. H. Wang, J. S. Leng and S. Y. Du, Fiber reinforced shape-memory polymer composite and its application in a deployable hinge, *Smart Materials & Structures*, 18, 024002 (2009).
142. P. Miaudet, A. Derre, M. Maugey, C. Zakri, P. M. Piccione, R. Inoubli and P. Poulin, Shape and temperature memory of nanocomposites with broadened glass transition, *Science*, 318, 1294-1296 (2007).
143. J. W. Cho, J. W. Kim, Y. C. Jung and N. S. Goo, Electroactive Shape-Memory Polyurethane Composites Incorporating Carbon Nanotubes, *Macromolecular Rapid Communications*, 26, 412-416 (2005).
144. S. Stankovich, D. A. Dikin, G. H. B. Dommett, K. M. Kohlhaas, E. J. Zimney, E. A. Stach, R. D. Piner, S. T. Nguyen and R. S. Ruoff, Graphene-based composite materials, *Nature*, 442, 282-286 (2006).
145. J. L. Vickery, A. J. Patil and S. Mann, Fabrication of Graphene–Polymer Nanocomposites With Higher-Order Three-Dimensional Architectures, *Advanced Materials*, 21, 2180-2184 (2009).
146. Q. Bao, H. Zhang, J.-x. Yang, S. Wang, D. Y. Tang, R. Jose, S. Ramakrishna, C. T. Lim and K. P. Loh, Graphene–Polymer Nanofiber Membrane for Ultrafast Photonics, *Advanced Functional Materials*, 20, 782-791 (2010).

147. H. Tobushi, E. Pieczyska, Y. Ejiri and T. Sakuragi, Thermomechanical Properties of Shape-Memory Alloy and Polymer and Their Composites, *Mechanics of Advanced Materials and Structures*, 16, 236-247 (2009).
148. B. Yang, W.M.Huang, C. Li, C.M.Lee and L. Li, On the effects of moisture in a polyurethane shape memory polymer, *Smart Materials and Structures*, 13, 191-195 (2004).
149. I. S. Gunes, G. A. Jimenez and S. C. Jana, Carbonaceous fillers for shape memory actuation of polyurethane composites by resistive heating, *Carbon*, 47, 981-997 (2009).
150. M. J. Percy, V. Michailidou, S. P. Armes, C. Perruchot, J. F. Watts and S. J. Greaves, Synthesis of Vinyl Polymer-silica Colloidal Nanocomposites via Aqueous Dispersion Polymerization, *Langmuir*, 19, 2072-2079 (2003).
151. J. I. Amalvy, M. J. Percy, S. P. Armes and H. Wiese, Synthesis and Characterization of Novel Film-Forming Vinyl Polymer/Silica Colloidal Nanocomposites, *Langmuir*, 17, 4770-4778 (2001).
152. N. G. Sahoo, Y. C. Jung, H. J. Yoo and J. W. Cho, Influence of carbon nanotubes and polypyrrole on the thermal, mechanical and electroactive shape-memory properties of polyurethane nanocomposites, *Composites Science and Technology*, 67, 1920-1929 (2007).
153. R. Sravendra and et al., Enhanced dispersion of carbon nanotubes in hyperbranched polyurethane and properties of nanocomposites, *Nanotechnology*, 19, 495707 (2008).
154. A. M. Schmidt, Electromagnetic activation of shape memory polymer networks containing magnetic nanoparticles, *Macromolecular Rapid Communications*, 27, 1168-1172 (2006).
155. H. Hosoda, S. Takeuchi, T. Inamura and K. Wakashima, Material design and shape memory properties of smart composites composed of polymer and ferromagnetic shape memory alloy particles, *Science and Technology of Advanced Materials*, 5, 503-509 (2004).
156. B. Mihaylova, Briggs, A., Hlatky, M., Armitage, J., Parish, S., Gray, A. and Collins, R., Statin cost-effectiveness in the United States for people at different vascular risk levels, *Circ Cardiovasc Qual Outcomes*, 2, 65-72 (2009).
157. N. Suprapakorn, S. Dhamrongvaraporn and H. Ishida, Effect of CaCO3 on the mechanical and rheological properties of a ring-opening phenolic resin: Polybenzoxazine, *Polymer Composites*, 19, 126-132 (1998).
158. J. Cho, M. S. Joshi and C. T. Sun, Effect of inclusion size on mechanical properties of polymeric composites with micro and nano particles, *Composites Science and Technology*, 66, 1941-1952 (2006).
159. A. Einstein, On the movement of small particles suspended in stationary liquids requied by the molecular-kinetic theory of heat, *Ann. Phys. (Leipzig)*, 17, 549-560 (1905).
160. H. M. Smallwood, Limiting Law of the Reinforcement of Rubber, *Journal of Applied Physics*, 5, 758-766 (1944).
161. C.-H. Hsueh and P. F. Becher, Effective Viscosity of Suspensions of Spheres, *Journal of the American Ceramic Society*, 88, 1046-1049 (2005).
162. E. Guth and R. Simha, Untersuchungen über die Viskosität von Suspensionen und Lösungen. 3. Über die Viskosität von Kugelsuspensionen, *Colloid & Polymer Science*, 74, 266-275 (1936).
163. E. Guth, Theory of Filler Reinforcement, *Journal of Applied Physics*, 16, 20-25 (1945).
164. W. Voigt, Über die Beziehung zwischen den beiden Elastizitätskonstanten isotroper Körper, *Wied. Ann*, 38, 573-587 (1889).

165. J. Halpin, Stiffness and expansion estimates for oriented short fiber composites, *Journal of Composite Materials*, 3, 732-734 (1969).
166. J. C. Halpin and J. L. Kardos, The Halpin-Tsai equations: a review, *Polymer Engineering and Science*, 16, 344-352 (1974).
167. T. Mori and K. Tanaka, Average stress in matrix and average elastic energy of materials with misfitting inclusions, *Acta Metallurgica*, 21, 571-574 (1973).
168. G. P. Tandon and G. J. Weng, The effect of aspect ratio of inclusions on the elastic properties of unidirectionally aligned composites, *Polymer Composites*, 5, 327-333 (1984).
169. T. D. Fornes and D. R. Paul, Modeling properties of nylon 6/clay nanocomposites using composite theories, *Polymer*, 44, 4993-5013 (2003).
170. H. Tobushi, H. Hara, E. Yamada and S. Hayashi, Thermomechanical properties in a thin film of shape memory polymer of polyurethane series, *Smart Materials Technologies and Biomimetics - Smart Structures and Materials 1996*, 2716, 46-57 (1996).
171. H. Tobushi, T. Hashimoto, S. Hayashi and E. Yamada, Thermomechanical constitutive modeling in shape memory polymer of polyurethane series, *Journal of Intelligent Material Systems and Structures*, 8, 711-718 (1997).
172. H. Tobushi, T. Hashimoto, N. Ito, S. Hayashi and E. Yamada, Shape fixity and shape recovery in a film of shape memory polymer of polyurethane series, *Journal of Intelligent Material Systems and Structures*, 9, 127-136 (1998).
173. H. Tobushi, N. Ito, K. Takata and S. Hayashi, Shape fixity and shape recovery in a film of shape memory polymer of polyurethane series, *Japan Institute of Metals, Proceedings, Vol 12, (Jimic-3), Pts 1 and 2*, 1080-1083 (1999).
174. H. Tobushi, K. Okumura, M. Endo and S. Hayashi, Thermomechanical properties of polyurethane-shape memory polymer, *Iutam Symposium on Mechanics of Martensitic Phase Transformation in Solids*, 101, 79-86 (2002).
175. H. Tobushi, S. Hayashi, K. Hoshio and Y. Ejiri, Shape recovery and irrecoverable strain control in polyurethane shape-memory polymer, *Science and Technology of Advanced Materials*, 9 (2008).
176. Y. P. Liu, K. Gall, M. L. Dunn, A. R. Greenberg and J. Diani, Thermomechanics of shape memory polymers: Uniaxial experiments and constitutive modeling, *International Journal of Plasticity*, 22, 279-313 (2006).
177. J. Diani, Y. P. Liu and K. Gall, Finite strain 3D thermoviscoelastic constitutive model for shape memory polymers, *Polymer Engineering and Science*, 46, 486-492 (2006).
178. T. E. a. H. Harada, The Thermoplastic Poly Coloring Picture Recording Medias and its Image Formation Method of using the Heat Sensitive Characteristic form Memory Ingredient, J. Patent, (2002).
179. T. Terai, Reversible Thermal Recording Media Comprising Shape Memory Polymers and Showing Good Image Storability, J. Patent, (2002).
180. D. J. Maitland, M. F. Metzger, D. Schumann, A. Lee and T. S. Wilson, Photothermal properties of shape memory polymer micro-actuators for treating stroke, *Lasers in Surgery and Medicine*, 30, 1-11 (2002).
181. W. Small, M. F. Metzger, T. S. Wilson and D. J. Maitland, Laser-activated shape memory polymer microactuator for thrombus removal following ischemic stroke: Preliminary in vitro analysis, *Ieee Journal of Selected Topics in Quantum Electronics*, 11, 892-901 (2005).
182. J. Carlos Rodríguez-Cabello and *e. al.*, *Protein-Based Smart Polymers,smart polymers applications in biotechnology and Biomedicine*, 2 ed., CRC press (2007).
183. H. D. T. William C. Jackson, Michael J. O'Brien,Emmanuil Rabinovich,Gabriel P.Lopez, Rapid prototyping of active microfluidic components based on magnetically

modified elastomeric materials *Journal of Vacuum Science & Technology B*, 19, 596-599 (2001).
184. G. M. Whitesides, E. Ostuni, S. Takayama, X. Jiang and D. E. Ingber, SOFT LITHOGRAPHY IN BIOLOGY AND BIOCHEMISTRY, *Annual Review of Biomedical Engineering*, 3, 335-373 (2001).
185. R. Jameson, Y. Chen, A. Pepin and D. Decanini, Imaging streamlines and interface profiles in microfluidic geometries, *Microelectronic Engineering*, 67-68, 930-937 (2003).
186. C. M. Yakacki, R. Shandas, C. Lanning, B. Rech, A. Eckstein and K. Gall, Unconstrained recovery characterization of shape-memory polymer networks for cardiovascular applications, *Biomaterials*, 28, 2255-2263 (2007).
187. S. Hayashi, Shape memory polyurethane elastmer molded article, U. Patent, (1992).
188. D. Ratna and J. Karger-Kocsis, Recent advances in shape memory polymers and composites: a review, *Journal of Materials Science*, 43, 254-269 (2008).
189. M. Cabanlit, D. Maitland, T. Wilson, S. Simon, T. Wun, M. E. Gershwin and J. Van de Water, Polyurethane Shape-Memory Polymers Demonstrate Functional Biocompatibility In Vitro, *Macromolecular Bioscience*, 7, 48-55 (2007).
190. S. G. Patrcik J. Hood, Frank Auffinger, METHOD OF MAKING AND USING SHAPE MEMORY POLYMER PATCHES U. Patent, (2007).
191. C. C. Fu, A. Grimes, M. Long, C. G. L. Ferri, B. D. Rich, S. Ghosh, S. Ghosh, L. P. Lee, A. Gopinathan and M. Khine, Tunable Nanowrinkles on Shape Memory Polymer Sheets, *Advanced Materials*, 21, 4472-4476 (2009).
192. Y. J. Liu, H. B. Lv, X. Lan, J. S. Leng and S. Y. Du, Review of electro-active shape-memory polymer composite, *Composites Science and Technology*, 69, 2064-2068 (2009).
193. O. Hood; Patrick J. (Bellbrook, Havens; David Ernest (Bellbrook, OH) Structural and optical applications for shape memory polymers (SMP) 6,986,855, U. S. Patent, (2006).
194. T. Hasan, Z. P. Sun, F. Q. Wang, F. Bonaccorso, P. H. Tan, A. G. Rozhin and A. C. Ferrari, Nanotube-Polymer Composites for Ultrafast Photonics, *Advanced Materials*, 21, 3874-3899 (2009).
195. S. Hayashi and H. Fujimura., Shape memory polymer foam, *US Patent*, (1991).
196. B. K. Kim, S. Y. Lee and M. Xu, Polyurethanes having shape memory effects, *Polymer*, 37, 5781-5793 (1996).
197. B. K. Kim, S. Y. Lee, J. S. Lee, S. H. Baek, Y. J. Choi, J. O. Lee and M. Xu, Polyurethane ionomers having shape memory effects, *Polymer*, 39, 2803-2808 (1998).
198. L. Krone, J. Mentz, M. Bram, H. P. Buchkremer, D. Stöver, M. Wagner, G. Eggeler, D. Christ, S. Reese, D. Bogdanski, M. Köller, S. A. Esenwein, G. Muhr, O. Prymak and M. Epple, The Potential of Powder Metallurgy for the Fabrication of Biomaterials on the Basis of Nickel-Titanium: A Case Study with a Staple Showing Shape Memory Behaviour, *Advanced Engineering Materials*, 7, 613-619 (2005).
199. Y. Sung-Min and et al., Effect of ZnO channel thickness on the device behaviour of nonvolatile memory thin film transistors with double-layered gate insulators of Al 2 O 3 and ferroelectric polymer, *Journal of Physics D: Applied Physics*, 42, 245101 (2009).
200. R. Nowak, *AEROSIL® fumed silica in unsaturated polyester resins and vinyl ester resins*, Evonik Degussa (2010).
201. L. G. Pedroni, M. A. Soto-Oviedo, J. M. Rosolen, M. I. Felisberti and A. F. Nogueira, Conductivity and mechanical properties of composites based on MWCNTs and styrene-butadiene-styrene block™ copolymers, *Journal of Applied Polymer Science*, 112, 3241-3248 (2009).

202. C. G. Cameron and M. S. Freund, Reversible and Efficient Materials-based Actuation by Electrolytic Phase Transformation, *Chemical Engineering & Technology*, 26, 1007-1011 (2003).
203. S. Lee, S.-Y. Da, A. A. Ogale and M.-S. Kim, Effect of heat treatment of carbon nanofibers on polypropylene nanocomposites, *Journal of Physics and Chemistry of Solids*, 69, 1407-1410 (2008).
204. M. H. Al-Saleh and U. Sundararaj, A review of vapor grown carbon nanofiber/polymer conductive composites, *Carbon*, 47, 2-22 (2009).
205. F. Hussain, M. Hojjati, M. Okamoto and R. E. Gorga, Review article: Polymer-matrix Nanocomposites, Processing, Manufacturing, and Application: An Overview, *Journal of Composite Materials*, 40, 1511-1575 (2006).
206. N. G. Sahoo, Y. C. Jung and J. W. Cho, Electroactive shape memory effect of polyurethane composites filled with carbon nanotubes and conducting polymer, *Materials and Manufacturing Processes*, 22, 419-423 (2007).
207. H. Koerner, G. Price, N. A. Pearce, M. Alexander and R. A. Vaia, Remotely actuated polymer nanocomposites[mdash]stress-recovery of carbon-nanotube-filled thermoplastic elastomers, *Nat Mater*, 3, 115-120 (2004).
208. , BS EN ISO 291:2008 Plastics-Standard atmospheres for conditioning and testing (2008).
209. Z. Wang, M. Lu, H. L. Li and X. Y. Guo, SWNTs-polystyrene composites preparations and electrical properties research, *Materials Chemistry and Physics*, 100, 77-81 (2006).
210. J. M. Yuan, Z. F. Fan, X. H. Chen, X. H. Chen, Z. J. Wu and L. P. He, Preparation of polystyrene-multiwalled carbon nanotube composites with individual-dispersed nanotubes and strong interfacial adhesion, *Polymer*, 50, 3285-3291 (2009).
211. M. K. Vyas, B. Nandan, K. Schneider and M. Stamm, Nanowear studies in reversibly switchable polystyrene-poly(acrylic acid) mixed brushes, *Journal of Colloid and Interface Science*, 328, 58-66 (2008).
212. T. Hasan, Z. Sun, F. Wang, F. Bonaccorso, P. H. Tan, A. G. Rozhin and A. C. Ferrari, Nanotube–Polymer Composites for Ultrafast Photonics, *Advanced Materials*, 21, 3874-3899 (2009).
213. B. Xu, Y. Q. Fu, M. Ahmad, J. K. Luo, W. M. Huang, A. Kraft, R. Reuben, Y. T. Pei, Z. G. Chen and J. T. M. De Hosson, Thermo-mechanical properties of polystyrene-based shape memory nanocomposites, *Journal of Materials Chemistry*, 20, 3442-3448 (2010).
214. S. Lefrant, M. Baibarac and I. Baltog, Raman and FTIR spectroscopy as valuable tools for the characterization of polymer and carbon nanotube based composites, *Journal of Materials Chemistry*, 19, 5690-5704 (2009).
215. V. Bershtein and V. Ryzhov, *Polymer Analysis and Characterization*, Springer Berlin / Heidelberg, 1994.
216. , BS ISO 20753:2008 Plastics —Test specimens, (2008).
217. , BS EN ISO 527-2:1996 BS 2782-3: Method 322:1994 Plastics — Determination of tensile properties—Part 2: Test conditions for moulding and extrusion plastics, (1996).
218. , BS EN ISO 527-1:1996 BS 2782-3: Method 321: 1994 ISO 527-1: 1993 Plastics—Determination of tensile properties —Part 1:General principles, (1996).
219. , BS ISO 23559:2007 Plastics —Film and sheeting— Guidance on the testing of thermoplastic films (2007).
220. , BS 3900-E12.1:2000, ISO 6441-1:1999 Methods of test for paints. Determination of Knoop hardness by measurement of the indentation length using a microscope, (2000).

221. , BS ISO 7619-1:2010 Rubber, vulcanized or thermoplastic. Determination of indentation hardness. Durometer method (Shore hardness), (2010).
222. T. Chudoba and F. Richter, Investigation of creep behaviour under load during indentation experiments and its influence on hardness and modulus results, *Surface and Coatings Technology*, 148, 191-198 (2001).
223. K. C. Maner, M. R. Begley and W. C. Oliver, Nanomechanical testing of circular freestanding polymer films with sub-micron thickness, *Acta Materialia*, 52, 5451-5460 (2004).
224. W. C. Oliver and G. M. Pharr, Measurement of hardness and elastic modulus by instrumented indentation: Advances in understanding and refinements to methodology, *Journal of Materials Research*, 19, 3-20 (2004).
225. W. C. P. Oliver, G. M. , Improved technique for determining hardness and elastic modulus using load and displacement sensing indentation experiments, *Journal of Materials Research*, 7, 1564-1583 (1992).
226. E. Wornyo, K. Gall, F. Z. Yang and W. King, Nanoindentation of shape memory polymer networks, *Polymer*, 48, 3213-3225 (2007).
227. D. Pham, L. Tonge, J. N. Cao, J. Wright, M. Papiernik, E. Harvey and D. Nicolau, Effects of polymer properties on laser ablation behaviour, *Smart Materials & Structures*, 11, 668-674 (2002).
228. H. Koerner, J. Kelley, J. George, L. Drummy, P. Mirau, N. S. Bell, J. W. P. Hsu and R. A. Vaia, ZnO Nanorod-Thermoplastic Polyurethane Nanocomposites: Morphology and Shape Memory Performance, *Macromolecules*, 42, 8933-8942 (2009).
229. R. L. Frost, G. A. Cash and J. T. Kloprogge, Rocky Mountain leather, sepiolite and attapulgite--an infrared emission spectroscopic study, *Vibrational Spectroscopy*, 16, 173-184 (1998).
230. R. L. Frost, O. B. Locos, H. Ruan and J. T. Kloprogge, Near-infrared and mid-infrared spectroscopic study of sepiolites and palygorskites, *Vibrational Spectroscopy*, 27, 1-13 (2001).
231. V. C. Farmer, *The Infrared spectra of minerals* London Mineralogical Society, London (1974).
232. M. Suarez and E. Garcia-Romero, FTIR spectroscopic study of palygorskite: Influence of the composition of the octahedral sheet, *Applied Clay Science*, 31, 154-163 (2006).
233. M. S. Augsburger, E. Strasser, E. Perino, R. C. Mercader and J. C. Pedregosa, Ftir and mosbauer investigation of a substituted palygorskite: Silicate with a channel structure, *Journal of Physics and Chemistry of Solids*, 59, 175-180 (1998).
234. D. M. A. Melo, J. A. C. Ruiz, M. A. F. Melo, E. V. Sobrinho and M. Schmall, Preparation and characterization of terbium palygorskite clay as acid catalyst, *Microporous and Mesoporous Materials*, 38, 345-349 (2000).
235. R. L. Frost and Z. Ding, Controlled rate thermal analysis and differential scanning calorimetry of sepiolites and palygorskites, *Thermochimica Acta*, 397, 119-128 (2003).
236. A. I. a. R. Bigot, Indentation size effect: reality or artefact? , *Journal of Materials Science*, 31, 3573-3577 (1996).
237. I. Manika and J. Maniks, Size effects in micro- and nanoscale indentation, *Acta Materialia*, 54, 2049-2056 (2006).
238. C. S. Han and S. Nikolov, Indentation size effects in polymers and related rotation gradients, *Journal of Materials Research*, 22, 1662-1672 (2007).
239. H. Lu, H. Shen, Z. Song, K. S. Shing, W. Tao and S. Nutt, Rod-Like Silicate-Epoxy Nanocomposites, *Macromolecular Rapid Communications*, 26, 1445-1450 (2005).

240. Y. S. Choi, M. H. Choi, K. H. Wang, S. O. Kim, Y. K. Kim and I. J. Chung, Synthesis of Exfoliated PMMA/Na-MMT Nanocomposites via Soap-Free Emulsion Polymerization, *Macromolecules*, 34, 8978-8985 (2001).
241. J. Kajaks, A. Flores, M. C. Garcu Gutiorez, D. R. Rueda and F. J. Balt?Calleja, Crystallization kinetics of poly(ethylene naphthalene-2,6-dicarboxylate) as revealed by microhardness, *Polymer*, 41, 7769-7772 (2000).
242. F. Ania, J. Martinez-Salazar and F. Baltá Calleja, Physical ageing and glass transition in amorphous polymers as revealed by microhardness, *Journal of Materials Science*, 24, 2934-2938 (1989).
243. B. K. Kim, Y. J. Shin, S. M. Cho and H. M. Jeong, Shape-memory behaviour of segmented polyurethanes with an amorphous reversible phase: The effect of block length and content, *Journal of Polymer Science Part B-Polymer Physics*, 38, 2652-2657 (2000).
244. B. S. Lee, B. C. Chun, Y.-C. Chung, K. I. Sul and J. W. Cho, Structure and Thermomechanical Properties of Polyurethane Block Copolymers with Shape Memory Effect, *Macromolecules*, 34, 6431-6437 (2001).
245. T. Takahashi, N. Hayashi and S. Hayashi, Structure and properties of shape-memory polyurethane block copolymers, *Journal of Applied Polymer Science*, 60, 1061-1069 (1996).
246. P. Pissis, L. Apekis, C. Christodoulides, M. Niaounakis, A. Kyritsis and J. Nedbal, Water effects in polyurethane block copolymers, *Journal of Polymer Science Part B: Polymer Physics*, 34, 1529-1539 (1996).
247. J. F. Su and et al., Indentation and two-way shape memory in a NiTi polycrystalline shape-memory alloy, *Smart Materials and Structures*, 16, S137 (2007).
248. K. Sakurai, Y. Shirakawa, T. Kashiwagi and T. Takahashi, Crystal transformation of styrene-butadiene block copolymer, *Polymer*, 35, 4238-4239 (1994).
249. J. Li, J. A. Viveros, M. H. Wrue and M. Anthamatten, Shape-Memory Effects in Polymer Networks Containing Reversibly Associating Side-Groups, *Advanced Materials*, 19, 2851-2855 (2007).
250. F. Li and R. C. Larock, Synthesis, Structure and Properties of New Tung Oil-Styrene-Divinylbenzene Copolymers Prepared by Thermal Polymerization, *Biomacromolecules*, 4, 1018-1025 (2003).
251. B. Xu, W. M. Huang, Y. T. Pei, Z. G. Chen, A. Kraft, R. Reuben, J. T. M. De Hosson and Y. Q. Fu, Mechanical properties of attapulgite clay reinforced polyurethane shape-memory nanocomposites, *European Polymer Journal*, 45, 1904-1911 (2009).
252. A. Bandyopadhyay, M. Maiti and A. K. Bhowmick, Synthesis, characterisation and properties of clay and silica based rubber nanocomposites, *Materials Science and Technology*, 22, 818-828 (2006).
253. Y. Xu and S. Van Hoa, Mechanical properties of carbon fiber reinforced epoxy/clay nanocomposites, *Composites Science and Technology*, 68, 854-861 (2008).
254. H. Fischer, Polymer nanocomposites: from fundamental research to specific applications, *Materials Science and Engineering: C*, 23, 763-772 (2003).
255. G. A. Buxton and A. C. Balazs, Modeling the dynamic fracture of polymer blends processed under shear, *Physical Review B*, 69 (2004).
256. G. A. Buxton and A. C. Balazs, Lattice spring model of filled polymers and nanocomposites, *Journal of Chemical Physics*, 117, 7649-7658 (2002).
257. G. A. Buxton and A. C. Balazs, Simulating the morphology and mechanical properties of filled diblock copolymers, *Physical Review E*, 67 (2003).
258. H. Q. Hou, J. J. Ge, J. Zeng, Q. Li, D. H. Reneker, A. Greiner and S. Z. D. Cheng, Electrospun polyacrylonitrile nanofibers containing a high concentration of well-aligned multiwall carbon nanotubes, *Chemistry of Materials*, 17, 967-973 (2005).

259. Q. Q. Ni, C. S. Zhang, Y. Q. Fu, G. Z. Dai and T. Kimura, Shape memory effect and mechanical properties of carbon nanotube/shape memory polymer nanocomposites, *Composite Structures*, 81, 176-184 (2007).
260. B.-S. Kim and P. T. Mather, Amphiphilic Telechelics Incorporating Polyhedral Oligosilsesquioxane:鈥?1. Synthesis and Characterization, *Macromolecules*, 35, 8378-8384 (2002).
261. H. M. Jeong, B. K. Ahn, S. M. Cho and B. K. Kim, Water vapor permeability of shape memory polyurethane with amorphous reversible phase, *Journal of Polymer Science Part B: Polymer Physics*, 38, 3009-3017 (2000).
262. Y. R. Lee, A. V. Raghu, H. M. Jeong and B. K. Kim, Properties of Waterborne Polyurethane/Functionalized Graphene Sheet Nanocomposites Prepared by an in situ Method, *Macromolecular Chemistry and Physics*, 210, 1247-1254 (2009).
263. Q. H. Meng, J. L. Hu and Y. Zhu, Shape-memory Polyurethane/Multiwalled carbon nanotube fibers, *Journal of Applied Polymer Science*, 106, 837-848 (2007).
264. S. Praveen, P. K. Chattopadhyay, P. Albert, V. G. Dalvi, B. C. Chakraborty and S. Chattopadhyay, Synergistic effect of carbon black and nanoclay fillers in styrene butadiene rubber matrix: Development of dual structure, *Composites Part A: Applied Science and Manufacturing*, 40, 309-316 (2009).
265. F. K. Li, W. Zhu, X. Zhang, C. T. Zhao and M. Xu, Shape memory effect of ethylene-vinyl acetate copolymers, *Journal of Applied Polymer Science*, 71, 1063-1070 (1999).
266. Y. Liu, H. Lv, X. Lan, J. Leng and S. Du, Review of electro-active shape-memory polymer composite, *Composites Science and Technology*, 69, 2064-2068 (2009).
267. M. Shahinpoor and K. J. Kim, Ionic polymer-metal composites: IV. Industrial and medical applications, *Smart Materials & Structures*, 14, 197-214 (2005).
268. G. Shuxiang, T. Nakamura, T. Fukuda and K. Oguro, *Robotics and Automation, 1997. Proceedings., 1997 IEEE International Conference on*, 1997, pp 266-271 vol.261.
269. R. Kornbluh, R. Pelrine, J. Eckerle and J. Joseph, Electrostrictive polymer artificial muscle actuators, *1998 Ieee International Conference on Robotics and Automation, Vols 1-4*, 2147-2154 (1998).
270. D.-H. Kim, M. R. Abidian and D. C. Martin, Conducting polymers grown in hydrogel scaffolds coated on neural prosthetic devices, *Journal of Biomedical Materials Research*, 71, 577-585 (2004).
271. P. Brochu and Q. B. Pei, Advances in Dielectric Elastomers for Actuators and Artificial Muscles, *Macromolecular Rapid Communications*, 31, 10-36.
272. R. Shankar, T. K. Ghosh and R. J. Spontak, Dielectric elastomers as next-generation polymeric actuators, *Soft Matter*, 3, 1116-1129 (2007).
273. R. Shankar, T. K. Ghosh and R. J. Spontak, Electroactive Nanostructured Polymers as Tunable Actuators, *Advanced Materials*, 19, 2218-2223 (2007).
274. Q. M. Zhang, H. Li, M. Poh, F. Xia, Z. Y. Cheng, H. Xu and C. Huang, An all-organic composite actuator material with a high dielectric constant, *Nature*, 419, 284-287 (2002).
275. Y. J. Liu, H. B. Lu, J. S. Leng and S. Y. Du, Shape-memory polymer Composite and Its Application, *Materials and Devices for Smart Systems Iii*, 1129, 243-248 (2009).
276. J. S. Plante and S. Dubowsky, On the properties of dielectric elastomer actuators and their design implications, *Smart Materials & Structures*, 16, S227-S236 (2007).
277. P. Pissis, L. Apekis, C. Christodoulides, M. Niaounakis, A. Kyritsis and J. Nedbal, Water effects in polyurethane block copolymers, *Journal of Polymer Science Part B-Polymer Physics*, 34, 1529-1539 (1996).

278. M. Rief, F. Oesterhelt, B. Heymann and H. E. Gaub, Single Molecule Force Spectroscopy on Polysaccharides by Atomic Force Microscopy, *Science*, 275, 1295-1297 (1997).
279. Z. M. Dang, Y. H. Lin and C. W. Nan, Novel ferroelectric polymer composites with high dielectric constants, *Advanced Materials*, 15, 1625-1629 (2003).
280. E.-B. F. Pecharroman C., Bartolome J.F., Lopez-Esteban S., Moya J.S. , New percolative BaTiO3-Ni composites with a high and frequency-independent dielectric constant ($\varepsilon_r \approx 80000$), *Advanced Materials*, 13, 1541-1544. (2001).
281. P. Potschke, S. M. Dudkin and I. Alig, Dielectric spectroscopy on melt processed polycarbonate - multiwalled carbon nanotube composites, *Polymer*, 44, 5023-5030 (2003).
282. O. Regev, P. N. B. ElKati, J. Loos and C. E. Koning, Preparation of conductive nanotube-polymer composites using latex technology, *Advanced Materials*, 16, 248-251 (2004).
283. Z. M. Dang, L. Wang, Y. Yin, Q. Zhang and Q. Q. Lei, Giant dielectric permittivities in functionalized carbon-nanotube/electroactive-polymer nanocomposites, *Advanced Materials*, 19, 852-857 (2007).
284. L. Karasek, B. Meissner, S. Asai and M. Sumita, Percolation concept: Polymer-filler gel formation, electrical conductivity and dynamic electrical properties of carbon-black-filled rubbers, *Polymer Journal*, 28, 121-126 (1996).
285. M. Kolb, R. Botet and R. Jullien, Scaling of Kinetically Growing Clusters, *Physical Review Letters*, 51, 1123 (1983).
286. R. Q. Ou, S. Gupta, C. A. Parker and R. A. Gerhardt, Fabrication and electrical conductivity of poly(methyl methacrylate) (PMMA)/Carbon black (CB) composites: Comparison between an ordered carbon black nanowire-like segregated structure and a randomly dispersed carbon black nanostructure, *Journal of Physical Chemistry B*, 110, 22365-22373 (2006).
287. A. K. Jonscher, Physical basis of dielectric loss, *Nature*, 253, 717-719 (1975).
288. Y. L. Yang, M. C. Gupta, K. L. Dudley and R. W. Lawrence, The fabrication and electrical properties of carbon nanofibre-polystyrene composites, *Nanotechnology*, 15, 1545-1548 (2004).
289. H. P. Xu, Z. M. Dang, D. H. Shi and J. B. Bai, Remarkable selective localization of modified nanoscaled carbon black and positive temperature coefficient effect in binary-polymer matrix composites, *Journal of Materials Chemistry*, 18, 2685-2690 (2008).
290. R. Shankar, T. K. Ghosh and R. J. Spontak, Electromechanical response of nanostructured polymer systems with no mechanical pre-strain, *Macromolecular Rapid Communications*, 28, 1142-1147 (2007).
291. F. El-Tantawy, K. Kamada and H. Ohnabe, Electrical properties and stability of epoxy reinforced carbon black composites, *Materials Letters*, 57, 242-251 (2002).
292. F. El-Tantawy, K. Kamada and H. Ohnabe, In situ network structure, electrical and thermal properties of conductive epoxy resin-carbon black composites for electrical heater applications, *Materials Letters*, 56, 112-126 (2002).
293. J. T. Fulcher, Y. C. Lu, G. P. Tandon and D. C. Foster, Thermomechanical characterization of shape memory polymers using high temperature nanoindentation, *Polymer Testing*, 29, 544-552.
294. B. A. Nelson, W. P. King and K. Gall, Shape recovery of nanoscale imprints in a thermoset "shape memory" polymer, *Applied Physics Letters*, 86, 103108 (2005).
295. J. N. Coleman, U. Khan, W. J. Blau and Y. K. Gun'ko, Small but strong: A review of the mechanical properties of carbon nanotube-polymer composites, *Carbon*, 44, 1624-1652 (2006).

296. X. Chen, S. Wei, A. Yadav, R. Patil, J. Zhu, R. Ximenes, L. Sun and Z. Guo, Poly(propylene)/Carbon Nanofiber Nanocomposites: Ex Situ Solvent-Assisted Preparation and Analysis of Electrical and Electronic Properties, *Macromolecular Materials and Engineering*, DOI: 10.1002/mame.201000341 (2011).
297. R. Kumar and A. I. Isayev, Thermotropic LCP/CNF nanocomposites prepared with aid of ultrasonic waves, *Polymer*, 51, 3503-3511 (2005).
298. K. Joseph, S. Thomas and C. Pavithran, Effect of chemical treatment on the tensile properties of short sisal fibre-reinforced polyethylene composites, *Polymer*, 37, 5139-5149 (1996).
299. M.-F. Yu, O. Lourie, M. J. Dyer, K. Moloni, T. F. Kelly and R. S. Ruoff, Strength and Breaking Mechanism of Multiwalled Carbon Nanotubes Under Tensile Load, *Science*, 287, 637-640 (2000).
300. M. Wong, M. Paramsothy, X. J. Xu, Y. Ren, S. Li and K. Liao, Physical interactions at carbon nanotube-polymer interface, *Polymer*, 44, 7757-7764 (2003).
301. S. Y. Fu, B. Lauke, E. Mader, C. Y. Yue and X. Hu, Tensile properties of short-glass-fiber- and short-carbon-fiber-reinforced polypropylene composites, *Composites Part A: Applied Science and Manufacturing*, 31, 1117-1125 (2000).
302. X. D. Li, H. S. Gao, W. A. Scrivens, D. L. Fei, X. Y. Xu, M. A. Sutton, A. P. Reynolds and M. L. Myrick, Nanomechanical characterization of single-walled carbon nanotube reinforced epoxy composites, *Nanotechnology*, 15, 1416-1423 (2004).
303. D. Tranchida, S. Piccarolo, J. Loos and A. Alexeev, Mechanical characterization of polymers on a nanometer scale through nanoindentation. A study on pile-up and viscoelasticity, *Macromolecules*, 40, 1259-1267 (2007).
304. F. Bedoui, F. Sansoz and N. S. Murthy, Incidence of nanoscale heterogeneity on the nanoindentation of a semicrystalline polymer: Experiments and modeling, *Acta Materialia*, 56, 2296-2306 (2008).
305. Y. Q. Fu, C. Shearwood, B. Xu, L. G. Yu and K. A. Khor, Characterization of spark plasma sintered Ag nanopowders, *Nanotechnology*, 21, 115707 (2010).
306. G. M. P. A. Bolshakov, Influences of pile-up on the measurement of mechanical properties by load and depth sensing indentation techniques, *Journal of Materials Research*, 13, 1049-1051 (1998).
307. Q. Zia, R. Androsch, H.-J. Radusch and S. Piccarolo, Morphology, reorganization and stability of mesomorphic nanocrystals in isotactic polypropylene, *Polymer*, 47, 8163-8172 (2006).
308. B. Y. Du, O. K. C. Tsui, Q. L. Zhang and T. B. He, Study of elastic modulus and yield strength of polymer thin films using atomic force microscopy, *Langmuir*, 17, 3286-3291 (2001).
309. X. Chen and J. J. Vlassak, Numerical study on the measurement of thin film mechanical properties by means of nanoindentation, *Journal of Materials Research*, 16, 2974-2982 (2001).
310. H. Tang, Z. Y. Liu, J. H. Piao, X. F. Chen, Y. X. Lou and S. H. Li, Electrical behaviour of carbon black-filled polymer composites: Effect of interaction between filler and matrix, *Journal of Applied Polymer Science*, 51, 1159-1164 (1994).
311. G. A. Buxton and A. C. Balazs, Predicting the mechanical and electrical properties of nanocomposites formed from polymer blends and nanorods, *Molecular Simulation*, 30, 249-257 (2004).
312. X. L. Ji, J. K. Jing, W. Jiang and B. Z. Jiang, Tensile modulus of polymer nanocomposites, *Polymer Engineering & Science*, 42, 983-993 (2002).
313. R. P. Singh, M. Zhang and D. Chan, Toughening of a brittle thermosetting polymer: Effects of reinforcement particle size and volume fraction, *Journal of Materials Science*, 37, 781-788 (2002).

314. C. K. Najeeb, J. H. Lee, J. Chang, W. S. Kang and J. H. Kim, Ultra Fast UV-Photo Detector Based on Single-Walled Carbon Nanotube/PEDOT-PSS Composites, *Journal of Nanoscience and Nanotechnology*, 9, 6928-6933 (2009).
315. M. Z. Rong, M. Q. Zhang, S. L. Pan, B. Lehmann and K. Friedrich, Analysis of the interfacial interactions in polypropylene/silica nanocomposites, *Polymer International*, 53, 176-183 (2004).
316. S. Gupta, Q. Zhang, T. Emrick, A. C. Balazs and T. P. Russell, Entropy-driven segregation of nanoparticles to cracks in multilayered composite polymer structures, *Nat Mater*, 5, 229-233 (2006).
317. T. D. Fornes, P. J. Yoon, D. L. Hunter, H. Keskkula and D. R. Paul, Effect of organoclay structure on nylon 6 nanocomposite morphology and properties, *Polymer*, 43, 5915-5933 (2002).
318. J. S. Bergstron and M. C. Boyce, Constitutive modeling of the time-dependent and cyclic loading of elastomers and application to soft biological tissues, *Mechanics of Materials*, 33, 523-530 (2001).
319. J. S. Bergstron and M. C. Boyce, Constitutive modeling of the large strain time-dependent behaviour of elastomers, *Journal of the Mechanics and Physics of Solids*, 46, 931-954 (1998).
320. H. M. Jeong, S. Y. Lee and B. K. Kim, Shape memory polyurethane containing amorphous reversible phase, *Journal of Materials Science*, 35, 1579-1583 (2000).
321. Y. S. Wong, Z. H. Stachurski and S. S. Venkatraman, Modeling shape memory effect in uncrosslinked amorphous biodegradable polymer, *Polymer*, 52, 874-880 (2010).
322. M. Iijima, M. Kobayakawa, M. Yamazaki, Y. Ohta and H. Kamiya, Anionic surfactant with hydrophobic and hydrophilic chains for nanoparticle dispersion and shape memory polymer nanocomposites, *J Am Chem Soc*, 131, 16342-16343 (2009).
323. A. Lendlein and R. Langer, Biodegradable, Elastic Shape-Memory Polymers for Potential Biomedical Applications, *Science*, 296, 1673-1676 (2002).
324. C. Liu, S. B. Chun, P. T. Mather, L. Zheng, E. H. Haley and E. B. Coughlin, Chemically Cross-Linked Polycyclooctene: Synthesis, Characterization, and Shape Memory Behaviour, *Macromolecules*, 35, 9868-9874 (2002).
325. J. Xu, W. Shi and W. Pang, Synthesis and shape memory effects of Si-O-Si cross-linked hybrid polyurethanes, *Polymer*, 47, 457-465 (2006).
326. I. A. Rousseau and P. T. Mather, Shape Memory Effect Exhibited by Smectic-C Liquid Crystalline Elastomers, *Journal of the American Chemical Society*, 125, 15300-15301 (2003).
327. K. Gall, M. L. Dunn, Y. Liu, G. Stefanic and D. Balzar, Internal stress storage in shape memory polymer nanocomposites, *Applied Physics Letters*, 85, 290-292 (2004).
328. J. Diani, Y. Liu and K. Gall, Finite strain 3D thermoviscoelastic constitutive model for shape memory polymers, *Polymer Engineering & Science*, 46, 486-492 (2006).
329. S. J. Tey and et al., Influence of long-term storage in cold hibernation on strain recovery and recovery stress of polyurethane shape memory polymer foam, *Smart Materials and Structures*, 10, 321 (2001).
330. M. Di Prima, K. Gall, D. L. McDowell, R. Guldberg, A. Lin, T. Sanderson, D. Campbel and S. C. Arzberger, Deformation of epoxy shape memory polymer foam. Part I: Experiments and macroscale constitutive modeling, *Mechanics of Materials*, 42, 304-314.
331. Z. D. Wang, D. F. Li, Z. Y. Xiong and R. N. Chang, Modeling Thermomechanical Behaviours of Shape Memory Polymer, *Journal of Applied Polymer Science*, 113, 651-656 (2009).

332. S. C. H. Lu and K. S. Pister, Decomposition of deformation and representation of the free energy function for isotropic thermoelastic solids, *International Journal of Solids and Structures*, 11, 927-934 (1975).
333. V. A. Lubarda, Constitutive theories based on the multiplicative decomposition of deformation gradient: Thermoelasticity, elastoplasticity, and biomechanics, *Applied Mechanics Reviews*, 57, 95-108 (2004).
334. A. Lion, On the large deformation behaviour of reinforced rubber at different temperatures, *Journal of the Mechanics and Physics of Solids*, 45, 1805-1834 (1997).
335. S. Govindjee and S. Reese, A Presentation and Comparison of Two Large Deformation Viscoelasticity Models, *Journal of Engineering Materials and Technology*, 119, 251-255 (1997).
336. J. C. Simo, R. L. Taylor and K. S. Pister, Variational and projection methods for the volume constraint in finite deformation elasto-plasticity, *Computer Methods in Applied Mechanics and Engineering*, 51, 177-208 (1985).
337. P. J. Flory, Thermodynamic relations for high elastic materials, *Transactions of the Faraday Society*, 57, 829-838 (1961).
338. C. Liang and C. A. Rogers, One-Dimensional Thermomechanical Constitutive Relations for Shape Memory Materials, *Journal of Intelligent Material Systems and Structures*, 1, 207-234 (1990).
339. E. A. Pieczyska, W. K. Nowacki, H. Tobushi and S. Hayashi, Thermomechanical properties of shape memory polymer subjected to tension in various conditions, *Qirt Journal*, 6, 189-205 (2009).
340. Q. H. Meng, J. L. Hu, L. Y. Yeung and Y. Hu, The Influence of Heat Treatment on the Properties of Shape Memory Fibers. II. Tensile Properties, Dimensional Stability, Recovery Force Relaxation, and Thermomechanical Cyclic Properties, *Journal of Applied Polymer Science*, 111, 1156-1164 (2009).
341. G. W. Scherer, Theories of relaxation, *Journal of Non-Crystalline Solids*, 123, 75-89 (1990).
342. G. W. Scherer, Use of the Adam-Gibbs Equation in the Analysis of Structural Relaxation, *Journal of the American Ceramic Society*, 67, 504-511 (1984).
343. J. Mijović, L. Nicolais, A. D'Amore and J. M. Kenny, Principal features of structural relaxation in glassy polymers. A Review, *Polymer Engineering & Science*, 34, 381-389 (1994).
344. A. J. Kovacs, J. J. Aklonis, J. M. Hutchinson and A. R. Ramos, Isobaric volume and enthalpy recovery of glasses. II. A transparent multiparameter theory, *Journal of Polymer Science: Polymer Physics Edition*, 17, 1097-1162 (1979).
345. Y. Zheng and G. B. McKenna, Structural Recovery in a Model Epoxy: Comparison of Responses after Temperature and Relative Humidity Jumps, *Macromolecules*, 36, 2387-2396 (2003).
346. A. G. Tool, Relation Between Inelastic Deformability and
Thermal Expansion of Glass in Its Annealing Range, *Journal of the American Ceramic Society*, 29, 240-253 (1946).
347. G. Adam and J. Gibbs, On the temperature dependence of cooperative relaxation properties in glass-forming liquids., *J. Chem. Phys.*, 139-146 (1965).
348. I. M. Hodge, Effects of annealing and prior history on enthalpy relaxation in glassy polymers. 6. Adam-Gibbs formulation of nonlinearity, *Macromolecules*, 20, 2897-2908 (1987).
349. Q. X. S. Xia, M. C. Boyce and D. M. Parks, A constitutive model for the anisotropic elastic-plastic deformation of paper and paperboard, *International Journal of Solids and Structures*, 39, 4053-4071 (2002).

350. E. M. Arruda and M. C. Boyce, A three-dimensional constitutive model for the large stretch behaviour of rubber elastic materials, *Journal of the Mechanics and Physics of Solids*, 41, 389-412 (1993).
351. H. J. Qi and M. C. Boyce, Constitutive model for stretch-induced softening of the stress-stretch behaviour of elastomeric materials, *Journal of the Mechanics and Physics of Solids*, 52, 2187-2205 (2004).
352. S. Cantournet, M. C. Boyce and A. H. Tsou, Micromechanics and macromechanics of carbon nano tube-enhanced elastomers, *Journal of the Mechanics and Physics of Solids*, 55, 1321-1339 (2007).
353. A. S. Argon, A theory for the low-temperature plastic deformation of glassy polymers, *Philosophical Magazine*, 28, 839 - 865 (1973).
354. R. N. Haward and G. Thackray, The Use of a Mathematical Model to Describe Isothermal Stress-Strain Curves in Glassy Thermoplastics, *Proceedings of the Royal Society of London. Series A, Mathematical and Physical Sciences*, 302, 453-472 (1968).
355. E. M. Arruda, M. C. Boyce and R. Jayachandran, Effects of strain rate, temperature and thermomechanical coupling on the finite strain deformation of glassy polymers, *Mechanics of Materials*, 19, 193-212 (1995).
356. L. Anand and N. M. Ames, On modeling the micro-indentation response of an amorphous polymer, *International Journal of Plasticity*, 22, 1123-1170 (2006).
357. H. Eyring, Viscosity, Plasticity, and Diffusion as Examples of Absolute Reaction Rates, *Journal of Chemical Physics*, 4, 283-291 (1936).
358. J. Sweeney, H. Shirataki, A. P. Unwin and I. M. Ward, Application of a necking criterion to PET fibers in tension, *Journal of Applied Polymer Science*, 74, 3331-3341 (1999).
359. M. C. Boyce, G. G. Weber and D. M. Parks, On the kinematics of finite strain plasticity, *Journal of the Mechanics and Physics of Solids*, 37, 647-665 (1989).
360. H. A. Khonakdar, S. H. Jafari, S. Rasouli, J. Morshedian and H. Abedini, Investigation and modeling of temperature dependence recovery behaviour of shape-memory crosslinked polyethylene, *Macromolecular Theory and Simulations*, 16, 43-52 (2007).